11-28-2013 12:00 AM

Characterization of the Corrosion and Oxide Film Properties of Alloy 600 and Alloy 800

Melissa Faichuk, *The University of Western Ontario*

Supervisor: Dr. David Shoesmith, *The University of Western Ontario*

A thesis submitted in partial fulfillment of the requirements for the Doctor of Philosophy degree in Chemistry

Characterization of the Corrosion and Oxide Film Properties of Alloy 600 and Alloy 800

(Thesis format: Integrated Article)

by

Melissa Gail Faichuk

Graduate Program
In
Chemistry

A thesis submitted in partial fulfillment
of the requirements for the degree of
Doctor of Philosophy

The School of Graduate and Postdoctoral Studies
The University of Western Ontario
London, Ontario, Canada

Abstract

The passive film properties of Alloy 600 and Alloy 800, both of which are used as steam generator tubing in CANDU reactors, have been studied using techniques such as polarization scans, electrochemical impedance spectroscopy and X-ray photoelectron and Auger electron spectroscopies. The composition of the oxides formed in a 0.1 M $Na_2S_2O_3$ solution have been characterized over a wide range of potentials from the pre-passive, through the passive to the transpassive regions. These changes have been correlated to the electrochemical behaviour. A second set of experiments was performed to determine the effectiveness of surface mechanical attrition treatment (SMAT) as a method of enhancing the corrosion resistance of the alloys by the creation of a nanostructured surface layer.

In chapters 3 and 4, the compositional and electrochemical characteristics of the oxide films formed on Alloy 600 and Alloy 800 are described as a function of applied film growth potential. A comparison of the two alloys is presented in Chapter 5. The results show that Alloy 800 exhibits a superior corrosion resistance than Alloy 600. This was attributed to the more facile formation of a Cr_2O_3 barrier layer due to the segregation of Fe to the outer surface of the oxide and the retention of Ni in the alloy surface. For Alloy 600, the more noble Ni is not so readily segregated to the outer surface which results in the formation of a thinner, less protective barrier layer.

The effects of surface deformation induced by SMAT on the properties of the oxides formed on Alloy 600 and Alloy 800 are discussed in Chapters 6 and 7. This treatment alters the composition of the films, and generally accelerates their degradation.

This can be attributed to an increase in ion mobility through the less coherent films formed on the SMAT damaged surfaces.

Key Words:

Corrosion, Stress Corrosion Cracking (SCC), Passivity, Passive Film, Bilayer Oxide, Barrier Layer, Alloy 600, Alloy 800, Cr_2O_3, $Na_2S_2O_3$, Surface Mechanical Attrition Treatment, SMAT.

Acknowledgements

Firstly, I would like to thank co-supervisors, Dr. Sridhar Ramamurthy and Dr. David Shoesmith for their guidance and support during my graduate work. Unlike many of my peers, I was lucky enough to have two fantastic supervisors to help guide me through my studies.

I would like to thank the members of the Shoesmith and Wren groups, as well as the staff at Surface Science Western. I feel incredibly lucky to have been able to work with and learn from such a knowledgeable and hardworking group of people.

Also, Dr. Clara Wren, who took me into her group as one of her own, and Dr. Jamie Noel, whose patience and humour taught so many invaluable things during my time at Western.

Without the love and support of my family, I would have never been able to accomplish what I have, and for that I am grateful.

Finally, I would like to thank Andrew for providing me with the unconditional love, support and encouragement necessary to get me through the last 5 years. You're the best!

Table of Contents

Symbols and Acronyms

Symbols

C	Capacitance
E	Amplitude
E_b	Binding energy
$E_b(k)$	Binding energy, core shell
$E_b(L)$	Binding energy, outer shell
E_{corr}	Corrosion potential
E_f	Fermi level
E_k	Kinetic energy
e^-	Electron
G	Modulus of rigidity
i	Current
l	Grain diameter
L	Film thickness
M	Metal atom
M_M	Metal cation
M^{n+}	Oxidized metal species
$M^{(x+y)}$	Metal cation in solution
n	Number of electrons
O^{2-}	Oxygen anion
Q_{CPE}	CPE parameter
R	Resistance
R_{CT}	Resistance, charge transfer
R_p	Resistance, polarization
R_s	Resistance, solution
t	Time
V	Potential
v	Potential difference
V_M	Cation vacancy
V_O	Oxygen vacancy
Z	Impedance
Z_{CPE}	Impedance of CPE
$\|Z\|$	Impedance modulus
Z’	Impedance, Real
Z’’	Impedance, Imaginary

α	CPE exponent
γ	Surface energy
λ	Inelastic mean free path
ν	Poisson's ratio
θ	Phase angle
σ_i	Stress
τ	Time constant
ϕ_{sp}	Work function
ω	Frequency

Acronyms

A600	Alloy 600
A800	Alloy 800
AC	Alternating Current
AES	Auger Electron Spectroscopy
BE	Binding Energy
CANDU	CANada Deuterium Uranium
CE	Counter Electrode
$Cr(OH)_3$	Chromium Hydroxide
Cr_2O_3	Chromium Oxide
DI	Deionized
D_2O	Deuterium Oxide (Heavy water)
EIS	Electrochemical Impedance Spectroscopy
FWHM	Full Width at Half Maximum
IMFP	Inelastic Mean Free Path
IGSCC	Intergranular Stress Corrosion Cracking
M-OH	Metal Hydroxide
M-O	Metal Oxide
Ni_{CF}	Nickel cation fraction
$Ni(OH)_2$	Nickel Hydroxide
PDM	Point Defect Model
PWR	Pressure Water Reactor
RE	Reference Electrode
R_P	Polarization Resistance
SAM	Scanning Auger electron Microscope
SCC	Stress Corrosion Cracking
SCE	Saturated Calomel Electrode
SEM	Scanning Electron Microscopy
SG	Steam Generator
SHE	Saturated Hydrogen Electrode

SMAT	Surface Mechanical Attrition Treatment
SS	Stainless Steel
SO_4^{2-}	Sulphate
S^{2-}	Sulphide
$S_2O_3^{2-}$	Thiosulphate
UHV	Ultra-High Vacuum
V_{SCE}	Potential vs. SCE
WE	Working Electrode
XPS	X-ray Photoelectron Spectroscopy
ZrO_2	Zirconium Oxide

List of Tables

List of Figures

Chapter 1. Introduction

1.1 Thesis Objectives

Ni-Cr-Fe alloys, such as Alloy 600 and Alloy 800, form passive oxide surface films essential for their protection against corrosion. These films have been characterized in various chemical environments [1-11], and their electrochemical behaviour studied [6, 9, 12-19]. Following experiments by Coriou, *et al.,* [20, 21] who demonstrated that Alloy 600 was susceptible to stress corrosion cracking (SCC), significant progress has been made in an attempt to further understand this process [22-40]. Included in this progress are a number of studies focused on the effect of S and reduced S species on Ni-Cr-Fe alloys, and how these species influence the oxide film and enhance SCC susceptibility [5, 40-56]. Despite this knowledge, studies have not yet been conducted which examine and attempt to correlate the oxide film composition and electrochemical behaviour of Alloy 600 and Alloy 800 in $S_2O_3^{2-}$ containing solutions. A comparison of their behaviour in $Na_2S_2O_3$ solutions could provide insight into the improved resistance to SCC of Alloy 800 compared to Alloy 600.

A surface modification technique, surface mechanical attrition treatment (SMAT), was investigated as a possible method of enhancing corrosion resistance. This technique involves the modification of a sample surface through repeated, random, multidirectional particle impacts which creates surface deformations and induces strain in the alloy surface. This treatment can ultimately lead to nanoscale grain refinement in the surface, which is thought to enhance the properties of the alloy in this layer [57, 58]. The

experiments performed were used to determine how this technique might affect the corrosion resistance of Alloy 600 and Alloy 800.

Three primary objectives were defined for this thesis: (1) Investigation of the oxides formed on Alloy 600 and Alloy 800 in the presence of $S_2O_3^{2-}$; (2) Comparison of the oxides formed in this solution to determine what makes Alloy 600 susceptible to SCC but Alloy 800 relatively immune; (3) Determination of the role of SMAT in changing the surface oxide properties of these alloys and what affect this may have on their electrochemical behaviour.

To achieve these objectives, several electrochemical and surface analytical techniques were employed. The electrochemical behaviour of the passive film was investigated using electrochemical impedance spectroscopy (EIS) and anodic polarization measurements. Surface analytical techniques, such as Auger electron spectroscopy (AES) and X-ray photoelectron spectroscopy (XPS) were used to obtain elemental composition information on the electrochemically grown oxide films. The five distinct areas of study in this thesis are the following:

- A comprehensive study of the oxide film composition and the electrochemical behaviour of Alloy 600 in $Na_2S_2O_3$.
- A comprehensive study of the oxide film composition and the electrochemical behaviour of Alloy 800 in $Na_2S_2O_3$.
- A comparison of the differences in behaviour of the two alloys.

- A comprehensive study of the oxide film composition and the electrochemical behaviour of SMAT Alloy 600 in $Na_2S_2O_3$.

- A comprehensive study of the oxide film composition and electrochemical behaviour of SMAT Alloy 800 in $Na_2S_2O_3$.

1.2 Materials Background

1.2.1 Alloy 600 and Alloy 800

Alloy 600 and Alloy 800 are Ni-Cr-Fe base alloys designed for use in high temperature environments and possess high strength, good workability and resistance to corrosion. The elemental composition of these alloys, obtained from Rolled Alloys Inc., is given in Table 1.1.

Table 1.1 Chemical composition of Alloy 600 and Alloy 800 SG tubing (wt%) from Rolled Alloys Inc.

	Ni	Cr	Fe	Mn	Al	Ti	Si	C
Alloy 600	72.97	16.14	9.65	0.34	0.27	0.23	0.15	0.03
Alloy 800	30.86	20.37	45.76	0.72	0.40	0.53	0.54	0.07

Alloy 600 is designed for applications that require resistance to heat and corrosion. Compared to stainless steel (SS), the high Ni content gives this alloy superior corrosion resistance under reducing conditions, and in the presence of alkaline solutions. Ni also provides improved weldability, and metallurgical and thermal stability. It is resistant to corrosion by high purity water, and the Ni component also makes it resistant to Cl^- induced SCC, making it a superior product compared to austenitic SS in aqueous environments [59-61]. The addition of Cr to the Ni matrix improves resistance to high

temperature oxidation and enhances resistance to pitting and crevice corrosion. Cr can also provide corrosion resistance in S containing environments, which can increase the rate of intergranular stress corrosion cracking (IGSCC) at moderate temperatures. This alloy is typically used for applications that require resistance to corrosion and heat, making it an ideal candidate to replace SS as steam generator (SG) tubing in nuclear reactors [61].

Alloy 800 is designed for high temperature corrosion applications, and was fabricated to address the eventually recognized shortcomings of Alloy 600. At low temperatures, the general corrosion resistance of Alloy 800 is similar to that of other austenitic Ni-Cr-Fe alloys. At elevated temperatures, however, it offers superior resistance to oxidation, carburizing, and sulfidation resulting from the high Cr content compared to Alloy 600. The Ni content of Alloy 800, while lower than that of Alloy 600, remains high enough to resist SCC and maintain a ductile, austenitic structure. The enhanced Fe content also improves resistance to high temperature carburizing environments, controls thermal expansion, and reduces alloy cost. The properties of Alloy 800 are further enhanced by increasing the concentrations of Al, to improve resistance to oxidation at elevated temperatures, and Ti, which can preferentially combine with C to reduce susceptibility to IGSCC caused by Cr carbide precipitation [59, 62]. Alloy 800, however, is not without its shortcomings, a susceptibility to SCC under specific conditions having recently been demonstrated [26, 28, 32].

1.3 Corrosion

1.3.1 Corrosion Principles

Corrosion is the result of interactions between materials and their environment. While the mechanisms can vary, the process typically involves the oxidation of a metal. Corrosion reactions in aqueous solutions can be characterized by four features: (1) The electrified interface between the metal and solution; (2) transfer of positive charge from the metal to an oxidant in the solution, resulting in the oxidation of the metal to a higher valence state (anodic reaction); (3) transfer of positive charge from the solution to the metal, resulting in the reduction of an oxidant in the solution to a lower valence state (cathodic reaction); (4) transfer of charge by electrolyte ions in the solution between the anode and cathode [63]. The driving force for corrosion is the difference in electrochemical potentials between the metal oxidation and oxidant reduction reactions. To approach equilibrium, this inequality in electrochemical potentials must be reduced through changes to the chemical states of the metal and the oxidant. In the simplest case, the corrosion reaction is the transfer of oxidized atoms from the solid into the solution,

$$M \rightarrow M^{n+} + ne^{-} \tag{1.1}$$

where M represents the metal, M^{n+} the oxidized metal species and ne^- the number of electrons transferred. The metal oxidation must be sustained by the consumption of electrons by an oxidant, where *Ox* represents the soluble oxidant and *Red* the reduced form of the oxidant.

$$Ox + ne^{-} \rightarrow Red \tag{1.2}$$

Metal oxidation occurs on a site referred to as the anodic reaction site while the electrons are received at the cathodic reaction site. The three cathodic reactions most commonly encountered are (1.3) oxygen reduction, (1.4) water reduction and (1.5) proton reduction,

$$O_2 + 4H^+ + 4e^- \rightarrow 2H_2O \quad (pH < 7) \tag{1.3}$$

$$O_2 + 2H_2O + 4e^- \rightarrow 4OH^- \quad (pH > 7) \tag{1.4}$$

$$2H^+ + 2e^- \rightarrow H_2 \tag{1.5}$$

As a consequence of the transfer of ions and electrons on the metal surface, differences in electrical potential, $\Delta\phi_a$ and $\Delta\phi_c$, develop between the metal and the aqueous solution at the anodic and cathodic sites, respectively [64].

$$\Delta\phi_a = \phi_{M,a} - \phi_{S,a} \tag{1.6}$$

$$\Delta\phi_c = \phi_{M,c} - \phi_{S,c} \tag{1.7}$$

The anodic and cathodic sites are designated by the subscripts *a* and *c*, while subscripts *M* and *S* represent the metal and solution phases. The driving potential for the corrosion reaction in the solution, $\Delta\phi_S$, is given by:

$$\Delta\phi_S = \phi_c - \phi_a \tag{1.8}$$

Once formed, the oxidized metal, M^{n+}, can dissolve into the aqueous phase or combine with an oxygen or hydroxide ion to form an oxide/hydroxide layer. The extent of dissolution and the nature of the film formation reaction are highly dependent on the environment [64].

1.4 Passivation

Passivity refers to the loss of chemical reactivity experienced by metals/alloys under particular environmental conditions. All of the major alloying elements in alloys 600 and 800; Fe, Ni and Cr, are capable of passivation by the formation of a stable inert surface oxide film [63, 65]. The typical electrochemical behaviour of a material that demonstrates passivity is shown in Figure 1.1 and can be divided into three regions; (1) active, (2) passive and (3) transpassive.

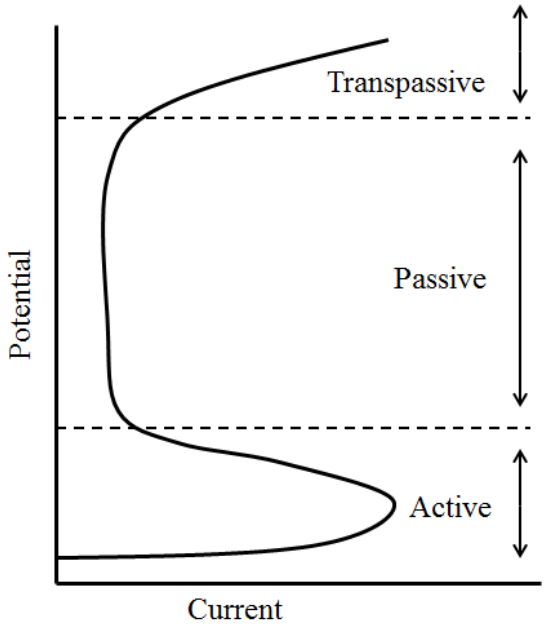

Figure 1.1 Schematic polarization curve for an active-passive metal/alloy indicating the active, passive and transpassive regions.

In the active region, an increase in potential results in a rapid increase in the current since the metal is unprotected. At a specific potential the current begins to decrease, signalling the onset of inhibition of metal dissolution by the onset of oxide film formation.

Eventually, the oxide becomes electrochemically unstable and the current starts to increase again in the transpassive region (3).

1.5 Bilayer Oxide Film Formation

Passive films generally form as bilayers, with a highly disordered barrier layer adjacent to the metal and an outer layer comprised of a hydrated or precipitated phase that may incorporate anions/cations from the solution phase, Figure 1.2.

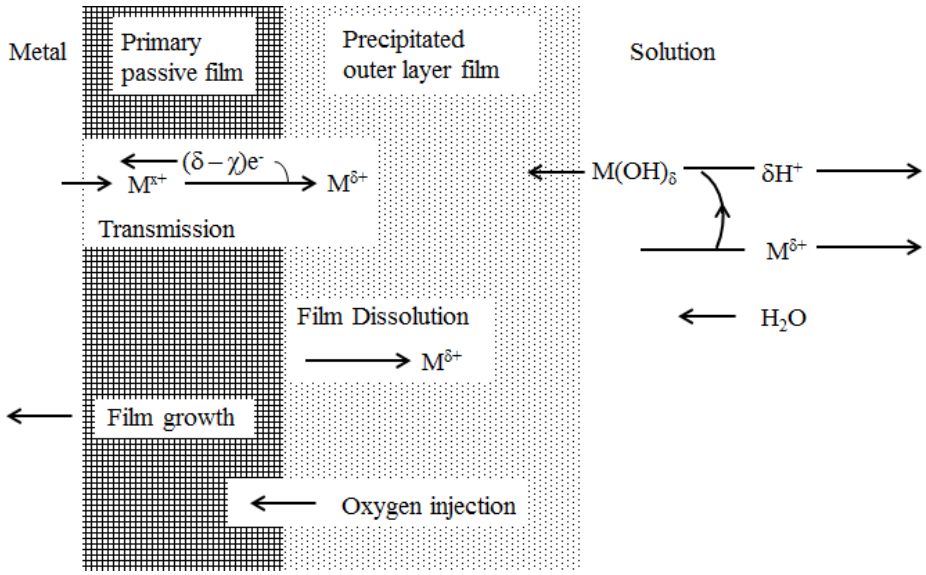

Figure 1.2 Schematic showing the formation of a bilayer passive film on a metal surface through the movement of the metal interstitial cation, M^{x+}, and its dissolution/precipitation at the oxide/solution, $M^{\delta+}$ (aq) [76].

Numerous studies have shown that the structure of the passive film on Cr-containing alloys, such as the Ni-Cr-Fe alloys investigated in this study, also consists of a bilayer oxide, with a Cr rich inner barrier layer and an outer layer containing a mixture of Fe, Ni and Cr, depending on the immersion environment [5, 7, 8, 11, 55, 66-77]. Passivity is largely attributed to the Cr rich barrier layer, since it is also observed in the absence of

the outer layer in solutions that are highly acidic or basic when the precipitation or accumulation of an outer layer is prevented [76].

1.6 Oxide Film Growth Mechanisms

Experimentally, film growth kinetics follow either: (1.9) logarithmic or (1.10) inverse logarithmic laws, where L is the film thickness, t is time and A, B, C and D are constants.

$$L = A + B \ln t \tag{1.9}$$

$$\frac{1}{L} = C - D \ln t \tag{1.10}$$

Several models have been proposed to explain film growth via one or other of these laws [78]. One of the earliest models for film growth was proposed by Mott [79] and extended by Mott and Cabrera [80]. A series of assumptions were made in the development of this model. The first assumption is that film growth is due to the transport of metal cations across the oxide film to the film/solution interface where oxide formation occurs by reaction with the electrolyte. Secondly, it is assumed that transport of the cations through the film is assisted by the high electric field strength existing within the oxide. Thirdly, the field strength is taken to be constant through the film. Finally, the rate limiting step for film growth is assumed to be the emission of metal cations from the metal into the film at the metal/film interface. Development of this model led to a rate law that closely resembled the inverse logarithmic law, equation 1.10.

Sato and Cohen [81] developed the “place-exchange” mechanism in 1964 to explain the results from their study of Fe in a pH 8.4 borate buffer solution. According to

this model, a layer of O is first adsorbed onto the metal surface, which then exchanges charge and places with the underlying metal. A second layer of O is then adsorbed and the two M-O pairs rotate simultaneously. Repetition of this process results in film thickening. A schematic of this process is shown in Figure 1.3. Development of this model yielded a logarithmic rate law, equation 1.9.

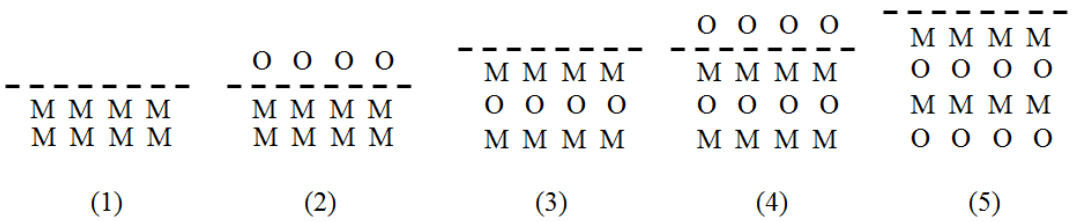

Figure 1.3 Illustration of oxide film growth by the place-exchange mechanism; M, metal ion, O oxygen ion. Adsorption of the oxygen onto the metal surface (2) then allows for both charge and "place-exchange" between the oxygen and metal (3). A second layer of oxygen is adsorbed onto the surface (4), and a second "place-exchange occurs with two M-O pairs (5) [78].

The model developed by Mott and Cabrera was modified by Fehlner and Mott [82], to provide an alternative to the "place-exchange" model, whose mechanism does not provide a convincing argument for films that grow thicker than two monolayers. With this modification, the following assumptions were made: (1) oxide ion diffusion is responsible for film growth; (2) incorporation of an oxide ion from the environment into the film at the film/solution interface is the rate limiting step; (3) the field strength is independent of film thickness; and (4) the activation energy for the rate limiting step increases linearly with thickness. This model also leads to a logarithmic law, equation 1.9.

More recently, Macdonald developed the point defect model (PDM-I) first conceived in 1979 [78, 83-85]. Several assumptions were made in the development of this model, including: (1) the oxide layer is a point defect phase containing cation vacancies and oxygen vacancies; (2) the concentration of point defects is much greater than in the isolated, bulk oxides, indicating the presence of continuous defect generation/annihilation processes; (3) defects are generated and annihilated at the metal/film and film/solution interfaces; (4) the electric field strength is independent of voltage and distance through the film; (5) The potential is distributed across the interphase region with drops at the metal/film interface, the film/solution interface and across the film; and (6) the potential drop across the film/solution interface is linearly dependent upon the applied potential and pH. This model successfully predicts the inverse logarithmic growth law (1.10), and can be extended to deal with passivity breakdown [85]. However, as was the case with the Mott/Cabrera and Fehlner/Mott models, the point defect model cannot account for the existence of steady-states in both the passive current density and film thickness and the formation of the bilayer films shown to be present on many metals and alloys.

A second generation of this model, PDM-II, incorporated a bilayer structure on the metal surface [76, 85]. While many assumptions from PDM-I remained, specific additional features include: (1) the recognition of the role played by barrier layer dissolution; (2) the recognition that interfacial reactions can be either lattice conservative or non-conservative processes; and (3) the possibility that interstitial cations as well as cation and oxygen vacancies can be involved in the growth of the barrier layer.

1.7 Stress Corrosion Cracking

SCC refers to the corrosion-assisted cracking of a metal or alloy caused by the simultaneous presence of tensile stress and a specific corrosive medium. Typically, SCC is defined as the failure of a material through slow, environmentally-induced crack propagation. The crack propagation is the result of an interaction between mechanical stress and corrosion, as well as specific metallurgical requirements in terms of alloy composition and structure. The stress concentration required to propagate a crack typically does not exceed the critical value required for mechanical failure of the material, and normal ductility standards are often observed. Propagation occurs at a very slow rate until the stresses in the ligaments of the metal exceed the fracture strength, when failure occurs. This type of corrosion is of great concern since it is extremely difficult to detect in the early/intermediate stages, and failure in an industrial setting could prove to be catastrophic [63, 86].

The process of SCC occurs in three steps: crack initiation, propagation and failure. Most commonly, SCC is initiated at pre-existing features on the surface, such as pits, grain boundaries or physical defects. SCC will propagate if a mechanism exists for concentrating the electrochemical energy release rate at the crack tip. SCC is unique in that corrosion proceeds along a narrow front to retain the geometry of the crack, implying that most of the exposed surfaces, including the walls of the crack, remain inactive. The transition from being electrochemically active at the crack tip to relatively inactive at the walls of the crack can only be achieved if a passive film is formed on the walls. This implies that the metal is in the active state and protective films cannot grow over the crack tip, or the presence of tensile stress can fracture the film that does form. Anodic

polarization curves can be used to anticipate the potential range over which SCC is most likely. At potentials where the alloy is in transition between the active corrosion and passive states, the necessary conditions for simultaneous film formation and crack tip dissolution will be met [63].

Many factors can affect a materials susceptibility to SCC, such as grain size. A Petch-type relationship between the grain diameter, l, and the stress at constant strain, σ_i, can be observed in equation 1.11,

$$\sigma_i = \sigma_0 + \frac{k}{\sqrt{l}} \tag{1.11}$$

where k and σ_0 are constants, and k may be related to the surface energy associated with the formation of new surfaces by fracture through,

$$k = \frac{6\pi G\gamma}{1-\nu}^{1/2} \tag{1.12}$$

where G is the modulus of rigidity, γ the surface energy and ν Poisson's ratio. The plastic flow characteristics of a material are influenced by grain size. Equation 1.11, showing the relationship between the stress, σ_i, and the grain size, l, arises from the resistance to the formation of a slip band at a grain boundary. This relationship can be shown to be relevant to the plastic behaviour of metals, since the grain-size dependence of SCC may simply reflect the fact that SCC is related to the plastic flow of the material [63, 86]

1.8 SCC in CANDU Nuclear Reactors

1.8.1 General Overview

The Canadian CANDU (CANada Deuterium Uranium) nuclear reactor provides a clean and reliable energy source as an alternative to the burning of conventional fossil fuels. The basic arrangement of the reactor is shown in Figure 1.4.

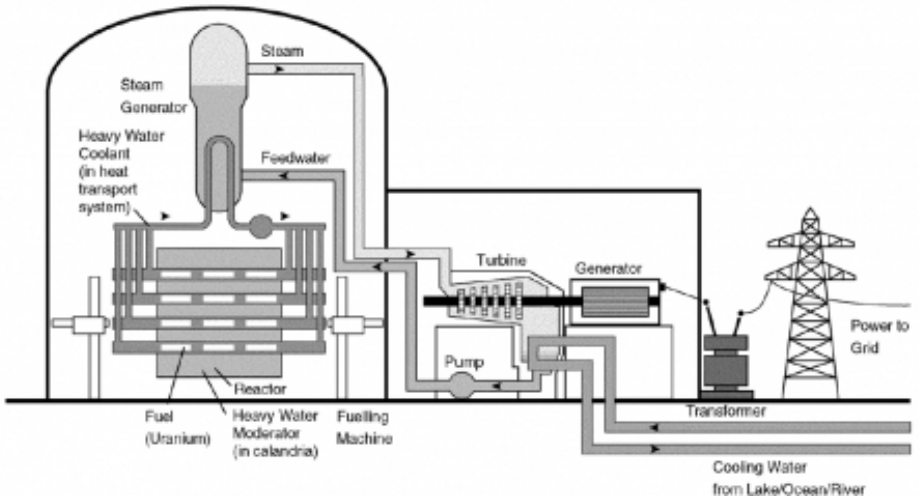

Figure 1.4 Schematic of a CANDU plant**.**

Fission of the UO_2 fuel in the reactor core produces a large amount of heat which is absorbed by the heavy-water (D_2O) coolant in the primary coolant loop. Circulation of the primary water through a heat exchanger allows heat transfer to the light-water secondary cooling loop, which powers a steam turbine with an electrical generator. Separating the primary water from the secondary water while allowing efficient heat transfer is the function of the SG tubing, constructed out of a Ni-Cr-Fe base alloy; typically Alloy 600, 690 or 800. The failure of this tubing as a result of corrosion is an

important issue for reasons relating to safety, reactor lifetime, and the cost associated with reactor shut down and material replacements.

1.8.2 SCC of SG Tubing Materials Alloy 600 and Alloy 800

A great deal of attention has been placed on nuclear power generation as a viable alternative to fossil fuel combustion, and a very high standard must be placed on the integrity of the reactor components to ensure safe operation. Heat exchanger tubing was originally fabricated from austenitic SS, such as AISI Type 304, until these materials were found to be highly susceptible to SCC in caustic and Cl^- containing solutions [27, 29, 31, 32, 38, 87]. From a reactor standpoint this was problematic, since Cl^- species are difficult to completely remove from an aqueous environment and can concentrate on SG tubing surfaces. Consequently, SS was replaced with Alloy 600, whose higher Ni content ensured improved corrosion resistance. The elevated Ni content minimized the alloy's susceptibility to transgranular SCC in the presence of Cl^- [27, 38]. Another candidate, Alloy 800, with lower Ni, but higher Fe and Cr contents compared to Alloy 600, also demonstrated excellent resistance to SCC in pure water and Cl^- containing solutions [27, 32, 88-91].

Throughout the past several decades that Alloy 600 has been in service, numerous reports detailing Alloy 600 SG tubing succumbing to SCC on the primary and secondary sides have emerged [43, 88]. In a laboratory setting, Coriou *et. al*., established that Alloy 600 could undergo SCC [20, 21], and since then, IGSCC of Alloy 600 has been observed to occur in a number of different environments. Alloy 600 has been shown to be susceptible to SCC in the presence of H_2 [11, 88, 92, 93] and in the presence of impurities

such as Pb [28, 36, 37, 94-96] and O_2 [31, 36]. It has also experienced IGSCC under highly stressed conditions, regardless of mill annealing, cold working or stress relieving [27].

By contrast, there have been no reports to date of SCC failures of SG tubing in CANDU plants that use Alloy 800, which has been in service for over 40 years [14, 97]. In laboratory experiments, higher stresses and temperatures are required to initiate SCC compared to Alloy 600 [98]. Alloy 800 was also shown to be resistant to IGSCC in high temperature water containing both Pb and O_2 [27].

One major issue that appears to affect the corrosion performance of both alloys is the presence of reduced S species. Recently, numerous reports have shown that reduced S species can enhance IGSCC [5, 26, 45, 47, 49]. S has been identified as an important impurity that is introduced into the secondary water from various sources, such as feed water, resin sources or condenser leaks [5, 45]. Under SG operating conditions, common S species such as SO_4^{2-}, can be reduced to lower valence species such as $S_2O_3^{2-}$ or S^{2-} by hydrazine, whose addition to the SG coolant can reduce the dissolved O concentrations to control corrosion. Lower valence S species are considered to be more corrosive than SO_4^{2-} [45]. Through electro-reduction or disproportionation reactions, S is easily generated from $S_2O_3^{2-}$, equations (1.13) and (1.14) [12, 49].

$$S_2O_3^{2-} + 6H^+ + 4e^- \rightarrow 2S + 3H_2O \quad (1.13)$$

$$S_2O_3^{2-} + H^+ \rightarrow S + HSO_3^- \quad (1.14)$$

The deposition of S on the surface of SG materials has been shown to affect oxide film stability, and promote localized corrosion [86, 88, 99, 100]. On Ni and Ni base alloys,

the presence of S has been shown to catalyze anodic dissolution and hinder film formation [48, 101]. A proposed mechanism suggests that the adsorbed S species on the surface of the metal/alloy causes strong metal-S bonds, weakening the metal-metal bonds of the outermost atoms. This lowers the energy required for anodic dissolution, as observed experimentally by Marcus, *et al*., [101]. Reduced S species are also thought to retard crack tip re-passivation during IGSCC [49].

1.9 Surface Mechanical Attrition Treatment (SMAT)

The grain structure and grain boundary character of the surface layer of a material can be artificially engineered by applying a source of external energy, to induce the formation of an extremely high density of crystalline defects and cascades of dislocations. Examples of such processes include shot peening [102] and laser irradiation [103]. Shot peening has the advantage of low cost and high throughput, but the rough surface of the small shots impacting the surface can result in wear and damage to the nanostructured layer during treatment [58].

SMAT is a technique based off shot peening principles and can induce a large number of defects into the surface layer of the bulk material, transforming the microstructure and creating a thin, nanocrystalline layer [58, 104]. This technique has been successfully applied to a number of materials, including pure metals and alloys [58, 105-109]. Nanostructured materials are known to possess properties that differ greatly from their bulk counterparts including enhanced physical properties, improved tribology and super plasticity at low temperatures [104, 110-114]. SMAT utilizes ultrasonic vibrations at a frequency as high as 20 kHz to accelerate small particles (shots) towards a

sample surface. High strain rates lead to severe plastic deformation in the top layers of the specimen, penetrating to depths of 100 microns. Figure 1.5 illustrates the experimental arrangement for SMAT.

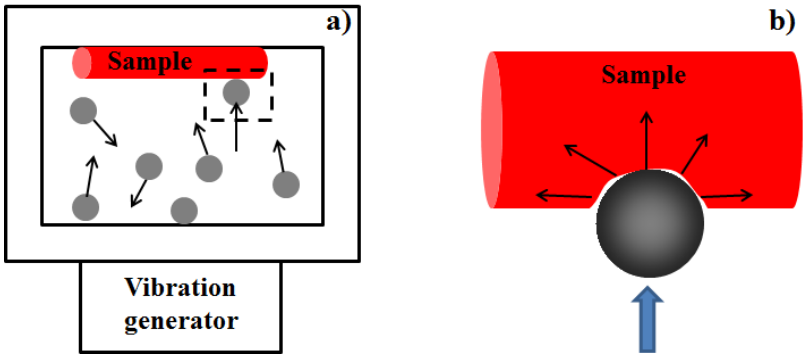

Figure 1.5 Schematic illustrations of (a) the SMAT set-up showing the sample (in red) and shots inside of the chamber and (b) the impact of the shot on the samples surface, creating the multidirectional plastic deformation in the sample.

Both the sample specimen and spherical shots are placed in a reflecting chamber that is vibrated by an ultrasound vibration generator. The size of the shot can vary between 1 mm and 10 mm in diameter, and the vibration frequency of the chamber can range from 50 Hz to 20 kHz. Depending on the vibration frequency, shot size, composition and distance from the specimen, the shot velocity can range from 1 to 20 m/s. Each impact will induce plastic deformation at a high strain rate in the surface layer of the sample, as schematically shown in Figure 1.5. As a consequence of this treatment, the impact creates severe plastic deformation and grain refinement down to the nanometer regime on the entire sample surface. A schematic cross section of a treated sample, Figure 1.6, illustrates how the strain and microstructure characteristics can change as a function of depth in to the sample. At the surface both the strain concentration and degree of grain

refinement are highest. At progressively deeper locations into the sample, the strain rate decreases, as does the degree of refinement until the coarse grain matrix is reached.

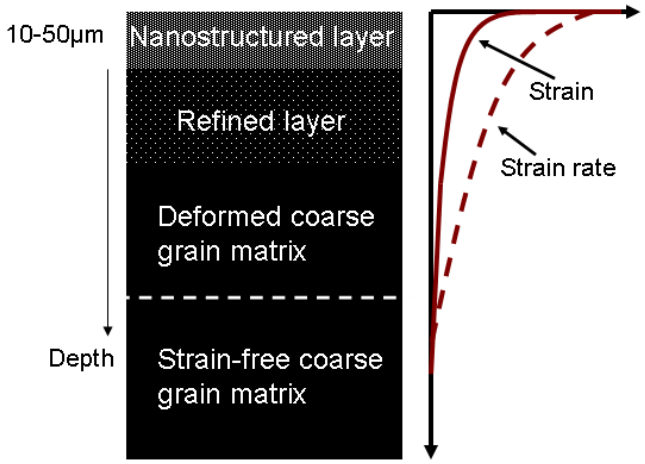

Figure 1.6 The sample cross section illustrating the effects of SMAT as a function of penetration depth [58].

When compared to the traditional shot peening method, several differences can be noted, one of which is the larger shot size (1-10 mm for SMAT vs. 0.2-1 mm for shot peening). The shots used for SMAT possess a very smooth surface, which prevents wear and other damage to the treated surface caused by the normal shot peening process. The velocity at which the SMAT shots impact the surface is also much lower (1-20 m/s) compared to shot peening (100 m/s), and the angle of impact using SMAT is random and multidirectional, not fixed. These factors lead to the enhanced degree of grain refinement observed in surfaces treated by SMAT.

1.10 Thesis Summary

The work presented in this thesis is divided into two primary components. Chapters 3 through 5 identify the compositional and electrochemical differences between

the oxide films formed on Alloy 600 and Alloy 800. Chapters 6 and 7 discuss the effects of surface mechanical attrition treatment on the composition and behaviour of the oxide films formed on these same alloys. Chapter 8 will include a summary of the results presented in this thesis, and the future direction of this project.

References

[1] L.A.S. Ries, M. Da Cunha Belo, M.G.S. Ferreira, I.L. Miller, Corros. Sci., 50 (2008) 676-686
[2] N.S. McIntyre, D.G. Zetaruk, D. Owen, J. Electrochem. Soc., 126 (1979) 750-760
[3] V. Maurice, W.P. Yang, P. Marcus, J. Electrochem. Soc., 145 (1998) 909-920
[4] M. Seo, N. Sato, Corros., 36 (1980) 334-339
[5] E.H. Lee, K.M. Kim, U.C. Kim, Mater. Sci. Eng., A449 (2007) 330-333
[6] D.-J. Kim, H.-C. Kwon, H. Kim, Corros. Sci., 50 (208) 1221-1227
[7] M. Da Cunha Belo, N.E. Hakiki, M.G.S. Ferreira, Electrochim. Acta., 44 (1999) 2473-2481
[8] P. Marcus, J.M. Grimal, Corros. Sci., 33 (1992) 805-814
[9] R.S. Dutta, R. Purandare, A. Lobo, S.K. Kulkarni, G.K. Dey, Corros. Sci., (2004) 2937-2953
[10] R.S. Dutta, J. Jagannath, G.K. Dey, P.K. Dey, Corros. Sci., 48 (2006) 2711-2726
[11] T. Dan, T. Shoji, Z. Lu, K. Sakaguchi, J. Wang, E.-H. Han, W. Ke, Corros. Sci., 52 (2010) 1228-1236
[12] T. Nickchi, A. Alfantazi, Corros., 68 (2012) 1-11
[13] J.-S. Baek, J.-G. Kim, D.-H. Hur, J.-S. Kim, Corros. Sci., 45 (2003) 983-994
[14] X. Li, J. Wang, E.-N. Han, W. Ke, Corros. Sci., 67 (2013) 169-178
[15] J.-J. Park, S.-I. Pyun, S.-B. Lee, Electrochim. Acta., 49 (2004) 281-292
[16] R. M. Carranza, M.G. Alvarez, Corros. Sci., 38 (1996) 909-925
[17] A.M. Olmedo, M. Villegas, M.G. Alvarez, J. Nucl. Mater., 229 (1996) 102-114
[18] T. Nickchi, A. Alfantazi, Corros. Sci., 52 (2010) 4035-4045
[19] T. Nickchi, A. Alfantazi, Electrochim. Acta., 58 (2011) 743-749
[20] H. Coriou, L. Grall, Y. Legall, S. Vettier, 3rd Metallurgy Symposium on Corrosion, North Holland publishing Co., Amsterdam (1960)
[21] H. Coriou, L. Grall, Y. De Gall, S. Vettier, Colloque sur les Materiaux de Reacteurs, Stockholm, North-Holland Publishing Co., Amsterdam, The Netherlands, (1959) 161-174
[22] W.-T. Tsai, C.-H. Chou, Mater. Sci. Eng., A288 (2000) 5-11
[23] W.-T. Tsai, M.-J. Sheu, J.-T. Lee, Corros. Sci., 38 (1996) 33-45
[24] C.L. Briant, C.S. O'Toole, E.L. Hall, Corros., 42 (1986) 15-27
[25] R.C. Scarberry, S.C. Pearman, J.R. Crum, Corros., 32 (1976) 401-406
[26] W. Yang, Z. Lu, D. Huang, D. Kong, G. Zhao, J. Congleton, Corros. Sci., 43 (2001) 963-977
[27] P.K. De, S.K. Ghosal, Corros., 37 (1981) 341-349
[28] D. Van Rooyen, Corros., 31 (1975) 327-337
[29] R.C. Scarberry, S.C. Pearmen, J.R. Crum, Corros., 32 (1976) 401-406
[30] K. Sieradzki, R.C. Newman, J. Phys. Chem. Solids., 48 (1987) 1101-1113
[31] H.R. Copson, G. Economy, Corros., 24 (1968) 55-65
[32] J.R. Cels, Corros., 34 (1978) 198-209
[33] P.M Scott, 9th International Symposium on Environmental Degradation of Materials in Nuclear Power Systems – Water Reactors, (1999) 3-12
[34] D.-J. Kim, H.P. Kim, S.S. Hwang, J.S. Kim, J.Park, Met. Mater. Int., 16 (2010) 259-266
[35] C.H. Shen, P.G. Shewmon, Metall. Trans., A21 (1990) 1261-1271

[36] H.R. Copson, S.W. Dean, Corros., 21 (1965) 1-8
[37] S.S. Hwang, J.S. Kim, J.Y. Kim, Met. Mater. Int., 9 (2003) 389-394
[38] J.S. Armijo, Corros., 24 (1968) 319-325
[39] H. Coriou, L. Grall, C. Mahieu, M. Pelas, Corros., 22 (1966) 280-290
[40] C. Tsai, W.-T. Tsai, J.-T. Lee, Corros. Sci., 34 (1993) 741-757
[41] W. Yang, Z. Lu, D. Huang, D. Kong, G. Zhao, J. Congleton, Corros. Sci., 43 (2001) 963-977
[42] W.-T. Tsai, C.-S. Chang, J.-T. Lee, Corros., 50 (1994) 98-105
[43] R. Bandy, R. Roberge, R.C. Newman, Corros., 39 (1983) 391-398
[44] I.J. Yang, Corros., 49 (1993) 576-585
[45] T. Sakai, K. Aoki, T. Shigemitsu, Y. Kishi, Zairyo-to-Kankyo, 40 (1991) 736-741
[46] W.-T. Tsai, C.-H. Chou, Mater. Sci. Eng., A288 (2000) 5-11
[47] Z. Fang, R. W. Staehle, Corros., 55 (1999) 355-379
[48] P. Marcus, A. Teissier, J. Oudar, Corros. Sci., 24 (1984) 259-268
[49] D. Tromans, L. Frederick, Corros., 40 (1984) 633-639
[50] A. Elbiache, P. Marcus, Corros. Sci., 33 (1992) 261-269
[51] J. Oudar, P. Marcus, Appl. Surf. Sci., 3 (1979) 48-67
[52] R. C. Newman, Corros., 41 (1985) 450- 453
[53] I. Betova, M. Bojinov, O. Hyokyvirta, T. Saario, Corros. Sci., 52 (2010) 1499-1507
[54] R. Bandy, R. Roberge, R.C. Newman, Corros. Sci., 23 (1983) 995-1006
[55] R. Bandy, D. Van Rooyen, Corros., 40 (1984) 281-289
[56] P. Marcus, J.M. Grimal, Corros. Sci., 31 (1990) 377-382
[57] K. Lu, J. Lu, J. Mater. Sci. Technol., 15 (1999) 193-197
[58] K. Lu, J. Lu, Mater. Sci. Eng., A375-377 (2004) 38-45
[59] G.T. Murray, Handbook of Materials Selection for Engineering Applications, Marcel Dekker (1997)
[60] P.A. Schweitzer, Encyclopedia of Corrosion Technology, CRC Press (2004)
[61] Special Metals Products Company Inc. Product Catalogue, http://www.specialmetals.com, (accessed Sept 03, 2013)
[62] Special Metals Products Company Inc. Product Catalogue, http://www.specialmetals.com, (accessed Sept 03, 2013)
[63] L. L. Shreir, R.A. Jarman, G.T. Burstein, Corrosion: Metal/Environmental reactions, Butterworth-Heinemann (1994)
[64] ASM Int. Fundamentals of Electrochemical Corrosion, http://www.asminternational.org, (accessed September 3, 2013)
[65] R.H. Jones, Stress Corrosion Cracking: Materials Performance and Evaluation, ASM International, (1992)
[66] J. Robertson, Corros. Sci., 32 (1991) 443-465
[67] L.A.S. Ries, M. Da Cunha Belo, M.G.S. Ferreira, I.L. Miller, Corros. Sci., 50 (2008) 676-686
[68] D.D. Macdonald, A. Sun, Electrochim. Acta., 51 (2006) 1761-1779
[69] N.E. Hakiki, S. Boudin, B. Rondot, M. Da Cuhna Belo, Corros. Sci., 37 (1995) 1908-1822
[70] J. Robertson, Corros. Sci., 29 (1969) 1275-1291
[71] D. Hamm, C.-O.A. Olsson, D. Landolt, Corros. Sci., 44 (2002) 1009-1025

[72] A.C. Lloyd, D.W. Shoesmith, N. S. McIntyre, J.J. Noel, J. Electrochem. Soc., 150 (2003) B120-B130
[73] P. Jakupi, D. Zagidulin, J.J. Noel, D.W. Shoesmith, Electrochim. Acta., 56 (2011) 6251-6259
[74] N.E. Hakiki, M. Da Cunha Belo, A.M.P. Simoes, M.G.S. Ferreira, J. Electrochem. Soc., 145 (1998) 3821-3829
[75] F. Gaben, B. Vuillemin, R. Oltra, J. Electrochem. Soc., 151 (2004) B595-B604
[76] D.D. Macdonald, J. Electrochem. Soc., 139 (1992) 3434-3449
[77] W. Yang, Z. Lu, D. Huang, D. Kong, G. Zhao, J. Congleton, Corros. Sci., 43 (2001) 963-977
[78] C.Y. Chao, L.F. Lin, D.D. Macdonald, J. Electrochem. Soc., 128 (1981) 1187-1194
[79] N.F. Mott, T. Faraday Soc., 43 (1947) 429-434
[80] N. Cabrera, N.F. Mott, Rep. Prog. Phys., 12 (1949) 163-184
[81] N. Sato, M. Cohen, J. Electrochem. Soc., 3 (1964) 512-519
[82] F.P. Fehlner, N.F. Mott, Oxidation of Metals, 2 (1970) 59-99
[83] L.F. Lin, C.Y. Chao, D.D. Macdonald, J.Electrochem. Soc., 128 (1981) 1194-1198
[84] C.Y. Chao, L.F. Lin, D.D. Macdonald, J. Electrochem. Soc., 129 (1982) 1874-1979
[85] D.D. Macdonald, Electrochim. Acta., 56 (2011) 1761-1772
[86] M.G. Fontana, Corrosion Engineering, McGraw Hill Inc, (1986)
[87] B.E. Wilde, Corros., 25 (1969) 359-365
[88] R.S. Dutta, J. Nucl. Mater., 393 (2009) 343-349
[89] P. Berge, J.R. Donati, Nucl. Tech., 55 (1981) 88
[90] G.P. Airey, A.R. Vaia, R.G. Aspden, Nucl. Tech., 55 (1981) 436
[91] R.S. Pathania, R.D. Cleland, Corros., 41 (1985) 575-581
[92] N. Totsuka, Z. Szklarska-Smialowska, Corros., 43 (1987) 734-738
[93] G. Economy, R.J. Jacko, F.W. Pement, Corros., 43 (1987) 727-737
[94] S.S. Hwang, H.P. Kim, Y.S. Lim, J.S. Kim, L. Thomas, Corros. Sci., 49 (2007) 3797-3811
[95] D.-J. Kim, H. Kim, S. Hwang, J. Kim, J. Park, Met. Mater. Int., 16 (2010) 259-266
[96] A.K. Agrawal, J.P.N Paine, Proceedings of the 4th International Symposium on Environmental Degradation of Materials in Nuclear Power Systems – Water Reactors, Jekyll island, Georgia, USA, August 6-10 (1989) 7-1.
[97] M.D. Pandey, S. Datla, R.L. Tapping, Y.C. Lu, Nucl. Eng. Des., 239 (2009) 1862-1869
[98] J.S.Armijo, Corros., 10 (1968) 319-325
[99] P. Marcus, I. Olefjord, Corros., 42 (1986) 91-98
[100] J. Oudar, P. Marcus, Appl. Surf. Sci., 3 (1979) 48-67
[101] P. Marcus, A. Teissier, J. Oudar, Corros. Sci., 24 (1984) 259-268
[102] S. Bagheri Fard, M. Guagliano, Fracttura ed Intergrita Strutturale, 7 (2009) 3-16
[103] J.-K Shin, J.-H. Suh, J.-S. Kim, S.-J.L. Kang, Surf. Coating Technol., 107 (1998) 94-100
[104] K. Lu, Mater. Sci. Eng., R16 (1996) 161-221

[105] N.R. Tao, M.L. Sui, J. Lu, K. Lu, Nanostruct. Mater., 11 (1999) 433-440
[106] G. Liu, J. Lu, K. Lu, Mater. Sci. Eng., A286 (2000) 91-95
[107] G. Liu, S.C. Wang, X.F. Lou, J. Lu, K. Lu, Scripta Mater., 44 (2001) 1791-1795
[108] X. Wu, N. Tao, Y. Hong, B. Xu, J. Lu, K. Lu, Acta. Mater., 50 (2002) 2075-2084
[109] N.R. Tao, Z.B. Wang, W.P. Tong, M.L. Sui, J. Lu, K. Lu, Acta. Mater., 50 (2002) 4603-4616
[110] H. Gleiter, Prog. Mater. Sci., 33 (1988) 223-315
[111] C. Suryanarayana, Int. Mater. Rev., 40 (1995) 41-64
[112] D.G. Morris, Mechanical Behaviour of Nanostructured Materials, Trans. Tech. Publications Ltd., Switzerland, (1998) 70
[113] S.X. McFadden, R.S. Mishra, R.Z. Valiev, A.P. Zhilyaev, A.K. Mukherjee, Nature, 298 (1999) 684
[114] J. Lu, M.L. Sui, K. Lu, Science, 287 (2000) 1463

Chapter 2. Experimental Principles and Details

2.1 Electrochemical Techniques

2.1.1 Electrode Cell Arrangement

A three-electrode electrochemical cell is used in this study, consisting of a working electrode (WE), a counter electrode (CE) and a reference electrode (RE), connected to a potentiostat to control the potential and measure the current. A schematic of this arrangement is shown in Figure 2.1.

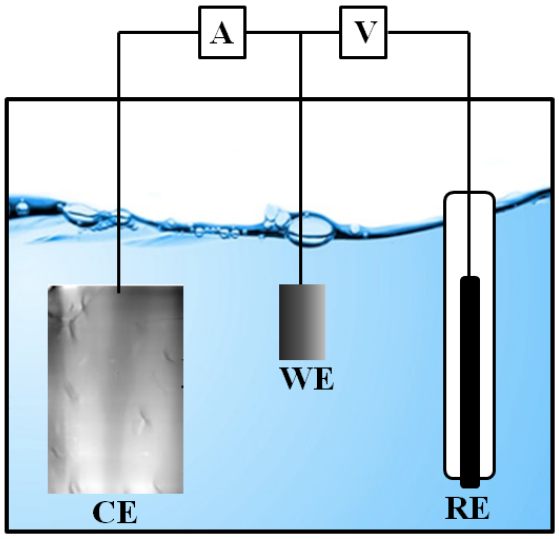

Figure 2.1 Schematic of the arrangement for a three-electrode cell.

In a typical three-electrode set-up, current flows between the CE and the WE, while the potential difference is controlled between the WE and RE. In these experiments, the WE is either Alloy 600 or Alloy 800. The CE in the cell functions as the current source or sink, and for these experiments, a sheet of Pt with a large surface area relative to the WE is used. The function of the RE is to act as a point of reference in the electrochemical cell

for potential measurement and control. The saturated calomel electrode (SCE) is stable, has a well-known potential of 0.241 V vs. the standard hydrogen electrode (SHE), and is easy to maintain. Current flow through the RE is kept close to zero since the connection between the WE and RE has high input impedance. This ensures that the potential of the RE remains constant [1].

2.1.2 Anodic Polarization Curve

An external potential is applied to the WE and scanned over a predetermined potential range while the current response generated is measured. The scan rate can influence the type of information obtained. The scan rate used in these experiments (0.1667mV/s) is slow in an attempt to achieve steady-state conditions. True steady-state conditions are not always met, however, as passive systems can require days to attain true steady-state conditions.

2.1.3 Potentiostatic Polarization

This technique is used to grow oxide films with properties close to those expected at steady-state, which is referred to as having achieved a time-independent thickness and composition.

2.1.4 Electrochemical Impedance Spectroscopy (EIS)

Electrochemical impedance spectroscopy (EIS) can be used to extract the electrochemical information available from an electrochemical system over an infinite bandwidth. This technique is commonly used to measure the resistive and capacitive properties of an electrochemical interface, especially one covered by an oxide film. EIS

is used to study the system's current response to the application of an AC potential signal, and the measurements are carried out at different frequencies [2, 3].

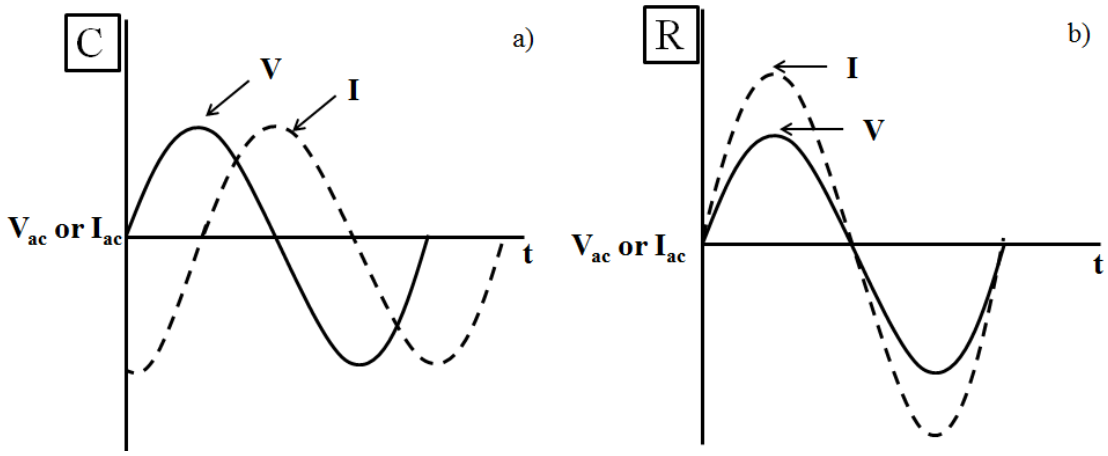

Figure 2.2 Schematic demonstrating the relationship between the input sinusoidal potential and the current response across (a) a capacitor and (b) a resistor.

In a linear system, the signal response can be shifted in phase, Figure 2.2 (a), and have different amplitudes, Figure 2.2 (b), compared to the initial signal. The phase shift is a result of capacitive behaviour and the amplitude change depends on the resistance.

Ohm's law defines resistance as a ratio between potential, *v*, and current, *i*.

$$v = iR \tag{2.1}$$

Under Ohm's law, the potential difference is constant. If the signal is sinusoidal, the following is observed:

$$v = V\sin(\omega t) \tag{2.2}$$

where v is the potential difference, ω is the frequency of the sinusoidal signal, V is its amplitude, and t is the time. Applying this signal to a circuit with a single resistor gives the current response,

$$i = \left(\frac{V}{R}\right)\sin(\omega t) \tag{2.3}$$

Since the response will be completely resistive, i and V will be in phase. If the sinusoidal signal is applied to a single capacitor, current will flow when the potential difference changes, as shown in equation 2.4,

$$i = C\frac{d(V\sin\omega t)}{dt} = C\omega V\cos(\omega t) = \omega CV\sin(\omega t + \frac{\pi}{2}) \tag{2.4}$$

If the response is completely capacitive, i and V will be 90° out of phase.

Impedance, Z, which is analogous to resistance, R, is a measure of the ability of a circuit to resist the flow of current in response to an alternating current (AC) potential signal. The impedance of a resistor is represented by,

$$Z_1 = R \tag{2.5}$$

While the impedance of a capacitor is shown in equation 2.6,

$$Z_2 = \frac{1}{j\omega C} \tag{2.6}$$

The total impedance of the system, shown as resistor and a capacitor in series can be defined as,

$$Z(\omega) = Z_1 + Z_2 = R + xC = R + \frac{1}{j\omega C} \tag{2.7}$$

Equation 2.7 shows that the impedance can be described by a complex number, where $j = \sqrt{-1}$. The real component of the impedance is constant and described by R, while the imaginary component of the impedance, $(1/j\omega C)$, is described by C.

The impedance data collected can provide electrical information about a system, such as an oxide film on a metal surface. This simplest representation of this type of interface is by a resistor and a capacitor in parallel, and the time constant, τ, measures the accumulation of charge at the interface, where,

$$\tau = RC \tag{2.8}$$

The equivalent circuit shown in Figure 2.3 contains one time constant and the physical representation of the impedance data.

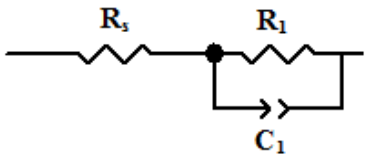

Figure 2.3 Equivalent circuit containing one time constant.

A single resistor, R_s, is used to account for the resistance to current flow in solution, while the resistive element, R_1, takes into account the resistance associated with the oxide film interface. The capacitance is associated with the surface oxide film, and represents the charge storage capacity. Constant phase elements (CPE) are commonly used in place of capacitors to account for non-ideal behaviour. Differences in film thickness, dielectric constants or defect densities make it necessary to use CPEs to account for these non-homogeneities. The impedance of a CPE is defined by,

$$Z_{CPE} = \frac{1}{Q(j\omega)^{\alpha}} \tag{2.9}$$

where Q is the CPE parameter and α the CPE exponent. Both resistors and capacitors are examples of CPEs, where a perfect capacitor will possess a value of $\alpha = 1$, while that of a resistor will possess a value of $\alpha = 0$. Typically, a CPE will require that $0 < \alpha < 1$.

Impedance data can be graphically represented in the form of a Nyquist plot, as shown in Figure 2.4.

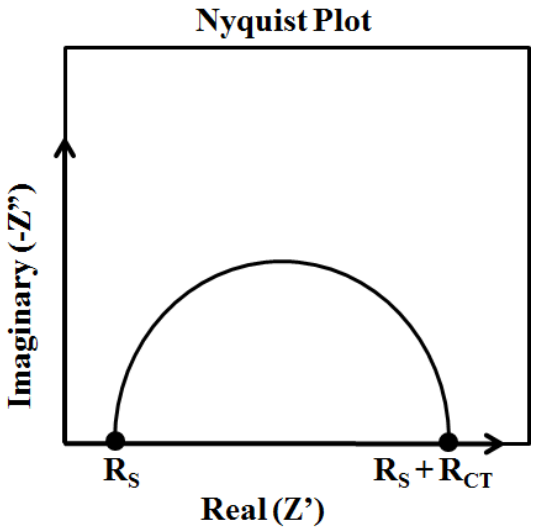

Figure 2.4 Various components of the Bode plot representing a single time constant equivalent circuit.

The Nyquist plot utilizes both the real (R), and imaginary, ($1/j\omega C$) components, and typically takes the form of a semi-circle for each time constant. At the two points of intersection of the semi-circle with the x-axis (real component) the impedance is purely resistive and represents the value of the solution resistance, R_s, and the total sum of all

the resistive elements, respectively. The Bode plot in Figure 2.5 shows the impedance modulus, ($|Z|$), and phase angle, (θ), plotted as a function of the log of frequency (ω).

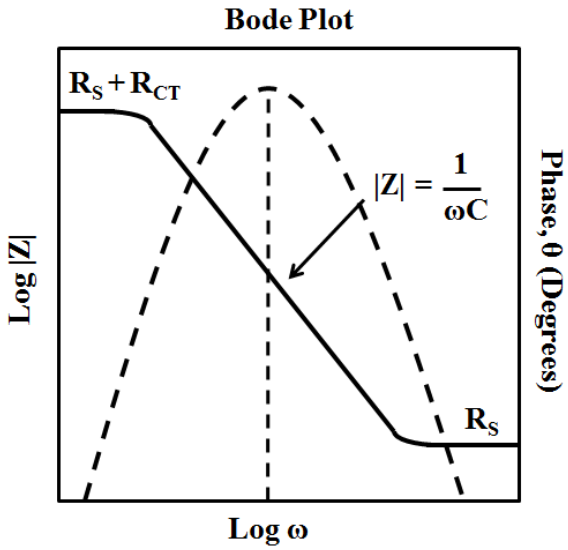

Figure 2.5 Bode plot representing a single time constant equivalent circuit.

In the log $|Z|$ versus log frequency plot, the impedance modulus at high and low frequencies is constant and independent of frequency. At the high frequency end, the response is due to R_s, while at the low frequency end, the response is a sum of the resistive elements ($R_s + R_{CT}$). A capacitive response can be measured where the slope of the line = -1.

2.2 Surface Analysis Techniques

2.2.1 Scanning Electron Microscopy (SEM)

Scanning electron microscopy (SEM) can be used to obtain images through a focused, high resolution electron beam. The electron beam interacts with the atoms on the surface and the scattered electrons contain information regarding the composition and

topography of the surface. The energy of the electron beam can range between 0.2 keV and 40 keV. The beam is focused by a series of condenser lenses, to a spot between 0.4 to 5 nm in diameter. Afterwards, the focused beam passes through a pair of deflection coils, which deflect the beam along the x and y axis, scanning the sample surface. When the incident electron beam hits the surface, scattering and absorption cause energy loss of the incident beam within a certain volume of the sample, known as the interaction volume. This volume is dependent on the beam energy and the atomic number and density of the sample. Within this interaction volume, energy exchange between the beam and the sample occurs. A reflection of high energy electrons via elastic scattering and lower energy secondary electrons by inelastic scattering can be detected. To ensure the free passage of electrons to and from the detector, the samples are placed in a high vacuum chamber. Detection of the secondary electrons occurs from the top few nanometers of the surface, yielding information on the surface topography. Electrons at higher points on the sample are more likely to be detected [4]**.**

2.2.2 X-ray Photoelectron Spectroscopy (XPS)

X-ray photoelectron spectroscopy (XPS) is a non-destructive method for studying the electronic structure of atoms, molecules and solids. The basic experiment involves the bombardment of a material *in vacuo* with a photon source. Capable of penetrating several nanometers, the absorption of an X-ray by an atom in the solid sample leads to the ejection of a core shell electron.

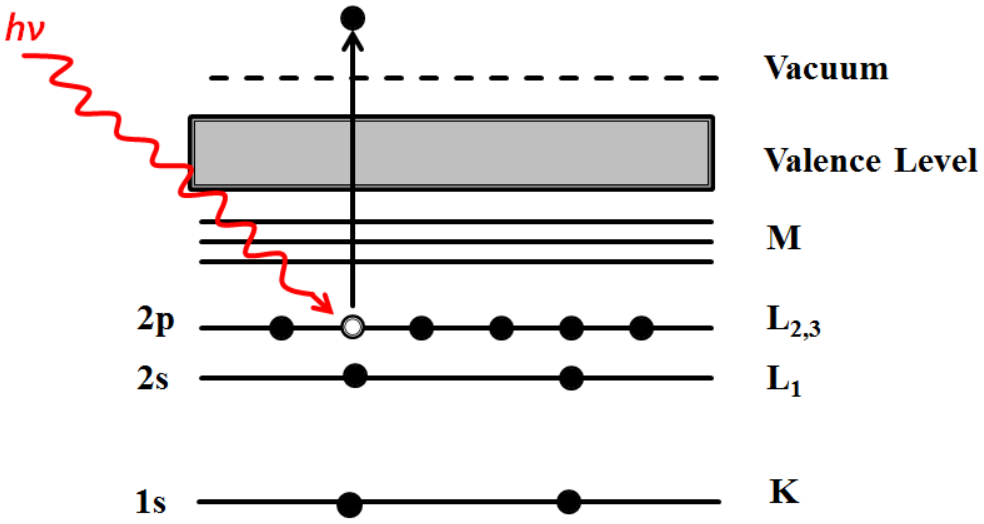

Figure 2.6 Schematic demonstrating the principles of XPS, and the ejection of a core level photoelectron.

The kinetic energy of this electron is characteristic of the atom from which it was ejected and can be used to identify all elements in the periodic table with the exception of He and H. The kinetic energy of the emitted electrons, E_k, can be measured and the atomic core level binding energy, E_b, relative to the Fermi level, E_F, of the sample can be determined using equation 2.10. The work function of the spectrometer, ϕ_{sp}, is typically 4-5 eV.

$$E_k = h\nu - E_b - \phi_{sp} \tag{2.10}$$

Chemical state information can be extracted since binding energies are sensitive to the chemical environment of the atom. Chemical environments that de-shield the atom will cause the core electrons to shift to increased binding energies.

This technique is surface sensitive due to the low probability that electrons generated below the surface will be capable of leaving the sample and making their way

to the detector while still retaining their original energy to contribute to the peak signal. The depth of analysis is dependent on, λ, the inelastic mean free path (IMFP) which is defined as the average distance travelled between inelastic collisions for an electron of the appropriate energy. 95% of the detected signal that contributes to the peak will come from a depth that is three times the escape depth, 3λ [5].

2.2.3 Auger Electron Spectroscopy (AES)

Auger electron spectroscopy (AES) is a method for determining the elemental composition of the outermost atomic layer of a material. A specimen is probed with an electron beam, between 3 and 30 keV in energy, resulting in the ejection of core level electrons from atoms at the surface. The vacancy left behind by the ejected electron can be filled by an outer level electron, with the excess energy being used to emit another electron (the Auger electron).

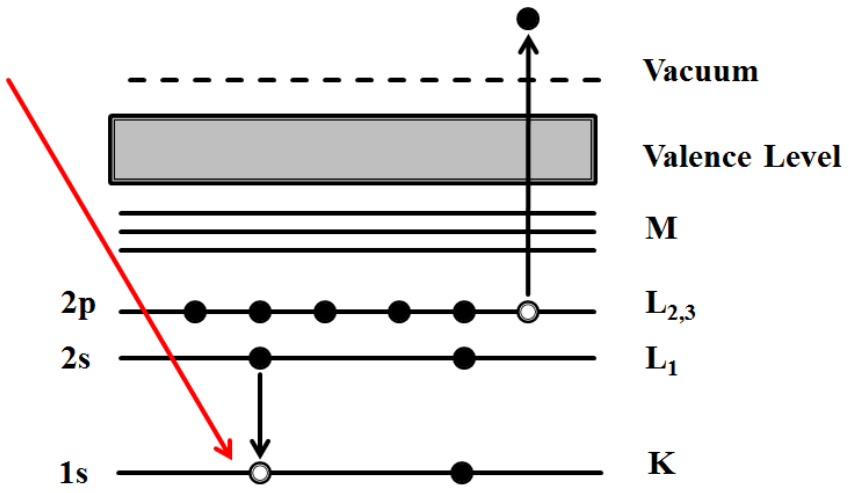

Figure 2.7 Schematic demonstrating the principles of AES, and the ejection of an Auger electron.

This technique is highly surface sensitive due to the strong inelastic scattering of the low-energy electrons, and experiments must be run under high vacuum, HV, conditions. Only Auger electrons from the outermost atomic layers are emitted without energy loss and can contribute to the Auger peaks in the spectrum, as the IMFP of these electrons is only a few atomic layers. Auger electrons that having undergone elastic collision contribute to the background signal at lower kinetic energies. Similar to XPS, He and H cannot be detected. The Auger electron kinetic energies are characteristic of the emitting atoms and can be used in elemental identification. The kinetic energies of the Auger electron will depend on the binding energy of the atomic energy levels involved, and not on the incident beam energy. For example, the kinetic energy, E_k, of the Auger electron KL_2L_3 is given approximately by equation 2.11,

$$E_k(KL_2L_3) = E_b(K) - E_b(L_2) - E_b(L_3) \tag{2.11}$$

where $E_b(K)$ is the binding energy of the core level, while $E_b(L_2)$ and $E_b(L_3)$ are the binding energies of the first and second outer shells, respectively.

Depth profiling is performed as a means of determining the distribution of elemental components in a film. The sample surface is bombarded with a well-focused ion beam (Ar^+), removing the outermost layer in succession. The ablated layer is detected and analyzed for the individual components [5].

2.3 Experimental Procedures

2.3.1 SMAT Sample Preparation

Alloy 600 and 800 tubing was cut into 10 cm long sections, which were treated by Professor Jian Lu and his coworkers at the Hong Kong Polytechnic University in Hong Kong. The length of the treatment zone on each alloy ranged between 70 to 80 mm. For Alloy 600, treatment parameters were varied by altering either the shot composition or the duration of treatment. Both stainless steel, SS, and ceramic zirconium oxide, ZrO_2, balls were used. Both sets of balls were 20 g in weight. The duration of SMAT for Alloy 600 using SS shots was either 30, 90 or 120 minutes. Using the ZrO_2 balls, the duration of treatment was either 15 or 30 minutes. On Alloy 800, treatment parameters were varied by altering the shot size as well as duration of treatment. Only SS balls were used, but the weights used were either 20 g or 40 g. Treatment times for this alloy were either 90 or 120 minutes.

2.3.2 Electrochemical Cell

All potentials were measured against an SCE (+ 0.241 V vs. SHE), obtained from Schott instruments in Mainz, Germany. The CE was prepared from a Pt sheet, and the WE fabricated from either Alloy 600 or Alloy 800 supplied by Rolled Alloys Inc, located in Mississauga, ON, Canada. The WE was constructed from a cross section cut from the SG tubing 1 cm in diameter using a diamond saw. These rectangular prismatic electrodes, with an exposed outer surface area averaging 20 mm^2, were spot welded to a stainless steel wire, and lightly polished with a suspension of 0.05 μm Buehler micro-polish in water. After rinsing first with deionized (DI) water and acetone, the samples

were painted with a Microshield™ masking aid from SPI-CHEM, located in West Chester, PA, USA, so that only one surface was exposed.

A Solartron potentiostat (model 1286/1287) and frequency response analyzer (model 1250/1255) were used in the electrochemical experiments. Corrware™ and Zplot™ software (Scribner and Associates, located Southern Pines, NC, USA) were used to control experiments, and CorrView™ and ZView™ were used for data analysis. Prior to each electrochemical experiment, a cathodic potential of -1.2 V_{SCE}, was applied to the electrode for one hour to remove air formed oxides. The anodic polarization measurements began 150 mV below E_{corr}, were terminated at 1.0 V_{SCE}, and were recorded at a scan rate of 0.1667 mV/sec. EIS was performed by applying a 10 mV sinusoidal potential stimulus at the applied potential (E_{APP}), which was applied for three hours prior to the measurement. The frequency varied over a range 10^5 Hz to 0.005 Hz.

2.3.3 Solution Preparation

Electrolyte solutions were prepared from ultra-pure DI water with a resistivity of 18.2 MΩ·cm. The water was purified using a Millipore Synergy® System. Reagent grade chemicals provided by Alpha Aesar, located in Ward Hill, MA, USA, were used to prepare the electrolyte solutions to the appropriate concentrations. To achieve the desired de-aerated conditions, solutions were purged with ultra-high purity Ar gas from Praxair, located in London, ON, Canada, for thirty minutes prior to preforming an experiment and a flow of Ar was maintained throughout an experiment.

2.3.4 SEM Sample Mounting

Using the same sample preparation described in section 3.2, the cross sectional samples subjected to SEM analysis were mounted using the cold mounting epoxy resin MA2 from Presi™. Samples subjected to SEM analysis were finely polished, starting with a 500 grit polishing pad and slowly working up to a 0.05 μm alumina suspension in water.

2.4 Surface Analytical Instrumentation and Procedures

SEM was performed using a Hitachi S-4500 field emission SEM in the high resolution mode. Electron gun voltage was set to 15.0 kV, and the instrument base pressure was 6 x 10^{-6} Torr.

The XPS analyses were performed on an AXIS Ultra Kratos spectrometer using a monochromatic Al Kα radiation source (10 or 15 mA, 14 kV). To calibrate the work function of the instrument, the binding energy (BE) for the Au $4f_{7/2}$ peak was set to 83.96 eV and the spectrometer dispersion was adjusted using the Cu $2p_{3/2}$ peak, with a BE of 932.62 eV. The instrument base pressure was held at approximately 2.5 × 10^{-8} Torr. For each electrode, survey spectra were collected over a 256 × 256 μm area, at a pass energy of 160 eV with a 0.7 eV energy step over a BE range of 1100 eV to 0 eV. High resolution scans of the Ni $2p_{3/2}$, Cr $2p_{3/2}$, Fe $2p_{3/2}$, C 1s and O 1s peaks were obtained from the same area at a pass energy of 20 eV using a step size of 0.05 eV. The BE ranges for these elements were 890 eV to 847 eV, 595 eV to 570 eV, 540 eV to 525 eV, and 295 eV to 278 eV, respectively. Spectral analyses were performed using CasaXPS™ software. High resolution spectra were charge–corrected with reference to the main line

of the C 1s spectrum at 285.0 eV. High resolution spectra were de-convoluted using standard peak fitting from reference materials for Ni $2p_{3/2}$, Cr $2p_{3/2}$, O 1s and C 1s [6, 7, 8]. All XPS spectral analyses were performed using CasaXPS software (version 2.3.14).

AES analyses were conducted using a PHI 660 scanning Auger electron microscope (SAM) with an input beam excitation energy of 5 keV and a beam current of 300 nA. An Ar^+ ion beam was used for sputtering to obtain depth profiles. Following removal of the electrode from the electrochemical cell, the wire attached to the electrode was stripped of the masking agent and cut down to ensure a proper fit in the microscope sample holder. The instrument base pressure was held at approximately 2.5×10^{-8} Torr. For each electrode, a survey scan was collected over an area of 2 x 2 μm with a 1.0 eV energy step over an energy range of 30 eV to 1030 eV. During depth profiling, Fe (636 eV to 660 eV), Ni (833 eV to 859 eV), Cr (522 eV to 539 eV), O (497 eV to 519 eV), C (260 eV to 238 eV) and S (137 eV to 163 eV) were the key elements analyzed. Data collection was accomplished using AugerMap and data analysis using AugerScan. Sputtering-time profiles were converted into depth profiles using a sputtering rate determined by depth profiling a reference specimen under similar conditions. This sputter rate was calculated to be 9.6 nm/min.

References

[1] K.J. Vetter, Electrochemical Kinetics, Academic Press, (1967)

[2] E.E. Stanbury, R.A. Buchanan, Fundamentals of Electrochemical Corrosion, ASM Int. (2000)

[3] M. Orazem, B. Tribollet, Electrochemical Impedance Spectroscopy, J. Wiley & Sons, (2008)

[4] R.F. Egerton, Physical Properties of Electron Microscopy: An Introduction to TEM, SEM, and AEM, Springer, (2005)

[5] D. Briggs, J.T. Grant, Surface Analysis by Auger and X-ray Photoelectron Spectroscopy, IM Publications, (2003)

[6] M.C. Biesinger, C. Brown, J.R. Mycroft, R.D. Davidson, N.S. McIntyre, Surf. Interface Anal., 36 (2004) 1550-1563

[7] M.C. Biesinger, B.P. Payne, L.W.M. Lau, A. Gerson, R. St.C. Smart, Surf. Interface Anal., 41 (2009) 324-332

[8] M.C. Biesinger, B.P. Payne, A.P. Grosvenor, L.W.M. Lau, A. Gerson, R. St.C. Smart, Appl. Surf. Sci., 257 (2011) 2717-2730

Chapter 3. Behaviour of the Oxide Films Formed on Alloy 600 Steam Generator Tubing in a 0.1M $Na_2S_2O_3$ Solution

3.1 Introduction

SCC is the result of simultaneous exposure of a susceptible material to a corrosive environment and residual or applied tensile stress, resulting in localized fracture. This type of corrosion can be severe, as catastrophic damage can occur even though the stress levels are within the specified range for normal operating conditions [1-3]. In CANDU nuclear reactors, the function of SG tubing is to contain and separate the primary and secondary water circuits, as well as to transfer heat from the primary to the secondary water. There is a strong incentive to understand the SCC of SG tubing since its failure can result in the contamination of secondary water with highly radioactive primary water. The operating conditions of the tubing demand that it withstand elevated temperatures and pressures, which together with manufacturing and formation residual stress can lead to SCC. Alloy 600 has been used to fabricate SG tubing, but, over a number of years, numerous failures have exposed underlying issues, and it is now well-known to be susceptible to SCC [4-15].

Many publications have detailed the corrosion behaviour of Alloy 600 in a variety of aqueous solutions; sodium sulphate (Na_2SO_4) [16-18], sodium hydroxide (NaOH) [19], sodium thiosulphate ($Na_2S_2O_3$) [6, 13, 18, 20-23], and boric acid (H_3BO_3) [24]. The behaviour in $Na_2S_2O_3$ is of particular interest, since polarization curves showed regions of increased current density within the passive region, a feature not observed in Na_2SO_4 or H_3BO_3 solutions. This behaviour has also been observed, but to a much lesser extent,

on the current alloy of choice, Alloy 690 [20]. Little is known about the structure or behaviour of the passive film formed on these alloys in $Na_2S_2O_3$, and it is still unclear what occurs within the oxide on the surface of the alloy to cause the apparent enhancement of passive dissolution current observed. This is an important issue since $S_2O_3^{2-}$ is known to be an SCC agent [5, 13, 14, 18, 21, 25]. The aim of this study is to examine the surface composition of the oxide film formed at various potentials in $Na_2S_2O_3$ using AES and XPS and to determine the electrochemical behaviour at these potentials with EIS.

3.2 Experimental

3.2.1 Sample Preparation

Alloy 600 tubing sections, 9.5 mm in diameter, were procured from Rolled Alloys Inc. Canada in the mill-annealed condition. The composition of this alloy is presented in Table 3.1.

Table 3.1 Chemical composition of Alloy 600 SG tubing (wt%).

Element	Ni	Cr	Fe	Mn	Al	Ti	Si	C
Composition %	72.97	16.14	9.65	0.34	0.27	0.23	0.11	0.03

Small rectangular prismatic coupons were cut from this tubing using a Buehler diamond-tipped saw. The average area on the outer surface was ~ 20 mm^2. The coupons were extensively polished, finishing with a 0.05 micron alumina grit polishing pad and washed with DI water and sonicated in acetone.

3.2.2 Electrochemical Measurements

Electrodes were assembled by spot welding a SS wire onto the polished coupon. The back and sides of the coupon, as well as the wire, were coated with a Microsheild™ masking aid. A solution of 0.1 M $Na_2S_2O_3$ was used for the electrochemical experiments and was prepared using DI water with a resistivity of 18.2 MΩ•cm. This solution had a room temperature pH of approximately 6.5.

The three-electrode cell consisted of a Pt foil CE, a SCE reference (0.241 V vs SHE), and the Alloy 600 electrode acting as the WE. To purge the system of oxygen, Ar gas was vigorously bubbled through the solution for thirty minutes, and a steady flow of Ar gas maintained for the duration of the experiment.

At the beginning of each experiment, a potential of -1.2 V_{SCE} was applied for one hour to reduce air-formed oxides on the electrode surface. Potentiodynamic polarization experiments were run at a scan rate of 0.167 mV/s using a Solartron 1286 potentiostat. The experiments were started 0.150 V_{SCE} below the measured corrosion potential, (E_{corr}), and were terminated at 1.0 V_{SCE}. Investigation of the oxide film properties were conducted using EIS. The electrode was cathodically cleaned at -1.2 V_{SCE} for one hour, and then controlled at an applied potential for three hours. The potentials selected were determined based on the anodic polarization curve. Subsequently, a sinusoidal potential perturbation was applied to the electrode and the sinusoidal current response monitored. The frequency range employed was from 65 kHz to 0.005 Hz. Measurements were made using a Solartron 1250 frequency response analyzer. The data was collected and analyzed using ZPlot™ and ZView™ software, respectively.

3.2.3 Surface Analysis

3.2.3.1 Auger Electron Spectroscopy (AES)

AES analyses were conducted on the electrodes after electrochemical film growth at various potentials. On removal from the electrochemical cell, electrodes were rinsed with DI water and methanol. Data was obtained using a PHI 660 Auger electron spectrometer using an excitation energy of 5 keV. An Ar^+ ion beam was used for sputtering to obtain depth profiles. To prevent charging of the electrode in the spectrometer, the masking agent was stripped from the sample and the wire removed to fit the coupon into the sample holder. A survey scan was acquired for each electrode, and during depth profiling the intensity for the elements Ni, Cr, Fe, C, S and O were monitored as a function of sputtering time. Sputtering-time profiles were converted into depth-time profiles using a sputtering profile recorded on a reference sample of the alloy. The sputtering rate determined from the reference sample was 9.6 nm/min, and was assumed to be the same for both air and anodically formed oxides.

3.2.3.2 X-ray Photoelectron Spectroscopy (XPS)

XPS analyses were conducted on electrodes after anodic oxidation. On removal from the electrochemical cell, electrodes were rinsed with DI water and methanol. Measurements were made on an AXIS Ultra Kratos spectrometer using a monochromatic Al Kα electron source (15 mA, 14 kV). To calibrate the work function of the instrument, the BE for the Au $4f_{7/2}$ line was set to 83.96 eV and the spectrometer dispersion was adjusted using the Cu $2p_{3/2}$ peak with a BE of 932.62 eV. The instrument base pressure was held at ~ 2.5 x 10^{-8} Torr. Survey scans were recorded over an area of 256 μm x 256

μm at a pass energy of 160 eV between 0 eV and 1100 eV. High resolution scans of the Ni $2p_{3/2}$, Cr $2p_{3/2}$, C 1s and O 1s peaks were obtained from the same area at a pass energy of 20 eV using a step size of 0.05 eV. The windows for these elements were (890 eV to 847 eV), (595 eV to 570 eV), (540 eV to 525 eV), and (295 eV to 278 eV), respectively. Spectral analyses were performed using CasaXPS™ software. With the exception of the Cr $2p_{3/2}$ peak, all spectra have been charge corrected to the main line of the C 1s spectrum at 285.0 eV.

3.3 Results

3.3.1 Anodic Polarization

The potentiodynamic response of Alloy 600 in a de-aerated 0.1 M $Na_2S_2O_3$ solution is shown in Figure 3.1. The generally S-shape curve obtained is typical of a passive alloy. The corrosion potential was -0.4 V_{SCE} and the passive region can be defined as the potential range between -0.3 V_{SCE} and 0.3 V_{SCE}. However, within this region, an anodic peak is observed at 0.1 V_{SCE}. Similar peaks have been reported [13, 21, 26, 27]. In the presence of $S_2O_3^{2-}$, the oxide film formed on Alloy 600 is subject to anodic dissolution, along with the inability to re-passivate, creating an unstable film in these conditions [18, 22, 25-28]. It has also been previously reported that the passive behaviour of Alloy 600 is heavily influenced by Cr [13, 26, 29, 30]**,** making it possible that the removal of Cr could be responsible for the increase in current density observed.

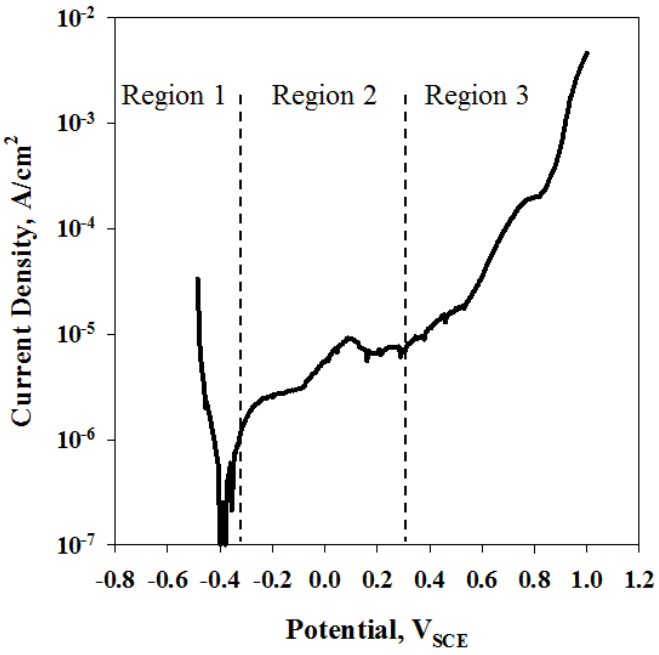

Figure 3.1 Anodic polarization curve for Alloy 600 in 0.1 M $Na_2S_2O_3$ solution. The curve is divided into three regions: (1) pre-passive, (2) passive and (3) transpassive.

Based on the anodic polarization curve, three separate regions were defined; (1) pre-passive, (2) passive, and (3) transpassive regions. Below -0.3 V_{SCE} (region 1), the passive film is not fully formed. Region 2, located between -0.3 V_{SCE} and 0.3 V_{SCE} includes the anodic peak at 0.1 V_{SCE}. The marginal stability of the passive oxide film resulting from the presence of $S_2O_3^{2-}$ is indicated by the slow overall increase in current throughout this region. The change in the slope of the current density with increasing potential greater than 0.3 V_{SCE} is indicative of the onset of transpassive behaviour (region 3).

3.3.2 Electrochemical Impedance Spectroscopy (EIS)

The properties of the oxidized films grown on the surface of the alloy at potentials between -0.6 V_{SCE} and 0.75 V_{SCE} were determined using EIS. Figure 3.2 shows the

spectra obtained at a number of applied potentials plotted as (a) Nyquist and (b) Bode plots.

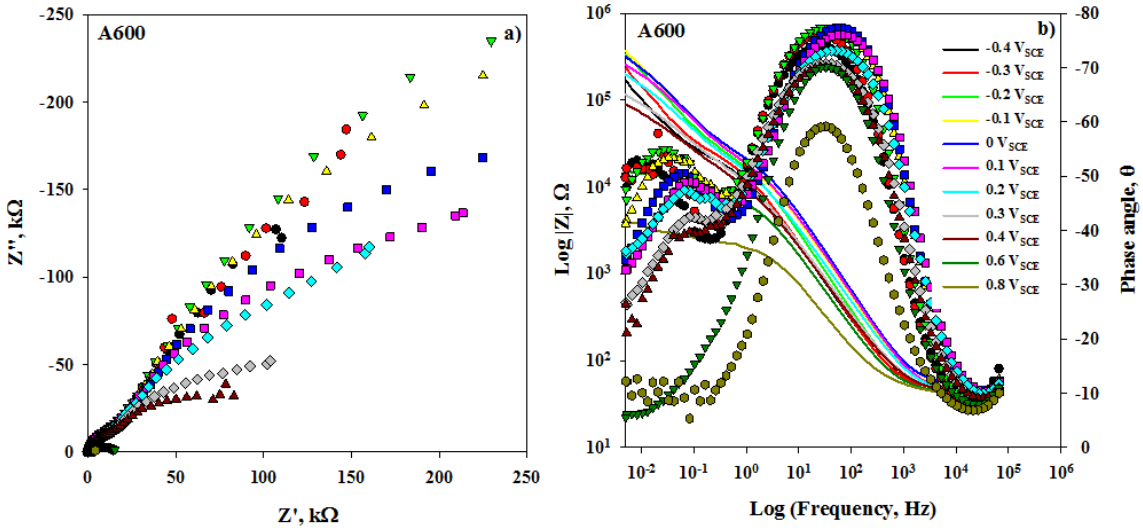

Figure 3.2 EIS spectra recorded on films grown on Alloy 600 (a) Nyquist plots and (b) Bode plots.

Both the Nyquist and Bode plots show that a frequency-independent real resistance is not achieved at frequencies down to 0.005 Hz. The non-semi-circular Nyquist plots, Figure 3.2 (a), show a significant frequency dispersion indicating a non-homogeneous surface response [31-33]. The Bode plots, Figure 3.2 (b), highlight the changes in the spectra as a function of frequency. At the low frequency limit, both the phase angle, θ, and the total impedance, $|Z|$, decrease as a function of film growth potential.

A graphical representation of the two time constant equivalent circuit used to fit the spectra is shown in Figure 3.3. In this circuit, CPE's are used in place of capacitors since the measured capacitance response is non-ideal. The impedance of a CPE is given by equation 3.1 [32].

$$Z_{CPE} = \frac{1}{Q(j\omega)^{\alpha}} \tag{3.1}$$

In this equation, Q is a fitting parameter independent of frequency and the exponent α has a value between 0 and 1. When α = 1, Q represents a capacitor, whereas if α = 0, Q represents a resistor.

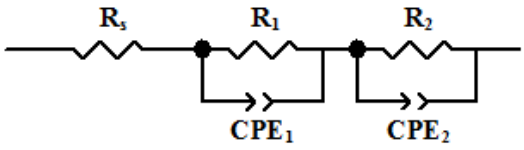

Figure 3.3 EIS equivalent circuit used to model the spectra collected for Alloy 600.

The use of this approximation has been well documented [16, 30, 34-36]. In the circuit shown in Figure 3.3, the first time constant, R_1/CPE_1 represents the outer oxide layer and interface, the second time constant, R_2/CPE_2 represents the barrier layer and inner oxide/alloy interface, and R_S is the solution resistance.

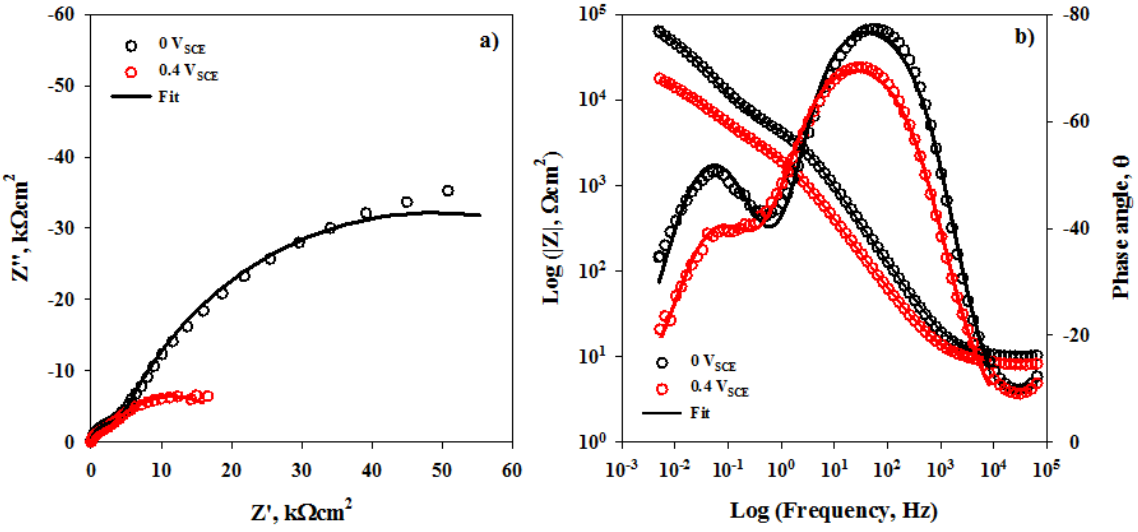

Figure 3.4 EIS plots comparing the fit to the acquired data at 0 V_{SCE} and 0.4 V_{SCE}: (a) Nyquist plots; (b) Bode plots.

Examples of the fitted spectra are shown in Figure 3.4 at two different potentials, (a) 0 V_{SCE} and (b) 0.4 V_{SCE}. Both plots show a good correlation between the fit and the experimental data over the measured potential range. The χ^2 values were all in the range of 10^{-4}. The resolved parameter values obtained from these fits are listed in Table 3.2.

Table 3.2 Summary of the parameters obtained from the fitted EIS spectra.

E (V_{SCE})	R_2 ($k\Omega cm^2$)	CPE_2 (μFcm^{-2})	n	R_1 ($k\Omega cm^2$)	CPE_1 (μFcm^{-2})	n	Rs (Ωcm^2)	χ^2 (10^{-4})
-0.4	98.87	423.8	0.7860	3.244	76.73	0.8878	8.730	7.37
-0.3	110.4	307.9	0.8069	3.338	65.68	0.9175	8.926	13.8
-0.2	139.6	183.8	0.8016	3.234	50.52	0.9479	8.846	19.3
-0.1	125.8	147.1	0.7911	3.111	38.54	0.9246	8.742	27.2
0	90.84	138.0	0.7851	3.373	27.08	0.9508	9.626	22.1
0.1	67.06	142.5	0.7765	2.766	33.91	0.9396	7.780	30.9
0.2	57.69	193.5	0.7571	2.612	53.68	0.9058	7.756	26.4
0.3	27.61	287.1	0.7503	2.289	89.85	0.8729	7.928	12.2
0.4	19.96	341.7	0.7407	1.989	99.70	0.8685	8.020	11.8
0.6	1.760	764.6	0.7168	1.265	91.49	0.8927	8.074	9.41

The values of the exponent, n, recorded for the first time constant, (CPE_1/R_1) are much closer to 1 than those obtained for the second time constant, (CPE_2/R_2), suggesting that the barrier oxide layer demonstrated more frequency dispersion than the outer layer. The sum of R_s, the barrier layer (R_2) and outer layer (R_1) resistances yields the polarization resistance (R_P), equation 3.2, which is inversely proportional to the passive dissolution corrosion rate, equation 3.3,

$$R_p = R_1 + R_2 + R_s \tag{3.2}$$

$$Corrosion\ Rate = R_p^{-1} \tag{3.3}$$

Changes in the R_p, combined with the outer and barrier layer resistances are plotted in Figure 3.5 as a function of potential. In region 1, the barrier layer resistance increases as the passive film develops and, as will be shown below, the Cr^{3+} oxide barrier layer forms. At potentials greater than -0.2 V_{SCE}, both the outer and barrier layer resistances begin to decrease. This coincides with the current increase leading eventually to the peak current at ~ 0.1 V_{SCE} in region 2, suggesting this anodic peak involves the partial destruction of the barrier layer. In region 3, the onset of transpassivity leads to a more extensive loss of film resistance in both layers.

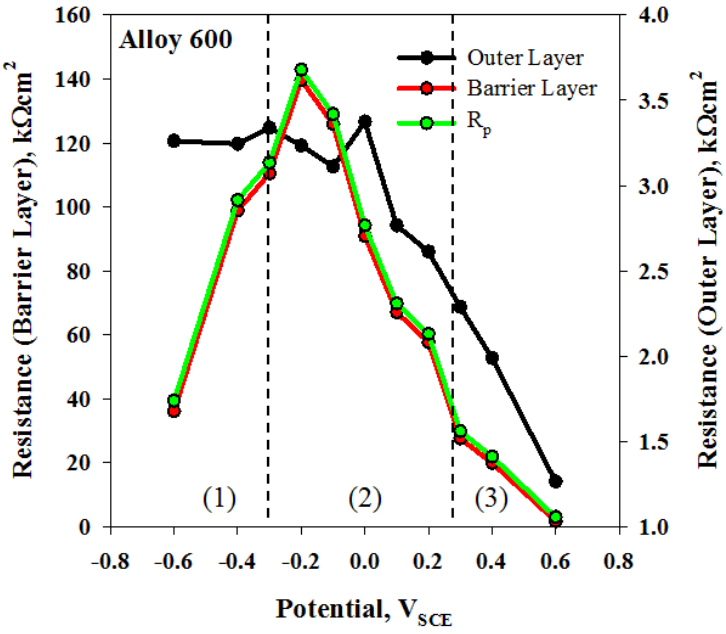

Figure 3.5 Changes in oxide film resistance as a function of applied film growth potential for Alloy 600 in a 0.1 M $Na_2S_2O_3$ solution. The plot is divided into three regions: (1) pre-passive, (2) passive and (3) transpassive.

As shown by the trends exhibited by R_p in Figure 3.5, the barrier layer is the primary contributor to the overall corrosion protection offered by the passive film.

3.3.3 Surface Analysis - AES

It is well established that the passive film formed on this alloy, and other materials of similar composition, possess a bilayer structure. The protective Cr rich barrier layer forms at the oxide/alloy interface beneath a less protective and sometimes porous outer layer containing mainly Ni and Fe [18, 29, 30, 37-49]. To determine the film thickness, it is essential to first establish the position of the oxide/alloy interface. Due to ion beam mixing during depth profiling, this interface can be difficult to locate. Sato, *et al.,* estimated the position of the interface through extrapolation of the profile for the O peak to the x-axis [50], but a simpler approach was taken here. The location of this interface was estimated to be at approximately the depth at which the O concentration reaches 50% of its maximum value [42, 51-53].

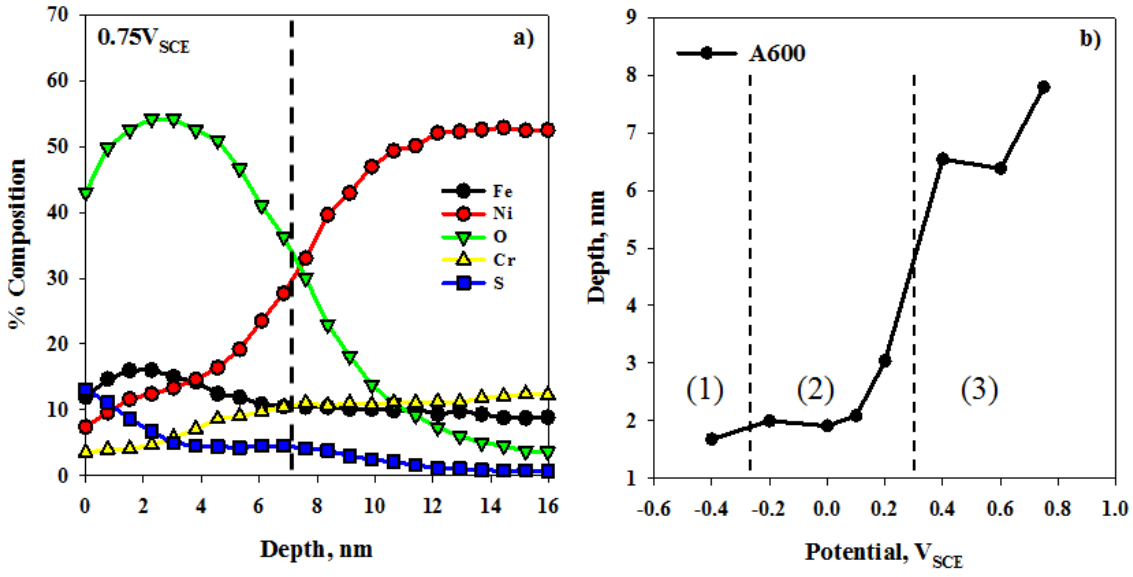

Figure 3.6 (a) AES depth profile of the oxide formed on Alloy 600 at 0.75 V_{SCE}: (b) the change in oxide film thickness as a function of film growth potential. The dashed line in (a) indicates the oxide/metal interface.

Figure 3.6 (a) shows a depth profile recorded on an oxide film grown electrochemically at 0.75 V_{SCE}. The elements observed were O, Fe, Ni, Cr and some impurities such as S and C (not shown). Using the procedure noted above, the oxide/alloy interface was located, yielding a film thickness of ~7.8 nm. From the depth profiles recorded over the full potential range, the change in oxide film thickness was determined as a function of potential, Figure 3.6 (b). This figure shows two distinct regions of film growth with increasing potential, in agreement with previous studies [54, 55]. Only marginal changes in film thickness are observed over the potential range containing the anodic peak, region 2. This indicates that while the enhanced anodic current in this region suggests film breakdown, this does not immediately lead to film thinning. Once the process responsible for the anodic peak is complete (i.e., by ~ 0.1 V_{SCE}), the film begins to thicken substantially.

Using AES depth profiles similar to that shown in Figure 3.6 (a), changes in elemental composition can be extracted as a function of oxide depth. This data can be converted into cation fractions for each alloying element (Fe, Ni, and Cr). These fractions were calculated by taking the total % composition of an element (Ni), and dividing it by the sum of the alloying elements (Ni, Fe and Cr) for each data point in the depth profile.

$$Ni_{CF} = \frac{Ni_{\%comp.}}{Ni_{\%\ comp.} + Cr_{\%\ comp.} + Fe_{\%\ comp.}} \tag{3.4}$$

An example is presented in Figure 3.7, allowing a comparison between the cation fractions and the original depth profiles, Figure 3.6 (a). This comparison yields a clearer picture of the compositional changes in the film as a function of depth, such as enrichment in Fe at the outer surface, and of Cr as a function of potential in the inner

region of the film. To emphasize the changes in composition in different regions of the film, plots of cation fractions were broken down into sections, Figure 3.7.

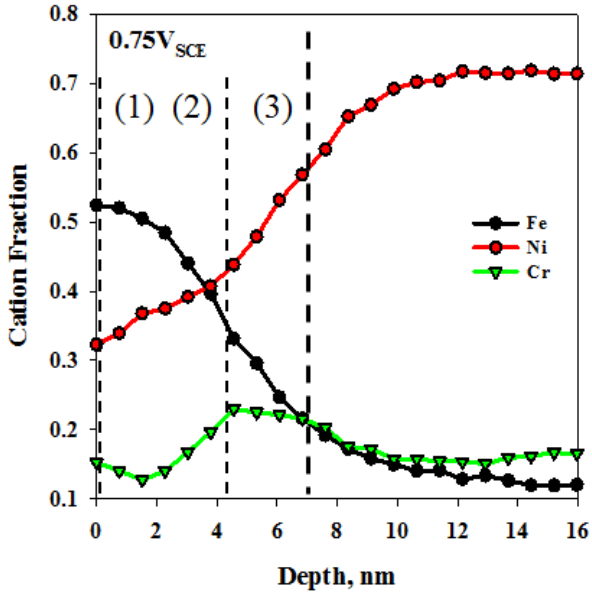

Figure 3.7 Plot of the corresponding cation fractions obtained from Figure 3.6. (1) indicates the position of the outer layer, (2) the position of the barrier layer, and (3) the oxide/alloy interface.

The total film thickness was indicated by line 3 drawn at the oxide/alloy interface. The position of the outer layer (line 1) was set at the solution/oxide interface and the location of the barrier layer at the peak in the Cr content (line 2). The Fe, Ni and Cr contents at these locations are shown as a function of film growth potential in Figure 3.8.

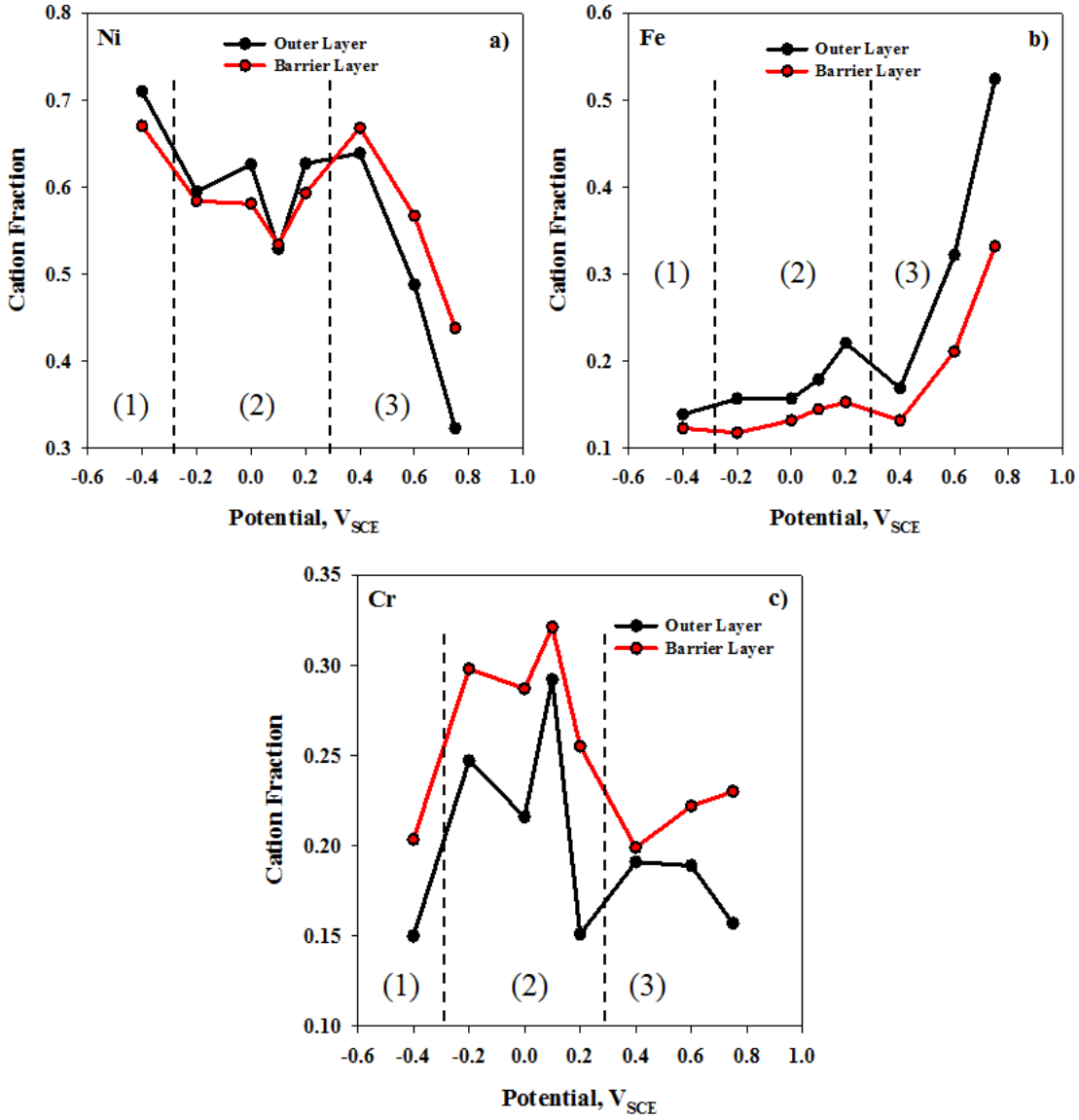

Figure 3.8 Changes in the (a) Ni, (b) Fe and (c) Cr cation fractions as a function of potential for the outer and barrier layers. The plots are divided into three regions: (1) pre-passive, (2) passive and (3) transpassive.

Changes in the Ni cation fraction in the outer and the barrier layer are shown in Figure 3.8 (a). The Ni content of the outer layer only marginally exceeds that of the barrier layer in regions 1 and 2. At the potential of the anodic peak (0.1 V_{SCE}), a drop in Ni concentration in both oxide layers is observed, while at transpassive potentials (region

3) the Ni concentration becomes progressively more depleted as the potential is increased.

The Fe cation fractions are plotted in Figure 3.8 (b) and are inversely related to those of Ni. In both the barrier and the outer layer, the Fe content is low throughout potential regions 1 and 2. A slight increase in Fe content is observed at a potential of 0.2 V_{SCE}; i.e., immediately after the location of the anodic peak, region 2. The enrichment in Fe within the oxide film increases as the potential increases in region 3. This is particularly the case in the outer surface layer, where the accumulation of Fe is accompanied by a depletion of Ni.

Figure 3.8 (c), shows that the Cr content increases to a maximum through potential region 1 and early in potential region 2, particularly in the barrier layer. At potentials above the anodic peak, the Cr content begins to decrease again. The critical Cr concentration required to develop a protective Cr oxide layer is approximately 15 % [38] at, and beyond which, the behaviour of the alloy begins to resemble that of pure Cr [29, 30**.** In this study, a significant portion of the Cr is located within the outer layer, but the majority resides in the barrier layer. A strong correlation exists between the amount of Cr present in the barrier layer, and the impedance behaviour of the oxide film. The Cr content of the barrier layer increases then decreases with the film resistance. The decrease is easily observed after the anodic peak when the decrease in film resistance becomes most marked and accompanied by an increase in current in the polarization scan, Figure 3.1.

3.3.4 Surface Analysis - XPS

To identify the chemical state of individual elements, the composition of the oxide film formed at various applied potentials was also studied using XPS. High resolution spectra for the Ni $2p_{3/2}$, Cr $2p_{3/2}$ and O 1s peaks after film formation at 0 V_{SCE} are shown in Figure 3.9.

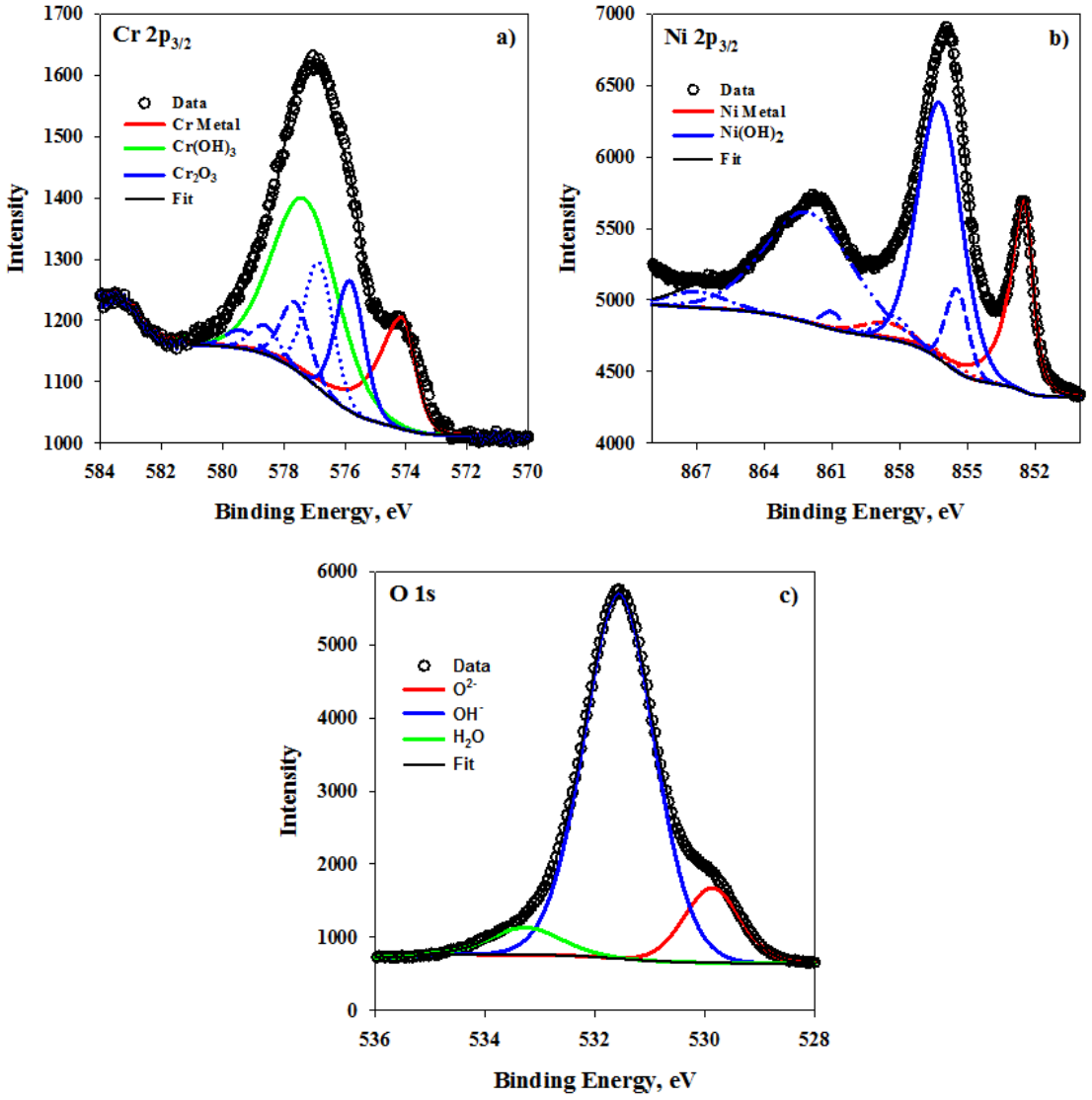

Figure 3.9 Fitting of the (a) Cr $2p_{3/2}$, (b) Ni $2p_{3/2}$, and (c) O 1s XPS high resolution spectra for an oxide film grown at 0 V_{SCE}.

The Cr $2p_{3/2}$ peak was fitted according to the contributions made by the different chemical states. At least three chemical forms of Cr were identified; metallic Cr at 574.1 eV, a Cr oxide species (Cr_2O_3) at 575.8 eV and a Cr hydroxide species ($Cr(OH)_3$ / CrOOH) with a peak position ranging from 577.2 eV in region 1 to 577.9 eV in region 3. Although the identity of the hydroxide component could not be verified, the XPS instrument being insufficient to resolve the peaks for the two compounds, it was assumed to be $Cr(OH)_3$. The full width at half maximum (FWHM) values for these peaks are 1.00, 1.10 and 2.50, respectively. Although only one peak for the Cr^{III} oxidation state is observed in the spectra, both the oxide and hydroxide components are required to achieve an adequate fit. Attempts to fit either component individually produced BE's inconsistent with reported literature values [56, 57]. Peak fitting procedures show that the Cr^{III} oxide species exhibit a discrete structure containing five peaks indicative of multiplet splitting [56, 57]. The BE's for both the metal and oxide components are within 0.2 eV of the reported literature values, with Cr metal typically observed at 574.2 eV and Cr_2O_3 at 575.7 eV. The BE of the Cr hydroxide component is found to vary, depending on the applied potential. Within region 1 and the early stages of region 2, $Cr(OH)_3$ is detected within 0.2 eV of the reported literature value of 577.1 eV [56, 57]. Near the positive limit of region 2 and within region 3, the BE's of the hydroxide species are shifted as a result of preferential charging. A physical separation between the $Cr(OH)_3$ and the conducting alloy substrate due to the presence of the Cr_2O_3 barrier layer can insulate the hydroxide from the alloy, leading to charging during analysis.

The Ni $2p_{3/2}$ spectra indicates the presence of only two chemical species; Ni metal, detected at 852.5 eV, and a hydroxide species, ($Ni(OH)_2$) detected at ~ 855.5 eV

(with a satellite at +5.7 eV with respect to the main signal). The FWHM values for these peaks are 0.94, 1.02 and 1.10, respectively. The Ni metal signals are all within 0.2 eV of the reported literature value, 852.6 eV [57, 58]. At all potentials, the BE of $Ni(OH)_2$ is shifted with respect to the reported literature value of 854.9 eV. As discussed above for the Cr hydroxide component, the location of $Ni(OH)_2$ at the solution/oxide interface would insulate it from the conductive alloy surface, resulting in higher than anticipated BE's. The presence of both Cr and Ni metal in the spectra indicates that the oxide film formed at 0 V_{SCE} is very thin.

Fitting of the O 1s spectra required three separate components. The first peak at 529.9 eV is characteristic of an anhydrous metal oxide species, M-O (O^{2-}), while the second peak at 531.6 eV can be attributed to the hydrated metal oxide species, M-OH (OH^-). The final peak is due to residual water (H_2O) on the sample surface. With the exception of O^{2-} peak at 0.75 V_{SCE}, whose BE was shifted with respect to the reported literature values, all of the O species detected are observed at BE's within 0.2 eV of recorded literature values [56-60].

Fe was not included in the analysis since the Fe $2p_{3/2}$ peak overlaps the Ni LMM Auger line, and cannot be quantitatively resolved. The experimental BE's obtained are listed in Table 3.3.

Table 3.3 The measured BE's for the various chemical states of O, Cr and Ni obtained through XPS analysis.

E (V_{SCE})	O^{2-} (eV)	OH^- (eV)	Cr (0) (eV)	Cr_2O_3 (eV)	$Cr(OH)_3$ (eV)	Ni (0) (eV)	$Ni(OH)_2$ (eV)
-0.6	529.9	531.6	574.1	575.6	577.3	852.6	855.5
-0.4	529.8	531.5	574.1	575.6	577.3	852.5	855.4
-0.2	530.0	531.6	574.1	575.9	577.2	852.6	855.4
0	529.9	531.5	574.1	575.9	577.3	852.5	855.4
0.1	529.8	531.5	574.1	575.8	577.2	852.5	855.4
0.2	530.1	531.7	574.1	575.9	577.8	852.5	855.5
0.4	529.6	531.5	574.1	575.8	577.5	852.5	855.4
0.6	530.0	531.7	574.1	575.9	577.9	852.7	855.7
0.75	532.3	531.5	574.1	575.8	577.5	852.4	855.5

The variations in Cr composition in the oxide film, and the composition normalized to the total elemental content determined from the survey scans are plotted in Figure 3.10 (a) and (b) respectively.

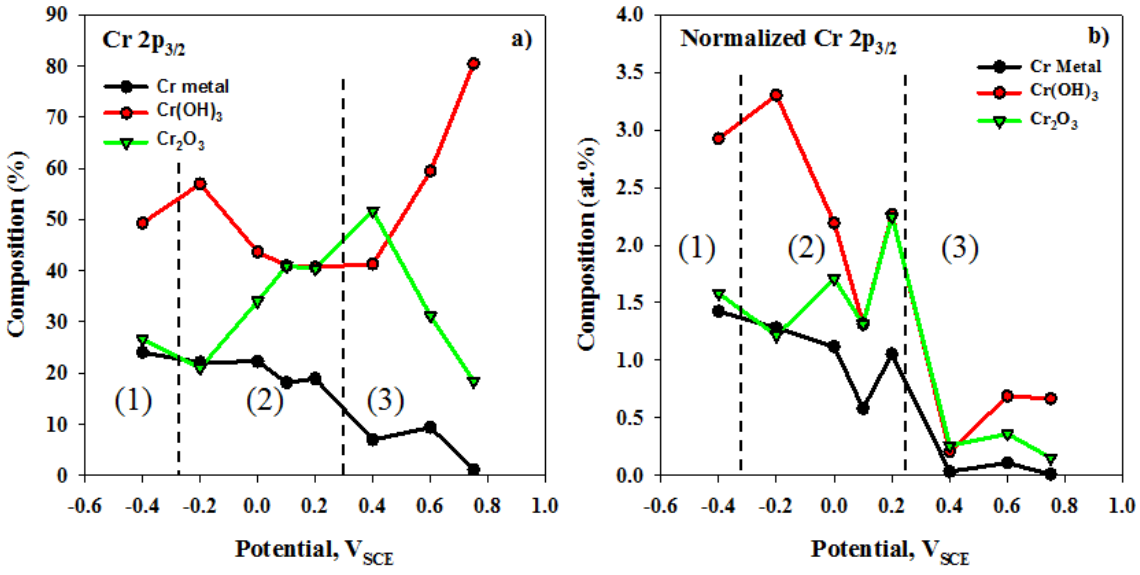

Figure 3.10 Changes in the Cr components in films grown at various potentials obtained by de-convolution of the Cr $2p_{3/2}$ peak: (a) percentage composition; (b) composition normalized against the total Cr content measured in the survey scan.

The relative amounts of individual Cr species are shown in Figure 3.10 (a) and these amounts, normalized against the total Cr content, are shown in Figure 3.10 (b) plotted as an atomic percentage (at. %). Prior to passivation, region 1 in Figure 3.1, $Cr(OH)_3$ is the predominant Cr species. Formation of the passive film in region 2 resulted in the expected increase in Cr_2O_3, even though the total amount of Cr found in the film is reduced. For potentials $\geq$ 0.4 V_{SCE} the film is almost completely depleted in Cr. This observation, combined with the decrease in Cr_2O_3 content over this potential range, confirms the destruction of the barrier layer by the onset of transpassive behaviour in region 3.

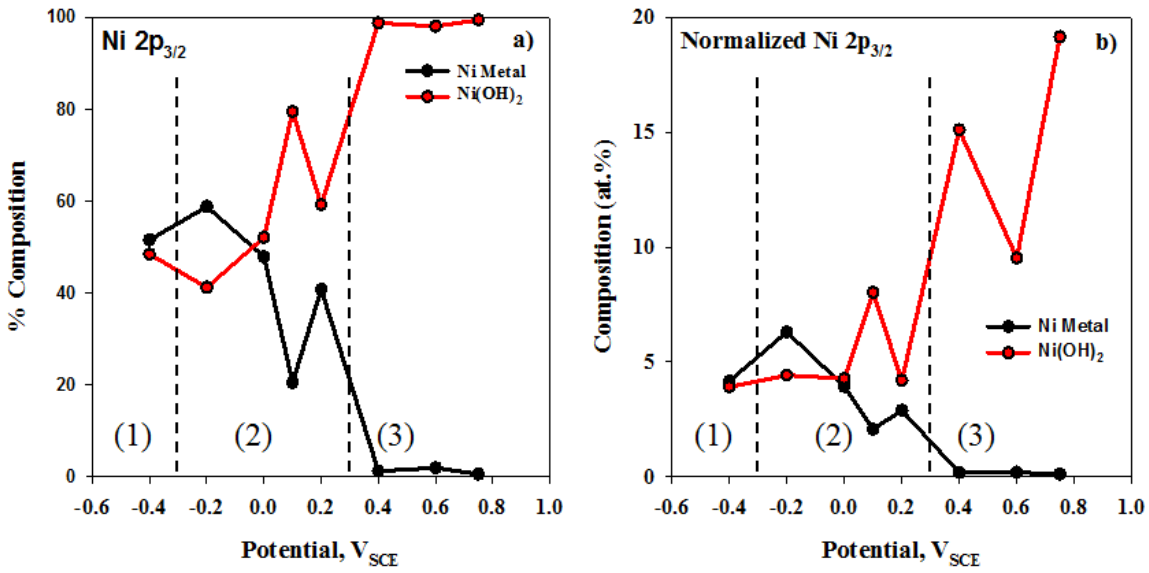

Figure 3.11 Changes in the Ni components in films grown at various potentials obtained by de-convolution of the Ni $2p_{3/2}$ peak: (a) percentage composition; (b) composition normalized against the total Ni content measured in the survey scan.

Similar compositional data for Ni, obtained from the Ni $2p_{3/2}$ peak, is presented in Figure 3.11. In region 1, and in the early stages of region 2, Ni metal is the dominant

component detected. At potentials more positive than the anodic peak, $Ni(OH)_2$ becomes the dominant Ni film component. A spike in $Ni(OH)_2$ content is observed in both plots at 0.1 V_{SCE}, accompanied by a decrease in Ni metal content. Also, the total amount of $Ni(OH)_2$ detected fluctuates at transpassive potentials.

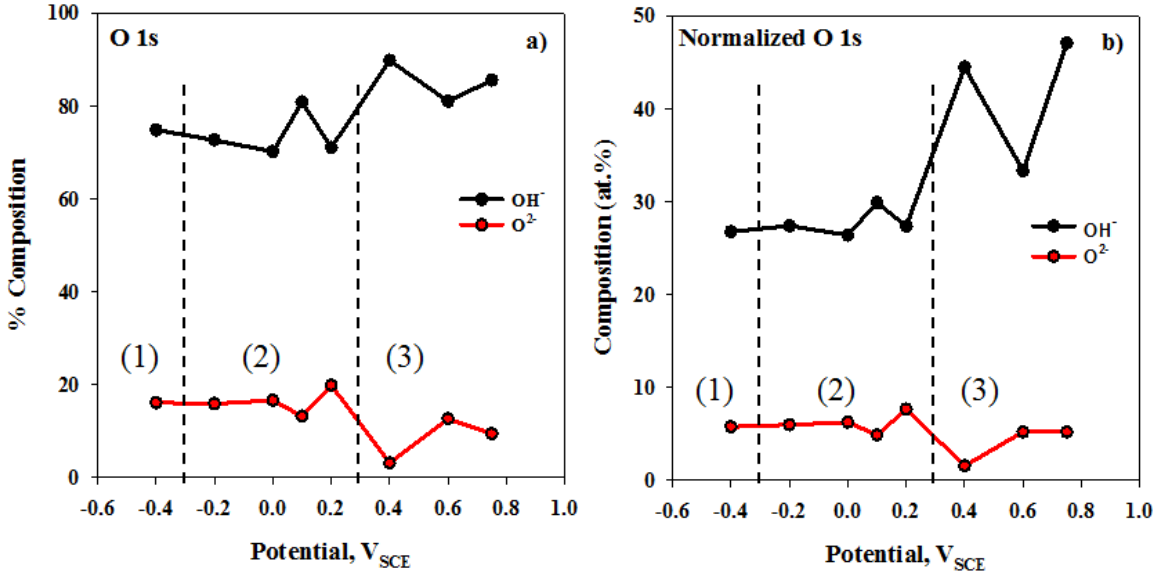

Figure 3.12 Changes in the O components in films grown at various potentials obtained by de-convolution of the O 1s band: (a) percentage composition; (b) composition normalized against the total O content measured in the survey scan.

Figure 3.12 (a) and (b) indicates that the M-OH (OH^-) species is the primary O component of the oxide film, with M-O (O^{2-}) being a significantly smaller contributor. Comparison of Figure 3.11 and Figure 3.12 show the majority of the OH^- is present as $Ni(OH)_2$. Spikes at 0.1 V_{SCE} and 0.4 V_{SCE} are observed in both the Ni $2p_{3/2}$ and O 1s spectra. The O^{2-} contribution is likely a result of Cr_2O_3 at potentials in the passive region, and to Fe oxides at potentials in the transpassive region.

The decrease in the Ni and Cr metal signals with increasing potential in Figure 3.10 and Figure 3.11 is consistent with the interpretation of the AES depth profiles. To observe a metal signal on an oxide covered surface, the film must be thin enough to allow electron escape without inelastic collisions. Probing deeper into the sample decreases the likelihood of acquiring such electrons. The depth at which > 95% of these electrons can be analysed is typically 3λ (λ – IMFP), although this value can vary, depending on the material being analysed [52, 61, 62]**.** The approximate depth of the passive film calculated from the AES data averaged 2 nm. Based on the IMFP of either Ni or Cr [52], this oxide film was thin enough to view signals from the alloy. In region 3, where the film thickness can range between 5 nm to 8 nm, the metal signal becomes almost undetectable.

3.3.5 Sulphur

S has been identified as a major impurity located on the secondary side of pressurized water reactors (PWR's) [63], and its detrimental effect on the corrosion resistance of metals and alloys has been thoroughly studied [27, 64-69**]**. Through electro-reduction or disproportionation reactions, S is easily generated from $S_2O_3^{2-}$ [70, 71].

$$S_2O_3^{2-} + 6H^+ + 4e^- \rightarrow 2S + 3H_2O \quad (3.5)$$

$$S_2O_3^{2-} + H^+ \rightarrow S + HSO_3^- \quad (3.6)$$

S species with a lower valence number are typically considered to be much more corrosive than $S_2O_3^{2-}$ [27]. Delayed passive film formation, along with enhanced anodic dissolution can result from S being adsorbed on the surface [27, 64, 65, 69]. Typically,

impurities such as S or Cl can be incorporated into the oxide film and several reports have shown S to be present in the outer oxide layer [18, 25, 47, 52].

AES depth profiles, such as the one in Figure 3.6 (a), can be used to determine the S content of the oxide film and to show that the S content is highly dependent on the potential at which the oxide film is grown. Using AES depth profiles, Figure 3.13 (a), the S at the solution/oxide interface, in the barrier layer and at the oxide/alloy interface are determined as a function of potential, Figure 3.13 (b).

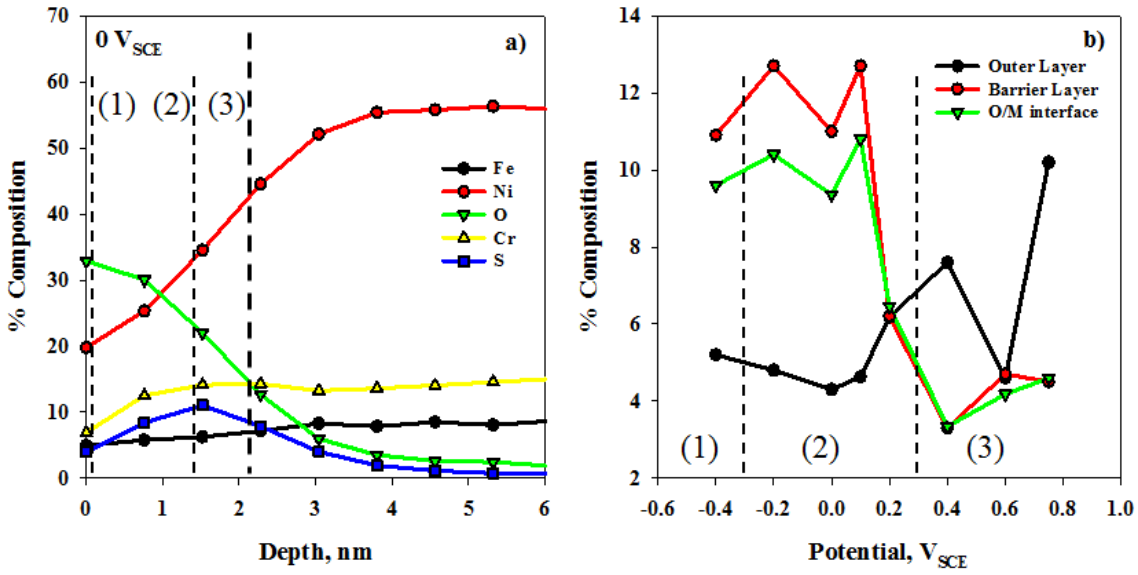

Figure 3.13 (a) AES depth profile recorded after oxidation at 0 V_{SCE}: (1) the outer layer; (2) the barrier layer; and (3) the oxide/alloy interface: (b) changes in S content at the predetermined locations.

The majority of S is detected within the barrier layer in region 1 and the initial stage of region 2. At potentials positive to the anodic peak, 0.1 V_{SCE}, a loss of S within the barrier layer is observed, accompanied by its accumulation in the outer layer at transpassive potentials.

The chemical state of S in the oxide was investigated using XPS. Since high resolution data was not collected for this element, peak fitting was applied to the S 2p signal present in the survey scans.

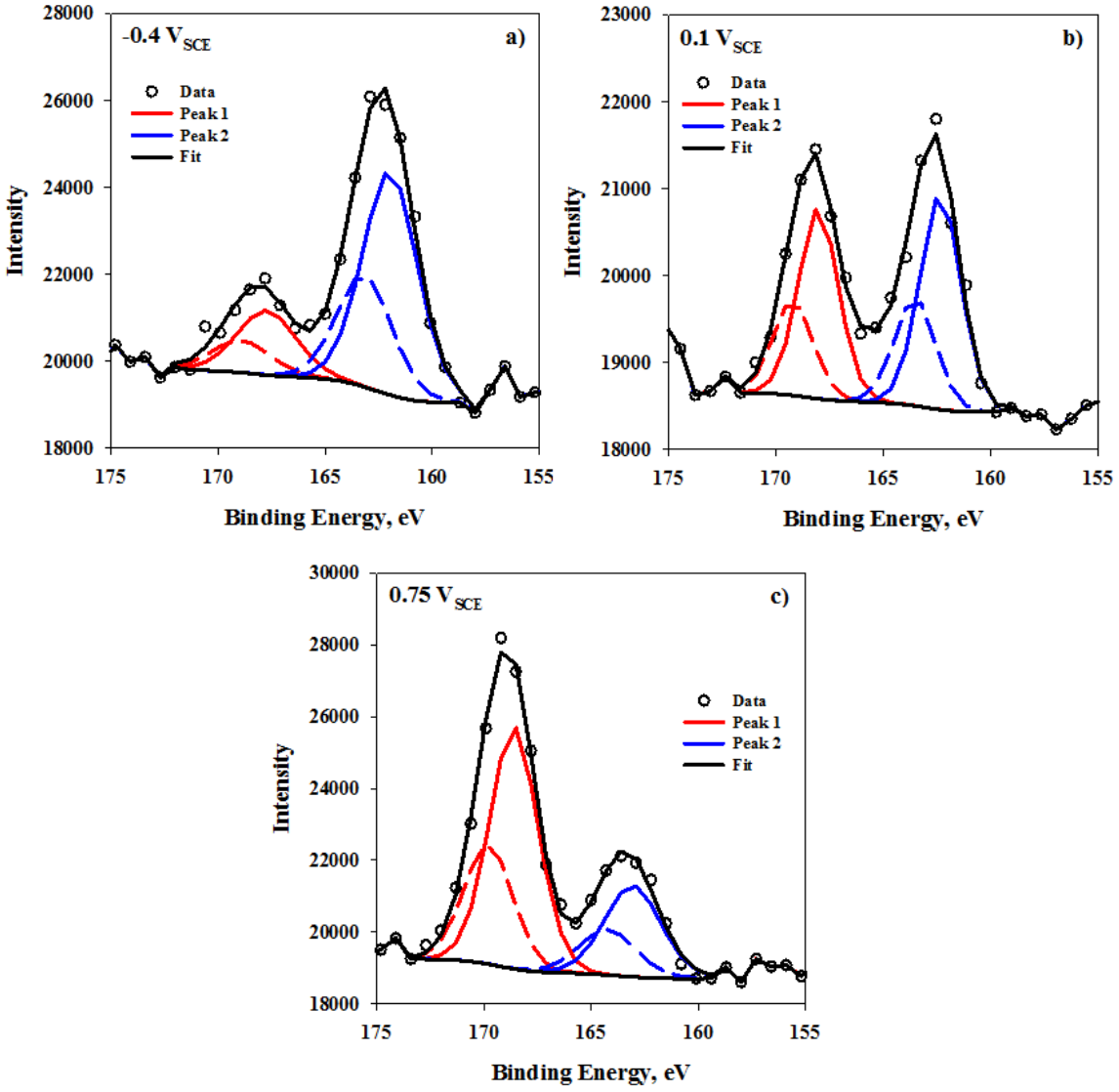

Figure 3.14 Fitted XPS survey spectra of the S 2p peak for oxide films grown at (a) -0.4 V_{SCE}, (b) 0.1 V_{SCE}, and (c) 0.75 V_{SCE}.

Examples of fitted spectra are shown in Figure 3.14 for (a) -0.4 V_{SCE}, (b) 0.1 V_{SCE} and (c) 0.75 V_{SCE}. Two peaks are observed at BE's of ~168 eV (peak 1) and ~163 eV (peak 2). Contributions to peak 1 are likely the result of oxidized S species such as a SO_4^{2-} component while peak 2 could be attributed to more reduced S species, such as $S_2O_3^{2-}$ or S^{2-} [37, 61]. Figure 3.14 shows a decrease in peak 1 accompanied by an increase in peak 2 as the film growth potential increases, indicating that the S species are becoming more oxidized at higher applied potentials.

3.4 Discussion

The results obtained in this study can be understood in terms of the PDM, which was developed and refined by Macdonald *et al.,* [48, 72-75].

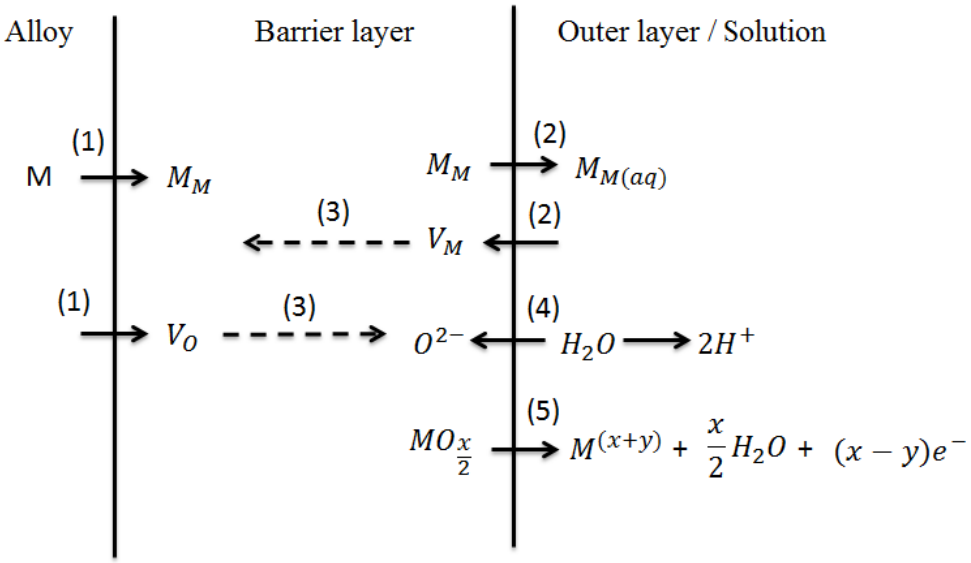

Figure 3.15 Schematic description of the point defect model: M: metal atom, M_M: metal cation on the metal sub-lattice of the barrier layer, V_M: cation vacancy on the metal sub-lattice of the barrier layer, V_O: O vacancy on the O sub-lattice of the barrier layer, O^{2-}: O anion on the O sub-lattice of the barrier layer, $M^{(x+y)}$: metal cation in solution [48].

This model, whose physiochemical processes are outlined in Figure 3.15, was developed to describe the reactions involved in the growth and dissolution of a passive bilayer film. Consistent with the data presented here, the outer layer is thought to be composed of a porous mixture of both Ni and Fe hydroxides, whose formation occurs through the hydrolysis of cations ejected from the barrier layer and subsequently precipitated on the outer surface. The formation of the outer layer through precipitation as opposed to the solid state growth mechanism of the barrier layer is consistent with the observations that solution species are incorporated into the outer layer but not the barrier layer. The inner layer is primarily composed of a much thinner and more resistive anhydrous Cr oxide (Cr_2O_3).

Figure 3.15 shows the injection of a lattice cation, M_M, accompanied by the creation of an O vacancy, V_O, (1). The ejection of the cation into the outer layer/solution is accompanied by the creation of a cation vacancy, V_M (2). Transport of the cation and anion vacancies occurs across the oxide film are shown in (3) and injection of an oxide ion and the elimination of the O vacancy are shown in (4). The transpassive dissolution of the barrier layer is shown in (5).

Changes in the film composition can be categorized according to the separate regions, and are illustrated schematically in Figure 3.16. The oxide present on the surface of the electrode in region 1 is a thin film and contains primarily $Ni(OH)_2$, and $Cr(OH)_3$. The film resistance gradually increases with the Cr concentration, due to the formation of the barrier layer. A slight increase in the film thickness is also observed.

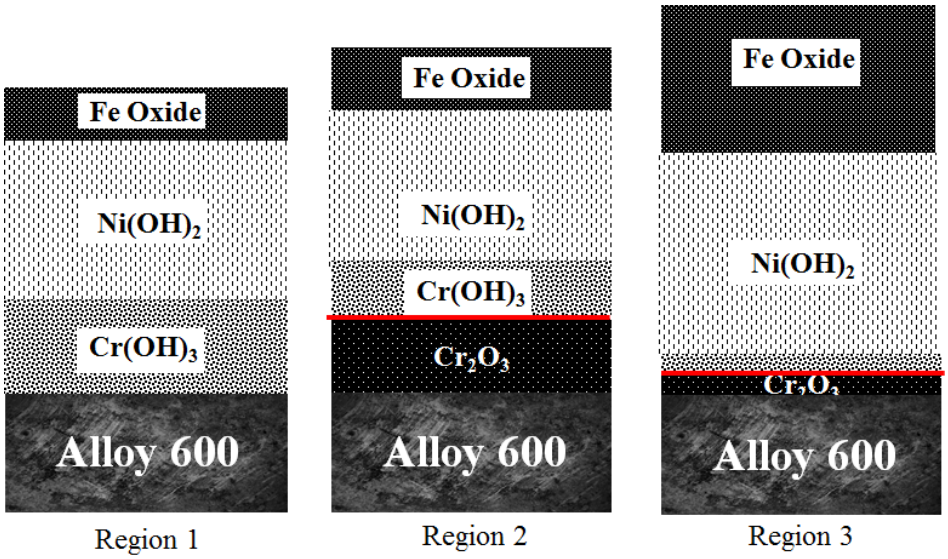

Figure 3.16 Schematic of the changes in the structure and composition of the oxide film as a function of potential. Regions 1, 2, and 3 are defined in Figure 3.1. The different components are indicated, and a division between the outer and barrier layers is marked by the red line.

The initial stages of region 2 are characterized by the formation of the passive film on the surface of the electrode. The Cr_2O_3 barrier layer is established, with the measured concentrations reaching a maximum value in the barrier layer of the film. The oxide film resistance reaches a maximum value in the initial stages of this region as well. Species which precipitated out from solution, $Ni(OH)_2$, Fe oxide and $Cr(OH)_3$, are the primary constituents of the outer oxide layer. Cr_2O_3 is known to be a thin, compact layer, so any substantial changes in film thickness are likely the result of alterations to the composition of the outer layer. The passive region shows minor fluctuations in film thickness and, unsurprisingly, minor changes in Fe and Ni content are observed. In region 3, the film exhibited transpassive behaviour. The lower potential range of this region coincides with the tail end of the anodic peak. Beyond the anodic peak, at 0.3 V_{SCE}, the film resistance drops, coinciding with the decrease in Cr^{III} associated with the Cr_2O_3 barrier layer.

Region 3 is also characterized by a thickening of the film attributed to $Ni(OH)_2$ and Fe oxides on the outer layer. These observations indicate that the anodic peak can be attributed to the onset of Cr^{III} oxidation and the destruction of the Cr_2O_3 barrier layer. This allows enhanced Ni and Fe oxidation and their accumulation in the outer layer of the film.

Surface analyses showed that S remained on the electrode as the barrier layer grew. The correlation between the Cr and S peak suggests that the Cr barrier layer is able to retain the S trapped on the surface. As the barrier layer is degraded at more positive potentials, the S is removed from the alloy/oxide interface and accumulated in the outer oxide film. XPS analyses indicate the reduced S present in the barrier layer at low potentials is re-oxidized and accumulates in the outer regions of the film at higher potentials. It is not surprising that S in the oxidized form accumulates in the outer, more porous regions of the film.

3.5 Conclusions

The oxide detected on the surface of Alloy 600 in a $Na_2S_2O_3$ solution is a bilayer film, comprising a protective Cr_2O_3 rich barrier layer and a non-protective, porous outer layer containing $Ni(OH)_2$, $Cr(OH)_3$ and Fe oxides. Growth of the passive barrier layer can be explained using the PDM. S was found to be incorporated into the Cr barrier layer, as well as the porous outer layer. Approaching the end of the passive potential range, region 2, the observation of the anodic peak, combined with the impedance data suggests partial breakdown of the oxide. At transpassive potentials, the barrier layer is broken down, and the protective properties of the film are lost. Despite this, the oxide

film continues to grow at higher potentials, accumulating Ni hydroxides and Fe oxides on the surface.

References

[1] K. Sieradzki, R.C. Newman, J. Phys. Chem. Solids, 48 (1987) 1101-1113
[2] R.H. Jones, Stress Corrosion Cracking: Materials Performance and Evaluation, ASM International, (1992)
[3] L.L. Shreir, R.A. Jarman, G.T. Burstein, Corrosion: Metal/Environmental reactions, Butterworth-Heinemann (1994)
[4] R.C. Scarberry, S.C. Pearman, J.R. Crum, Corros., 32 (1976) 401-406
[5] R. Bandy, R. Roberge, R.C. Newman, Corros. Sci., 23 (1983) 995-1006
[6] R. Bandy, R. Roberge, R.C. Newman, Corros., 39 (1983) 391-398
[7] R. Bandy, D. Van Rooyen, Corros., 40 (1984) 281-289
[8] H. Coriou, L. Grall, C. Mahieu, M. Pelas, Corros., 22 (1966) 280-290
[9] H.R. Copson, G. Economy, Corros., 24 (1968) 55-65
[10] H.R. Copson, S.W. Dean, Corros., 21 (1965) 1-8
[11] D.-J. Kim, H. Kim, S. Hwang, J. Kim, J. Park, Met. Mater. Int., 16 (2010) 259-266
[12] J.R. Cels, Corros., 34 (1978) 198-209
[13] M.-C. Tsai, W.-T. Tsai, J.-T. Lee, Corros. Sci., 34 (1993) 741-757
[14] W-T. Tsai, Z-H. Lee, J-T. Lee, M-C. Tsai, P-H. Lo, Mater. Sci. Eng., A118 (1989) 121-129
[15] D. Van Rooyen, Corros,. 31 (1975) 327-337
[16] J.-J. Park, S.-I. Pyun, S.-B. Lee, Electrochim. Acta., 49 (2004) 281-292
[17] M. Bojinov, G. Fabricius, P. Kinnuneb, T. Laitinen, K. Makela, T. Saario, G. Sundholm, K. Yliniemi, Electrochim. Acta., 47 (2002) 1697-1712
[18] E.H. Lee, K.M. Kim, U.C. Kim, Mater. Sci. Eng., A449 (2007) 330-333
[19] J.-S. Baek, J.-G. Kim, D.-H. Hur, J.-S. Kim, Corros. Sci., 45 (2003) 983-994
[20] W.-T. Tsai, C.-H. Chou, Mater. Sci. Eng., A288 (2000) 5-11
[21] W.-T. Tsai, M.-J. Sheu, J.-T. Lee, Corros. Sci., 38 (1996) 33-45
[22] I.J. Yang, Corros., 49 (1993) 576-585
[23] W.-T. Tsai, C.-H. Chou, Mater. Sci. Eng., A288 (2005) 5-11
[24] D.-J. Kim, H.-C. Kwon, H. Kim, Corros. Sci., 50 (208) 1221-1227
[25] T. Sakai, K. Aoki, T. Shigemitsu, Y. Kishi, Zairyo to Kankyo 40 (1991) 736-741
[26] W.-T. Tsai, C.-S. Chang, J.-T. Lee, Corros., 50 (1994) 98-105
[27] Z. Fang, R. W. Staehle, Corros., 55 (1999) 355-379
[28] W. Yang, Z. Lu, D. Huang, D. Kong, G. Zhao, J. Congleton, Corros. Sci., 43 (2001) 963-977
[29] M. Da Cunha Belo, N.E. Hakiki, M.G.S. Ferreira, Electrochim. Acta., 44 (1999) 2473-2481
[30] L.A.S. Ries, M. Da Cunha Belo, M.G.S. Ferreira, I.L. Miller, Corros. Sci., 50 (2008) 676-686
[31] R. M. Carranza, M.G. Alvarez, Corros. Sci., 38 (1996) 909-925
[32] E. Barsoukov, J. R. Macdonald, Impedance Spectroscopy: Theory, Experiment, and Applications, J. Wiley & Sons, (2005)
[33] K. Juttner, W.J. Lorenz, Corros. Sci., 29 (1989) 279-288
[34] T. Nickchi, A. Alfantazi, Corros. Sci., 52 (2010) 4035-4045
[35] W. Lai, W. Zhao, F. Wang, C. Qi, J. Zhang, Surf. Interface Anal., 41 (2009) 531-539

[36] S.-H. Song, P. Xiao, J. Mater. Sci., 38 (2003) 499-506
[37] P. Marcus, J.M. Grimal, Corros. Sci., 33 (1992) 805-814
[38] J. Robertson, Corros. Sci., 32 (1991) 443-465
[39] D.D. Macdonald, A. Sun, Electrochim. Acta., 51 (2006) 1761-1779
[40] J. Robertson, Corros. Sci., 29 (1969) 1275-1291
[41] D. Hamm, C.-O.A. Olsson, D. Landolt, Corros. Sci., 44 (2002) 1009-1025
[42] T. Dan, T. Shoji, Z. Lu, K. Sakaguchi, J. Wang, E.-H. Han, W. Ke, Corros. Sci., 52 (2010) 1228-1236
[43] A.C. Lloyd, D.W. Shoesmith, N. S. McIntyre, J.J. Noel, J. Electrochem. Soc., 150 (2003) B120-B130
[44] P. Jakupi, D. Zagidulin, J.J. Noel, D.W. Shoesmith, Electrochim. Acta., 56 (2011) 6251-6259
[45] N.E. hakiki, M. Da Cunha Belo, A.M.P. Simoes, M.G.S. Ferreira, J. Electrochem. Soc., 145 (1998) 3821-3829
[46] F. Gaben, B. Vuillemin, R. Oltra, J. Electrochem. Soc., 151 (2004) B595-B604
[47] P. Marcus, J.M. Grimal, Corros. Sci., 31 (1990) 377-382
[48] D.D. Macdonald, J. Electrochem. Soc., 139 (1992) 3434-3449
[49] W. Yang, Z. Lu, D. Huang, D. Kong, G. Zhao, J. Congleton, Corros. Sci., 43 (2001) 963-977
[50] M. Seo, N. Sato, Corros., 36 (1980) 334-339
[51] L. Zhang, D.D. Macdonald, Electrochim. Acta., 43 (1998) 2661-2671
[52] S. Mischler, A. Vogel, H.J. Mathieu, D. Landolt, Corros. Sci., 32 (1991) 925-944
[53] A.S. Lim, A. Atrens, Appl. Phys., A54, (1992) 343-349
[54] A.K Agrawal, W.N. Stiegelmeyer, W.E. Berry, EPRI NP-4504LD, EPRI, USA, 1986
[55] E. Sikora, D. Macdonald, Electrochim. Acta., 48 (2002) 69-77
[56] M.C. Biesinger, C. Brown, J.R. Mycroft, R.D. Davidson, N.S. McIntyre, Surf. Interface. Anal., 36 (2004) 1550-1563
[57] M.C. Biesinger, B.P. payne, A.P. Grosvenor, L.W.M. Lau, A. Gerson, R. St.C. Smart, Appl. Surf. Sci., 257 (2011) 2717-2730
[58] M. C. Biesinger, B. P. Payne, L.M.M. Lau, A. Gerson, R.St.C. Smart, Surf. Interface Anal., 41 (2009) 324-332
[59] P. Keller, H.-H. Strehblow, Corros. Sci., 46 (2004) 1939-1952
[60] H. Luo, C.F. Dong, X.G. Li, K. Xiao, Electrochimica Acta., 64 (2012) 211-220
[61] S. Bera, S. Rangarajan, S.V. Narasimhan, Corros. Sci., 42 (2000) 1709-1724
[62] C.J. Powell, Surf. Sci., 44 (1974) 29-46
[63] V.W. Jones, Proceedings EPRI 1987 PWR Plant Chemists' Meeting (1987)
[64] J. Oudar, P. Marcus, Appl. Surf. Sci., 3 (1979) 48-67
[65] R. C. Newman, Corros., 41 (1985) 450- 453
[66] P. Marcus, A. Teissier, J. Oudar, Corros. Sci., 24 (1984) 259-268
[67] J. Oudar, P. Marcus, Appl. Surf. Sci., 3 (1979) 48-67
[68] P. Marcus, A. Teissier, J. Oudar, Corros. Sci., 24 (1984) 259-268
[69] P. Marcus, I. Olefjord, Corros., 42 (1986) 91-98
[70] D. Tromans, L. Frederick, Corros., 40 (1984) 633-639
[71] T. Nickchi, A. Alfantazi, Corros., 68 (2012) 1-11

[72] L.F. Lin, C.Y. Chao, D.D. Macdonald, J. Electrochem. Soc., 128 (1981) 1194-1198
[73] C.Y. Chao, L.F. Lin, D.D. Macdonald, J. Electrochem. Soc., 128 (1981) 1187-1194
[74] C.Y. Chao, L.F. Lin, D.D. Macdonald, J. Electrochem. Soc., 129 (1982) 1874-1979
[75] D.D. Macdonald, Electrochim. Acta., 56 (2011) 1761-1772

Chapter 4. Behaviour of the Oxide Films Formed on Alloy 800 Steam Generator Tubing in a 0.1 M $Na_2S_2O_3$ Solution

4.1 Introduction

The Fe-Ni-Cr base Alloy 800 is one of several possible candidates to replace Alloy 600 as SG tubing in CANDU reactors. The performance of nuclear power plants requires the uninterrupted operation of the SG tubing, and should be improved by the high temperature strength and corrosion resistance of Alloy 800 [1, 2]. Unfortunately, recent reports have shown that Alloy 800 can be susceptible to SCC under specific conditions [3, 4, 5]. Tensile stresses applied to the SG tubing make it potentially susceptible to SCC.

Typically, SCC is defined as the failure of a material through slow, environmentally induced crack propagation, which occurs as a result of a combined interaction between mechanical stress and the corrosion reaction. This type of corrosion is problematic, since it is extremely difficult to detect in early or intermediate stages. The stress concentration required to propagate the crack typically does not exceed the critical values required for mechanical failure of the material, and normal ductility standards are often observed. The propagation of the crack occurs at a very slow rate until the stresses in the ligament of the metal exceed the fracture strength, and failure occurs. A number of different factors can affect the susceptibility of a material to SCC, such as environment, tensile stress, and the composition of the alloy [3, 4, 6-8].

In this investigation, the passive oxide film formed on Alloy 800 was studied in an aqueous 0.1 M $Na_2S_2O_3$ solution. Originating from oil contamination, deoxygenating

agents, etc., $S_2O_3^{2-}$ is known to cause localized corrosion through the adsorption of S onto the surface, leading to accelerated anodic dissolution [9]. The effects of S species are well known on Alloy 600 [10-18], but not as well characterized on Alloy 800 [9, 19]. The properties of the passive film on Alloy 800 were studied after growth at various potentials using electrochemical techniques such as anodic polarization and EIS. The electrochemical behaviour of the oxide film was correlated to compositional changes using surface analytical techniques such as AES and XPS.

4.2 Experimental

4.2.1 Sample Preparation

Alloy 800 tubing sections with a 9.5 mm diameter were procured from Rolled Alloys Canada in the mill-annealed condition. The composition is presented in Table 4.1.

Table 4.1 Chemical composition of Alloy 800 SG tubing (wt%).

Element	Ni	Cr	Fe	Mn	Al	Ti	Si	C
Composition %	30.86	20.37	45.76	0.72	0.40	0.53	0.54	0.07

Rectangular prismatic coupons were cut using a Buehler diamond-tipped saw. The average area on the outer surface of these coupons was ~ 20 mm^2. The coupons were extensively ground and polished, finishing with a 0.05 micron alumina grit polishing pad, washed with DI water and sonicated in acetone.

4.2.2 Electrochemical Measurements

Electrochemical measurements were carried out on electrodes assembled by spot welding a stainless steel wire onto the back of a polished coupon. The back and sides of the coupon, as well as the wire, were coated with a Microshield™ masking aid, leaving a single, flat, exposed face. A 0.1 M $Na_2S_2O_3$ solution (pH ~ 6.5; room temperature) was used in all electrochemical experiments and was prepared using DI water with a resistivity of 18.2 MΩ•cm. The three-electrode cell contained a Pt foil CE and a SCE reference (0.2412 V vs. SHE), with the Alloy 800 electrode acting as the WE. The solution was vigorously sparged with Ar gas for thirty minutes to remove oxygen and a steady flow of Ar was subsequently maintained for the duration of the experiment. Prior to experiments, electrodes were cathodically cleaned at -1.2 V_{SCE} for one hour. Potentiodynamic polarization experiments were run using a Solartron 1286 potentiostat at a scan rate of 0.167 mV/s. The experiments were started 0.15 V below the measured corrosion potential and terminated at 1.0 V_{SCE}.

Oxide films were grown at an applied potential in the range -0.4 V_{SCE} to 0.75 V_{SCE} for three hours. The film growth potentials were selected based on the anodic polarization behaviour. The properties of the oxides were investigated by EIS. An input sinusoidal potential with an amplitude of ± 10 mV was applied at the film growth potential and the frequency varied over the range 65 kHz to 0.005 Hz using a Solartron 1255 frequency response analyzer. The data was collected and analyzed using ZPlot™ and ZView™ software, respectively.

4.2.3 Surface Analysis

4.2.3.1 Auger Electron Spectroscopy (AES)

AES analyses were conducted on the electrodes after electrochemical film growth. On removal from the cell, electrodes were rinsed with DI water and methanol and dried. Data was obtained using a PHI 660 scanning Auger electron microscope with an excitation energy of 5 keV. An Ar^+ ion beam was used for sputtering to obtain depth profiles. Following removal of the electrode from the electrochemical cell, the wire attached to the electrode was stripped of the masking agent and cut down to ensure a proper fit in the microscope sample holder. A survey scan was acquired for each electrode, and during depth profiling the intensity for the elements Ni, Cr, Fe, C, O and S was monitored as a function of sputtering time. Sputtering-time profiles were converted into depth profiles using a sputtering rate determined by depth profiling a reference specimen under similar conditions. It was assumed that the sputtering rate was the same for both air and anodically formed oxides.

4.2.3.2 X-ray Photoelectron Spectroscopy (XPS)

XPS analyses were conducted on electrodes after film growth at various potentials. Following removal from the electrochemical cell, electrodes were immediately rinsed with DI water and methanol. An AXIS Ultra Kratos spectrometer with a monochromatic Al Kα x-ray source (10 mA, 14 kV) was employed for analyses. To calibrate the work function of the instrument, the BE for the Au $4f_{7/2}$ peak was set to 83.96 eV and the spectrometer dispersion was adjusted using Cu $2p_{3/2}$, with a BE of 932.62 eV. The instrument base pressure was held at ~ 2.5 x 10^{-8} Torr. For each

electrode, survey spectra were collected over an area of 256 × 256 μm, at a pass energy of 160 eV with a 0.7 eV energy step over a BE range of 1100 eV to 0 eV. High resolution scans of the Ni $2p_{3/2}$, Cr $2p_{3/2}$, Fe $2p_{3/2}$, C 1s and O 1s peaks were obtained from the same area at a pass energy of 20 eV using a step size of 0.05 eV. The BE ranges for these elements were (890 eV to 847 eV), (595 eV to 570 eV), (540 eV to 525 eV), and (295 eV to 278 eV), respectively. Spectral analyses were performed using CasaXPS™ software. With the exception of Cr $2p_{3/2}$, high resolution spectra were charge corrected with reference to the main line of the C 1s spectrum at 285.0 eV.

4.3 Results

4.3.1 Anodic Polarization

A potentiodynamic polarization curve recorded on Alloy 800 in a de-aerated 0.1 M $Na_2S_2O_3$ solution at 25°C is shown in Figure 4.1. The anodic polarization curve can be divided into three regions. Region 1, when the passive film is not fully formed, is located at potentials less than -0.3 V_{SCE}. The passive region can be considered as the potential range (region 2) between -0.3 V_{SCE} and 0.3 V_{SCE}, and encompasses the anodic peak observed at 0.1 V_{SCE}. For potentials ≥ 0.3 V_{SCE}, the rise in current density indicates an onset of transpassive behaviour (region 3). The anodic peak suggests a significant change in oxide film properties in this potential range. Similar anodic peaks have been observed on this, and a number of other Fe-Ni-Cr alloys, but have not been well characterized [10, 11, 16, 17, 19-23].

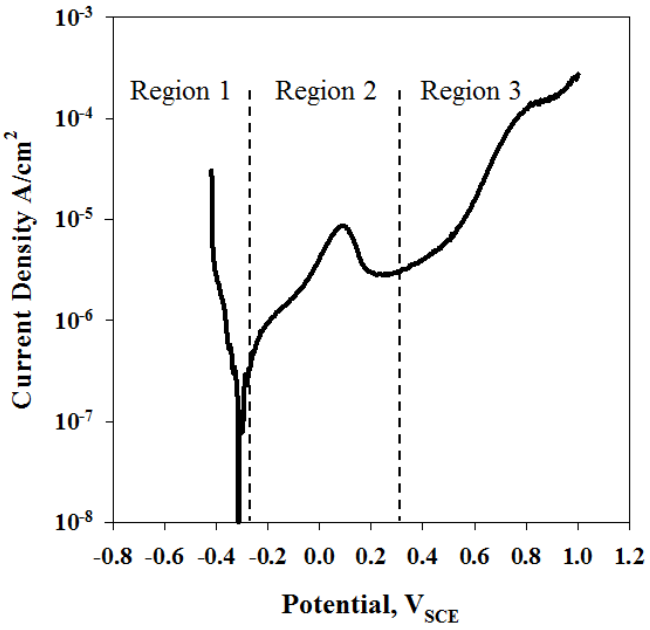

Figure 4.1 Anodic polarization curve for Alloy 800 in 0.1 M $Na_2S_2O_3$ solution. The curve is divided into three regions: (1) pre-passive; (2) passive; (3) transpassive.

A previous study on Alloy 600 in chapter 3 suggested that this rise in current density is the result of partial oxide film breakdown. Based on this polarization curve, several potentials were selected for further electrochemical and surface analytical study.

4.3.2 Electrochemical Impedance Spectroscopy (EIS)

EIS spectra were recorded on the oxide films grown on the surface of Alloy 800 at potentials in the range -0.4V_{SCE} to 0.8 V_{SCE}, Figure 4.2. The Nyquist plots in Figure 4.2 (a) appear as depressed semi-circles, a feature commonly observed when the electrode surface is non-homogeneous.

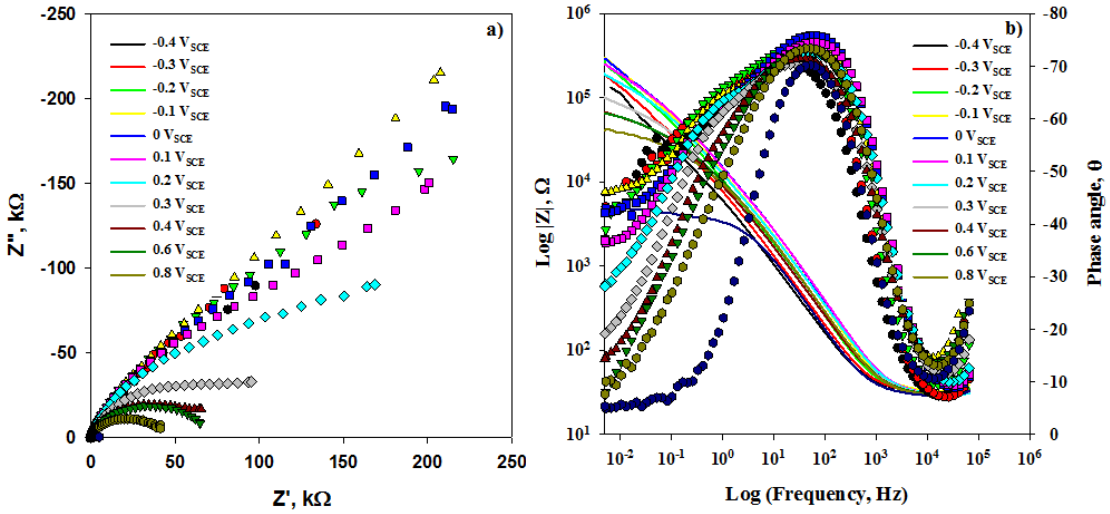

Figure 4.2 EIS spectra recorded on films grown for three hours displayed as (a) Nyquist and (b) Bode plots.

The Bode plots, which highlight changes in the spectra over the full frequency range, are shown in Figure 4.2 (b). At potentials greater than -0.1 V_{SCE}, the total impedance, |Z|, along with the phase angle, θ, decreases at the low frequency limit as the potential increases.

The EIS data was analyzed using an equivalent circuit containing three time constants in series, Figure 4.3.

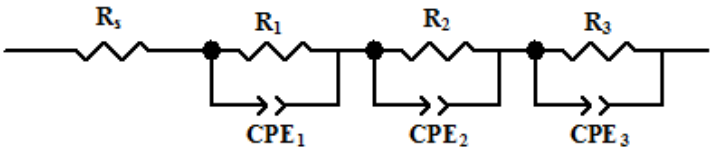

Figure 4.3 Equivalent circuit used to model EIS spectra recorded on Alloy 800.

This model has been used to fit spectra recorded on passive films on other similar Ni and Fe base alloys [20, 21]. This model includes three time constants in series, combined

with a single resistive element. CPE's are used to account for the inhomogeneous properties of the oxide indicated by the depressed semi-circles in Figure 4.2 (a) [24-26]. This equivalent circuit was chosen to represent the bilayer oxide film on the surface of the alloy. The solution resistance is represented by R_s, the outer and barrier oxide layers are represented by the combination R_1/CPE_1 and R_2/CPE_2, respectively. The R_3/CPE_3 time constant was included to account for charge transfer processes. Whether the charge transfer is dominated by the oxide/alloy or the solution/oxide interface will vary with potential. Figure 4.4 shows examples of spectra fitted to the circuit proposed in Figure 4.3.

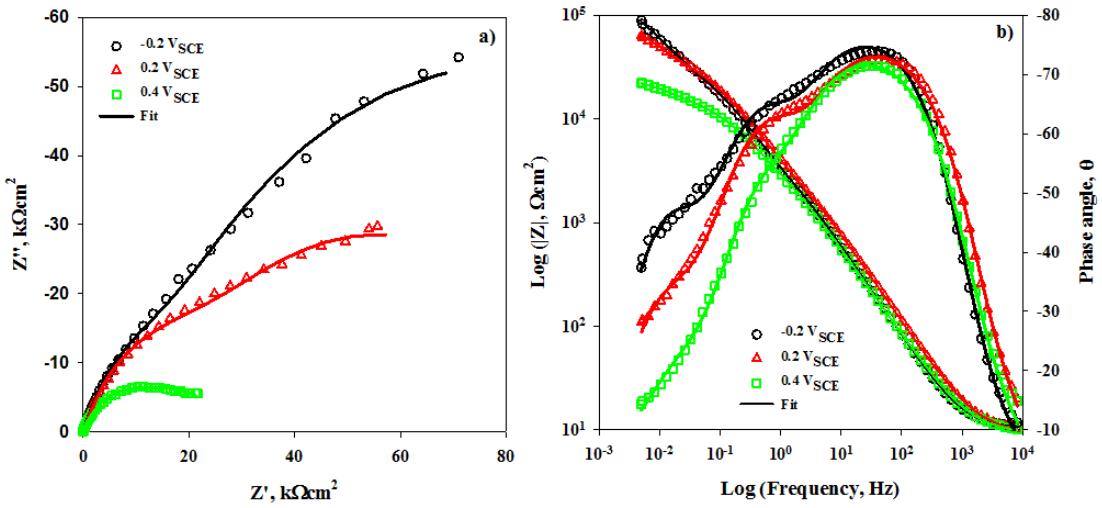

Figure 4.4 EIS plots comparing the fit to the acquired data at film growth potentials of -0.2 V_{SCE}, 0.2 V_{SCE}, and 0.4 V_{SCE} in 0.1 M $Na_2S_2O_3$: (a) Nyquist and (b) Bode plots.

The model fits the spectra over the whole potential range investigated. A compilation of the calculated values for individual circuit elements is given in Table 4.2.

Table 4.2 Summary of the parameters obtained from the fitted EIS spectra.

E (V_{SCE})	R_2 ($k\Omega cm^2$)	CPE_2 (μFcm^{-2})	n	R_1 ($k\Omega cm^2$)	CPE_1 (μFcm^{-2})	n	R_3 ($k\Omega cm^2$)	CPE_3 (μFcm^{-2})	n
-0.4	77.13	237.2	0.8187	2.971	294.2	0.8848	0.7227	254.8	0.8436
-0.3	117.1	265.4	0.8453	12.79	179.0	0.8554	1.030	1721	0.8565
-0.2	130.7	190.9	0.8557	16.27	103.5	0.8680	0.7200	126.8	0.9031
-0.1	214.3	164.5	0.8366	19.60	81.66	0.8601	0.7230	78.88	0.9316
0	179.3	180.4	0.8462	23.03	67.52	0.8719	1.200	59.96	0.9277
0.1	126.0	207.1	0.8386	25.93	65.40	0.8607	1.070	65.38	0.9138
0.2	69.70	263.0	0.8281	23.42	74.33	0.8435	0.7398	98.62	0.8892
0.3	24.98	488.9	0.8046	15.68	96.23	0.8273	0.6583	179.2	0.8497
0.4	14.18	59.10	0.7699	10.85	108.7	0.8393	1.0220	127.3	0.8696
0.5	12.57	414.8	0.8582	8.139	98.37	0.8683	1.359	87.31	0.8622
0.6	7.635	537.6	0.7768	5.655	108.6	0.8775	1.3602	68.10	0.8897
0.8	0.7111	3459	0.5368	0.8583	103.9	0.9255	0.2884	88.92	0.9593

The resistance for both the outer and barrier layer oxides, as well as the polarization resistance, R_p, as a function of applied potential is shown in Figure 4.5. The protective properties of the barrier layer are clear, its resistance being generally an order of magnitude greater than that of the outer layer. The resistance of the barrier layer increased markedly through region 1 and the early stages of region 2, consistent with the development of improved passivity. The decrease in barrier layer resistance begins near -0.1 V_{SCE}, which coincides with the onset of the anodic current peak. The decrease continues as the potential approaches the anodic peak region, indicating that the enhanced current in this region can be attributed partially to the breakdown of this barrier layer. As the potential is increased into region 3, the barrier layer resistance continues to decrease, consistent with the onset of transpassivity. The resistance of the outer layer also increases throughout region 1 and the early stages of region 2, but reaches a maximum value at the anodic peak.

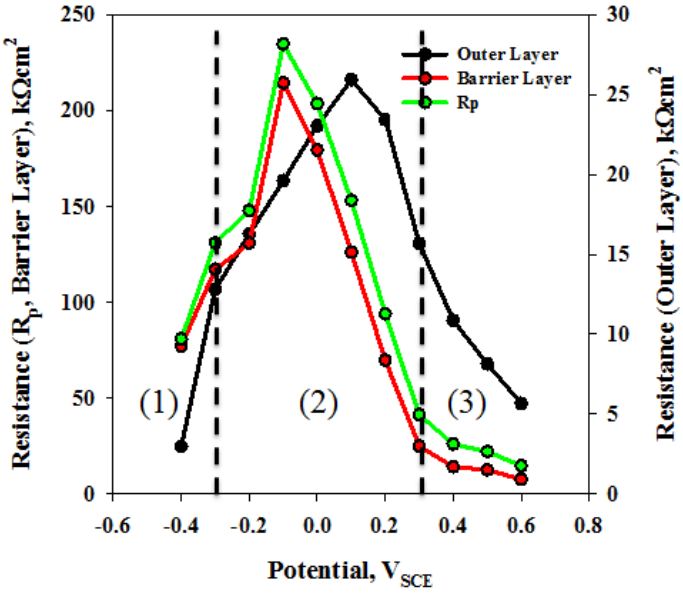

Figure 4.5 Polarization resistance, R_p, barrier and outer oxide layer resistances as a function of applied potential.

The resistance of this outer layer decreases with increasing potential beyond the anodic peak and approaches values similar to those measured for the barrier layer in region 3. This indicates that at potentials positive to the anodic peak the outer layer becomes increasingly important in maintaining passivity. This is confirmed from a plot of R_p, the sum of all resistances.

4.3.3 Surface Analysis - AES

AES depth profiles were measured on oxide films grown potentiostatically at film growth potentials ranging from -0.4 V_{SCE} to 0.75 V_{SCE}. Figure 4.6 shows examples of profiles recorded in (a) region 1 (-0.4 V_{SCE}), (b) region 2 (0.2 V_{SCE}) and (c) region 3 (0.75 V_{SCE}), respectively. The oxide thickness can be estimated from these plots as the depth at which the O signal decreases to 50% of its maximum value [27-30].

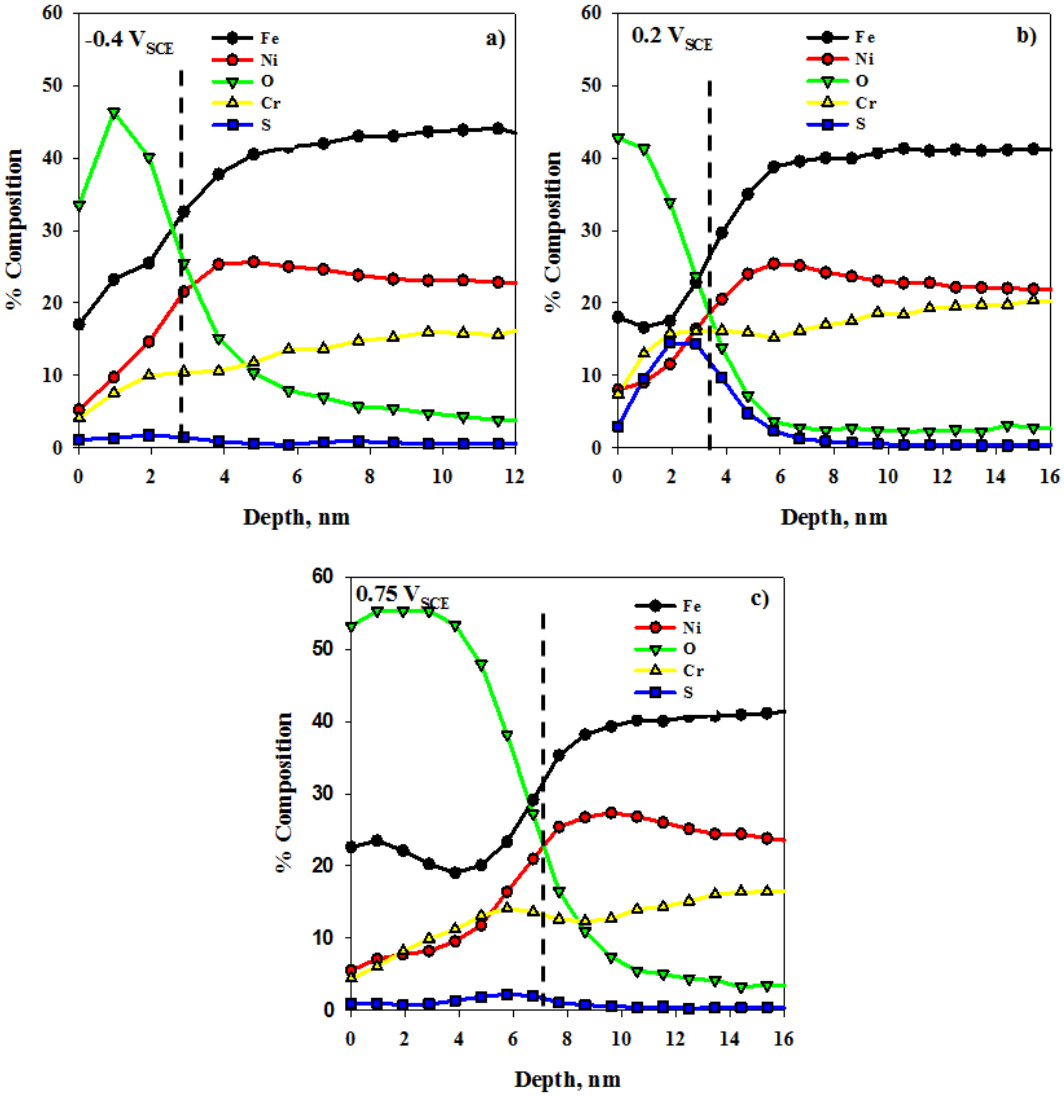

Figure 4.6 AES depth profiles for oxide films grown on Alloy 800 at (a) -0.4 V_{SCE}, (b) 0.2 V_{SCE}, and (c) 0.75 V_{SCE}. The dashed line indicates the oxide/alloy interface.

Ion beam mixing makes identifying the precise location of this interface difficult, making the thickness an estimate. Changes in the oxide film thickness as a function of film growth potential are plotted in Figure 4.7.

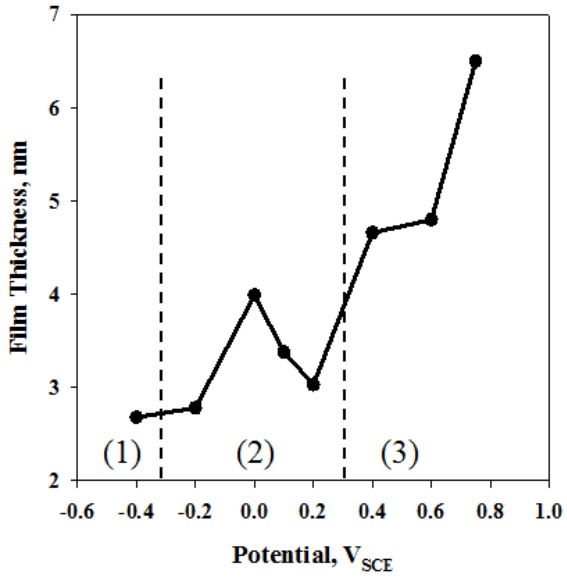

Figure 4.7 Oxide film thickness on Alloy 800 as a function of film growth potential determined from AES depth profiles.

The thickening of the oxide film as the applied film growth potential becomes increasingly positive has been observed elsewhere [31, 32]. The drop in film thickness between 0 V_{SCE} and 0.2 V_{SCE} coincides with the rise in current density associated with the anodic peak, Figure 4.1, and could be due to either a change in composition, growth mechanism, or physical properties of the film. For instance, a porous oxide would sputter at a much faster rate than a dense oxide of similar thickness, giving the appearance of a thinner film. At transpassive potentials a much thicker oxide film is formed.

The AES depth profiles also reveal changes in the elemental composition of the oxide with depth. The Fe, Ni and Cr contents of the film are best expressed as cation fractions and can be calculated as described in detail in chapter 3. These fractions are plotted as a function of depth for the oxide films grown at (a) -0.4 V_{SCE}, (b) 0.2 V_{SCE} and (c) 0.75 V_{SCE} in Figure 4.8.

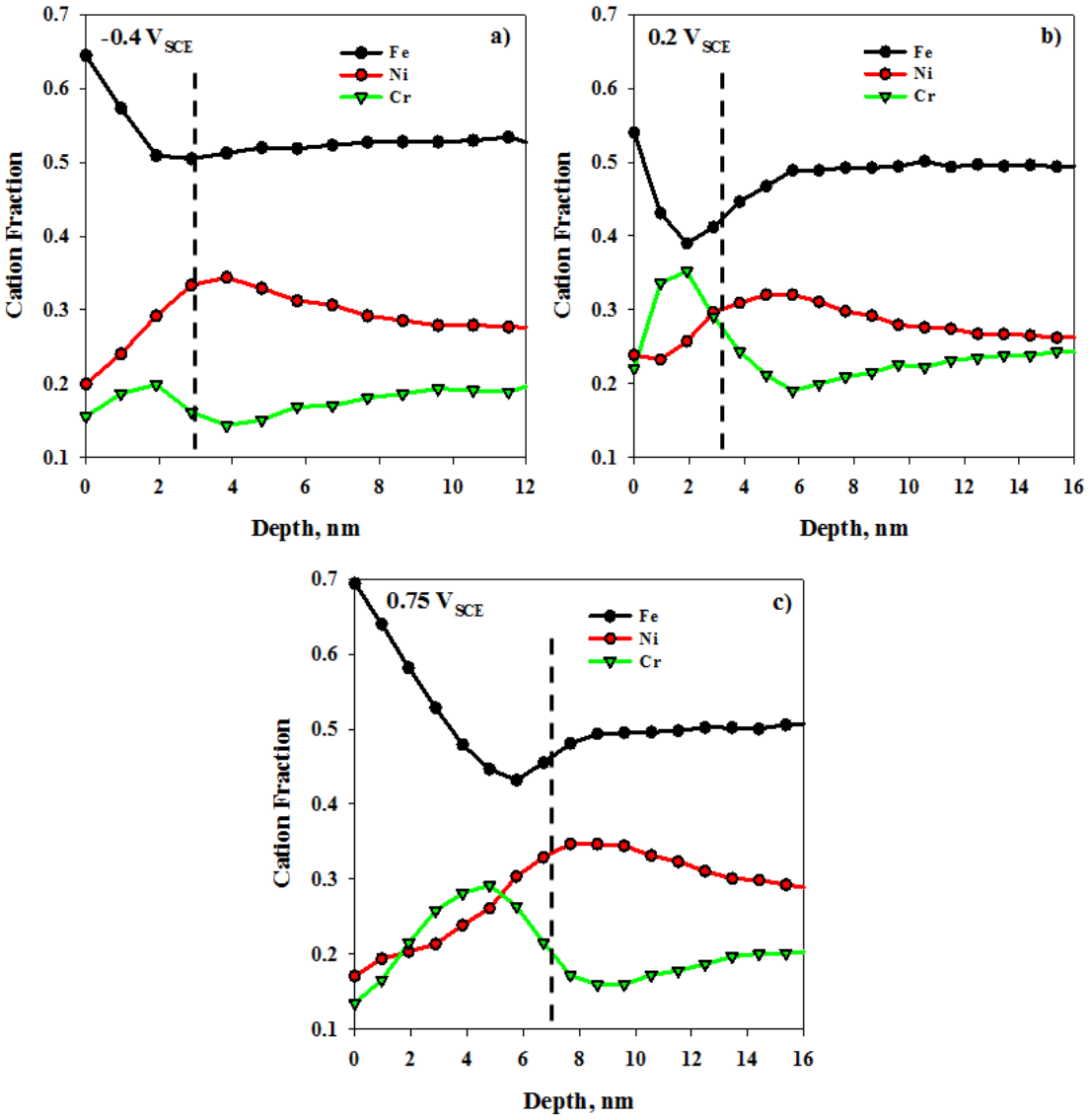

Figure 4.8 Cation fractions in the oxide films grown at -0.4 V_{SCE}, 0.2 V_{SCE} and 0.75 V_{SCE}. The vertical lines indicate the locations of the oxide/alloy interface.

After growth at -0.4 V_{SCE} (region 1) the film is composed mainly of Fe with small amounts of Ni and Cr. At this potential, there is no well-defined bilayer oxide. At 0.2 V_{SCE} (region 2), Figure 4.8 (b), a clear bilayer film is present with a Cr rich barrier layer underlying an outer oxide film composed primarily of Fe and Ni. At 0.75 V_{SCE} (region 3), Figure 4.8 (c), the inner barrier layer is still distinguishable and the outer oxide layer

is highly enriched in Fe, but depleted in Ni, relative to the alloy composition. This accumulation of Fe on the surface of the alloy at transpassive potentials accounts for the rise in film thickness observed, Figure 4.7. The effect of electrochemical film formation on the composition of the bulk alloy can also be seen in the cation fractions in the depth profiles in Figure 4.8. Depletion in Cr and enrichment in Ni within the top 6 nm to 8 nm of the oxide/alloy interface is observed. While concentrated in the outer layer, Fe is not retained within the barrier layer. It is also slightly depleted in the top 2 nm of the alloy surface at 0.2 V_{SCE} (passive region) and at 0.75 V_{SCE} (transpassive region), Figure 4.8 (b) and (c), respectively.

The concentration of Fe, Ni and Cr present in the outer oxide layer and the barrier layer can be estimated from the depth profiles in Figure 4.8 using the procedure described in Chapter 3. The elemental composition of the outer layer is estimated from the cation fractions at the solution/oxide interface, and that of the barrier layer from the fractions at the location of the maximum in the Cr depth profile. These cation fractions are plotted as a function of film growth potential in Figure 4.9. The Fe, Figure 4.9 (a), and Cr, Figure 4.9 (b), contents are inversely related. The Fe content decreases as the film growth potential is increased in the pre-passive region (1) and into the passive region (2). Conversely, the Cr content, especially in the barrier layer, increases in this potential range. This is expected, the least noble alloying element, Fe, being released to the solution while the highly insoluble Cr^{III} state accumulates in the oxide, especially in the barrier layer.

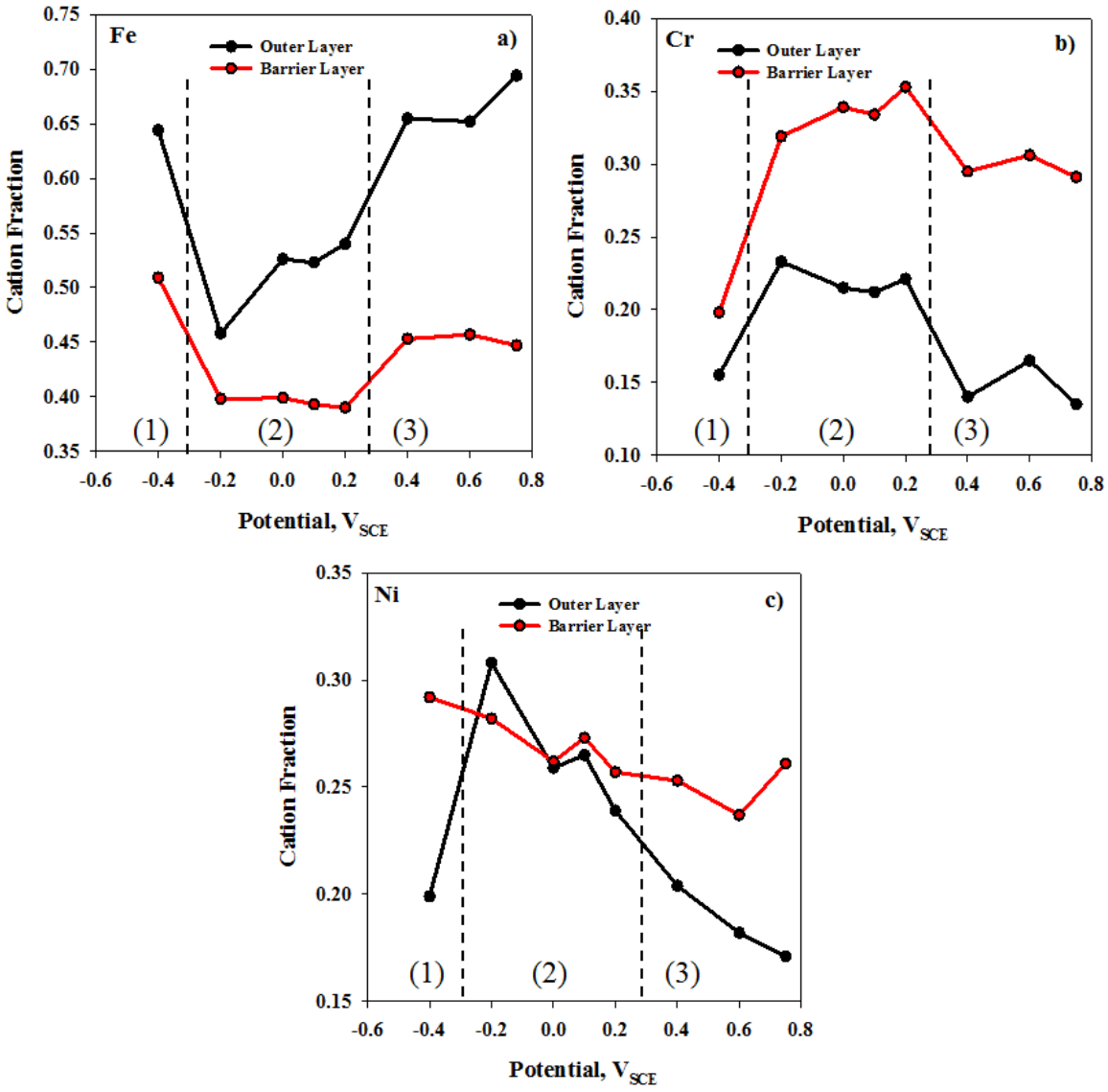

Figure 4.9 Cation fractions of (a) Fe, (b) Cr, and (c) Ni in the outer and barrier layers as a function of film growth potential.

The Ni content of the barrier layer is substantially higher than that in the outer layer in region 1, Figure 4.9 (c). However, this does not indicate a preferred loss of Ni^{II} to the solution since the Ni is shown to be concentrated in the surface of the substrate alloy, Figure 4.8 (a) and (b).

At potentials beyond the anodic peak, Figure 4.1, i.e., in region 3, the Cr content in both layers decreases, but only marginally within the barrier layer, and the Fe content of the outer oxide increases substantially, becoming the dominant cation in the oxide. Also, in the outer oxide within this potential range (> 0.2 V_{SCE}) the Ni content, while maintained in the barrier layer, becomes depleted in the outer oxide, Figure 4.9 (c). Despite this apparent depletion, Ni remains concentrated in the alloy surface, Figure 4.8 (c). This combination of observations suggests that beyond the anodic peak, as the potential increases into the transpassive region, the segregation of Fe to the outer layer protects the barrier layer from transpassive dissolution and also prevents the Ni release to solution, leading to its concentration in the surface of the alloy.

4.3.4 Surface Analysis - XPS

The oxide films grown at various potentials were analyzed by XPS. Figure 4.10 shows examples of fitted spectra for the (a) Cr $2p_{3/2}$, (b) Ni $2p_{3/2}$, (c) O 1s and (d) Fe $2p_{3/2}$ peaks. With the exception of Cr, all spectra were charge corrected by fixing the C 1s peak at a BE of 285.0 eV. Table 4.3 includes the BE's extracted from the fitted spectra. Fitting of the Cr $2p_{3/2}$ spectra shows the presence of metallic Cr at 573.9 eV, Cr oxide species (Cr_2O_3) at 576.0 eV and Cr hydroxide species ($Cr(OH)_3$) at 577.7 eV [33, 34]. The $Cr(OH)_3$ component was recorded at a much higher BE than expected. A possible reason for this was proposed earlier in chapter 3, where $Cr(OH)_3$, an insulator, is not in electrical contact with the alloy surface since it is at the solution/oxide interface and separated from the alloy by the insulating barrier layer. By contrast, Cr_2O_3, which constitutes the barrier layer, is in direct conductive contact with the alloy and no significant shift in BE would be expected.

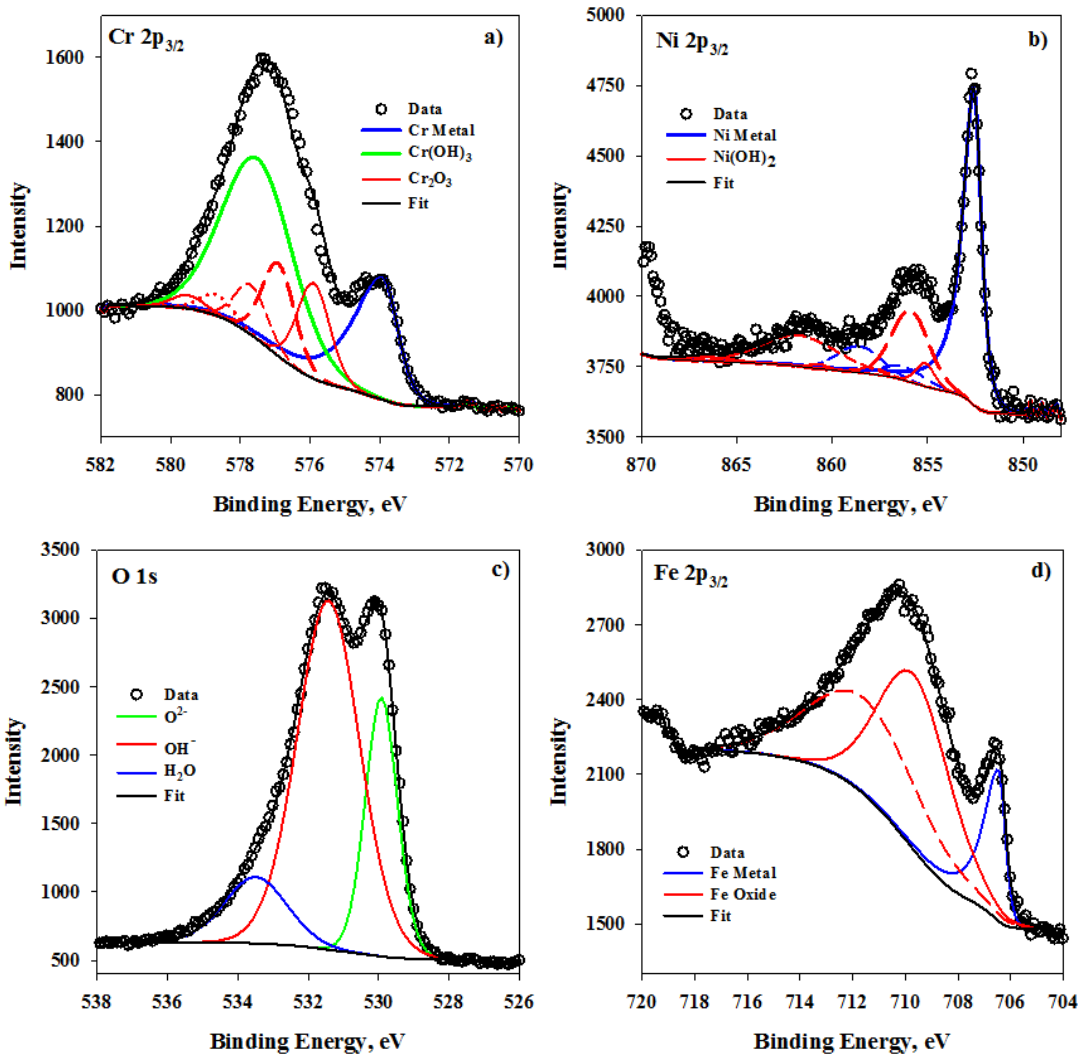

Figure 4.10 High resolution XPS spectra for the (a) Cr $2p_{3/2}$, (b) Ni $2p_{3/2}$, (c) O 1s and (d) Fe $2p_{3/2}$ peaks recorded on an electrode potentiostatically treated at 0.4 V_{SCE}. Fitting of figures (a) through (c) was accomplished using normal peak fitting procedures. Fitting of figure (d) was accomplished with the sole purpose of identifying the peak area.

The Ni $2p_{3/2}$ spectrum, Figure 4.10 (b) contains only two chemical species; Ni metal at 852.5 eV, and Ni hydroxide ($Ni(OH)_2$) detected between a BE range of 854.8 eV to 855.2 eV, depending on the potential [33, 35]. The shift in the BE of $Ni(OH)_2$ with film growth potential suggests that this component is also located in the outer layer and is

not in good electrical contact with the alloy surface. The presence of the metal signal in both the Ni and Cr spectra suggests that the oxide film is very thin. Typically, the metal component can be detected as long as the film thickness does not exceed 3λ, which for a Ni or Cr oxide is ~ 6 nm [28]. After film growth at 0.4 V_{SCE}, the calculated oxide thickness determined by AES depth profiling, Figure 4.7, is just under 5 nm and detection of the metal by XPS would be expected.

Table 4.3 Measured BE's for the various chemical states of O, Cr and Ni in oxide films formed potentiostatically.

E (V_{SCE})	O^{2-} (eV)	OH^- (eV)	Cr (0) (eV)	Cr_2O_3 (eV)	$Cr(OH)_3$ (eV)	Ni (0) (eV)	$Ni(OH)_2$ (eV)
-0.4	529.8	531.5	573.9	576.2	577.8	852.5	855.1
-0.2	529.8	531.5	573.9	575.8	577.4	852.4	855.1
0	529.8	531.4	574.0	576.1	577.7	852.4	855.0
0.1	529.9	531.4	573.9	575.9	577.6	852.5	855.1
0.2	529.9	531.4	573.9	576.0	577.6	852.5	854.9
0.4	529.7	531.3	573.9	576.1	577.7	852.3	854.8
0.6	529.9	531.3	574.0	576.0	577.7	852.4	854.9
0.75	530.0	531.4	573.9	576.0	577.7	852.7	855.2

For the O 1s spectra, the first peak at 529.9 eV is characteristic of an anhydrous oxide species, M-O, while the second peak at 531.4 eV can be assigned to a hydrated oxide species, M-OH. The final peak at 533.5 eV can be attributed to residual water on the electrode surface. These values are within acceptable experimental error compared to literature values [36, 37].

Due to the overlap of the Ni LMM line with the Fe $2p_{3/2}$ peak, accurate fitting of the Fe $2p_{3/2}$ spectra could not be accomplished, making it difficult to resolve the separate states of Fe with certainty. The spectra was fit with three simple peaks under the

assumption that; a) the contribution from the Ni LMM line is negligible, and b) the main components of the spectra are from Fe metal and Fe oxide. Typical peak fitting procedures could not be applied so only the peak area was calculated. The lower BE peak was assumed to be Fe metal (red) and the peak area could be estimated using a single peak, Figure 4.10 (d). The features of the second larger peak are more complex, and required two peaks (blue) to accurately account for the peak area. Peaks in the Fe $2p_{3/2}$ spectra were positioned solely to determine the peak area, not to identify BE's.

Figure 4.11 shows the changes in (a) the Ni components detected in the high resolution scans, and (b) these changes normalized against the total Ni content determined in the survey scan as a function of film growth potential.

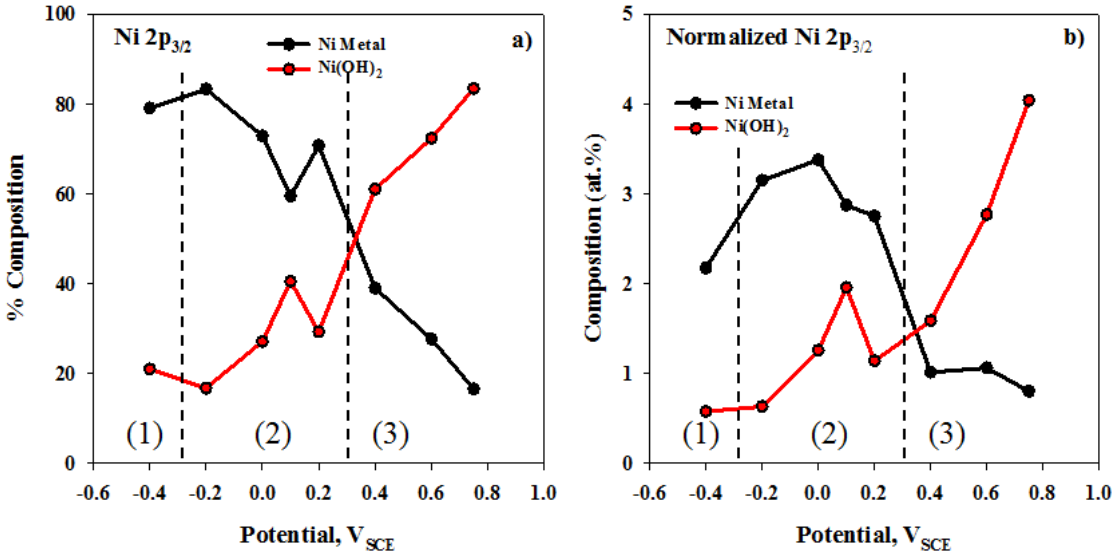

Figure 4.11 Changes in the Ni components in films grown at various potentials obtained by de-convolution of the Ni $2p_{3/2}$ peak: (a) percentage composition; (b) composition normalized against the total Ni content measured in the survey scan.

At potentials in region 1 and 2, the majority of the Ni is in the metallic form, consistent with the presence of a thin (2 nm to 4 nm) oxide, as determined by AES. As the oxide film thickens with increasing film growth potential, the Ni signal becomes dominated by $Ni(OH)_2$. A spike in the $Ni(OH)_2$ component is observed at a film growth potential of 0.1 V_{SCE}, coinciding with the position of the anodic peak in the polarization curve, Figure 4.11. It also coincides with the apparent drop in film thickness, Figure 4.7. These observations are consistent with the presence of a porous, more readily sputtered, $Ni(OH)_2$. As the film growth potential increases into region 3, $Ni(OH)_2$ becomes the primary form of Ni present predominantly in the outer layer of the oxide.

Figure 4.12 shows the various Cr components obtained through de-convolution of the Cr $2p_{3/2}$ peak, and for the same values normalized against the total Cr content detected in survey scans.

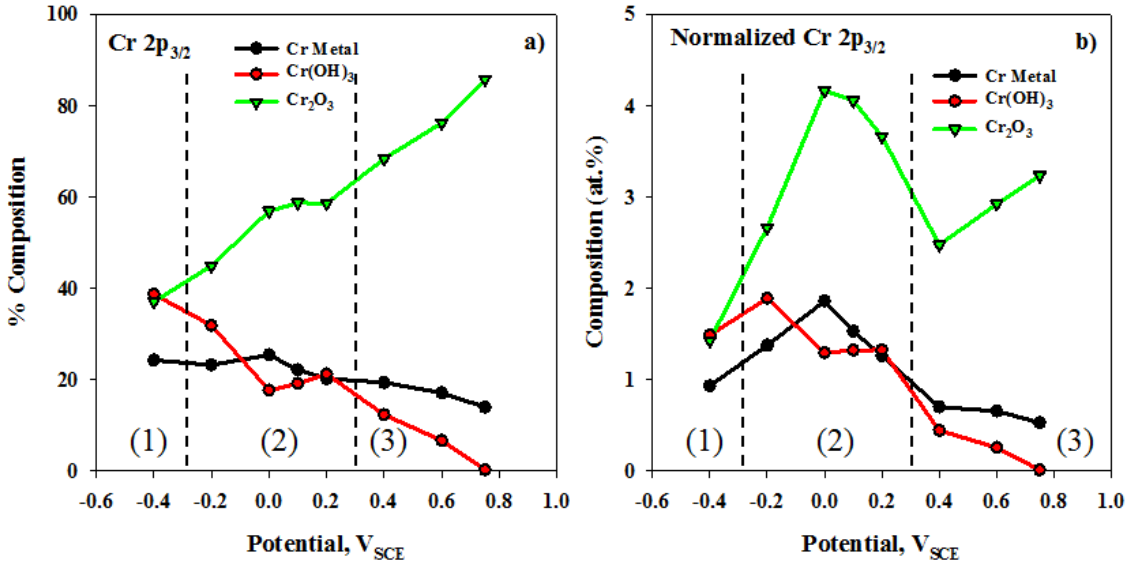

Figure 4.12 Changes in the Cr components in films grown at various potentials obtained by de-convolution of the Cr $2p_{3/2}$ peak: (a) percentage composition; (b) composition normalized against the total Cr content measured in the survey scan.

The majority of the Cr present is fixed in the barrier layer, Cr_2O_3. Small amounts of Cr metal and $Cr(OH)_3$ are present in regions 1 and 2 but decrease as the film growth potential is increased through regions 2 and 3. As with $Ni(OH)_2$, $Cr(OH)_3$ is located in the outer layer of the film. Figure 4.12 (a) and (b) shows that with increasing film growth potential the Cr_2O_3 becomes the dominant form of Cr. The Cr_2O_3 content increases over region 1 and in the early stages of region 2 as the barrier layer develops. A comparison to Figure 4.5 shows that this increase coincides with the increase in barrier layer resistance. The Cr_2O_3 content decreases over the film growth potential range 0 V_{SCE} to 0.4 V_{SCE}. This coincides with the potential range of the anodic peak, and is accompanied by a decrease in resistance of the barrier layer. This combination of features confirms that the increase in current in this potential range is a consequence of the partial destruction of the barrier layer. This would also explain the sudden increase in $Ni(OH)_2$ content of the film, Figure 4.11, which can be attributed to the accelerated dissolution of Ni^{2+} and its precipitation in the outer layer as $Ni(OH)_2$.

Figure 4.13 shows the total and the normalized % composition of the O 1s spectra. Over the whole potential range, M-OH is the dominant O species primarily associated with the hydroxides in the outer layer. The contribution from M-O increases with film growth potential in regions 1 and 2 as the barrier layer grows. The drop in M-O content from 0.1 V_{SCE} to 0.2 V_{SCE} coincides with the location of the anodic peak, the fall of the barrier layer resistance and occurs as soon as the Cr_2O_3 content begins to decrease. This confirms that the anodic peak can be attributed to the partial breakdown of the barrier layer. In the transpassive region (3), the M-O component continues to steadily

increase. This is accompanied by only a minor increase in Cr_2O_3 content, Figure 4.12 (b), and cannot be accounted for by an increase in barrier layer thickness.

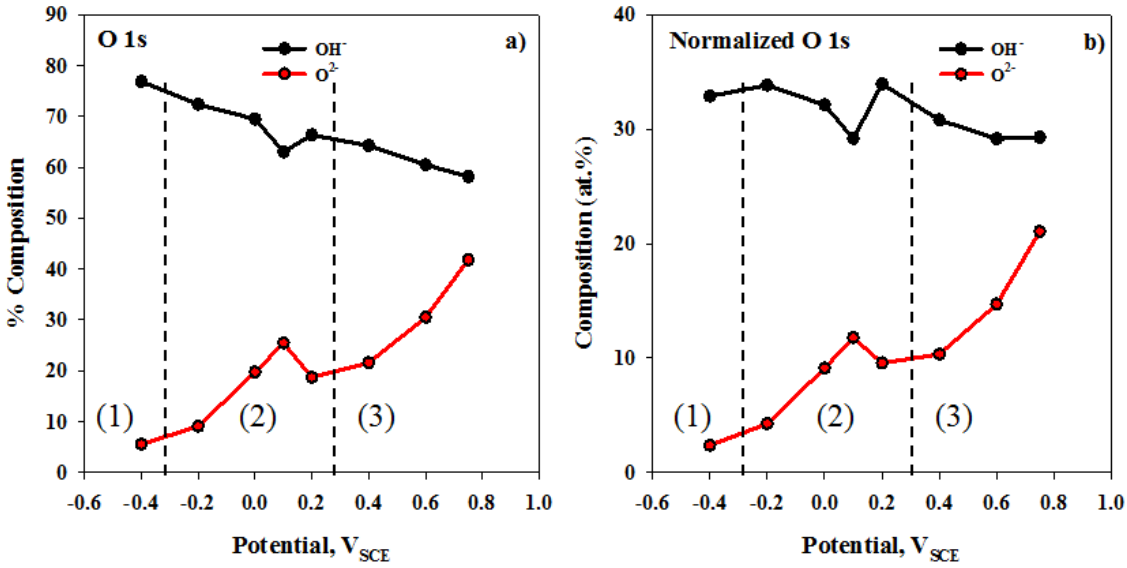

Figure 4.13 Changes in the O components in films grown at various potentials obtained by de-convolution of the O 1s peak: (a) percentage composition; (b) composition normalized against the total O content measured in the survey scan.

The changes in Fe metal and Fe oxide content for the (a) fitted and (b) normalized data are shown in Figure 4.14. Both plots show an increase in Fe oxide content as the film growth potential increases. This increase correlates with the O^{2-} content, Figure 4.13, and the increase in film thickness, Figure 4.7. The substantial increase in Fe and O content at potentials above 0.2 V_{SCE} (i.e., in region 3) indicate that film thickening is primarily due to the accumulation of Fe oxide.

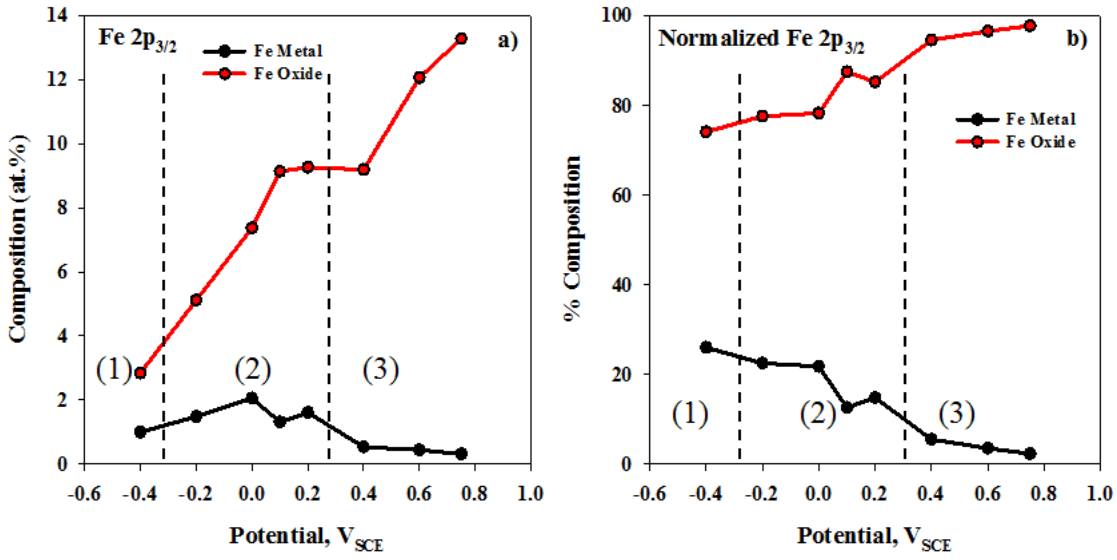

Figure 4.14 Variation in Fe species in the oxide film as a function of film growth potential: (a) relative amounts of Fe species determined by de-convolution of the Fe $2p_{3/2}$ peak, (b) these amounts normalized against the total Fe content obtained from the survey scan.

As expected, the estimated Fe metal content, Figure 4.14, drops substantially at potentials greater than 0.2 V_{SCE} when the overall oxide/hydroxide film thickens markedly.

4.3.5 Sulphur

The effect of $S_2O_3^{2-}$, and various other S species is known to de-stabilize the formation of Ni containing oxide films, enhance anodic dissolution [11, 14, 19, 38-42], and cause localized corrosion in pressurized water reactors [12, 15, 43]. Incorporation of S into the oxide film has been reported in previous studies [14, 15, 28, 44]. AES depth profiles, Figure 4.15 (a), show the distribution of S throughout the oxide film.

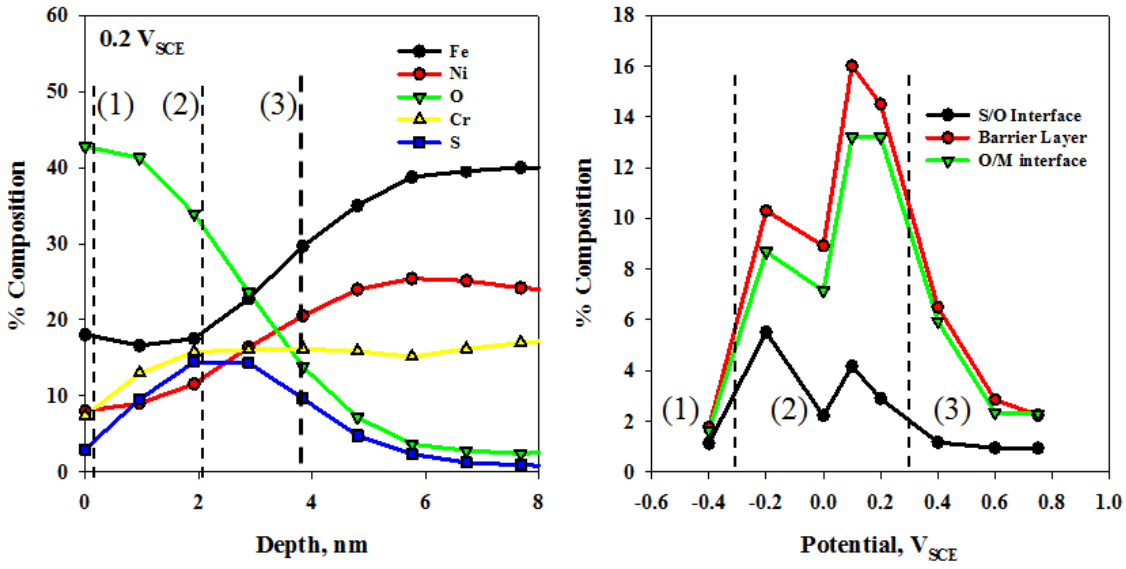

Figure 4.15 (a) AES depth profile recorded after film growth at 0.2 V_{SCE}. The vertical lines indicate the location of the outer layer (1), the barrier layer (2), and the oxide/alloy interface (3): (b) Changes in S content as a function of potential.

The S content was calculated at three different locations within the film; (1) at the solution/oxide interface (outer layer), (2) at the maximum in the S depth profile (barrier layer); and (3) at the oxide/alloy interface. The change in S at these locations was plotted against the film growth potential in Figure 4.15 (b), and shows that the majority of the S is located in the barrier layer. Comparison of the change in Cr content with film growth potential, Figure 4.9 (c) and Figure 4.12 (b), to that of S, Figure 4.15 (b), shows that both Cr and S exhibit a similar profile over the potential range -0.4 V_{SCE} to 0.4 V_{SCE}.

The oxidation state of S in the oxide film was investigated using XPS. Since high-resolution spectra were not collected for this element, peak fitting was applied to the S 2p signal present in the survey scans. Figure 4.16 shows the fits for film growth potentials of -0.4 V_{SCE} and 0.4 V_{SCE}.

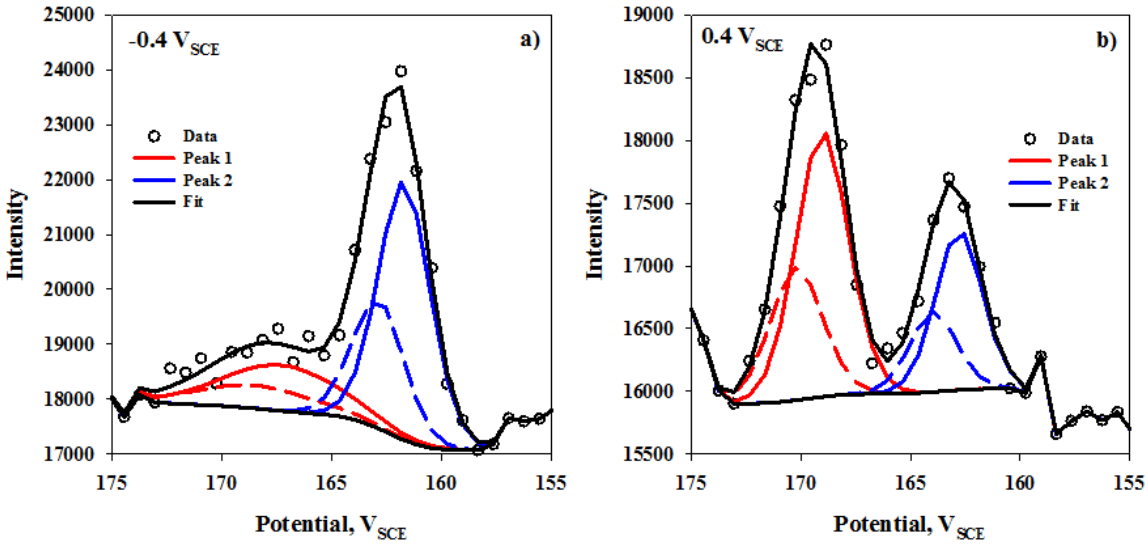

Figure 4.16 Fitted XPS survey spectra for the S 2p band for oxide films grown at (a) -0.4 V_{SCE} and (b) 0.4 V_{SCE}.

Two peaks are observed at BE's of ~ 168 eV (peak 1) and ~ 163 eV (peak 2). Contributions to peak 1 are likely the result of oxidized species such as SO_4^{2-}, while peak 2 could be attributed to more reduced S species, such as $S_2O_3^{2-}$ or S^{2-} [23, 45]. As observed previously for Alloy 600, reduced S species are dominant at low potentials, (-0.4 V_{SCE}) and oxidized forms at high potentials (0.4 V_{SCE}).

4.4 Discussion and Conclusions

The passive film formed on the surface of Alloy 800 is a typical bilayer film. The oxide was found to possess a barrier layer rich in Cr_2O_3 and an outer layer containing a mixture of $Ni(OH)_2$, Fe oxides and small amounts of $Cr(OH)_3$. Schematic illustrations showing the compositional changes in the oxide film between regions 1, 2 and 3, are shown in Figure 4.17.

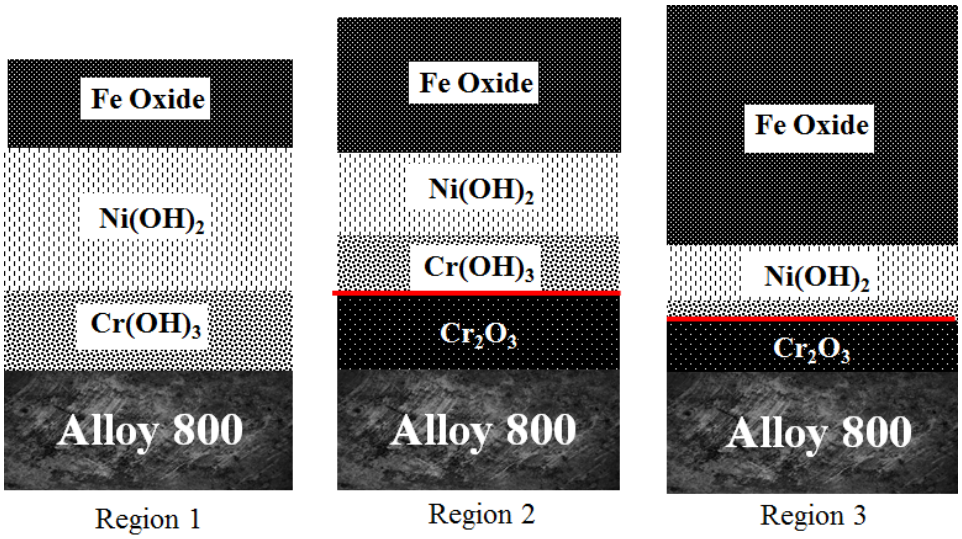

Figure 4.17 Schematic of the changes in the structure and composition of the oxide film as a function of potential. Regions 1, 2, and 3 are defined in Figure 4.1. The different components are indicated, and a division between the outer and barrier layers is marked by the red line.

In the pre-passive region ($\leq$ -0.3 V_{SCE}), Fe dissolves as Fe^{II} as it is the most unstable alloying element. As the potential increases through this region, the Cr content of the film increases (as Cr_2O_3) as the barrier layer develops, leading to only a slight increase in film thickness but a substantial increase in its resistance. The defect state of Cr_2O_3 (expressed as a non-stoichiometry) is believed to be important since defect states facilitate cation diffusion processes and their elimination will decrease film growth rates and increase film resistance [45]. The retention of Cr (as Cr_2O_3) in the barrier layer has been associated with the high heat of adsorption of O on Cr, combined with a relatively low Cr-Cr bond strength, which facilitates oxide nucleation [46]. The concentration of Ni on the surface of the alloy, and its low concentration in the oxide/hydroxide form, indicates that Ni as Ni^{II} is not released to solution in significant amounts in this potential range.

The passive region is limited in potential range by the onset of film breakdown indicated by the anodic peak in the polarization curve. The current increase associated with this peak leads to a partial destruction of the barrier layer, accompanied by a decrease in both the Cr_2O_3 and $Cr(OH)_3$ content. This breakdown of the barrier layer is accompanied by an increase in the release of Ni^{II} and its deposition in the outer regions of the film as porous $Ni(OH)_2$. The evidence that this deposit is porous is based on its rapid sputtering rate in AES depth profiling which leads to the illusion that the film thins over this potential range.

Typically, the transpassive behaviour (region 3) of Cr containing alloys is characterized by the oxidation of Cr^{III} to the much more soluble Cr^{VI} species, resulting in dissolution of the barrier layer oxide [47-50]. This is observed through the breakdown of the Cr_2O_3 barrier layer and the removal of $Cr(OH)_3$ from the outer layer. Degradation of the barrier layer in this manner allows the anodic oxidation and release of the Fe and Ni and an increase in thickness of the outer deposited oxide/hydroxide layer. Despite this increase in film thickness, the overall film resistance decreases, confirming the less protective nature of the outer oxide/hydroxide layer compared to that of the barrier layer present at lower potentials. Comparison of the resistances of the inner and outer layer show that the values become similar, and that both layers contribute almost equally to the overall resistance.

The cation fractions show the thickening of the outer layer is due to the accumulation of the Fe oxide (as opposed to hydroxide). Since the potential is now very positive, oxidized Fe will be in the Fe^{III} state leading to the accumulation of a highly insoluble oxide. This is consistent with thermodynamic expectations, the potential-pH

diagram confirming that Fe^{III} oxides/hydroxides are stabilized as conditions become more oxidizing at neutral pH [51]. The persistence of significant amounts of Cr_2O_3 well into the transpassive region suggests the presence of this outer layer of Fe^{III} oxide helps to partially protect the underlying barrier layer.

References

[1] P.K. De, S.K. Ghosal, Corros., 37 (1981) 341-349
[2] R.S. Dutta, J. Nucl. Mater., 393 (2009) 343-349
[3] D. Van Rooyen, Corros., 31 (1975) 327-337
[4] W. Yang, Z. Lu, D. Huang, D. Kong, G. Zhao, J. Congleton, Corros. Sci., 43 (2001) 963-977
[5] J.R. Cels, Corros., 34 (1978) 198-209
[6] K. Sieradzki, R.C. Newman, J. Phys. Chem. Solids, 48 (1987) 1101-1113
[7] R.H. Jones, Stress Corrosion Cracking: Materials Performance and Evaluation, ASM International, (1992)
[8] L.L. Shreir, R.A. Jarman, G.T. Burstein, Corrosion: Metal/Environmental reactions, Butterworth-Heinemann (1994)
[9] T. Nickchi, A. Alfantazi, Corros., 68 (2012) 1-11
[10]]W.-T. Tsai, M.-J. Sheu, J.-T. Lee, Corros. Sci., 38 (1996) 33-45
[11] Z. Fang, R. W. Staehle, Corros., 55 (1999) 355-379
[12] R. Bandy, R. Roberge, R.C. Newman, Corros., 39 (1983) 391-398
[13] R. Bandy, D. Van Rooyen, Corros., 40 (1984) 281-289
[14] T. Sakai, K. Aoki, T. Shigemitsu, Y. Kishi, Zairyo to Kankyo, 40 (1991) 736-741
[15] E.H. Lee, K.M. Kim, U.C. Kim, Mater. Sci. Eng., A449 (2007) 330-333
[16] W.-T. Tsai, C.-S. Chang, J.-T. Lee, Corros., 50 (1994) 98-105
[17] W.-T. Tsai, C.-H. Chou, Mater. Sci. Eng., A288 (2000) 5-11
[18] I.J. Yang, Corros., 49 (1993) 576-585
[19] W. Yang, Z. Lu, D. Huang, D. Kong, G. Zhao, J. Congleton, Corros. Sci., 43 (2001) 963-977
[20] T. Nickchi, A. Alfantazi, Corros. Sci., 52 (2010) 4035-4045
[21] T. Nickchi, A. Alfantazi, Electrochim. Acta., 58 (2011) 743-749
[22] M.G. Faichuk, S. Ramamurthy, W.M. Lau, Corros. Sci., 53 (2011) 1383-1393
[23] S. Bera, S. Rangarajan, S.V. Narasimhan, Corros. Sci., 42 (2000) 1709-1724
[24] R.M. carranza, M.G. Alverez, Corros. Sci., 38 (1996) 909-925
[25] E. Barsoukov, J. R. Macdonald, Impedance Spectroscopy: Theory, Experiment, and Applications, J. Wiley and Sons, (2005)
[26] K. Juttner, W.J. Lorenz, Corros. Sci., 29 279 (1989) 279-288
[27] L. Zhang, D.D. Macdonald, Electrochim. Acta., 43 (1998) 2661-2671
[28] S. Mischler, A. Vogel, H.J. Mathieu, D. Landolt, Corros. Sci., 32 (1991) 925-944
[29] T. Dan, T. Shoji, Z. Lu, K. Sakaguchi, J. Wang, E.-H. Han, W. Ke, Corros. Sci., 52 (2010) 1228-1236
[30] A.S. Lim, A. Atrens, Appl. Phys., A54 (1992) 343-349
[31] D. Hamm, C.-O.A. Olsson, D. Landolt, Corros. Sci., 44 (2002) 1009-1025
[32] E. Sikora, D.D. Macdonald, Electrochim. Acta., 48 (2002) 69-77
[33] M.C. Biesinger, B.P. payne, A.P. Grosvenor, L.W.M. Lau, A. Gerson, R. St.C. Smart Appl. Surf. Sci., 257 (2011) 2717-2730
[34] M.C. Biesinger, C. Brown, J.R. Mycroft, R.D. Davidson, N.S. McIntyre, Surf. Interface. Anal., 36 (2004) 1550-1563
[35] M. C. Biesinger, B. P. Payne, L.M.M. Lau, A. Gerson, R.St.C. Smart. Surf. Interface Anal., 41 (2009) 324-332
[36] P. Keller, H.-H. Strehblow, Corros. Sci., 46 (2004) 1939-1952

[37] H. Luo, C.F. Dong, X.G. Li, K. Xiao, Electrochim. Acta., 64 (2012) 211-220
[38] J. Oudar, P. Marcus, Appl. Surf. Sci., 3 (1979) 48-67
[39] P. Marcus, A. Teissier, J. Oudar, Corros. Sci., 24 (1984) 259-268
[40] I.J. Yang, Corros., 49 (1993) 576-585
[41] P. Marcus, I. Olefjord, Corros., 42 (1986) 91-98
[42] I. Betova, M. Bojinov, O. Hyokyvirta, T. Saario, Corros. Sci., 52 (2010) 1499-1507
[43] J.B. Lumsden, P.J. Stocker, Proceedings of the 4th Int. Symposium on Environmental Degredation of Materials in Nuclear Power System - Water Reactors, (1989) 6-38
[44] P. Marcus, J.M. Grimal, Corros. Sci., 31 (1990) 377-382
[45] P. Marcus, J.M. Grimal, Corros. Sci., 33 (1992) 805-814
[46] P. Marcus, Corros. Sci., 36 (1994) 2155-2158
[47] A.M. Olmedo, M. Villegas, M.G. Alvarez, J. Nucl. Mater., 229 (1996) 102-114
[48] D.-S. Kong, S.-H. Chen, C. Wang, W. Yang, Corros. Sci., 45 (2003) 747-758
[49] R.D. Armstrong, M. Henderson, J. Electroanal. Chem., 32 (1971) 1
[50] R.D. Armstrong, M. Henderson, J. Electroanal. Chem., 40 (1972) 121
[51] M. Pourbaix, Atlas of Electrochemical Equilibria in Aqueous Solutions, NACE International, (1974)

Chapter 5. A Comparison Study of the Oxide Films Formed on Alloy 600 and Alloy 800

5.1 Introduction

SCC is the result of the simultaneous exposure of a susceptible material to a corrosive environment and residual or applied tensile stress. This type of corrosion can be severe, as catastrophic damage can occur even though the stress levels are within the specified range for normal operating conditions [1-5]. In CANDU nuclear reactors, the function of SG tubing is to contain and separate the primary and secondary water circuits, as well as to transfer heat from the primary to the secondary water. The operating conditions of the tubing demand that it withstand temperatures, together with manufacturing and residual formation stress, that can lead to SCC. SCC of SG tubing can result in the contamination of secondary water with highly radioactive primary water. Thus, there is strong incentive to better understand this type of corrosion and methods for its prevention.

Alloy 600 had previously been characterized as a “superalloy” for fabricating SG tubing, but numerous failures have exposed underlying issues, and it is now well-known to be susceptible to pitting corrosion and SCC [1, 6-15]. The Fe-Ni-Cr base Alloy 800 is a candidate material to replace Alloy 600 as SG tubing, due to its high temperature strength and corrosion resistance [16, 17]. However, recent reports have shown that Alloy 800 may also be susceptible to SCC under certain conditions [1-3]. A greater understanding of the passive behaviour of these alloys is required to determine which features lead to SCC.

In the previous two chapters, studies on the passive oxide films formed on Alloy 600 and Alloy 800 in aqueous 0.1 M $Na_2S_2O_3$ solutions were presented. Originating from oil contamination, deoxygenating agents, etc., S is known to cause localized corrosion through adsorption onto the alloy surface [18]. The presence of reduced S species, such as $S_2O_3^{2-}$, can lead to an acceleration of anodic dissolution and enhanced susceptibility to SCC [7, 8, 19-26]. The formation and breakdown of this passive film was studied at various potentials using electrochemical techniques such as anodic polarization and EIS. The electrochemcial behaviour of the oxide film was then correlated to compositional changes using surface analytical techniques such as AES and XPS. This chapter compares the results obtained in chapters 3 and 4, and attempts to determine how and why the differences in composition of the two alloys change the corrosion resistance.

5.2 Experimental

5.2.1 Sample Preparation

Sections of Alloy 600 and Alloy 800 tubing with a 9.5 mm diameter were procured from Rolled Alloys Canada in the mill-annealed condition.

Table 5.1 Chemical composition of Alloy 600 and 800 SG tubing (wt%).

Element	Ni	Cr	Fe	Mn	Al	Ti	Si	C
Alloy 600	72.97	16.14	9.65	0.34	0.27	0.23	0.15	0.03
Alloy 800	30.86	20.37	45.76	0.72	0.40	0.53	0.54	0.07

The alloy compositions are presented in Table 5.1. Samples obtained from Alfa Aesar (Ward Hill, MA) of polished and cleaned pure Ni (99.995%), Fe (99.99%) and Cr

(99.99%) were used for analysis. Preparation of the samples has been described previously in chapters 3 and 4.

5.2.2 Electrochemical Measurements

A detailed description of experimental and analytical procedures can be found in chapters 3 and 4.

5.2.3 Surface Analysis

5.2.3.1 Auger Electron Spectroscopy (AES)

A detailed description of experimental and analytical procedures can be found in chapters 3 and 4.

5.2.3.2 X-ray Photoelectron Spectroscopy (XPS)

A detailed description of experimental and analytical procedures can be found in chapters 3 and 4.

5.3 Results

5.3.1 Anodic Polarization

Anodic polarization curves for Alloy 600 and Alloy 800 and the three main alloying elements, Ni, Fe and Cr are plotted in Figure 5.1. The curves are divided into three regions for the (1) pre-passive, (2) passive and (3) transpassive regions. The E_{corr} values for Ni and Fe confirm that, as expected, these two metals are active in this environment, especially Fe. This is confirmed by the high anodic current observed on the anodic polarization curves. Ni appears, however, to make an unsuccessful attempt to

passivate at ~ 0.4 V_{SCE}. The general similarity in behaviour of the two alloys and of Cr is expected since Cr is known to play the key role in maintaining passivity [27].

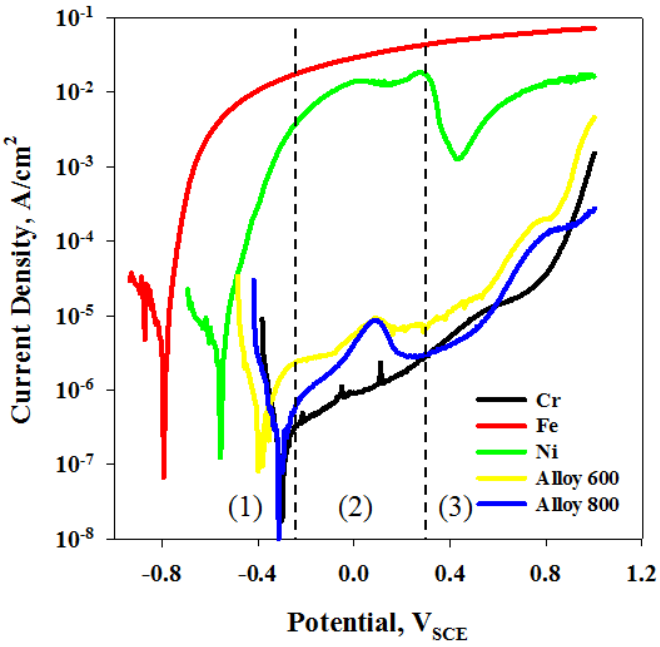

Figure 5.1 Anodic polarization curves for Cr, Fe, Ni, Alloy 600 and Alloy 800 in a de-aerated solution of 0.1 M $Na_2S_2O_3$. The curves for Alloy 600 and Alloy 800 are divided into three regions depicting (1) pre-passive (2), passive and (3) transpassive.

As expected, the E_{corr} value for Cr is similar to that of the high Cr Alloy 800 and more positive than that of the lower Cr Alloy 600. In the passive region (2) at potentials prior to the anodic peak, the passive current decreases in the order Alloy 600 > Alloy 800 > Cr; i.e., in the order of the relative Cr contents (16%, 20-21%, 100%). The anodic peak is only observed on the two alloys and not on pure Cr. This may reflect the quality of the passive film grown in region 2 at potentials negative to the peak. For potentials positive to the anodic peak, the current for Alloy 800 decreases to a value similar to that for Cr, while the current density measured for Alloy 600 does not. Lower currents are sustained

on Cr and Alloy 800 throughout the transpassive region (3), and both alloys exhibit a current plateau around 0.8 V_{SCE} which is not observed on Cr.

5.3.2 Electrochemical Impedance Spectroscopy (EIS)

Electrochemical impedance spectra were measured on both alloys as described in chapters 3 and 4, and the results analyzed using electrical equivalent circuits. The data collected for Alloy 600 could be fit using a circuit with two time constants in series, Figure 5.2 (a), while a three time constant circuit was required to fit the more complicated Alloy 800 spectra, Figure 5.2 (b).

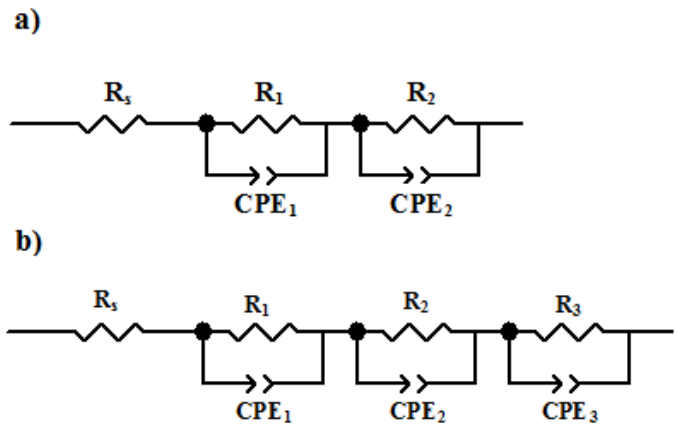

Figure 5.2 Equivalent circuits used to fit EIS spectra for (a) Alloy 600 and (b) Alloy 800.

It is well known that the passive film on Fe-Ni-Cr alloys is composed of a bilayer oxide with a Cr-rich inner barrier layer and a predominantly Fe/Ni outer layer [2, 25, 27-42]. Thus, the circuit elements (R_1/CPE_1 and R_2/CPE_2) for both alloys are taken to represent the impedance responses for the outer and barrier oxide layers, respectively. The third circuit element (R_3/CPE_3) for Alloy 800 is taken to represent a charge transfer process at the oxide/alloy interface. Both circuits include a circuit element, R_s, to account for the

solution resistance. CPE's are used to account for the non-uniform properties of the oxide layers. Examples of spectra fitted to these equivalent circuits are shown in Figure 5.3 for a film grown at 0 V_{SCE}. It is clear, especially in the Bode plots, that the alloys exhibit significant differences in response in the mid to low frequency range.

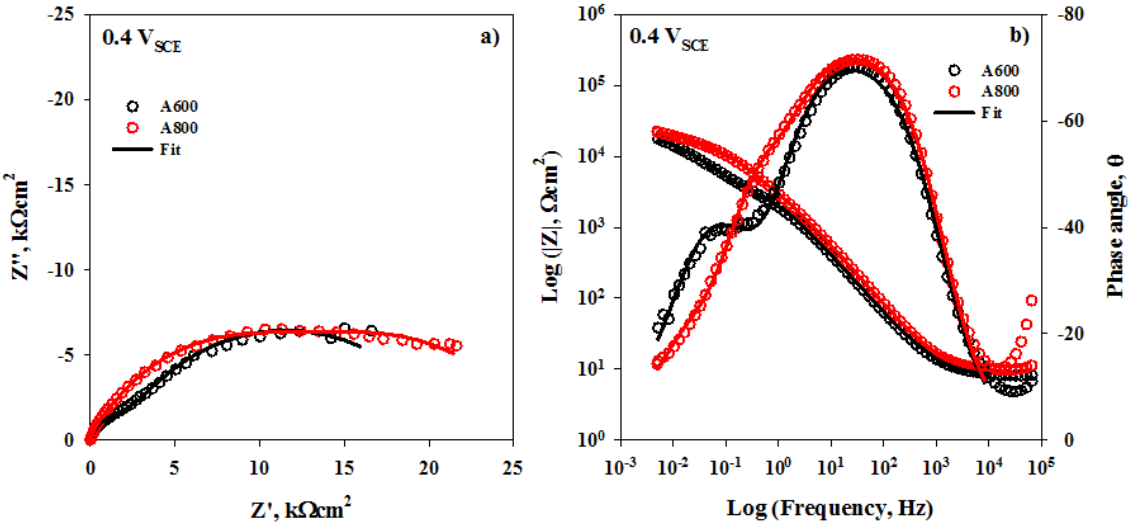

Figure 5.3 EIS spectra of Alloy 600 and Alloy 800 recorded at 0 V_{SCE} fitted to the equivalent circuits in Figure 5.2: (a) Nyquist and (b) Bode plots.

Resistance values for the barrier and outer layers of each alloy, obtained from fitted spectra, are plotted in Figure 5.4. As expected, the barrier layer resistance, Figure 5.4 (a), is up to an order of magnitude greater than that of the outer layer, Figure 5.4 (b). In the passive region (2), the barrier layer resistance on Alloy 800 is greater than that of Alloy 600. The barrier layer resistance on Alloy 600 begins to decrease as soon as the anodic current in the polarization curve begins to increase.

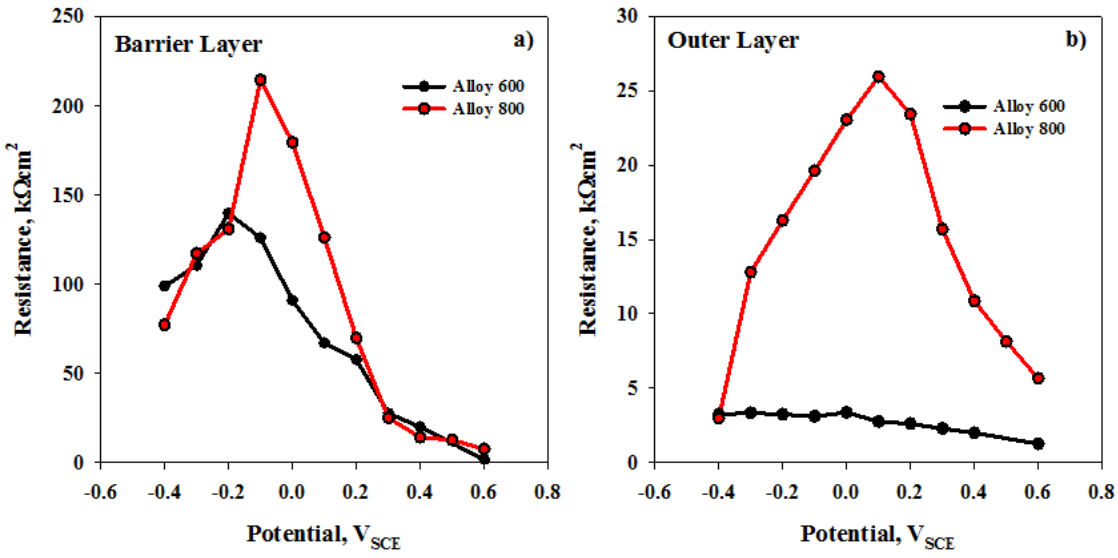

Figure 5.4 Changes in the (a) barrier and (b) outer layer resistances for Alloy 600 and Alloy 800.

By comparison, the barrier layer resistance on Alloy 800 increases in the early stages of the anodic peak region, Figure 5.1. This delay in barrier layer breakdown may reflect the higher Cr content of Alloy 800. For both alloys, the barrier layer resistance decreases as a consequence of the current increase associated with the anodic peak in the polarization curve, Figure 5.1. For potentials in and beyond the anodic peak region, the barrier layer resistance on Alloy 600 is substantially smaller than that on Alloy 800, consistent with the higher current observed in the potential range 0.1 V_{SCE} to 0.3 V_{SCE}. In region 3, the barrier layer resistances on both alloys approach the same value.

The outer oxide layer resistances for the two alloys are very different. For Alloy 600, the outer layer resistance changes very little as the film growth potential is increased from the pre-passive (1) into the passive (2) region. For potentials in and beyond that of the anodic peak, the outer layer resistance steadily decreases. For Alloy 800, the outer

layer resistance increases markedly throughout the pre-passive and passive regions, before declining at potentials in and beyond that of the anodic peak. At potentials beyond the anodic peak, the resistance for Alloy 800 remains substantially above that of Alloy 600.

5.3.3 Surface Analysis – Film Thickness (AES)

In potential regions 1 and 2, the difference in film thickness is up to 2 nm, with the film formed on Alloy 800 being thicker than that on Alloy 600, Figure 5.5. Figure 5.4 (a), however, shows the barrier layer resistance on the two alloys are effectively the same in region 1 and at low potentials in region 2. At these low potentials, the primary difference between the two alloys is in the outer oxide film resistance, Figure 5.4 (b). At pH ~ 6.5 (as was the case in these experiments) Fe is an active metal as indicated in Figure 5.1. The kinetically facile release of Fe^{2+} and its deposition as an outer layer oxide/hydroxide could explain the increased thickness and higher outer layer resistance on Alloy 800. The anodic reactivity of Ni is considerably lower and segregation to form a resistive outer layer does not appear to occur as readily. Interestingly, in the potential range of the anodic peak, the overall film thickness on Alloy 800 goes through a minimum, apparently thinning by up to 1 nm. In addition, the peak values of the barrier layer resistance and the outer layer resistance are offset in this potential region, illustrated in Figure 5.4 (a) and (b). These observations indicate that the degradation of the barrier layer on Alloy 800 in the anodic peak region initially leads to an increase in the resistance of the outer layer. Intuitively, one would expect this to be accompanied by an increase in film thickness, although the opposite is observed in the AES depth profile, Figure 5.5.

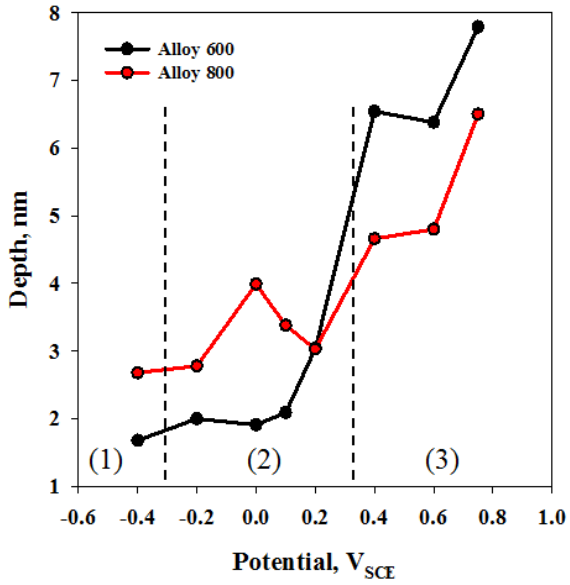

Figure 5.5 Oxide film thicknesses for Alloy 600 and Alloy 800 as a function of applied film growth potential.

Beyond the anodic peak, region 3, the film thickness on both alloys increases but the increase is more marked for Alloy 600 than Alloy 800. In the transpassive region, this can be attributed to the thickening of the outer layer. This layer accounts for the slower decrease in outer layer resistance on Alloy 800, Figure 5.4 (b), and demonstrates that the maintenance of protection after the anodic peak is better for Alloy 800 than Alloy 600. This is consistent with the lower current density observed in the polarization curve, Figure 5.1.

5.3.4 Surface Analysis – Cation Fractions

5.3.4.1 Fe

Identification of the oxide film components and their distribution within the film was accomplished using the AES depth profiles in combination with high resolution XPS. The Ni, Fe and Cr contents of the film, obtained from depth profiles (AES) and survey scans (XPS) were normalized by conversion into their respective cation fractions, and details of these calculations can be found in Chapters 3 and 4. Variations in the Fe content obtained from AES and XPS, which are shown in Figure 5.6 (a) and (b), respectively.

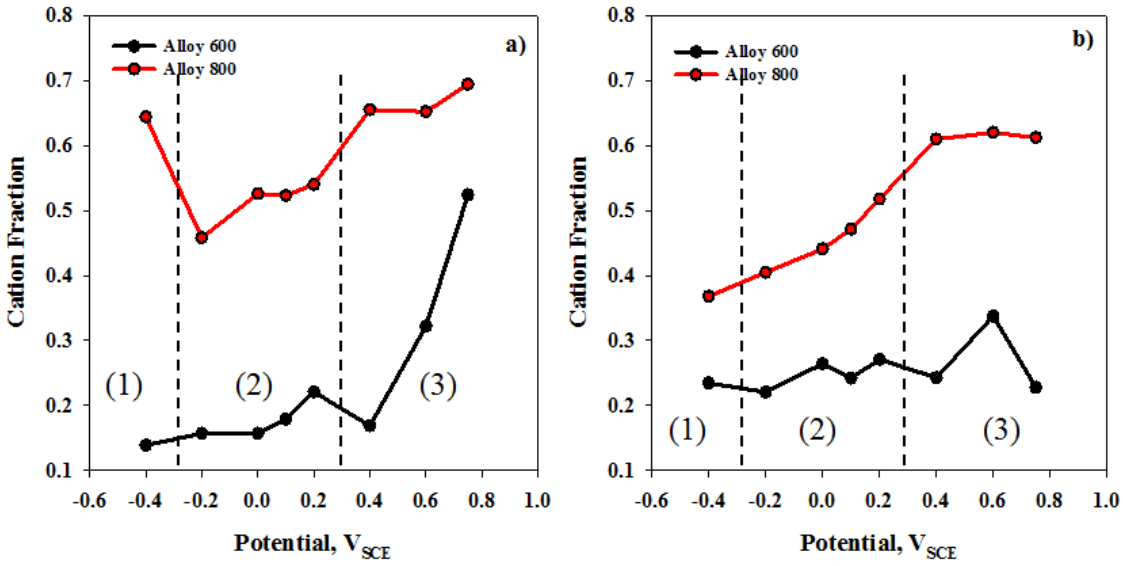

Figure 5.6 Cation fractions for Fe calculated from (a) AES profiles and (b) XPS survey scans. The plots are divided into three regions: (1) pre-passive, (2) passive and (3) transpassive.

The AES data accounts for Fe located on the surface of the outer oxide layer while the XPS data yields an average distribution of Fe throughout the entire film. The thicknesses

measured in the pre-passive (1) and passive (2) regions are small enough to allow for the detection of Fe in the substrate alloy by XPS. Figure 5.6 (a) shows Fe is the dominant cation in the outer film region on Alloy 800 as expected, since this element is the dominant alloy component. On Alloy 600, Fe is a minor component and its content in the oxide is low throughout regions 1 and 2. In the transpassive region, the Fe cation fraction increases on both alloys, especially on Alloy 600. While this would be expected on the Fe-dominated Alloy 800, it is more surprising on Alloy 600, since Fe is only a minor alloying component.

5.3.4.2 Ni

A comparison of the Ni cation fractions as a function of film growth potential is shown in Figure 5.7. The variation in Ni content on Alloy 800 is minor, with a gradual decrease being observed at higher potentials. This is not surprising since Ni is a minor component of this alloy. A comparison of the AES and XPS data show that they yield similar changes except in the transpassive region (3), when the Ni content of the outer layer, Figure 5.7 (a), decreases while the XPS data, Figure 5.7 (b), suggests the overall content in the film increases. AES results for Alloy 600 indicate that the relative Ni content in the outer regions of the film is high in the passive region but decreases substantially in the transpassive region. This relative decrease coincides with the marked increase in relative Fe content, Figure 5.6 (a). The XPS data, however, indicates that the general Ni content of the film increases, despite its obvious depletion in the outer layer. A comparison of Figure 5.7 (a) and (b) shows a minimum in relative Ni content in the outer oxide layer of the film at potentials within the anodic peak region, 0 V_{SCE} to 0.2 V_{SCE}. As indicated in Figure 5.6 (a), this is accompanied by a slight increase in Fe

content in the outer layer. A second increase in overall Ni content in the film is observed at 0.4 V_{SCE}, Figure 5.7 (b), even though the Ni content of the outer layer is decreasing, Figure 5.7 (a).

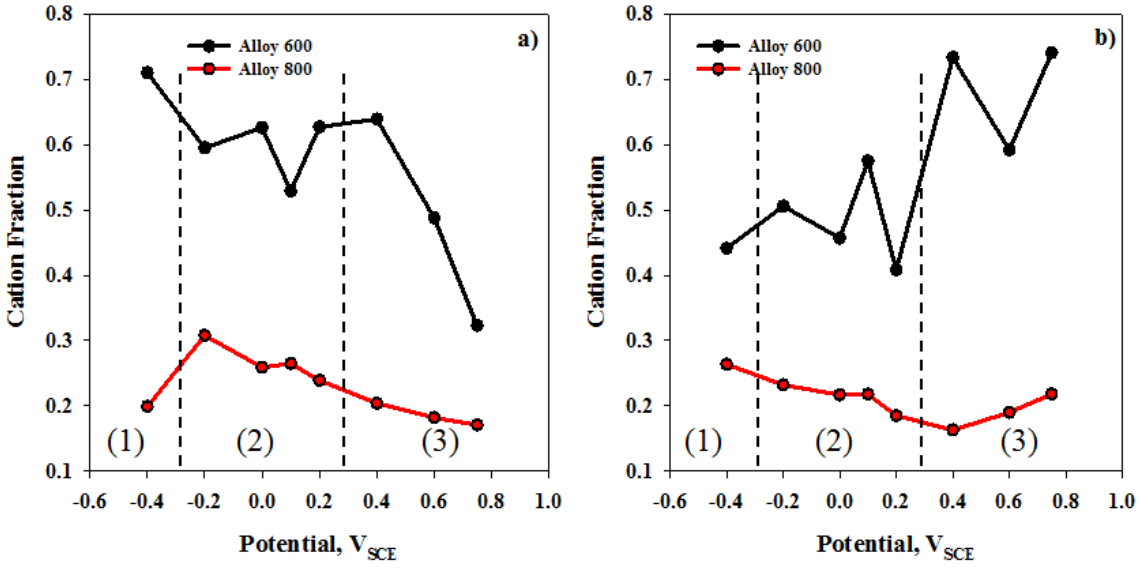

Figure 5.7 Cation fractions for Ni calculated from (a) AES profiles and (b) XPS survey scans. The plots are divided into three regions: (1) pre-passive, (2) passive and (3) transpassive.

Once again, the subsequent drop in Ni at a slightly higher film growth potential, Figure 5.7 (b), lead to an increase in Fe content of the film, Figure 5.6 (b). It is noteworthy that any similar fluctuations on Alloy 800 are minor.

5.3.4.3 Cr

Figure 5.8 shows the changes in the Cr cation fractions, with the values in Figure 5.8 (a) taken from the location in the depth profile where the Cr achieves a maximum value; i.e., the location of the barrier layer. As expected, the Cr content of the barrier layer achieves its maximum value in the passive region (2) and is higher for Alloy 800

than for Alloy 600. The XPS data, Figure 5.8 (b), also shows the general Cr content of Alloy 800 is greater than that of Alloy 600. However, two observations from this figure are significant, the first being that the increase in Cr content at 0.1 V_{SCE} for Alloy 600 coincides with the changes in Ni and Fe contents at the same film growth potential. This effect is much less marked, if it occurs at all, on Alloy 800.

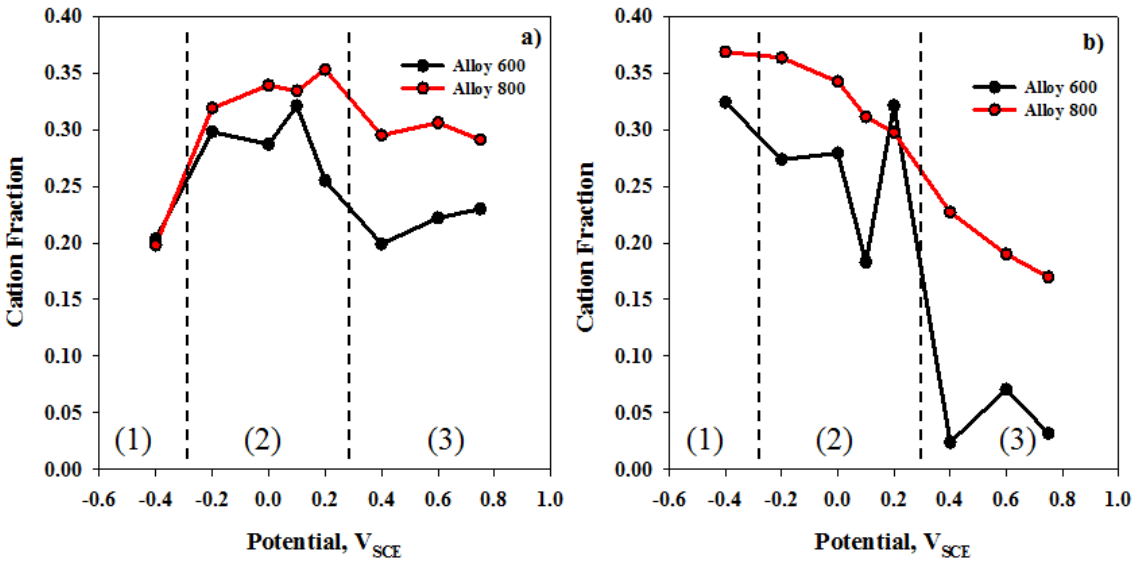

Figure 5.8 Cation fractions for Cr calculated from (a) AES profiles and (b) XPS survey scans. The plots are divided into three regions: (1) pre-passive, (2) passive and (3) transpassive.

Secondly, at higher potentials in the passive region and at potentials in the transpassive region, the Cr content of the barrier layer decreases markedly on Alloy 600 but only slightly on Alloy 800. The XPS data confirms that in the transpassive region the Cr content of the film is partially maintained on Alloy 800 but almost completely depleted on Alloy 600. This maintenance of the Cr content of the barrier layer on Alloy 800 is not reflected in a better barrier layer resistance for this alloy compared to Alloy 600, Figure 5.4 (a). The primary higher resistance for Alloy 800 in the transpassive region can be

attributed to the outer oxide layer, Figure 5.4 (b). In addition, the fluctuations in relative Ni and Fe content around 0.4 V_{SCE} on Alloy 600 in Figure 5.6 and Figure 5.7 are also visible in the Cr content, Figure 5.8, of both the barrier layer and the general oxide film.

5.3.5 Surface Analysis – AES Depth Profiles

5.3.5.1 Fe

Figure 5.9 shows the distribution of Fe in the oxide film and into the underlying substrate for both alloys as a function of film growth potential. In the pre-passive and passive regions, Fe is concentrated in the outer layer of the film for both alloys.

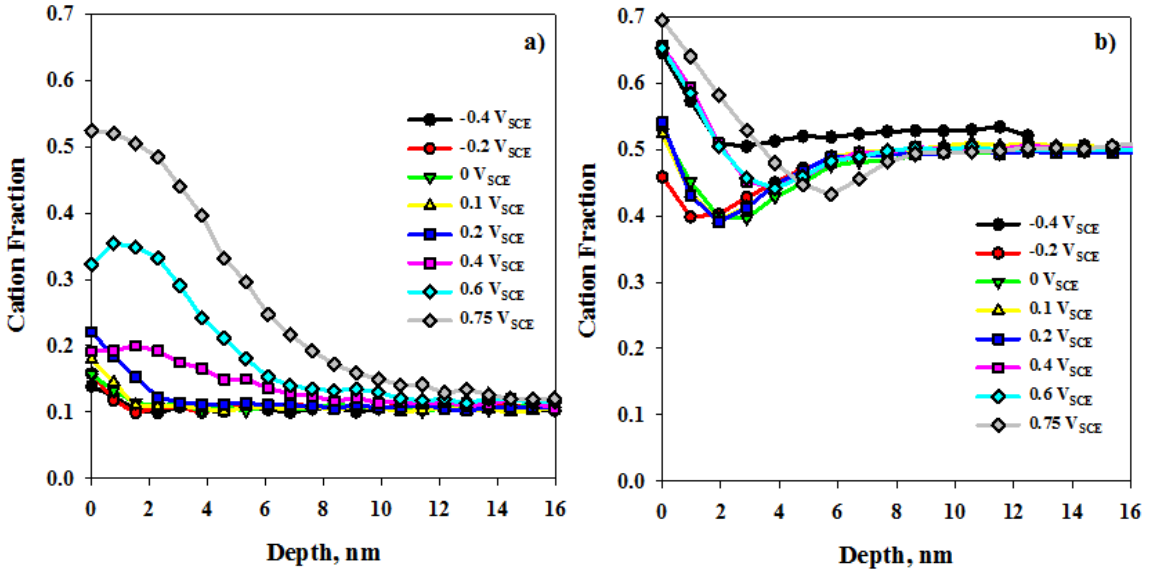

Figure 5.9 AES cation fractions of Fe plotted as a function depth for (a) Alloy 600 and (b) Alloy 800.

The shapes of the depth profiles in these potential regions are distinctly different for the two alloys. The Fe is concentrated in the outer region of the film on Alloy 600, but not depleted in the inner region (i.e., depleted with respect to its content in the alloy

substrate). For Alloy 800, however, the Fe is both concentrated in the outer layer, and depleted in the barrier layer compared to the bulk substrate content. This suggests that the increased thickness of the passive oxide film on Alloy 800 compared to Alloy 600, Figure 5.5, is a consequence of this segregation process. Beyond the anodic peak in the polarization curve, Figure 5.1, the Fe builds up in the outer regions of the films on both alloys as noted earlier, and the depletion profile in the barrier layer remains obvious for Alloy 800.

5.3.5.2 Ni

The changes in the Ni cation fractions as a function of depth for the various film growth potentials are shown in Figure 5.10.

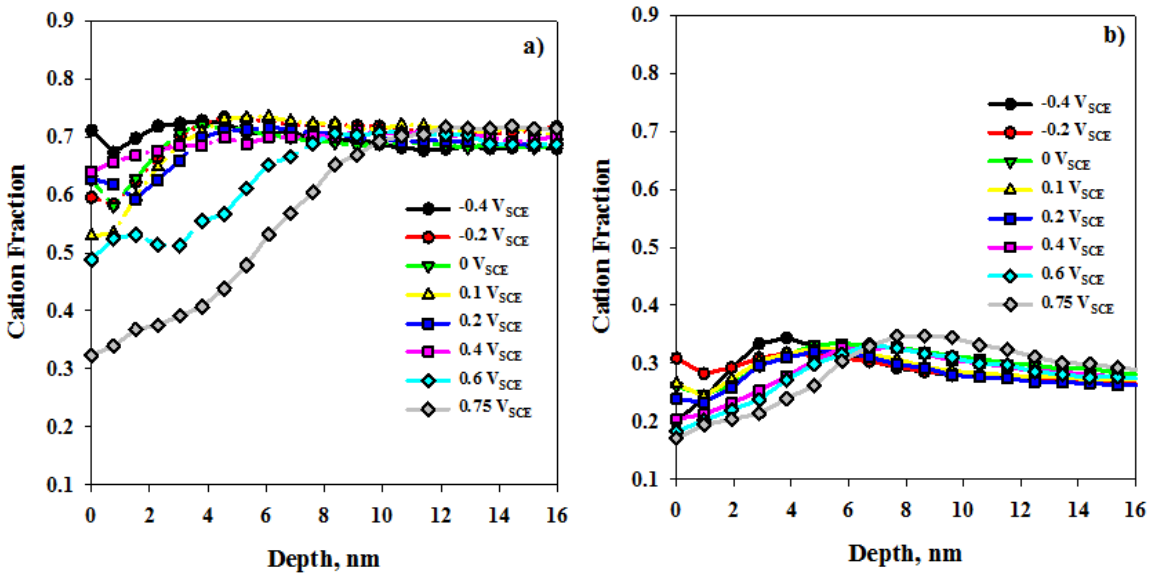

Figure 5.10 AES cation fractions of Ni plotted as a function depth for (a) Alloy 600 and (b) Alloy 800.

For both alloys, the Ni content in the oxide film is depleted relative to the bulk alloy concentration, with the majority of the Ni being located near the oxide/alloy interface. At potentials in regions 1 and 2, there appears to be a slight accumulation of Ni at the solution/oxide interface. For Alloy 600, the depletion of Ni in the oxide occurs predominantly at potentials greater than 0.2 V_{SCE}; i.e., at potentials positive to the anodic peak in the polarization curve, Figure 5.10 (a). This depletion is particularly marked in the transpassive region (3). For Alloy 800, Ni depletion is minor, including at potentials in region 3, and the depth profiles indicate that Ni, in fact, concentrates in the surface of the alloy, suggesting its release into solution is inhibited by the combination of the barrier and outer layers. The Alloy 600 depth profile at 0.4 V_{SCE} does not exhibit the same behaviour as observed at other potentials. The film at this potential contains much more Ni than expected based on the trends observed at other film growth potentials. The anodic polarization curve for Ni, Figure 5.1, shows an attempt to passivate at ~ 0.4 V_{SCE}, suggesting that Alloy 600 may be exhibiting similar behaviour to that of Ni at this potential. For Alloy 800 no similar effect at 0.4V_{SCE} is observed.

5.3.5.3 Cr

Figure 5.11 shows the changes in Cr cation fractions as a function of depth for various film growth potentials. The Cr content in the oxide on both alloys is localized within the barrier layer near the oxide/alloy interface. As expected, the highest Cr concentrations are observed at film growth potentials in the passive region (2), and the Cr cation fractions on Alloy 800 (0.33 to 0.36) are greater than on Alloy 600 (0.28 to 0.33). Compared to Alloy 800, the Cr content in the outer layer of Alloy 600 is typically higher and much more varied, indicating a greater mobility of Cr in the oxide on this alloy. For

Alloy 600, a number of features were noted in the transpassive region. The relative Cr content of the outer layer decreases, although a slight Cr enrichment persists on the outer surface. Except at 0.4 V_{SCE}, the maximum Cr content is still detected in close proximity to the oxide/alloy interface. As the Cr content of the barrier layer decreases, its position shifts to deeper locations as it becomes buried beneath the thickening outer Fe oxide layer, Figure 5.9 (a).

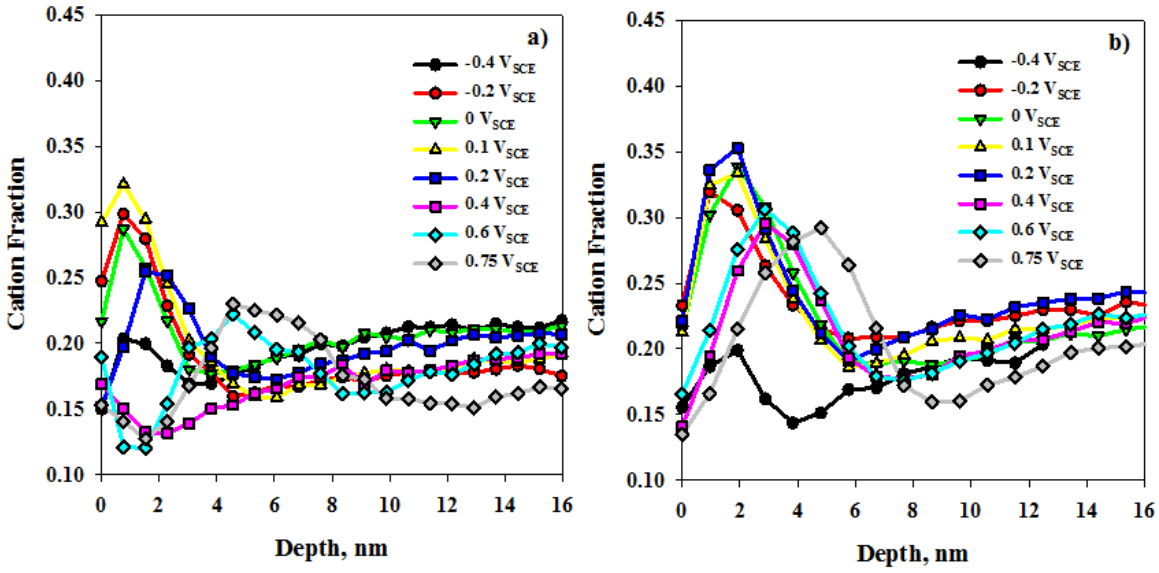

Figure 5.11 AES cation fractions of Cr plotted as a function depth for both (a) Alloy 600 and (b) Alloy 800.

Similar to Ni and Fe, the behaviour of Cr at 0.4 V_{SCE} on Alloy 600 shows significant deviation from the trends observed at other film growth potentials. As observed for Fe, Figure 5.9 (a), and Ni, Figure 5.10 (a), the Cr depth profile at 0.4 V_{SCE} is anomalous. The Cr peak disappears, suggesting the absence of the barrier layer at this potential. Combined with the enhanced Fe (inner layer) and Ni (outer layer) content, the oxide formed at this potential appears to be composed almost entirely of Fe and Ni. No similar

anomalous behaviour is exhibited by Alloy 800 at this potential, and the Cr content of the barrier layer remains considerably greater than that on Alloy 600.

5.3.6 Surface Analysis - XPS

A comparison of the high resolution XPS data for the two alloys was made for the Cr $2p_{3/2}$, Ni $2p_{3/2}$, O 1s, and Fe $2p_{3/2}$ peaks. The original data can be found in chapters 3 and 4. Figure 5.12 shows a comparison between the (a) Fe oxide, (b) $Ni(OH)_2$, (c) Cr_2O_3 and (d) M-O components. Figure 5.12 (a) and (d) show that the majority of Fe is in the form of Fe oxide, while Ni is predominantly present as $Ni(OH)_2$ in the outer layer. Both components show an overall increase as a function of film growth potential with Fe oxide dominant on Alloy 800 and $Ni(OH)_2$ on Alloy 600. For reasons described in Chapter 4, the exact nature of the Fe oxide is unidentified but is likely to change from magnetite in the passive region prior to film breakdown to an Fe^{III} oxide at positive potentials. The two surges in $Ni(OH)_2$ concentration on Alloy 600 are associated with the anodic peak in the polarization curve and the behaviour at 0.4 V_{SCE}, when the barrier layer on this alloy appears to be destroyed (at least temporarily). On Alloy 800, a similar, but much smaller surge is observed in the potential region of the anodic peak, but the increase in $Ni(OH)_2$ at 0.4 V_{SCE} is not observed. Perhaps most instructive is the change in Cr_2O_3 content, Figure 5.12 (c), which effectively defines the presence of the barrier layer. On Alloy 600, the development of this layer leads only to a marginal increase in Cr_2O_3 content and its development is disrupted by the current increase, Figure 5.1, in the potential range of the anodic peak. For potentials in the transpassive region, the Cr_2O_3 content drops to an effectively negligible level. This behaviour is consistent with the data from XPS survey

scans, Figure 5.8 (b), which show a very low overall Cr content within the detectable limit of the film.

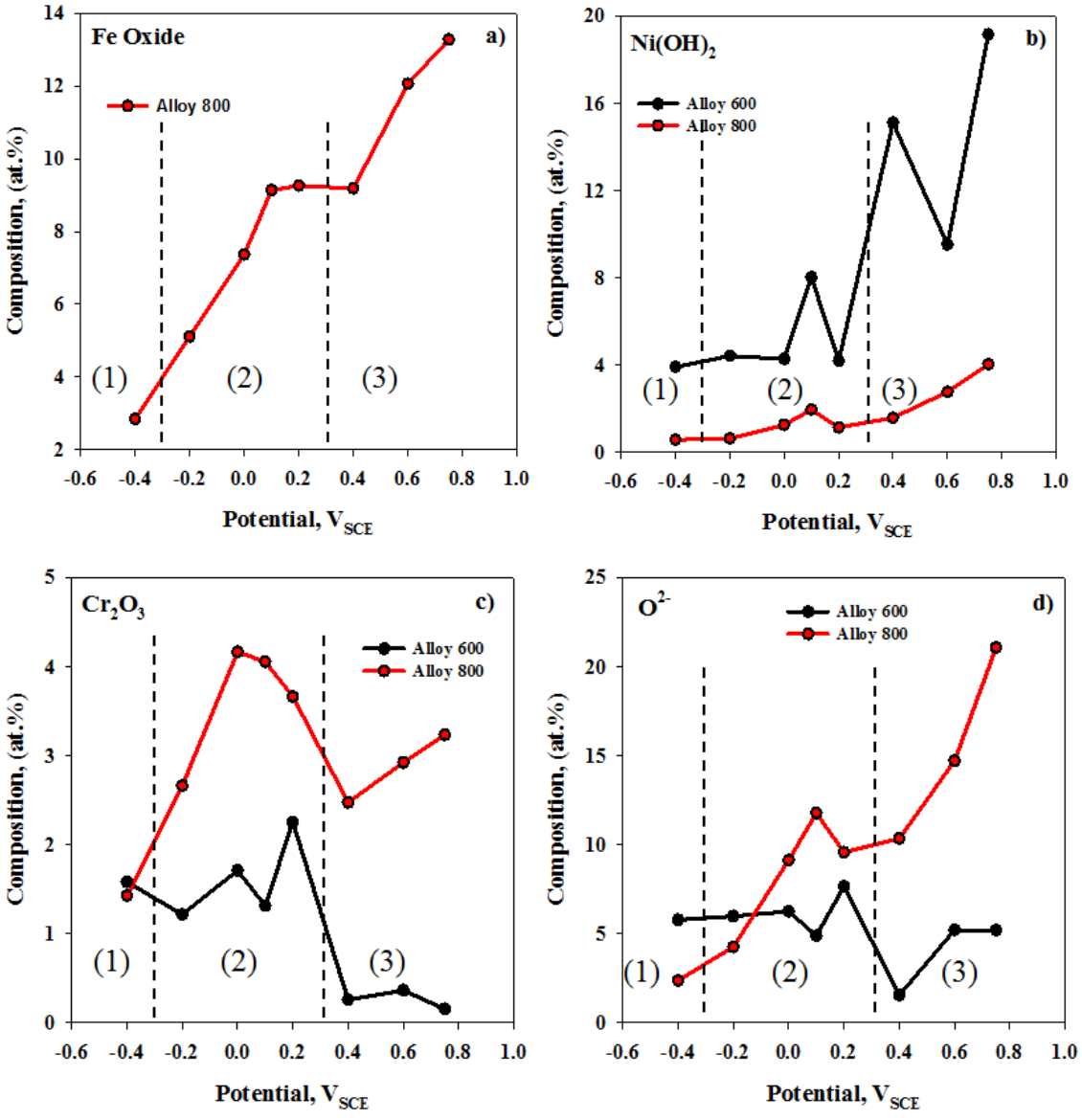

Figure 5.12 High resolution XPS data for (a) Fe oxide, (b) $Ni(OH)_2$, (c) Cr_2O_3, and (d) O^{2-} for Alloy 600 and Alloy 800.

By contrast, the Cr_2O_3 content of the Alloy 800 barrier layer increases steadily in the passive region, confirming the development of the Cr barrier layer as Fe segregates to the

outer layer. In addition, the Cr barrier layer is only partially destroyed in the anodic peak region and appears to be re-developed in the transpassive region as the Fe oxide content of the outer layer increases, Figure 5.12 (a).

5.3.7 Sulphur

The plots in Figure 5.13 contain data extracted from the AES depth profiles showing the changes in S as a function of depth in the oxide films formed at the various applied potentials for (a) Alloy 600 and (b) Alloy 800. Typically, the S peak reaches a maximum value well below the solution/oxide interface.

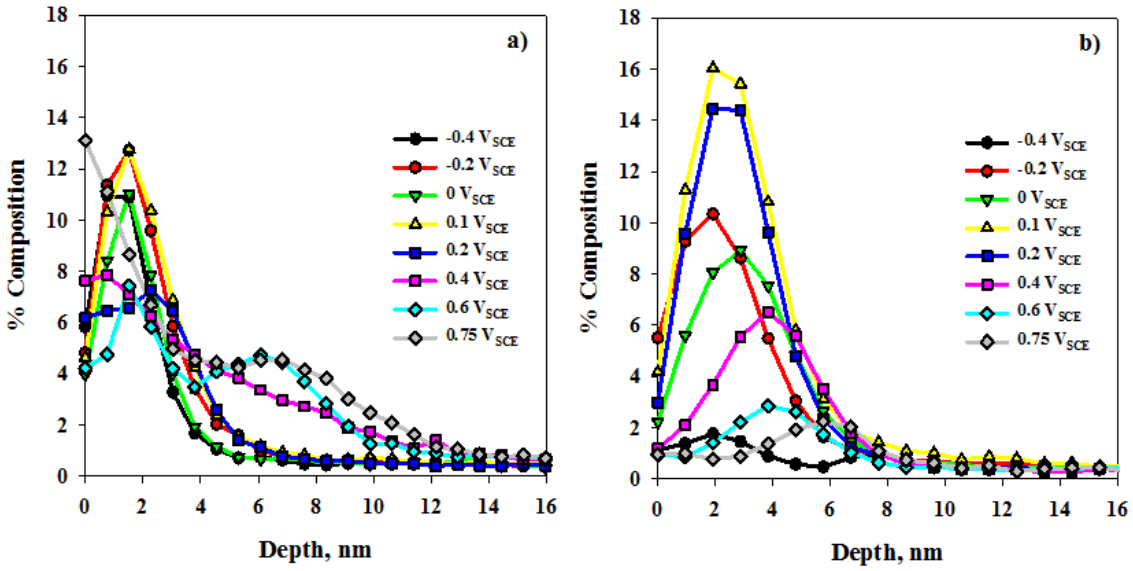

Figure 5.13 Changes in S content as a function of oxide depth at various potentials for (a) Alloy 600 and (b) Alloy 800 calculated from the AES depth profiles.

The distribution of S in the oxide is remarkably similar to that of Cr, Figure 5.11, suggesting that it is primarily concentrated within the barrier layer. Figure 5.14 compares the changes in Cr barrier layer content to that of S for (a) Alloy 600 and (b) Alloy 800.

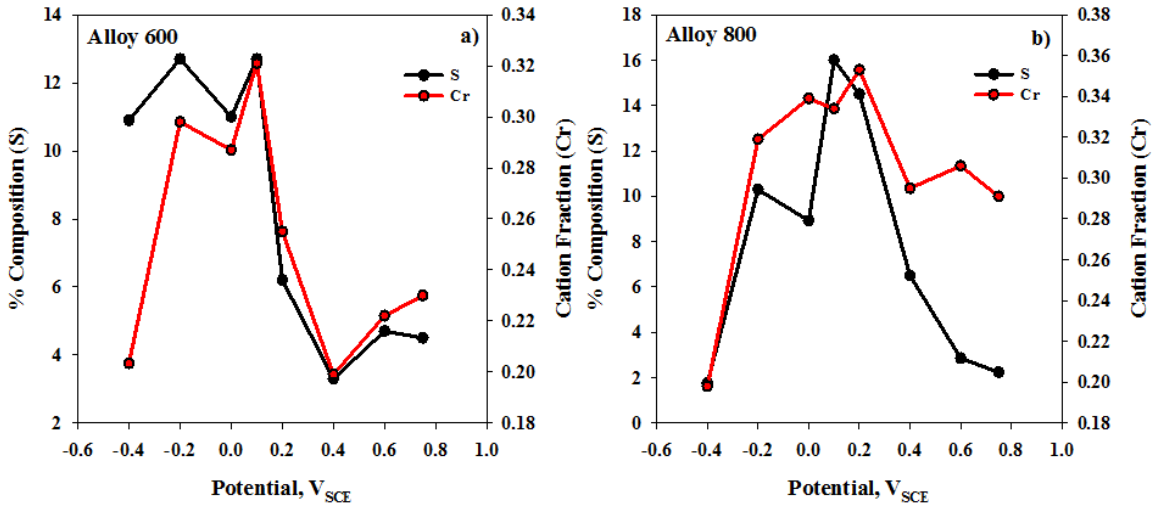

Figure 5.14 Plot of S and Cr for (a) Alloy 600 and (b) Alloy 800. The S value, obtained from the AES depth profile, was taken at a depth where the S peak reached a maximum value.

On Alloy 600, the association between Cr and S is maintained in the transpassive region when the barrier layer is destroyed but the inner regions of the film contain Cr. On Alloy 800, for which the Cr_2O_3 barrier layer appears to be partially maintained, S is not as readily retained. While not observed in the passive region, incorporation of S into the outer oxide film is observed on Alloy 600 at transpassive potentials, suggesting the degree of porosity of the $Ni(OH)_2$ dominant film is greater than the Fe oxide predominantly found on Alloy 800. The differences in outer layer and film porosity can be observed in the film resistance, Figure 5.4 (b).

5.4 Discussion

A comparison of the film growth behaviour between Alloy 600 and Alloy 800 can be broken down into a discussion of three distinct regions, based on the anodic polarization curve in Figure 5.1; the pre-passive and early stages of the passive region (-

0.4 V_{SCE} to 0 V_{SCE}); the anodic peak and late stages of the passive region (0 V_{SCE} to 0.3 V_{SCE}); and the transpassive region (0. 3 V_{SCE} to 0.75 V_{SCE}).

5.4.1 Pre-passive and Early Passive Region (-0.4 V_{SCE} to 0 V_{SCE})

Within this region, a passive film is shown to grow on both alloys. EIS studies show that in this section, the resistance of both the barrier layer and the outer layer increase substantially on Alloy 800 but only marginally on Alloy 600. The oxide film on Alloy 800 grows measurably thicker than on Alloy 600, although intuitively, this might not be expected since Alloy 800 contains considerably more Cr than Alloy 600 and a thinner, more resistive barrier layer oxide would be expected to form.

The two alloys show distinctly different segregation behaviour in this potential range. While the Ni content of the outer layer on Alloy 600 is high, as expected, Ni is not significantly depleted in the inner regions of the film, even though a Cr-enriched layer exists at the oxide/alloy interface. While the Cr_2O_3 content of the film increases with film growth potential, the increases are small and a considerable amount of Cr exists as the oxide $Cr(OH)_3$, which would account for the Cr in the surface layers of the film. For Alloy 800, Fe is clearly segregated to the outer surface of the film and depleted in the inner regions, Figure 5.9 (b), where the Cr content is highest, Figure 5.11 (b). That this segregation process leads to the formation of a barrier layer is confirmed by a marked increase in Cr_2O_3 content of the film. This, accompanied by a low, and decreasing $Cr(OH)_3$ content of the film as the film growth potential increases, would then explain the marked increase in barrier layer resistance, Figure 5.4 (a). This Fe/Cr segregation process leads to the retention of Ni in the surface of the alloy, Figure 5.10 (b).

The segregation of alloying elements in passive films is a well-known phenomenon and can occur as a consequence of either preferential oxidation of one element in the alloy or the preferential dissolution of another element from the film [43]. In Alloy 800, this process is readily achieved as Cr is preferentially oxidized, yielding the Cr_2O_3 barrier layer and the base alloying element, Fe, readily dissolved as Fe^{2+}. The accumulation of Fe in the outer regions of the film also contributes to the overall film resistance, although its absolute value is only 10% of that of the barrier layer, Figure 5.4, in this potential region. By comparison, the outer layer on Alloy 600 contributes only marginally to the overall resistance of the film.

5.4.2 Anodic Peak Region (0 V_{SCE} to 0.3 V_{SCE})

A key feature of the behaviour in region 2 is the presence of the anodic peak at ~0.1 V_{SCE}. This peak is observed on both alloys, but not on pure Cr, suggesting the susceptibility to this oxidation is related to the lower Cr content of the passive film relative to the pure Cr oxide present on the metal, Figure 5.1. The onset of this oxidation process leads to an immediate loss of barrier layer resistance, Figure 5.4 (a). On Alloy 600, this oxidation process leads to significant fluctuations in relative cation film content. For example, the Cr content on the outer layer of the film, Figure 5.8 (a), increases while the overall content of the film decreases, Figure 5.8 (b). While not easily interpretable, this is accompanied by fluctuations in the Cr_2O_3 content of the oxide, Figure 5.12 (c). The increase in Cr content of the outer layers of the film is followed by a decrease in the Ni content, Figure 5.7 (a), clearly indicating a disruption of the barrier layer and the transport of Cr to the outer regions of the film. This barrier layer disruption would be expected to involve the oxidation of Cr^{III} to Cr^{VI} (as CrO_4^{2-}). Its detection in the outer

regions of the film as Cr^{III} is most likely due to the reduction of Cr^{VI} to Cr^{III} during transfer from the electrochemical cell to the UHV chamber of the analytical instrument [44]. Reduction of the Cr species could also have been induced by the X-ray beam during XPS analyses.

For Alloy 800 no major degradation of the film structure occurs in the anodic peak region, despite the significant apparent decrease in film thickness between 0 V_{SCE} to 0.2 V_{SCE}, Figure 5.5, and a drop in barrier layer resistance, Figure 5.4 (a). The overall Cr content of the passive film on Alloy 800 begins to decrease as the current rises in the anodic peak region, Figure 5.8 (b), suggesting a degradation of the barrier layer. This is confirmed by the decrease in Cr_2O_3 content of the film, Figure 5.12 (c). Compared to Alloy 600, however, this loss of Cr_2O_3 content is relatively small, and this degradation of the barrier layer does not lead to any immediate major changes of the Fe and Ni contents of the film.

The slight increase in Ni, as $Ni(OH)_2$ in Figure 5.12 (b), offers a possible explanation for the apparent thinning of the passive film in this potential region (0 V_{SCE} to 0.2 V_{SCE}), Figure 5.5. As suggested in chapter 4, a degradation of the barrier layer and an increase in $Ni(OH)_2$ film content would be expected to induce some porosity into the film. This could increase the sputtering efficiency in AES leading to an apparent, not real, decrease in film thickness. These differences lead to significant changes in the impedance properties of the films. For both Alloy 600 and Alloy 800, the barrier layer resistances decrease as the current increases into the anodic peak region. However, for Alloy 800, but not for Alloy 600, the outer layer oxide resistance continues to increase up to 0.1 V_{SCE} before decreasing again. This increase coincides with increased Fe oxide

content, indicating that it is the accumulation of Fe, already present in substantial quantities prior to the anodic breakdown of the barrier layer, which accounts for the outer layer resistance.

5.4.3 Transpassive Region (0.3 V_{SCE} to 0.75 V_{SCE})

At potentials beyond the region of the anodic peak, the barrier layer resistance on both alloys decreases considerably. For Alloy 600, the Cr_2O_3 content of the film approaches zero, suggesting the complete destruction of this layer. This is confirmed by the almost complete loss of Cr from the film, except for the very outer layer. The movement of Cr to the outer layers is most likely to occur by the transport of Cr^{VI} (CrO_4^{2-}). Its observation in the outer layers as Cr^{III} ($Cr(OH)_3$) can be attributed to the reduction processes invoked above. The fluctuations in Ni content of the oxide at ~0.4 V_{SCE}, which coincide with changes in the Ni behaviour according to the polarization scans, also coordinate with the effective disappearance of the Cr_2O_3 barrier layer, Figure 5.8 (b), and the onset of a significant increase in Fe oxide content. This outer oxide layer confers little additional protection from transpassive dissolution. A comparison of the cation fractions for Ni, Figure 5.7, and Cr, Figure 5.8, shows these fractions are inversely related, suggesting that the fluctuations in Ni behaviour are related to the condition of the Cr oxide barrier layer rather than any intrinsic property of Ni, as might be inferred from the polarization curve for the metal, Figure 5.1.

For Alloy 800, the Cr content of the oxide, while decreasing with film growth potential in the transpassive region, remains considerably higher than for Alloy 600. The Cr_2O_3 content of the film is maintained and, in fact, increases slightly in the transpassive

region. In addition, the Fe content of the film, particularly in the outer layer, already high in the passive region, increases further in the transpassive region. This continuing segregation of Fe to the outer regions of the film enhances the relative retention of Ni in the surface of the substrate alloy. At these potentials in the transpassive region, this oxide will be an Fe^{III} oxide and highly insoluble at the pH of this experiment. This outer layer oxide maintains a significant resistance up to 0.6 V_{SCE}, i.e., well into the transpassive region. In fact, in the transpassive region for Alloy 800, the outer layer and barrier layer resistances are approximately equal, confirming that the Fe^{III} oxide layer provides a significant contribution to the overall resistance.

5.5 Conclusions

A passive oxide is more rapidly formed on Alloy 800 than on Alloy 600. The segregation of Fe to the outer regions of the film leads to a thicker passive layer, a more resistive inner Cr_2O_3 barrier layer, and the retention of Ni in the surface of the substrate alloy. In Alloy 600, the more noble Ni alloying element does not oxidize as readily and segregates to the outer regions of the film. As a consequence, the oxide film is thinner and the barrier layer not as quickly developed.

At slightly higher potentials this passive film is disrupted on both alloys. This disruption involves a destruction of the barrier layer, a process that appears to be assisted by the presence of S (most likely as S^{2-}) in the inner barrier layer, although the details of this effect remain to be elucidated.

For Alloy 600, this disruption eventually leads to the complete destruction of the barrier layer and the formation of an un-protective $Ni(OH)_2$ outer layer. For Alloy 800,

the barrier layer is only partially destroyed and a significant Cr_2O_3 content persists well into the transpassive region. The partial protection of the alloy/oxide interface can be attributed to the formation of a thick outer layer of insoluble Fe^{III} oxide.

References

[1] D. Van Rooyen, Corros., 31 (1975) 327-337
[2] W. Yang, Z. Lu, D. Huang, D. Kong, G. Zhao, J. Congleton, Corros. Sci., 43 (2001) 963-977
[3]].K. Sieradzki, R.C. Newman, J. Phys. Chem. Solids, 48 (1987) 1101-1113
[4] R.H. Jones, Stress Corrosion Cracking: Materials Performance and Evaluation, ASM International, (1992)
[5] L.L. Shreir, R.A. Jarman, G.T. Burstein, Corrosion: Metal/Environmental reactions, Butterworth-Heinemann (1994)
[6] Newsletter on Three Mile Island Unit 1, Nucl. News, 25 (1982) 47
[7] R. Bandy, R. Roberge, R.C. Newman, Corros., Sci., 23 (1983) 995-1006
[8] R. Bandy, R. Roberge, R.C. Newman, Corros., 39 (1983) 391-398
[9] R. Bandy, D. Van Rooyen, Corros., 40 (1984) 281-289
[10] H. Coriou, L. Grall, C. Mahieu, M. Pelas, Corros., 22 (1966) 280-290
[11] H.R. Copson, G. Economy, Corros., 24 (1968) 55-65
[12] H.R. Copson, S.W. Dean, Corros., 21 (1965) 1-8
[13] J.R. Cels, Corros., 34 (1978) 198-209
[14] M.-C. Tsai, W.-T. Tsai, J.-T. Lee, Corros. Sci., 34 (1993) 741-757
[15] W-T. Tsai, Z-H. Lee, J-T. Lee, M-C. Tsai, P-H. Lo, Mater. Sci. Eng., A118 (1989) 121-129
[16] P.K. De, S.K. Ghosal, Corros., 37 (1981) 341-349
[17] R.S. Dutta, J. Nucl. Mater., 393 (2009) 343-349
[18] T. Nickchi, A. Alfantazi, Corros., 68 (2012) 1-11
[19] I.J. Yang, Corros., 49 (1993) 576-585
[20] W.-T. Tsai, M.-J. Sheu, J.-T. Lee, Corros. Sci., 38 (1996) 33-45
[21] T. Sakai, K. Aoki, T. Shigemitsu, Y. Kishi, Zairyo to Kankyo 40 (1991) 736-741
[22] Z. Fang, R. W. Staehle, Corros., 55 (1999) 355-379
[23] T. Sakai, S. Okabayashi, K. Aoki, Proceedings of the 4th International Symposium on Degradation of Materials in Nuclear Power Systems- Water Reactors, Jekyll island, Georgia, 6-10 August (1989)
[24] R.C. Scarberry, S.C. Pearman, J.R. Crum, Corros., 32 (1976) 401-406
[25] E.H. Lee, K.M. Kim, U.C. Kim, Mater. Sci. Eng., A449 (2007) 330-333
[26] P. Marcus, A. Teissier, J. Oudar, Corros. Sci., 24 (1984) 259-268
[27] L.A.S. Ries, M. Da Cunha Belo, M.G.S. Ferreira, I.L. Miller, Corros. Sci., 50 (2008) 676-686
[28] P. Marcus, J.M. Grimal, Corros. Sci., 33 (1992) 805-814
[29] M. Da Cunha Belo, N.E. Hakiki, M.G.S. Ferreira, Electrochim. Acta., 44 (1999) 2473-2481
[30] J. Robertson, Corros. Sci., 32 (1991) 443-465
[31] D.D. Macdonald, A. Sun, Electrochim. Acta., 51 (2006) 1761-1779
[32] N.E. Hakiki, S. Boudin, B. Rondot, M. Da Cunha Belo, Corros. Sci., 37 (1995) 1809-1822
[33] J. Robertson, Corros. Sci., 29 (1989) 1275-1291
[34] D. Hamm, C.-O.A. Olsson, D. Landolt, Corros. Sci., 44 (2002) 1009-1025
[35] T. Dan, T. Shoji, Z. Lu, K. Sakaguchi, J. Wang, E.-H. Han, W. Ke, Corros. Sci., 52 (2010) 1228-1236

[36] A.C. Lloyd, D.W. Shoesmith, N. S. McIntyre, J.J. Noel, J. Electrochem. Soc., 150 (2003) B120-B130
[37] P. Jakupi, D. Zagidulin, J.J. Noel, D.W. Shoesmith, Electrochim. Acta., 56 (2011) 6251-6259
[38] N.E. Hakiki, M. Da Cunha Belo, A.M.P. Simoes, M.G.S. Ferreira, J. Electrochem. Soc., 145 (1998) 3821-3829
[39] N.E. Hakiki, S. Boudin, B. Rondot, M. Da Cunha Belo, Corros. Sci. 37, (1995) 1809
[40] F. Gaben, B. Vuillemin, R. Oltra, J. Electrochem. Soc., 151 (2004) B595-B604
[41] P. Marcus, J.M. Grimal, Corros. Sci., 31 (1990) 377-382
[42] D.D. Macdonald, J. Electrochem. Soc., 139 (1992) 3434-3449
[43] L. Zhang, D.D. Macdonald, Electrochim. Acta., 43 (1998) 2661-2671
[44] J.A. Bardwell, G.I. Sproule, B. MacDougall, M.J. Graham, A.J. Davenport, H.S. Isaacs, J. Electrochem. Soc., 139 (1992) 371-373

Chapter 6. Corrosion and Surface Film Properties of Alloy 600 Subjected to Surface Mechanical Attrition Treatment (SMAT)

6.1 Introduction

Alloy 600 was the predominant SG tubing material used in CANDU reactors for many years, until it was discovered to be susceptible to SCC [1-13]. This type of failure is common and highly sensitive to the structure and properties of the material. To avoid this problem, Alloy 600 was replaced in CANDU reactors with the more corrosion resistant Alloy 800. However, the SCC of this alloy has also been recently reported [10, 13, 14]. One novel approach to combat SCC is to optimize the surface microstructure of existing SG tubing. Extensive research on nanostructured materials show they display much different behaviour when compared to their coarse grained counter parts, such as an increase in hardness and strength, improved tribological properties and increased plasticity at low temperatures [15-20]. One method to achieve these modifications is through the use of SMAT. This technique was developed by Lu, *et al*., [21] who showed that a thin, nanostructured surface layer could be induced on metals and alloys [22-26]. In this technique, smooth, spherical balls are accelerated towards the sample at various angles and velocities. The repeated multidirectional impact of the balls can induce plastic deformation with a high strain rate on the surface, ultimately leading to grain refinement [17, 21].

Chapter 3 focused on the passive oxide film formed on Alloy 600 in the presence of $S_2O_3^{2-}$. Reduced S species can destabilize the oxide film through the acceleration of anodic dissolution, enhancing susceptibility to SCC [2-4, 27-33]. The oxide formed on

Alloy 600 possessed a highly protective Cr_2O_3 rich barrier layer, and a non-protective outer layer containing a mixture of $Ni(OH)_2$, $Cr(OH)_3$ and Fe oxides. This barrier layer was subject to breakdown at potentials in the passive region due to restructuring, and at transpassive potentials.

The aim of this study was to examine the effects of SMAT on the compositional and electrochemical properties of the oxide film. Electrochemical techniques such as anodic polarization and EIS were used to examine the effects of SMAT on the passive film properties in $Na_2S_2O_3$. AES and XPS were used to determine the changes in chemical composition of the oxide film resulting from SMAT.

6.2 Experimental

6.2.1 Sample Preparation

9.5 mm diameter Alloy 600 tubing sections were procured from Rolled Alloys Canada in the mill-annealed condition. The composition is presented in Table 6.1.

Table 6.1 Chemical composition of Alloy 600 SG tubing (wt%).

Element	Ni	Cr	Fe	Mn	Al	Ti	Si	C
Composition %	72.97	16.14	9.65	0.34	0.27	0.23	0.11	0.03

Several 6 inch sections of Alloy 600 tubing were shipped to Hong Kong Polytechnic University in Hong Kong to undergo SMAT. Process parameters such as shot composition and treatment time were varied. Samples were treated using either stainless steel (SS) or zirconium (Zr) shot, with a mass of 20 g each, for time periods of 15, 30, 90 or 120 minutes. The electrodes were designated according to the shot material and time

used. For example, a sample treated using zirconium shot for 30 minutes is designated A600zr30.

Small rectangular prismatic electrodes were carefully cut from this tubing using a Buehler diamond-tipped saw. The average exposed sample area on the outer surface of these electrodes was 20 mm^2. The electrodes were lightly polished with a 0.05 μm alumina grit polishing pad, washed with DI water, and sonicated in acetone.

6.2.2 Electrochemical Measurements

A detailed description of experimental and analytical procedures can be found in chapters 3 and 4.

6.2.3 Surface Analysis

6.2.3.1 Scanning Electron Microscopy (SEM)

Samples mounted in an epoxy resin were used for SEM analyses. After polishing to a mirror finish, the electrode surface was etched to reveal the grain boundaries. Electrochemical etching of the alloys was performed in a 10% HCl/methanol solution at 5 V for approximately 10 seconds. Electrodes were rinsed with DI water and methanol, dried, and gold coated to prevent charging of the electrode during SEM measurements. A Hitachi S-4500 SEM was used for sample analysis. Images were obtained at a beam voltage of 15.0 kV.

6.2.3.2 Auger Electron Spectroscopy (AES)

A detailed description of experimental and analytical procedures can be found in chapters 3 and 4.

6.2.3.3 X-ray Photoelectron Spectroscopy (XPS)

A detailed description of experimental and analytical procedures can be found in chapters 3 and 4.

6.3 Results

6.3.1 Surface Imaging: Scanning Electron Microscopy (SEM)

Electrochemical etching of cross sections of the mounted tubing revealed the intricate grain boundary structures of the SMAT SG tubing.

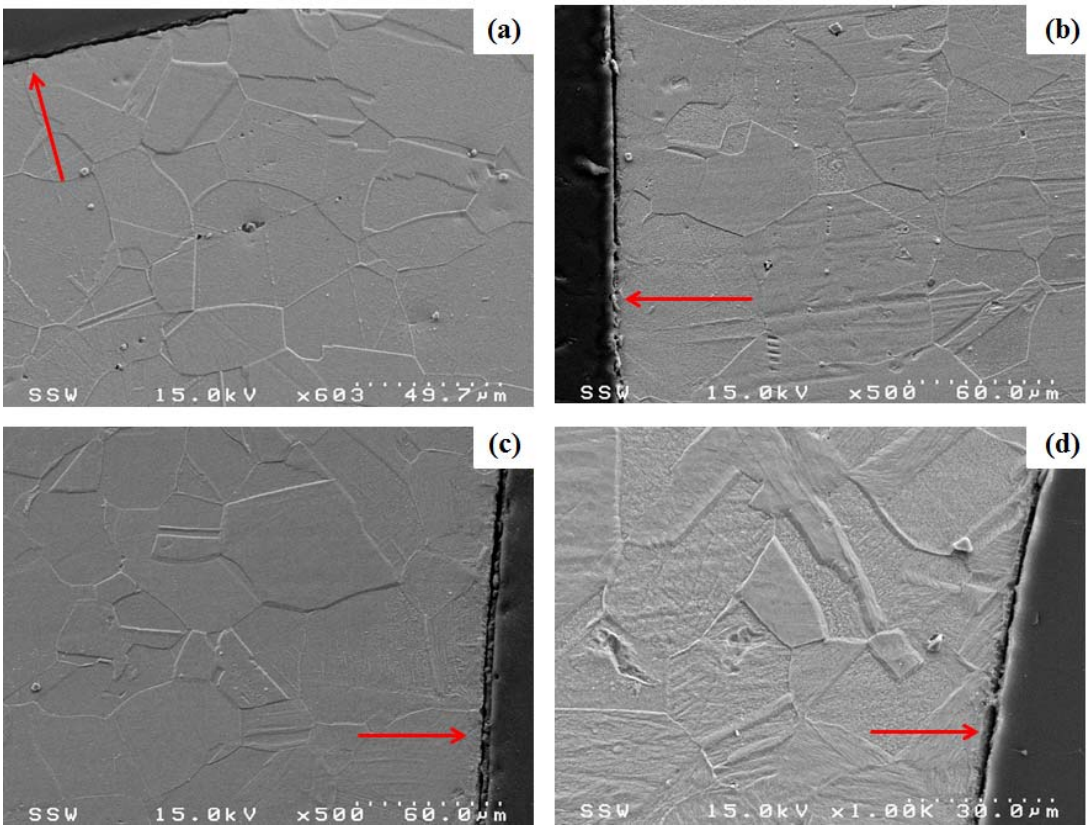

Figure 6.1 SEM images of cross sections of mounted electrodes: (a) A600, (b) A600zr15, (c) A600zr30 and (d) A600ss120. The red arrows indicate the location of the SMAT surface.

The SMAT process causes plastic deformation resulting from the repeated impact on an alloy and can lead to the nanocrystallization of the outer surface through progressive grain refinement. The thickness of the nanostructured layer that is produced can be up to 50 μm thick [21] and should be visible using electron microscopy**.** SEM images of the SMAT electrodes are shown in Figure 6.1. While individual grains can be easily resolved, there is no indication that a nanocrystalline structure was produced along the outer diameter of the SMAT electrodes.

6.3.2 Anodic Polarization

The influence of SMAT on the electrochemical behaviour is examined by measuring the potentiodynamic response of Alloy 600 and the SMAT electrodes A600zr15, A600zr30 and A600ss120 in 0.1 M $Na_2S_2O_3$ solution. These electrodes were chosen because their physical properties demonstrated the largest SMAT influences. Figure 6.2 shows that the general electrochemical behaviour of all of the electrodes is similar. All of the samples exhibit an anodic peak at 0.1 V_{SCE}, which has been observed previously in similar systems [11, 28, 30, 34, 35] and discussed in detail previously in chapters 3 through 5. The steady rise in current density after the anodic peak implies a degree of instability within the oxide as a consequence of the behaviour within the potential range of the peak. The anodic polarization curves are broken down into three regions, based on the electrochemical behaviour. At potentials in region 1, electrodes are in the pre-passive state, prior to passive film formation. A shift in the E_{corr} (the potential at which the current changes sign), Figure 6.2, is observed for the SMAT electrodes, ~ 10 mV in the cathodic direction with respect to A600. Similar results have been reported elsewhere [36**]**.

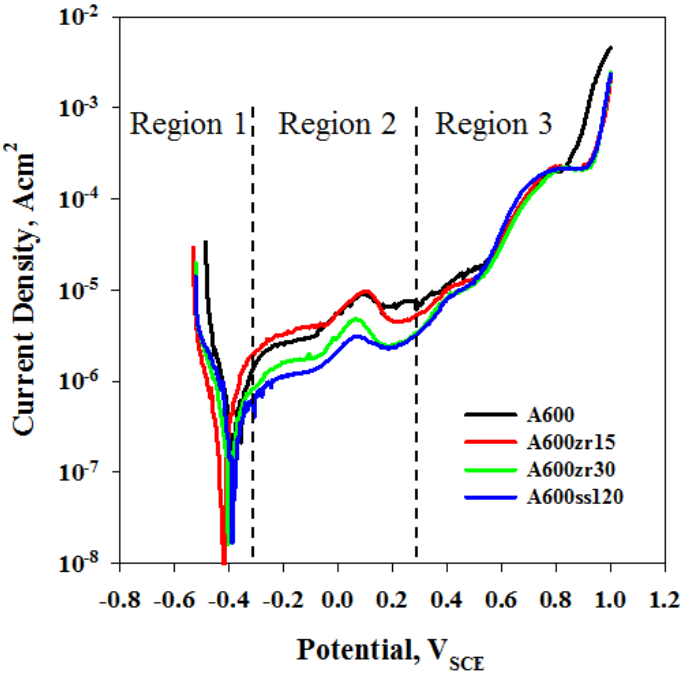

Figure 6.2 Anodic polarization curves recorded on the A600, A600zr15, A600zr30 and A600ss120 electrodes in 0.1M $Na_2S_2O_3$ solution: the three regions are defined as (1) pre-passive (2), passive and (3) transpassive.

Region 2 denotes the passive region, where the oxide film formed is expected to be protective. Region 3 is the transpassive region defined by the substantial current density increase. All of the electrodes show similar behaviour, with the anodic peak being universally present. The lightly treated A600zr15 shows almost identical behaviour to the untreated alloy, the current being almost the same for both electrodes in all three regions. For the two more aggressively treated electrodes, the currents are lower than for the untreated electrode throughout the passive region 2. In region 3 the electrodes all behave effectively identically. Prior to, and within, the anodic peak region, the lowest current is observed on the A600ss120 electrode.

6.3.3 Electrochemical Impedance Spectroscopy (EIS)

EIS measurements were made on the electrochemically treated A600 and the SMAT electrodes in the potential range -0.4 V_{SCE} to 0.75 V_{SCE}, Figure 6.3.

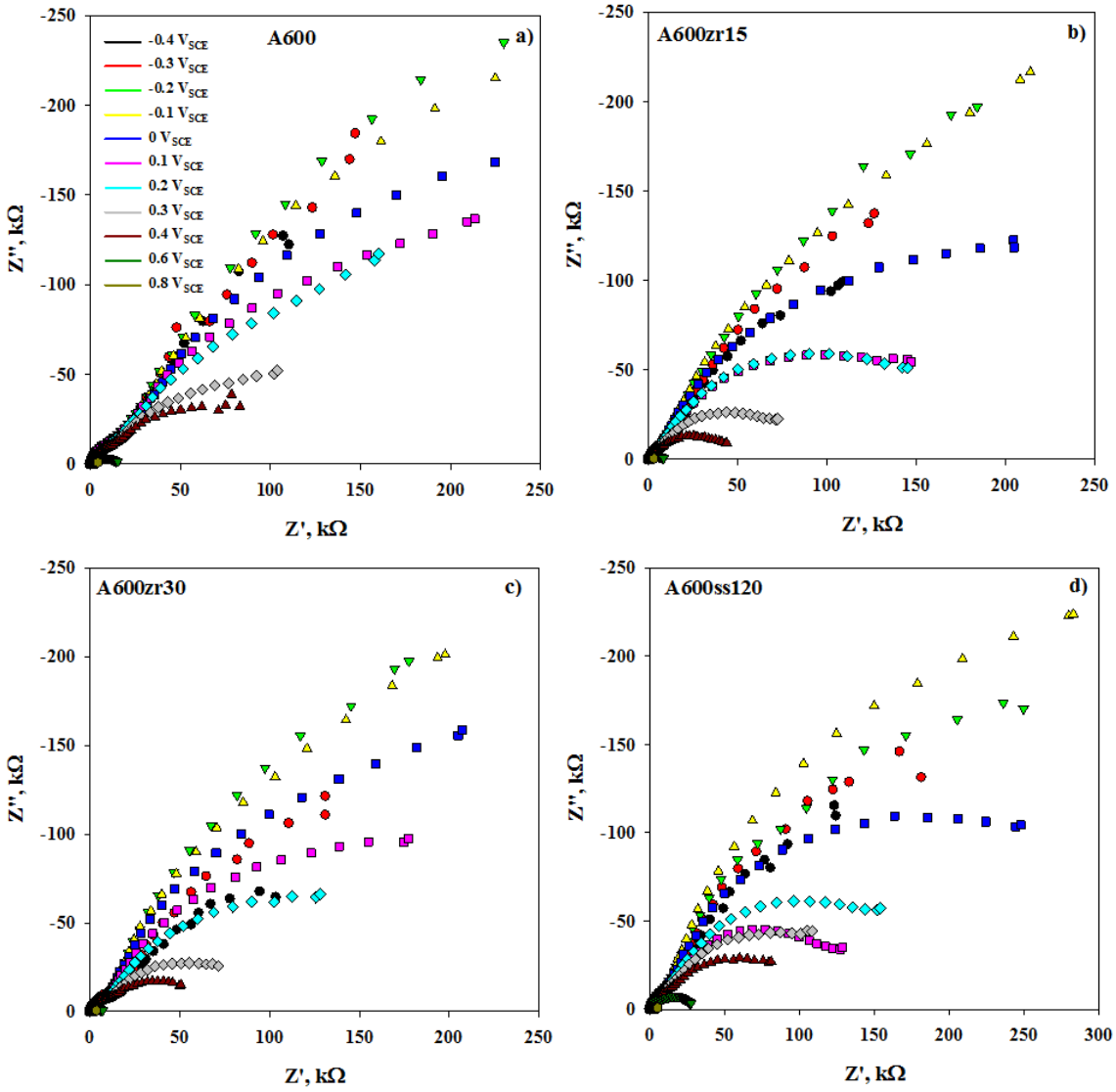

Figure 6.3 Nyquist plots recorded on the electrodes following potentiostatic treatment for three hours at various potentials: (a) A600, (b) A600zr15, (c) A600zr30, and (d) A600ss120.

The ideally semi-circular Nyquist plots appear depressed, indicating significant frequency dispersion on the electrode surface [37-39]. A high and low frequency response is visible

in the spectra for all four electrodes. The Bode plots are shown in Figure 6.4. Two easily resolved peaks in the phase angle, θ, are observed in the spectra at nearly every measured potential. A decrease in θ is observed at low frequencies as the applied potential is increased.

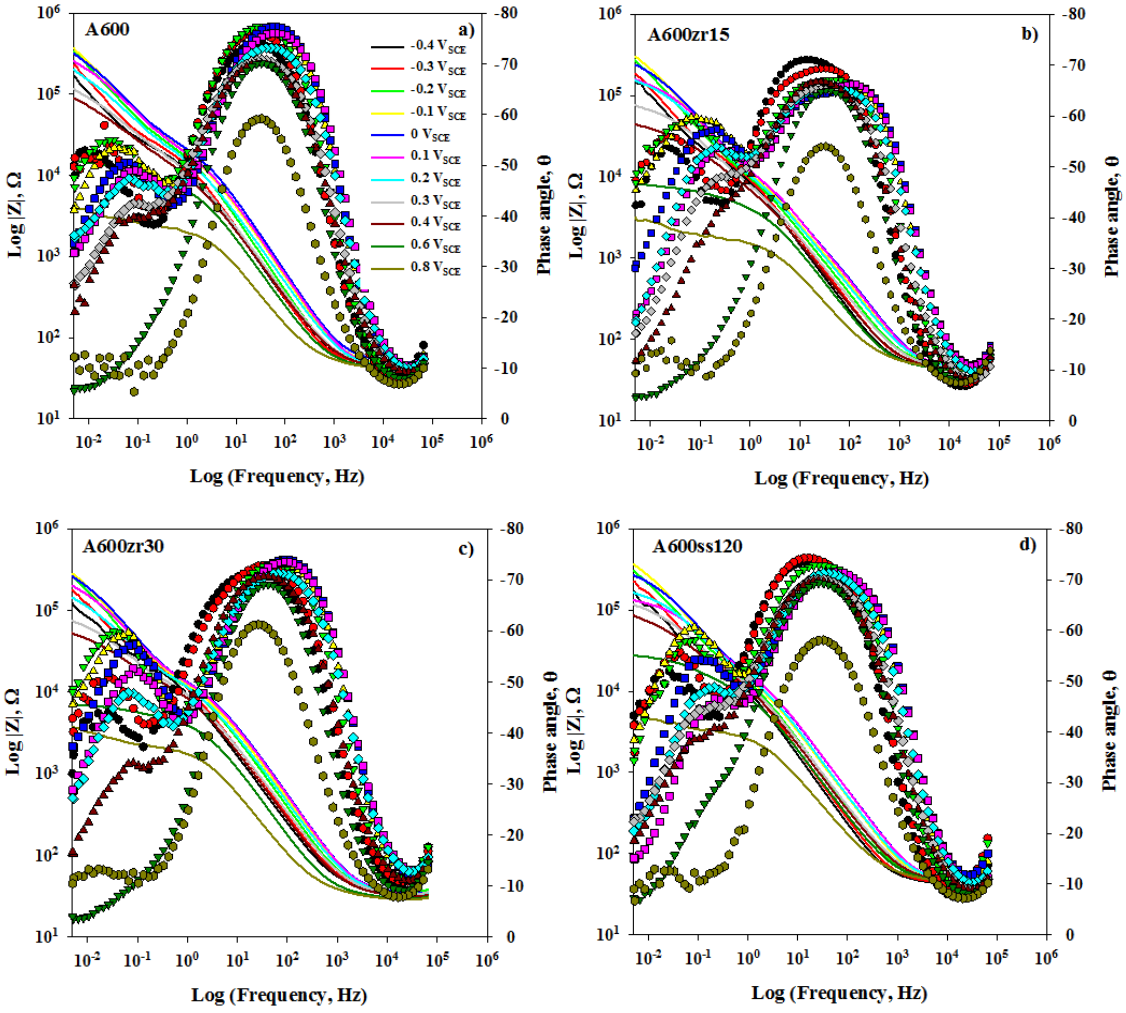

Figure 6.4 Bode plots recorded on the electrodes following potentiostatic treatment for three hours at various potentials: (a) A600, (b) A600zr15, (c) A600zr30, and (d) A600ss120.

A two time constant equivalent circuit, previously used to fit the spectra measured on Alloy 600 (chapter 3), Figure 6.5, was used to fit the spectra. The model contains two

time constants in series, as well as a single resistive element, R_s, which represents the solution resistance. Since the measured capacitance responses are not ideal, a CPE was used in place of capacitance.

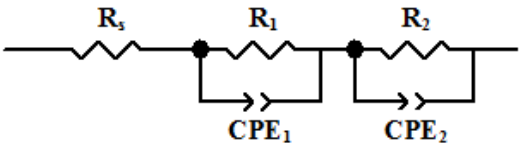

Figure 6.5 Equivalent circuit used to model EIS spectra recorded on A600, A600zr15, A600zr30 and A600ss120.

As described in chapter 3, the first time constant, R_1/CPE_1, represents the outer oxide layer while the second time constant, R_2/CPE_2, represents the inner barrier oxide layer. Examples of the fitting of spectra to this model are shown for all four electrodes in Figure 6.6.

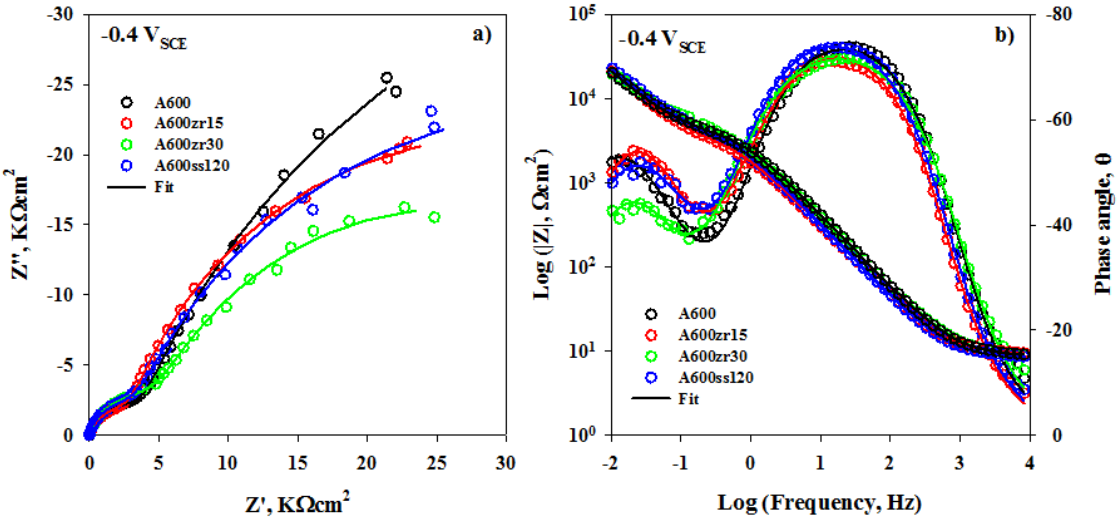

Figure 6.6 Examples of fitted EIS spectra (-0.4 V_{SCE}) for A600, A600zr15, A600zr30 and A600ss120: (a) Nyquist and (b) Bode plots.

Excellent fits were obtained for all the spectra and the numerical values of select circuit elements are tabulated in Table 6.2.

Table 6.2 Summary of the parameters obtained from the fitted EIS spectra for A600, A600zr15, A600zr30 and A600ss120.

Alloy	E (V_{SCE})	R_2 ($k\Omega cm^2$)	CPE_2 (μFcm^{-2})	n	R_1 ($k\Omega cm^2$)	CPE_1 (μFcm^{-2})	n
A600	-0.4	98.87	423.8	0.7860	3.244	76.73	0.8878
	-0.3	110.4	307.9	0.8069	3.338	65.68	0.9175
	-0.2	139.6	183.8	0.8016	3.234	50.52	0.9479
	-0.1	125.8	147.1	0.7911	3.111	38.54	0.9246
	0	90.84	138.0	0.7851	3.373	27.08	0.9508
	0.1	67.06	142.5	0.7765	2.766	33.91	0.9396
	0.2	57.69	193.5	0.7571	2.612	53.68	0.9058
	0.3	27.61	287.1	0.7503	2.289	89.85	0.8729
	0.4	19.96	341.7	0.7407	1.989	99.70	0.8685
	0.6	1.760	764.6	0.7168	1.265	91.49	0.8927
A600zr15	-0.4	29.28	526.4	0.7753	2.350	119.9	0.9110
	-0.3	54.21	454.1	0.8450	2.706	117.9	0.8529
	-0.2	88.67	341.9	0.8103	2.471	114.2	0.8436
	-0.1	136.0	200.0	0.7712	1.301	113.4	0.8518
	0	138.4	152.7	0.7581	0.9870	101.6	0.8429
	0.1	69.68	134.2	0.7628	0.9975	84.17	0.8388
	0.2	37.36	136.4	0.7624	1.044	83.07	0.8478
	0.3	36.96	160.4	0.7681	1.045	118.2	0.8180
	0.4	17.18	234.2	0.7413	0.8845	160.0	0.8447
	0.6	8.746	315.3	0.7398	1.011	157.8	0.8602
A600zr30	-0.4	15.64	473.7	0.7719	4.898	92.46	0.8946
	-0.3	43.22	447.6	0.8121	4.383	96.92	0.8420
	-0.2	78.36	301.7	0.8065	3.904	75.23	0.8590
	-0.1	145.0	201.5	0.8056	2.237	51.83	0.8875
	0	140.5	160.5	0.7886	2.010	41.33	0.8969
	0.1	99.26	141.6	0.7850	1.975	32.73	0.9139
	0.2	63.11	152.8	0.7771	2.072	35.49	0.9059
	0.3	44.16	208.7	0.7629	2.190	53.08	0.8716
	0.4	20.02	326.7	0.7482	2.233	78.18	0.8502
	0.6	12.57	431.6	0.7403	2.201	82.38	0.8658
A600ss120	-0.4	37.16	472.2	0.8008	3.259	111.7	0.9209
	-0.3	64.09	362.5	0.7938	2.796	108.1	0.9015
	-0.2	77.08	255.9	0.8059	2.482	96.74	0.9090
	-0.1	89.07	168.3	0.8019	1.901	80.06	0.9053
	0	119.2	135.4	0.7982	1.749	68.88	0.8711
	0.1	62.06	120.3	0.7987	2.017	53.36	0.8684
	0.2	26.50	128.8	0.7807	1.965	48.12	0.8900
	0.3	36.66	140.4	0.7651	1.808	61.73	0.9005
	0.4	26.50	212.7	0.7470	1.877	91.54	0.8851
	0.6	18.01	290.6	0.7354	2.080	98.56	0.8723

Changes in the outer and barrier oxide film resistances are plotted in Figure 6.7 for the four electrodes. Overall, the barrier layer resistance, Figure 6.7 (a), is nearly an order of magnitude greater than the outer layer resistance, Figure 6.7 (b).

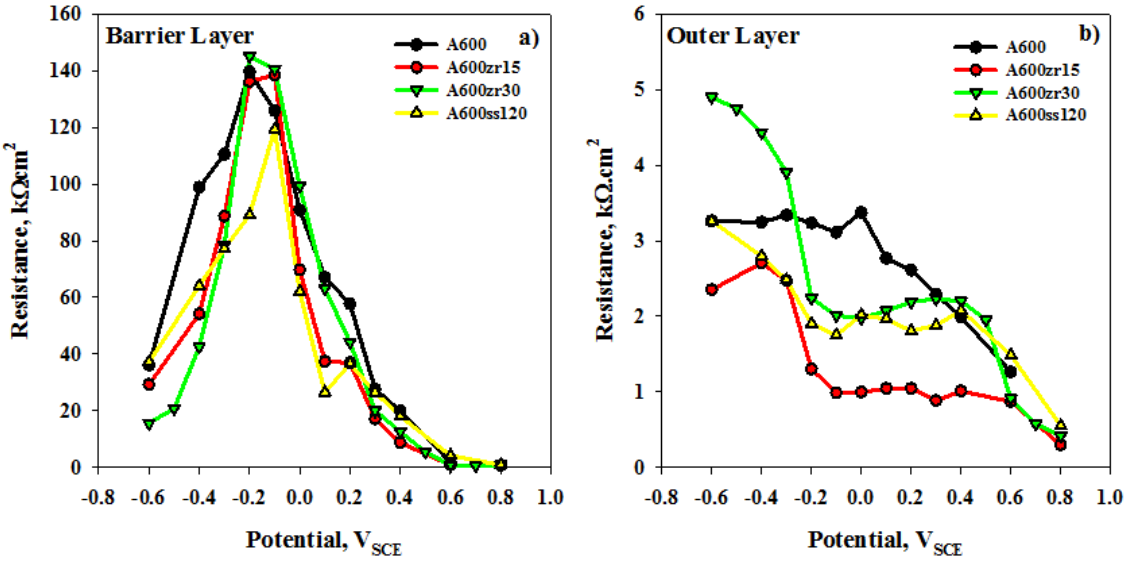

Figure 6.7 Changes in the (a) barrier and (b) outer layer film resistance as a function of applied potential for A600, A600zr15, A600zr30 and A600ss120.

The highest barrier layer resistance values for each electrode are recorded in region 2, at potentials prior to the anodic peak. This is expected since the passive oxide grows as the potential is increased into the passive potential range. In this region, the highest barrier layer resistance is observed for the untreated alloy, indicating that SMAT may impede formation of the passive film. Coinciding with the increase in current density associated with the anodic peak, Figure 6.2, the barrier layer resistance begins to decrease at potentials greater than ~ -0.1 V_{SCE}. The drop in resistance is slightly more rapid for the SMAT electrodes compared to the untreated A600. The resistance of the barrier layer on

the treated electrodes remains slightly lower compared to the untreated A600 at transpassive potentials (region 3).

Changes in the outer layer resistance show subtle differences between the untreated and the SMAT electrodes. In region 1, the differences in the outer layer resistances are small, with only that for the A600zr30 sample being noticeably higher than for the other electrodes. Within the anodic peak region (2) the outer layer resistance for the SMAT electrodes are all lower than that of the untreated alloy. This suggests that the film restructuring induced by the breakdown of the barrier layer in this region is adversely affected by the SMAT process. Within the tranpassive region, the resistance becomes effectively the same for the electrodes with that for A600zr15 being slightly lower.

6.3.4 Surface Analysis - AES

The oxide film thicknesses, calculated from AES depth profiles measured on potentiostatically grown oxide films, are shown in Figure 6.8. As previously discussed (chapter 3), the oxide thickness is calculated as the depth at which the O signal decreases to 50% of its maximum value in the depth profiles [40-43], although ion beam mixing makes the values only an estimate. In region 1 (at -0.4 V_{SCE}) the oxides on the two Zr treated alloys appear approximately twice as thick as that on the untreated and SS treated alloy. A possibility is that the oxides on these two alloys are more defective, allowing more rapid ion transport, leading to the growth of a thicker film. This would be consistent with the lower barrier layer resistances, Figure 6.7 (a), measured for these alloys.

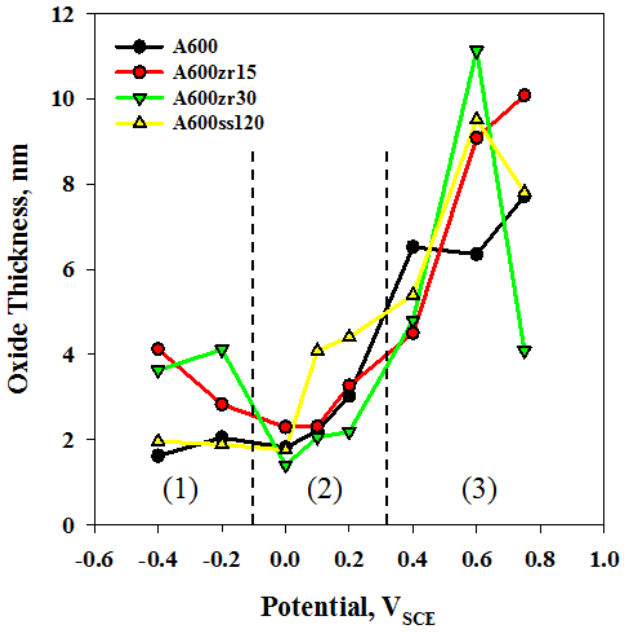

Figure 6.8 Oxide film thickness as a function of film growth potential for A600, A600zr15, A600zr30 and A600ss120 obtained from AES depth profiles.

The increased current during the anodic peak region leads to an apparent thinning of the passive film on the two Zr treated electrodes, but no observable change on the untreated and SS treated electrodes. This apparent loss of film thickness is likely due to the formation of a more porous and hence more readily sputtered film when the barrier layer is destroyed. This leads to a non-quantifiable increase in sputtering efficiency and an underestimate of the true film thickness. After the anodic peak, the film thickness on all four electrodes increases with potential into the transpassive region. This coincides with the decrease in barrier layer and outer layer resistances, Figure 6.7.

Changes in the Ni cation fractions as a function of oxide film depth, determined from AES measurements (as described in Chapter 5) are plotted for the range of film

growth potentials in Figure 6.9. The determination of cation fractions from depth profiles has been described in chapter 3. For all electrodes, the Ni content at the oxide surface is depleted with respect to the bulk alloy, the majority of the Ni being located in the inner regions of the oxide. In potential regions 1 and 2, the depletion of Ni at the solution/oxide interface is small.

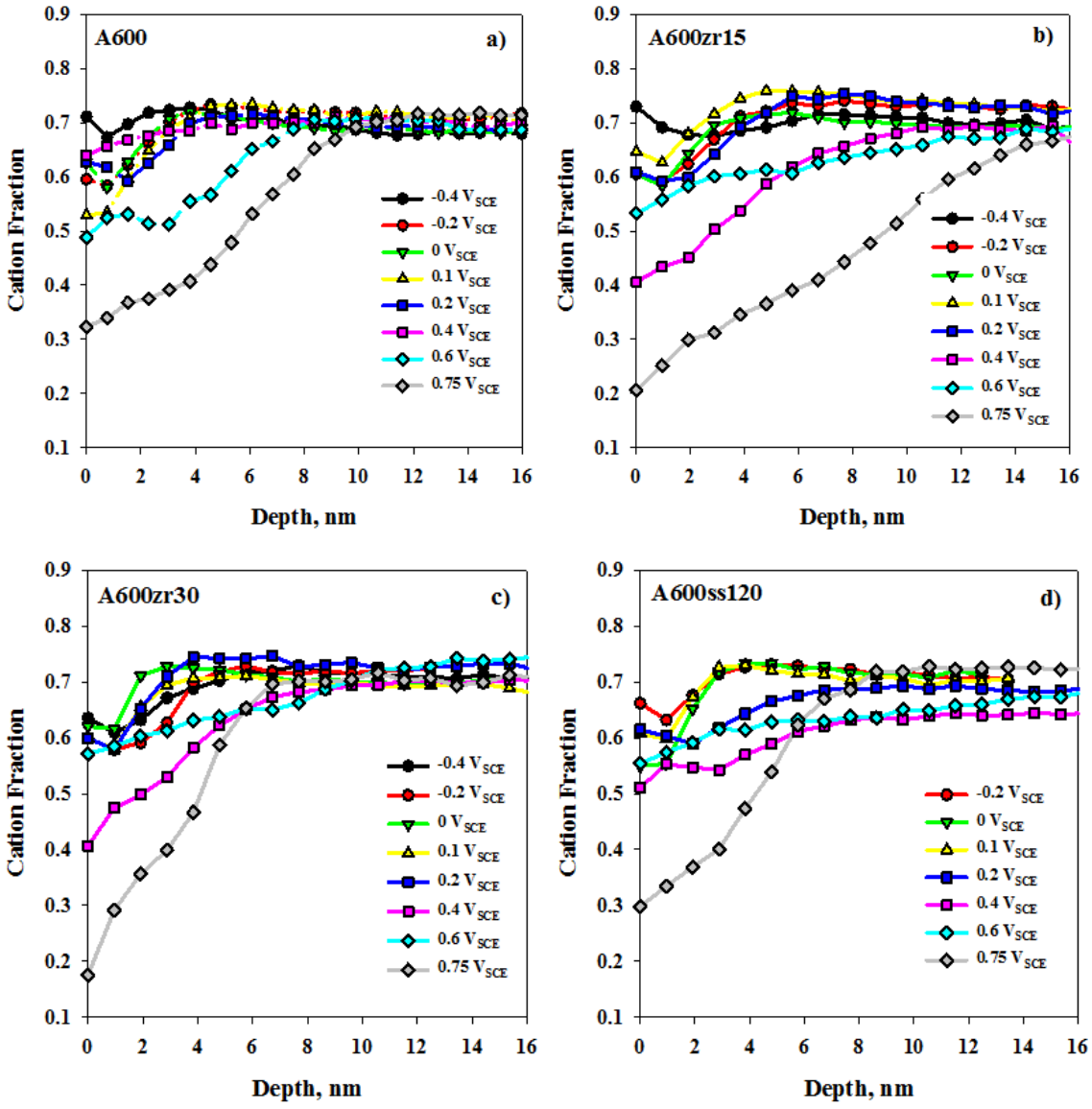

Figure 6.9 Ni cation fractions as a function of depth for (a) A600, (b) A600zr15, (c) A600zr30 and (d) A600ss120 for a range of film growth potentials.

This is consistent with the previously observed behaviour for this alloy, chapter 3, which showed little segregation of the noble Ni to the outer regions of the oxide due to passive film growth. A more substantial depletion in Ni is observed at transpassive potentials in region 3. As noted previously in chapter 5, the Alloy 600 profile at 0.4 V_{SCE}, Figure 6.9, does not fit into the sequence of profiles in region 3, the Ni cation fraction being higher than anticipated throughout the entire film. A similar phenomenon is observed on all the SMAT electrodes, but at 0.6 V_{SCE} rather than 0.4 V_{SCE}. This behaviour appears related to that of Ni metal as discussed previously in chapter 5.

The distribution of Fe throughout the oxide and in the alloy surface is shown for each electrode in Figure 6.10. In potential regions 1 and 2, the small amount of Fe present in the oxide is concentrated on the outer surface of the film. This is expected since Fe is readily oxidized at these potentials and its segregation to the surface to dissolve as Fe^{2+} and/or form magnetite is likely [44]. While the shape of the profiles with depth changes somewhat from electrode to electrode, the behaviour of Fe is effectively the same in these two regions for all the electrodes. At transpassive potentials in region 3, a significant rise in Fe content at the solution/oxide interface as the potential is increased is observed on all electrodes. As discussed in chapter 5 for both Alloy 600 and Alloy 800, the accumulation of Fe in the outer regions of the oxide can be attributed to the formation of insoluble Fe^{III} oxides at these positive potentials. The behaviour of the Fe profile at 0.4 V_{SCE} on A600, Figure 6.10 (a), is anomalous, with less Fe than expected being observed on the electrode surface. As observed for Ni, this anomalous behaviour occurs at a higher potential, 0.6 V_{SCE}, on the SMAT electrodes.

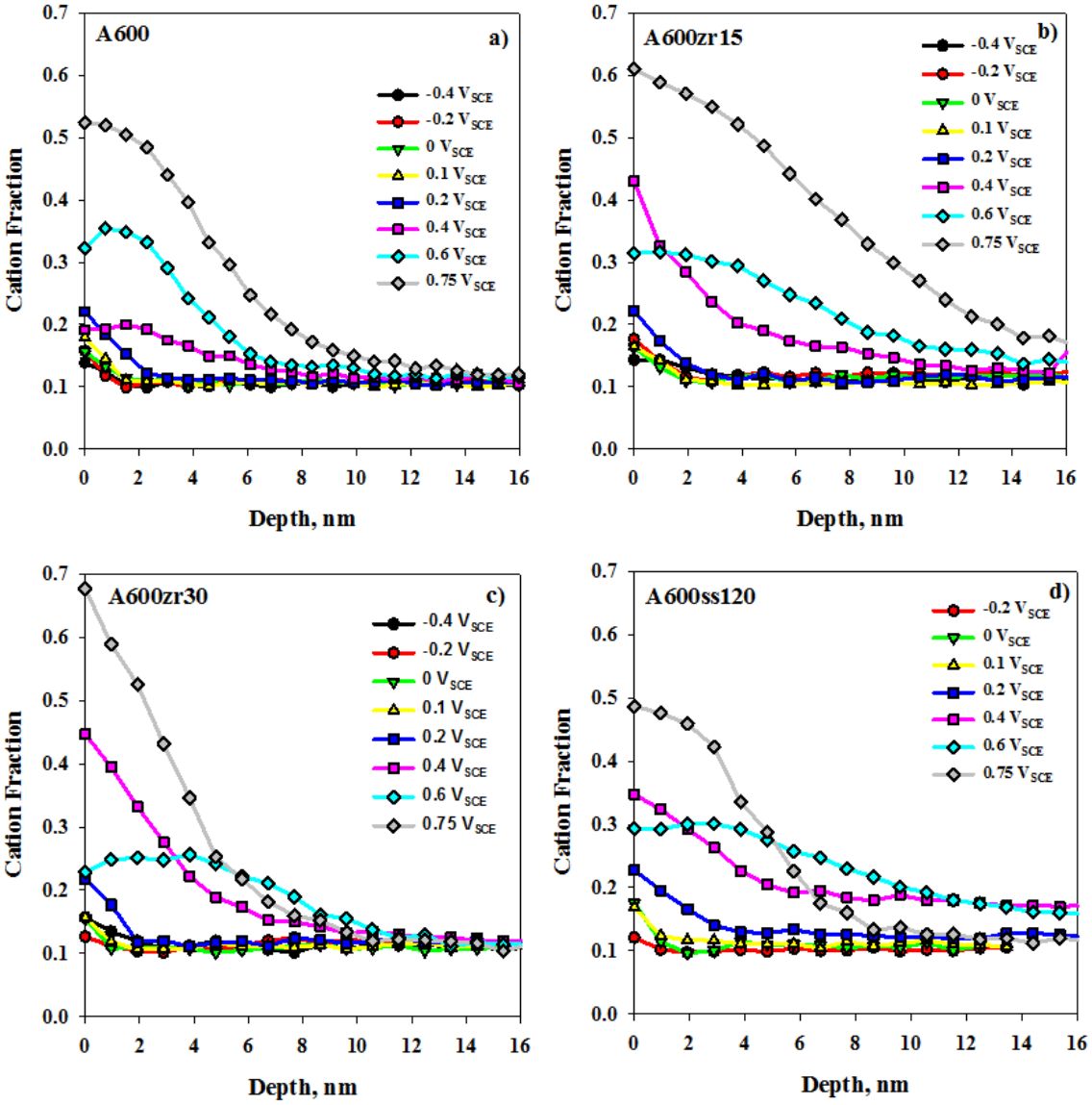

Figure 6.10 Fe cation fractions as a function of depth for (a) A600, (b) A600zr15, (c) A600zr30 and (d) A600ss120 for a range of film growth potentials.

Changes in the Cr fractions with depth and film growth potential are plotted in Figure 6.11. In regions 1 and 2, the majority of Cr is clearly localized in the barrier layer near the oxide/alloy interface. As expected, the observation is that the largest Cr

fractions were measured at potentials in the passive region (2); i.e., up to ~ 0 V_{SCE} when the barrier layer resistance achieves a maximum, Figure 6.7 (a).

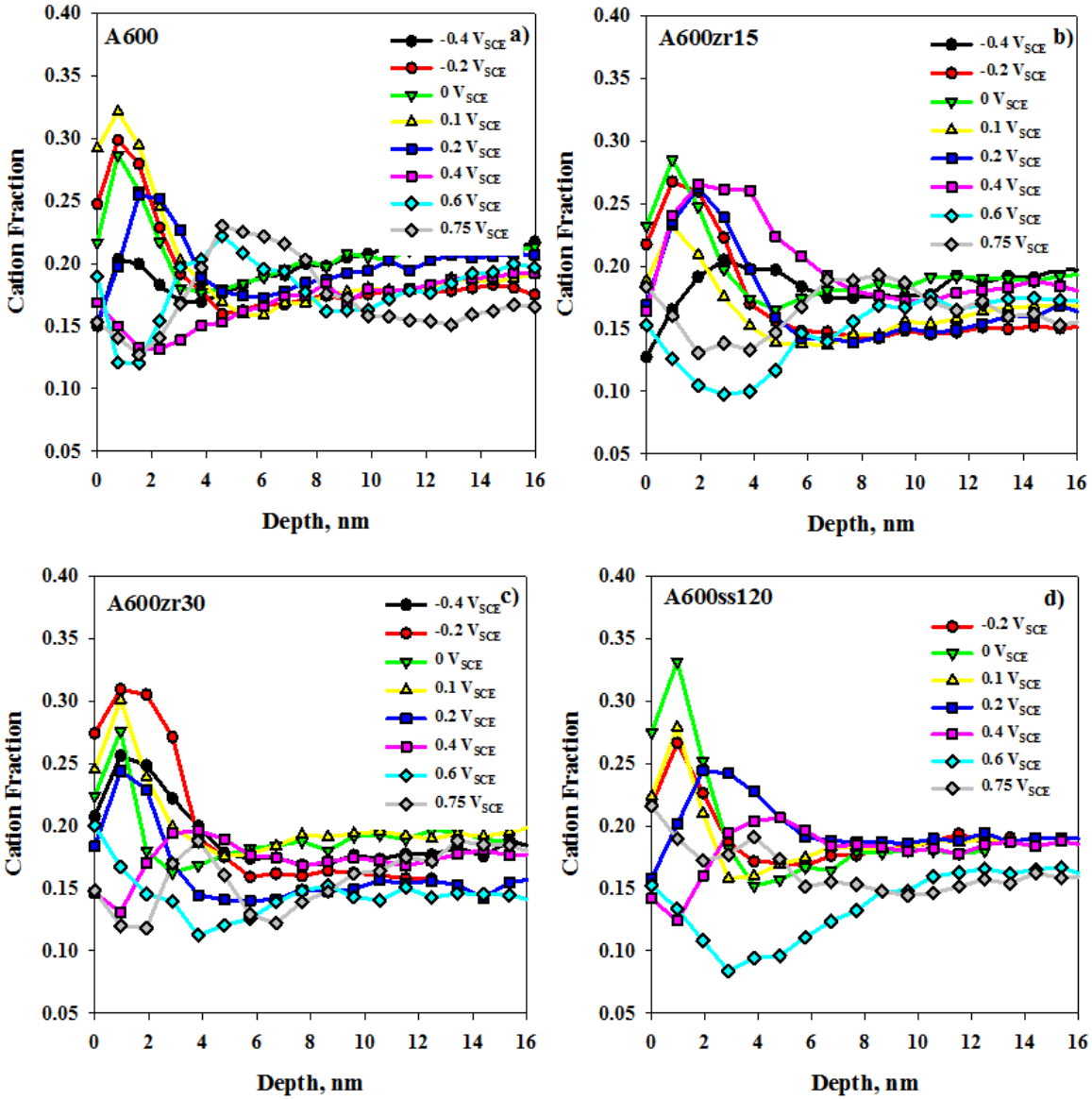

Figure 6.11 Cr cation fractions as a function of depth for (a) A600, (b) A600zr15, (c) A600zr30 and (d) A600ss120 for a range of film growth potentials.

Generally, there is no significant difference between the Cr content of the electrodes. At transpassive potentials in region 3, the Cr content in the inner regions of

the film decreases substantially as the barrier layer resistance decreases, Figure 6.7 (a). In the potential range 0.4 V_{SCE} to 0.6 V_{SCE}, the Cr depletion is inversely related to the Ni enrichment, the maximum depletion occurring at 0.6 V_{SCE} on the treated alloys compared to 0.4 V_{SCE} on A600. The degree of Cr depletion on A600zr15 and A600ss120 is particularly severe, the Cr cation fractions decreasing to below 0.10 compared to 0.13 for A600. In addition, the reappearance of Cr in the inner regions of the film at very positive potentials (0.6 V_{SCE} and 0.75 V_{SCE}) on A600 is not observed on the treated electrodes.

While the barrier layer resistance begins to decrease as soon as the potential enters the anodic peak potential region (i.e., $\geq$ -0.1 V_{SCE}) the Cr content of this layer is retained throughout the anodic peak region on all four electrodes, and does not become significantly depleted in the barrier layer until the potential region 0.2 V_{SCE} to 0.4 V_{SCE}; i.e., the onset of transpassivity. For the SMAT electrodes, this loss of Cr is delayed until the potential is in the range 0.4 V_{SCE} to 0.6 V_{SCE}. This loss of Cr appears to stimulate the release of Ni from the substrate alloy (at 0.4 V_{SCE} for A600 and 0.6 V_{SCE} for the treated electrodes).

This unexpectedly high release rate of Ni on destruction of the barrier layer is a consequence of the behaviour in the passive region, when Cr is more readily segregated into the oxide to form the Cr-enriched barrier layer. In the environment used (i.e., pH ~ 6.5) Ni is not readily segregated to the outer regions of the oxide film. Consequently, the formation of the Cr-enriched barrier layer will leave the surface of the alloy Cr-depleted and Ni-enriched. Once the barrier layer is subsequently destroyed at the beginning of the transpassive region, 0.2 V_{SCE} to 0.4 V_{SCE}, the exposed alloy acts more like Ni than a Ni-

Cr alloy, leading to the release of unexpected amounts of Ni, which is then detected as an enrichment of Ni in the oxide/hydroxide film.

The EIS measurements show that the barrier layer resistances of the untreated electrodes decrease more rapidly than that of the untreated electrodes. Despite this, the transpassive depletion of Cr is delayed to more positive potentials. This indicates that the loss of barrier layer resistance and the major depletion of Cr in the barrier layer are not straightforwardly related. The loss of barrier layer resistance is generally attributed to the injection of defects (cation vacancies) into the oxide. This appears to occur more readily on the treated electrodes than on the untreated electrode, suggesting the presence of more defect transport pathways in the oxides on these surfaces. There is some evidence to support this in the film thickness measurements obtained from AES depth profiles, which suggest that oxidation in the anodic peak region leads to a more porous oxide/hydroxide film.

Variations in the outer layer composition on the treated electrodes can be monitored through the changes in Ni and Fe contents at the solution/oxide interface as a function of film growth potential, Figure 6.12 (a) and (b). The Ni content in the outer layer is highest in regions 1 and 2, and decreases with increasing film growth potential, Figure 6.12 (a). Despite differences in content in the pre-passive region, the electrodes exhibit a similar content at low potentials in the passive region when the barrier layer is intact and most protective. After growth in the potential region of the anodic peak, the Ni and Fe contents of the film become erratic before decreasing (Ni) and increasing (Fe) substantially in the transpassive region 3.

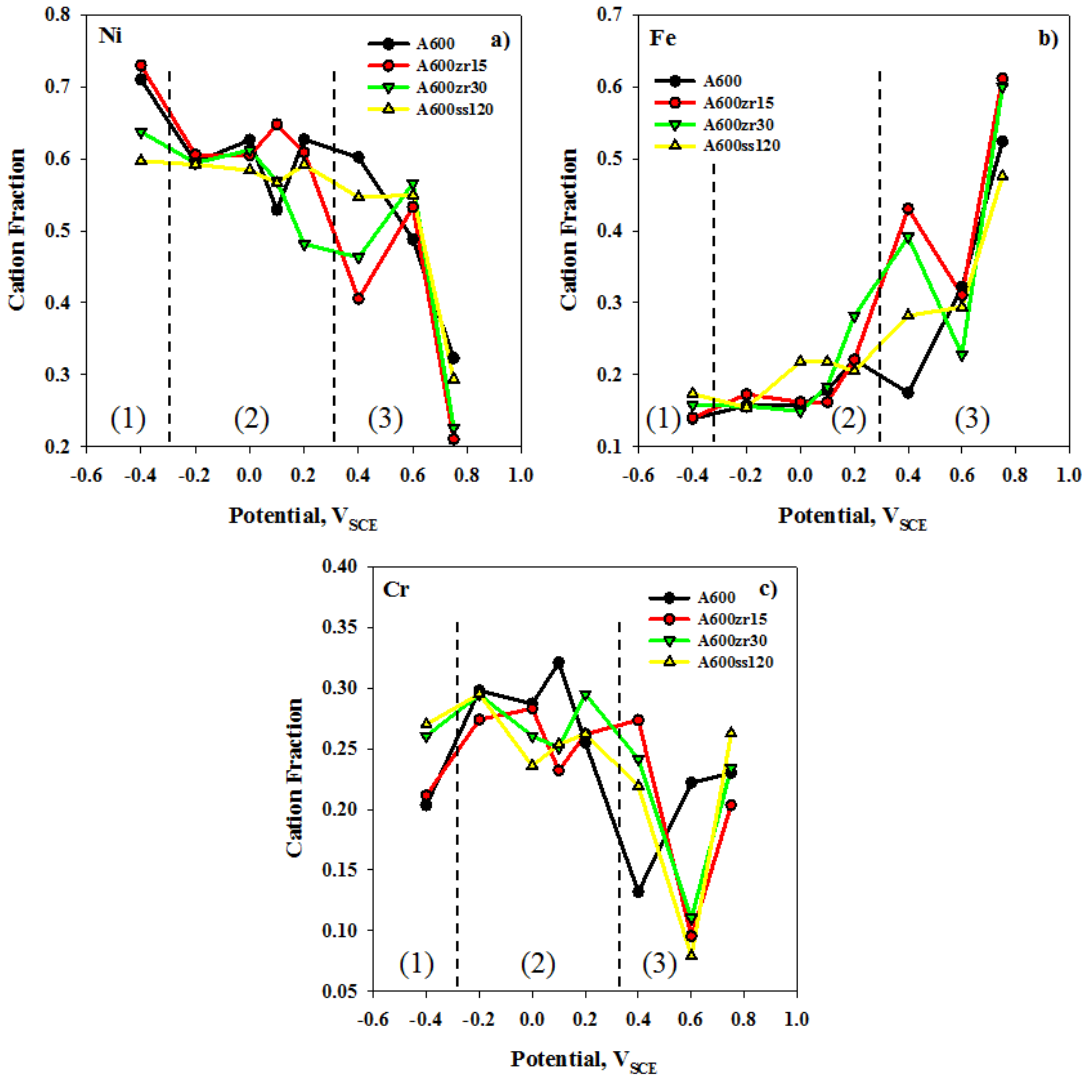

Figure 6.12 Cation fractions of (a) Ni, (b) Fe, and (c) Cr in the outer, (a) and (b), and barrier (c) layers as a function of applied potential.

The fraction of Fe at the outer oxide surface is shown, Figure 6.12 (b). Unlike Ni, the Fe content in the outer layer increases as a function of film growth potential, starting after the anodic peak potential. In regions 1 and 2, the Fe content is low for all electrodes and no significant changes with SMAT are observed. The A600ss120 electrode shows a slightly higher Fe content at potentials after the anodic peak. The changes in Fe content

become increasingly erratic in region 3, with a peak in Fe content at 0.4 V_{SCE} where Ni is correspondingly depleted, Figure 6.12 (a) on the SMAT samples

A loss of Ni and increase in Fe content of the outer layer requires enhanced transport of these metal cations through a defective barrier layer. Consequently, a low Ni content and high Fe content in the potential range, 0 V_{SCE} to 0.4 V_{SCE}, should be preceded by breakdown of the barrier layer. Thus, the low Ni/high Fe contents of the oxides on the treated electrodes in this potential range compared to that of the untreated alloy suggest barrier layer breakdown has more drastic consequences on the treated alloys. That this layer is more readily destroyed on these alloys is suggested by the barrier layer resistance measurements which show a more rapid decline with potential than on the untreated alloy.

Variations in the Cr barrier layer composition for each electrode as a function of film growth potential are shown in Figure 6.12 (c). As described in chapter 3, the values of cation fractions were obtained at the Cr peak maximum in the AES depth profiles and hence indicate the Cr content at the oxide/alloy interface; i.e., the location of the barrier layer. In region 1, the relatively low content for A600 and A600ss120 suggests that these electrodes may less readily form a Cr oxide barrier layer, but such a difficulty was not reflected in the barrier layer resistance measurements, Figure 6.7 (a). The relatively high Cr contents in region 2 are consistent with the presence of a passive film. The SMAT samples contained slightly less Cr overall in the passive region, consistent with the lower barrier layer resistance values, Figure 6.7 (a). The SMAT samples maintain a higher Cr content as the potential is increased into the transpassive region (3), although, again, this is not reflected in a higher barrier layer resistance, Figure 6.7 (a). The apparent film

breakdown at 0.4 V_{SCE} observed on A600 occurs at 0.6 V_{SCE} on the SMAT electrodes. On the SMAT electrodes in the potential region following the anodic peak, the retention of Cr in the inner regions of the film may be a consequence of the loss of Ni and the segregation of Fe to the outer regions of the film. However, the film resistances from EIS measurements do not show that this is reflected in any improved performance of either the barrier layer or the outer layer. While the release of Fe to form an Fe^{III} oxide at the outer surface may be indicated by these analyses, the overall Fe content is too small for this to influence the overall film resistance significantly.

6.3.5 Surface Analysis - XPS

Ni, Fe and Cr signals detected on the surface in XPS survey scans were converted into cation fractions and plotted as a function of applied potential, Figure 6.13. The fractions display similar behaviour to that observed in the AES measurements, Figure 6.12. Some differences in values are noted, especially in region 3, but this can likely be attributed to the different depths of analyses. AES profiles are representative of only the surface of the film, while XPS analyses sample depths up to 6 nm, and can include a contribution from the base alloy. Comparison of the profiles shows that the overall Fe, Ni and Cr contents of the oxides are similar in regions 1 and 2 but vary substantially in region 3. The untreated and lightly treated A600zr15 electrodes exhibit lower Ni/higher Fe contents in the passive region. Counter intuitively this is also combined with an increase in relative Cr content.

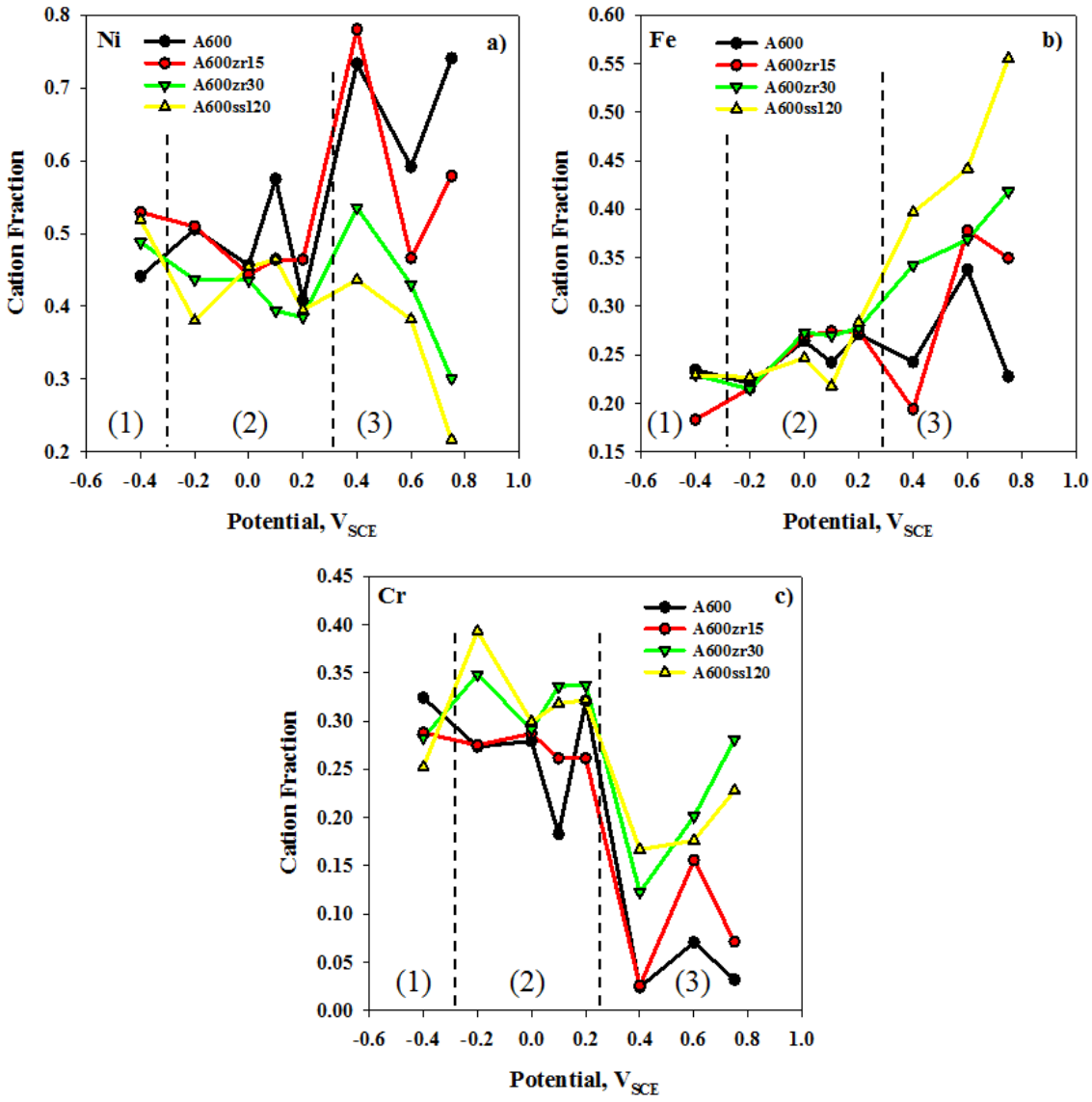

Figure 6.13 Cation fractions of the (a) Ni, (b) Fe and (c) Cr oxide film components determined from XPS survey scans.

Examples of fitted high resolution XPS spectra recorded on the A600zr30 electrode are shown in Figure 6.14 for the (a) Cr $2p_{3/2}$, (b) Ni $2p_{3/2}$ and (c) O 1s peaks. With the exception of Cr, all spectra were charge corrected by fixing the main signal of the C 1s peak at a binding energy (BE) of 285.0 eV.

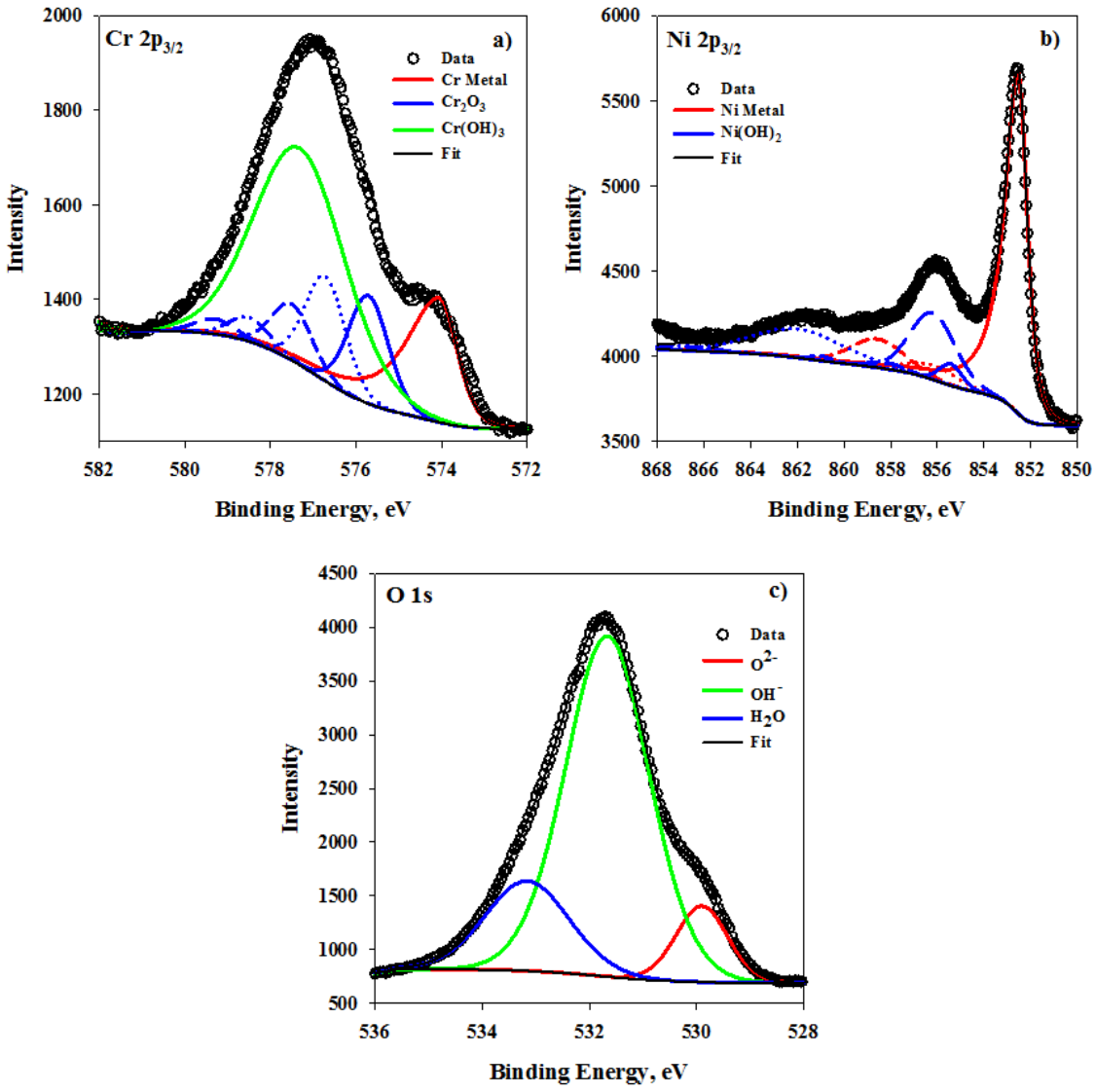

Figure 6.14 A600zr30 high resolution XPS spectra for the (a) Cr $2p_{3/2}$, (b) Ni $2p_{3/2}$ and (c) O 1s peaks recorded on an electrode potentiostatically treated at -0.2 V_{SCE}.

Table 6.3 lists the BE's extracted from the fitted spectra for all the electrodes. Details regarding the fitting of the spectra can be found in chapter 3.

Table 6.3 Measured BE's for the various chemical states of O, Cr and Ni in oxide films formed potentiostatically on A600, A600zr15, A600zr30 and A600ss120.

Alloy	E (V_{SCE})	O^{2-} (eV)	OH^- (eV)	Cr (0) (eV)	Cr_2O_3 (eV)	$Cr(OH)_3$ (eV)	Ni (0) (eV)	$Ni(OH)_2$ (eV)
A600	-0.4	529.9	531.6	574.1	575.6	577.3	852.6	855.5
	-0.2	529.8	531.5	574.1	575.6	577.3	852.5	855.4
	0	530.0	531.6	574.1	575.9	577.2	852.6	855.4
	0.1	529.9	531.5	574.1	575.9	577.3	852.5	855.4
	0.2	529.8	531.5	574.1	575.8	577.2	852.5	855.4
	0.4	530.1	531.7	574.1	575.9	577.8	852.5	855.5
	0.6	529.6	531.5	574.1	575.8	577.5	852.5	855.4
	0.75	530.0	531.7	574.1	575.9	577.9	852.7	855.7
A600zr15	-0.4	529.7	531.5	574.0	575.7	577.3	852.4	855.4
	-0.2	529.8	531.4	573.9	575.7	577.3	852.4	855.3
	0	529.9	531.5	573.9	575.7	577.3	852.4	855.3
	0.1	529.9	531.5	573.9	575.9	577.4	852.4	855.3
	0.2	529.9	531.5	574.0	576.1	577.7	852.4	855.1
	0.4	529.2	531.4	575.0	576.4	578.0	852.4	855.3
	0.6	530.2	531.7	574.0	575.7	577.3	852.8	855.5
	0.75	530.3	531.9	574.2	576.3	577.9	852.8	856.0
A600zr30	-0.4	529.9	531.6	574.0	575.7	577.3	852.5	855.4
	-0.2	529.9	531.7	574.0	575.7	577.3	852.5	855.4
	0	530.1	531.7	574.0	575.7	577.3	852.5	855.2
	0.1	530.1	531.7	574.0	575.9	577.5	852.6	855.5
	0.2	529.9	531.4	574.1	576.0	577.6	852.4	855.2
	0.4	530.2	531.8	574.1	576.1	577.7	852.4	855.8
	0.6	530.0	531.6	N/A	575.9	577.5	852.6	855.2
	0.75	530.3	531.9	N/A	575.9	577.4	852.7	855.7
A600ss120	-0.4	529.8	531.5	574.0	575.7	577.3	852.4	855.5
	-0.2	530.2	531.8	574.0	575.7	577.3	852.7	855.6
	0	530.1	531.3	574.0	575.7	577.4	852.7	855.6
	0.1	530.2	531.8	574.0	575.9	577.5	852.7	855.6
	0.2	530.2	531.8	574.0	575.9	577.5	852.7	855.5
	0.4	530.2	531.8	574.0	576.0	577.6	852.7	855.6
	0.6	530.2	531.7	574.0	575.9	577.5	852.8	855.5
	0.75	530.2	531.9	N/A	576.5	578.1	852.7	855.8

Changes in the Ni and Cr metal signals are plotted in Figure 6.15. The oxide film thickness can be estimated based on the relative intensities of the metal and oxide signals.

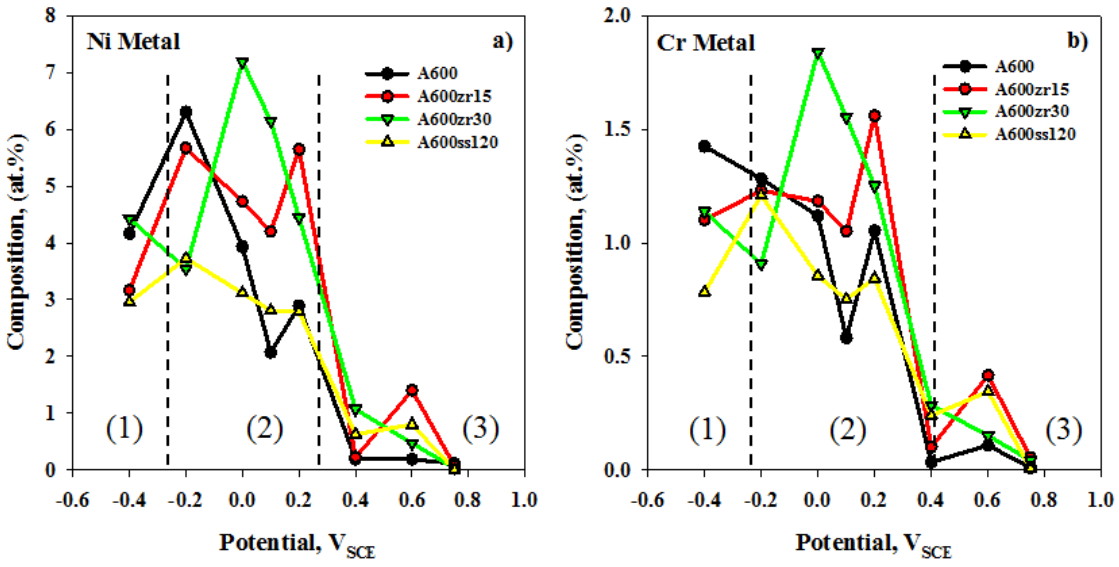

Figure 6.15 Changes in the composition (at. %) of (a) Ni and (b) Cr metal detected on the A600, A600zr15, A600zr30 and A600ss120 electrodes.

The inelastic mean free path, (λ), is defined as the average distance that an electron with a given energy can travel between successive inelastic collisions, and can be used to calculate oxide film thickness. Equation 6.1, shows that the film thickness, *t*, can be

$$t = \lambda \cos\phi \ln[1 + \frac{\frac{I_O}{S_O}}{\frac{I_S}{S_S}}] \qquad (6.1)$$

calculated from the inelastic mean free path of the oxide, λ, the sensitivity factors of the substrate, S_s, and the oxide, S_o, and the peak intensities of the substrate, I_s, and the oxide, I_o [45]. This equation typically requires a flat, uniform layer on a substrate to obtain an accurate measurement. Since the oxide films on the sample surfaces were neither flat nor uniform in composition, equation 6.1 was simplified to give relative changes in film thickness, estimated by using the metal and oxide peak intensities,

$$t = \frac{I_O}{I_S} \tag{6.2}$$

Equation 6.2 shows that the intensity of the metal signal, I_s, is inversely proportional to film thickness, t. Detection of the metal signal in the Ni $2p_{3/2}$ and Cr $2p_{3/2}$ spectra suggests that the oxide film thickness is less than or equal to the inelastic mean free path of the film components. The maximum distance these electrons can travel before undergoing inelastic collisions is 3λ, a depth of approximately 6 nm for a Ni or Cr oxide containing film [42]. As observed in the AES depth profiles, Figure 6.8, both the Ni and Cr metal plots in Figure 6.15 show an increase in film thickness with increasing potential. In agreement with the results in Figure 6.8, in region 1 and the initial stages of region 2, the oxide films on the treated electrodes appear to be thicker than that on A600. At the anodic peak potential, the metal signal in both Figure 6.15 (a) and (b) is stronger on the treated electrodes. This observation, along with the AES and impedance analysis suggests that the treated electrodes are more prone to film breakdown between 0 V_{SCE} and 0.2 V_{SCE}. The loss of the metal signal in region 3 reflects the rapid increase in film thickness in the transpassive region.

Figure 6.16 shows a comparison between the changes in (a) the $Ni(OH)_2$ components detected in the high resolution scans, and (b) these changes normalized against the total Ni content detected in the survey scans. Overall, except in region 1, each electrode experienced an increase in $Ni(OH)_2$ content as the film growth potential increased.

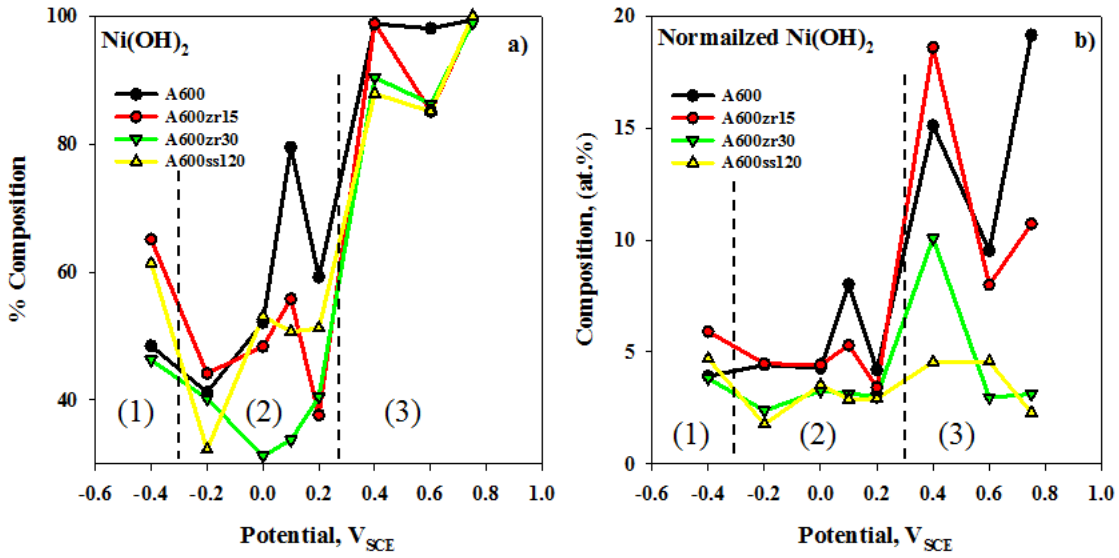

Figure 6.16 Variation in $Ni(OH)_2$ content of the oxide films, determined from high resolution XPS spectra, as a function of applied potentials: (a) relative amounts determined by de-convolution of the Ni $2p_{3/2}$ peak; (b) normalized against the total Ni content determined from XPS survey scans.

The SMAT samples contain less $Ni(OH)_2$ at passive potentials in region 2, particularly near the anodic peak. In region 3, the $Ni(OH)_2$ content of the samples continues to rise, and is not particularly dependent on electrode treatment. Considering that the AES measurements indicate a decrease in Ni content at the solution/oxide interface in region 3, Figure 6.12 (a), these XPS results suggest that a significant portion of the Ni may be buried beneath the solution/oxide interface. The $Ni(OH)_2$ content on the two most aggressively treated electrodes (A600zr30 and A600ss120) is also lower than that on A600 in region 3.

Figure 6.17 (a) shows the percentage content of Cr_2O_3 obtained by de-convolution of the Cr $2p_{3/2}$ peak. Figure 6.17 (b) shows these values normalized against the total Cr content detected in survey scans.

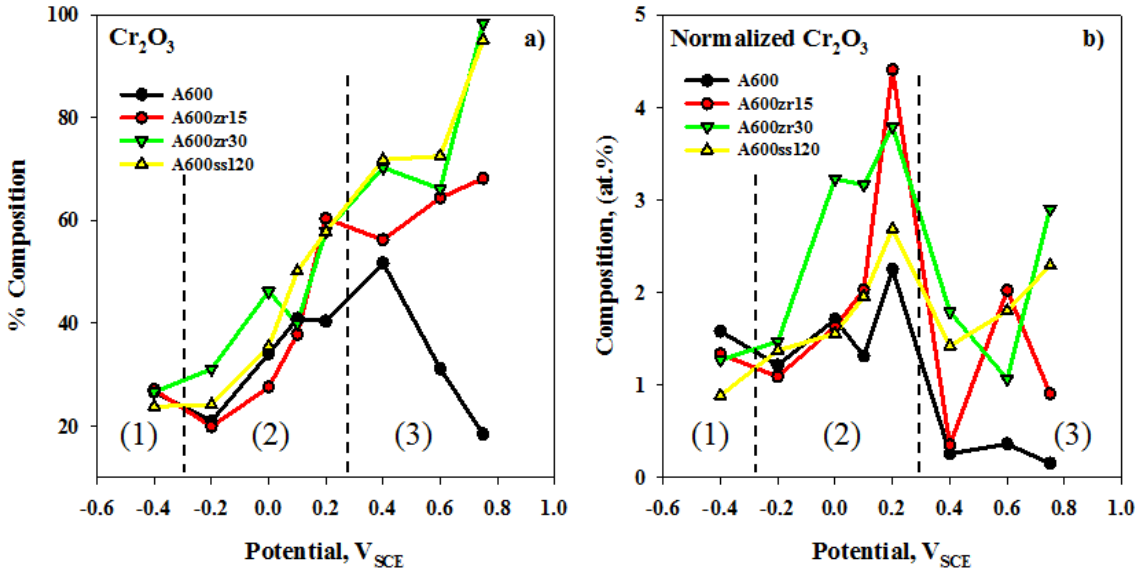

Figure 6.17 Variation in the Cr_2O_3 content of the oxide film as a function of applied potential: (a) relative amounts of Cr species determined by de-convolution of the Cr $2p_{3/2}$ peak; (b) normalized against the total Cr content determined from the survey scan.

The increase in Cr_2O_3 content in regions 1 and 2, prior to the anodic peak, confirms the formation of a barrier layer oxide, as indicated by the increase in barrier layer resistance, Figure 6.7 (a). Despite the film disruption caused by the anodic behaviour in the potential range of the peak in the polarization curve, the Cr_2O_3 content of the films continues to increase, particularly on the treated electrodes. This is not accompanied by increases in barrier layer resistance, Figure 6.7, which decrease over this potential range. In the transpassive region 3, the treated electrodes retain a significant Cr_2O_3 content while that of A600 becomes effectively negligible. While the film thickness increases in region 3, Figure 6.8, it is not thick enough to prevent detection of Cr_2O_3 if it were present under a thick outer layer.

Generally, Cr_2O_3 would be expected to be protective when present in a thin oxide film. However, its presence on surfaces with a low barrier layer resistance indicates it is not always present as a coherent protective layer on the metal surface. One possibility is that the Cr_2O_3 is only present on specific areas of the surface and does not act as a uniform coherent and protective layer. Its persistence on the treated electrode surfaces suggests that Ni/Fe transport may be occurring through a partially degraded barrier layer, possibly along open oxide grain boundaries adjacent to protected grains in the surface.

Changes in the $Cr(OH)_3$ content, Figure 6.18, shows that A600 retains a significantly larger amount of $Cr(OH)_3$ than the treated electrodes, especially in region 3.

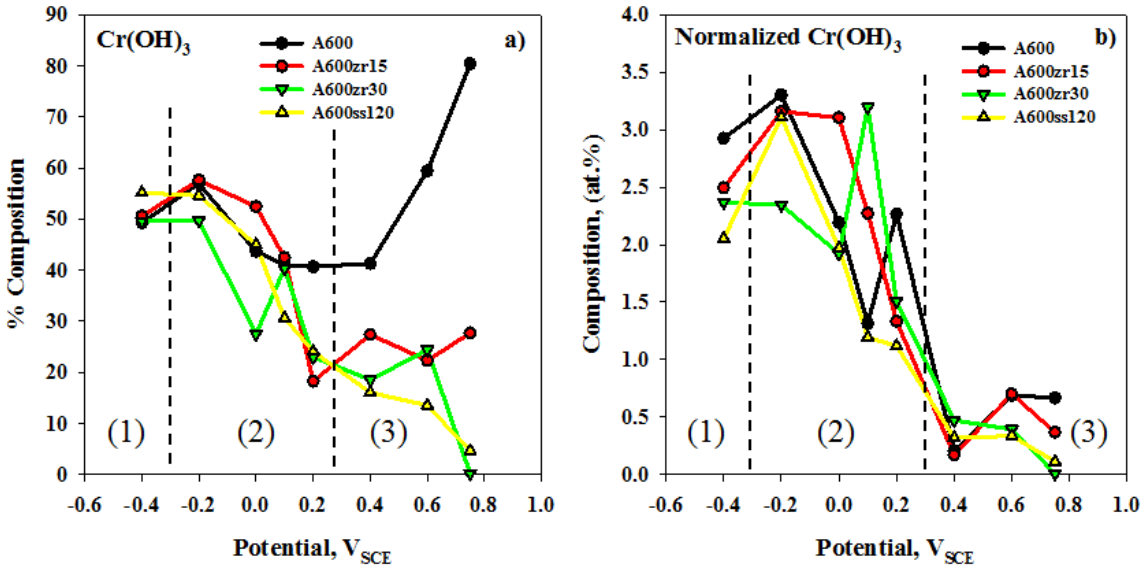

Figure 6.18 Variation in the $Cr(OH)_3$ content of the oxide films as a function of applied potential: (a) relative amounts of Cr species determined by de-convolution of the Cr $2p_{3/2}$ peak; (b) normalized against the total Cr content determined from the survey scan.

When normalized against the total Cr content, all the samples show a steady drop in the $Cr(OH)_3$ component through the entire passive region (2) and into the transpassive region (3).

A comparison was made between the M-OH and M-O components of the films, Figure 6.19. The similarities between Figure 6.19 (a) and Figure 6.13 (a) suggests that the majority of the M-OH component is present as $Ni(OH)_2$.

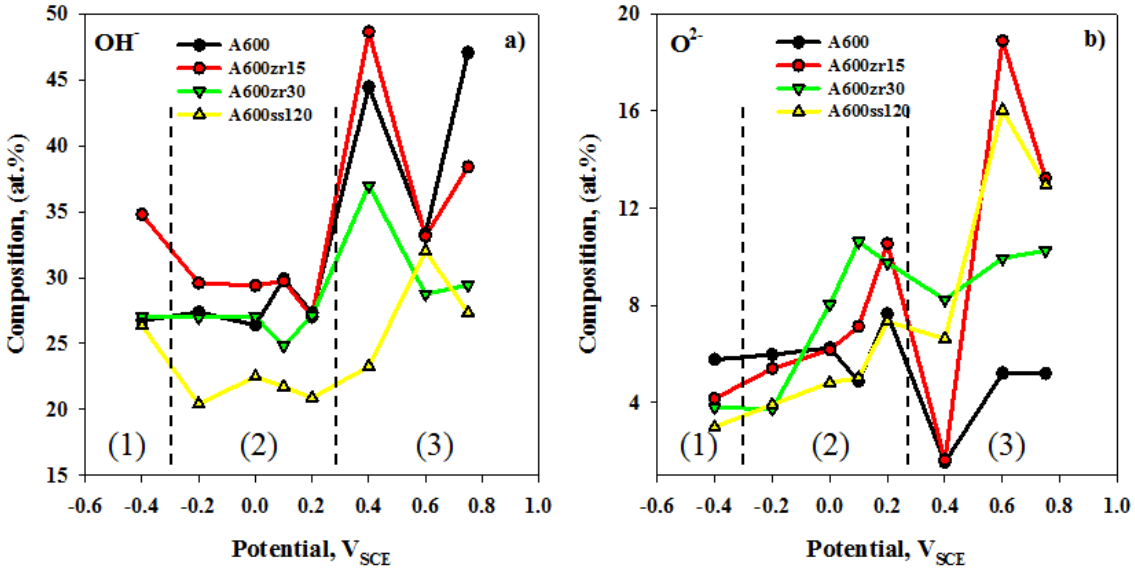

Figure 6.19 Changes in the (a) M-OH and (b) M-O compositions as a function of applied potential for A600, A600zr15, A600zr30 and A600ss120.

Both Cr_2O_3 and Fe oxides contribute to the M-O signal plotted in Figure 6.19 (b). The majority of the signal in regions 1 and 2 is from Cr_2O_3. In region 3, the increase is due to the build-up of Fe oxides, consistent with the behaviour shown in Figure 6.12 and Figure 6.13 (b).

6.3.6 Sulphur

Incorporation of S into the oxide film has been discussed previously in chapters 3 through 5 and is shown to occur in Figure 6.20, where the S component of the AES depth profiles is plotted as a function of depth for the various film growth potentials.

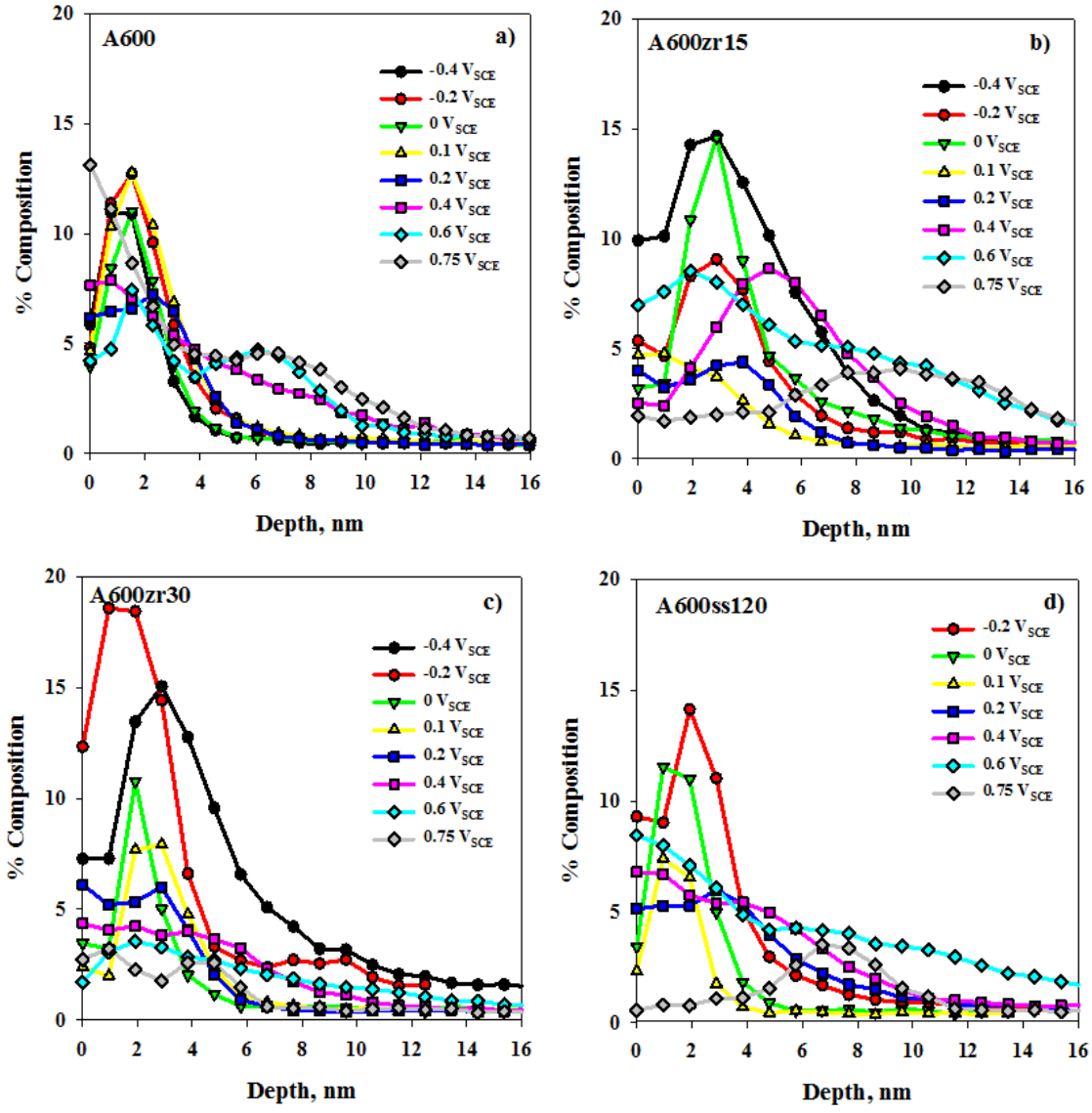

Figure 6.20 AES depth profiles for S as a function of applied potential for a) A600, b) A600zr15, c) A600zr30 and d) A600ss120.

At potentials in region 1 and the low potential stages of region 2, the S is located at the oxide/alloy interface, suggesting it is associated with the barrier layer. As the barrier layer is destroyed in the anodic peak potential region, the S content of the outer layer increases, but the majority is still retained close to the oxide/alloy interface. A concentration of S at this interface persists as the potential increases into the transpassive region 3. There is, however, an enhanced concentration in the outer surface layer relative to the peak near the oxide/alloy in region 3 consistent with the oxidative loss of S from the inner regions of the film under transpassive conditions.

For the SMAT electrodes, the depth profiles in Figure 6.20 show a similar tendency of S to be associated with the inner barrier layer in region 1 and the low potential range in region 2. However, as the potential progresses through the anodic peak potential region and into the transpassive region, S is not as readily retained at the oxide/alloy interface. It becomes more evenly distributed through the film, and very significantly depleted in the outer layers. This would suggest a much greater mobility of oxidized S through the oxide and its depletion rather than retention in the outer oxide.

This enhanced mobility of S in the oxide/hydroxide films on the treated alloys, once degradation of the barrier layer is induced in the anodic peak region, is consistent with the observations (above) that Ni loss from the film and Fe accumulation as oxide at the film/solution interface occurs more readily on these electrodes. This supports the claim that the barrier layer is more defective on the treated than on the untreated alloy.

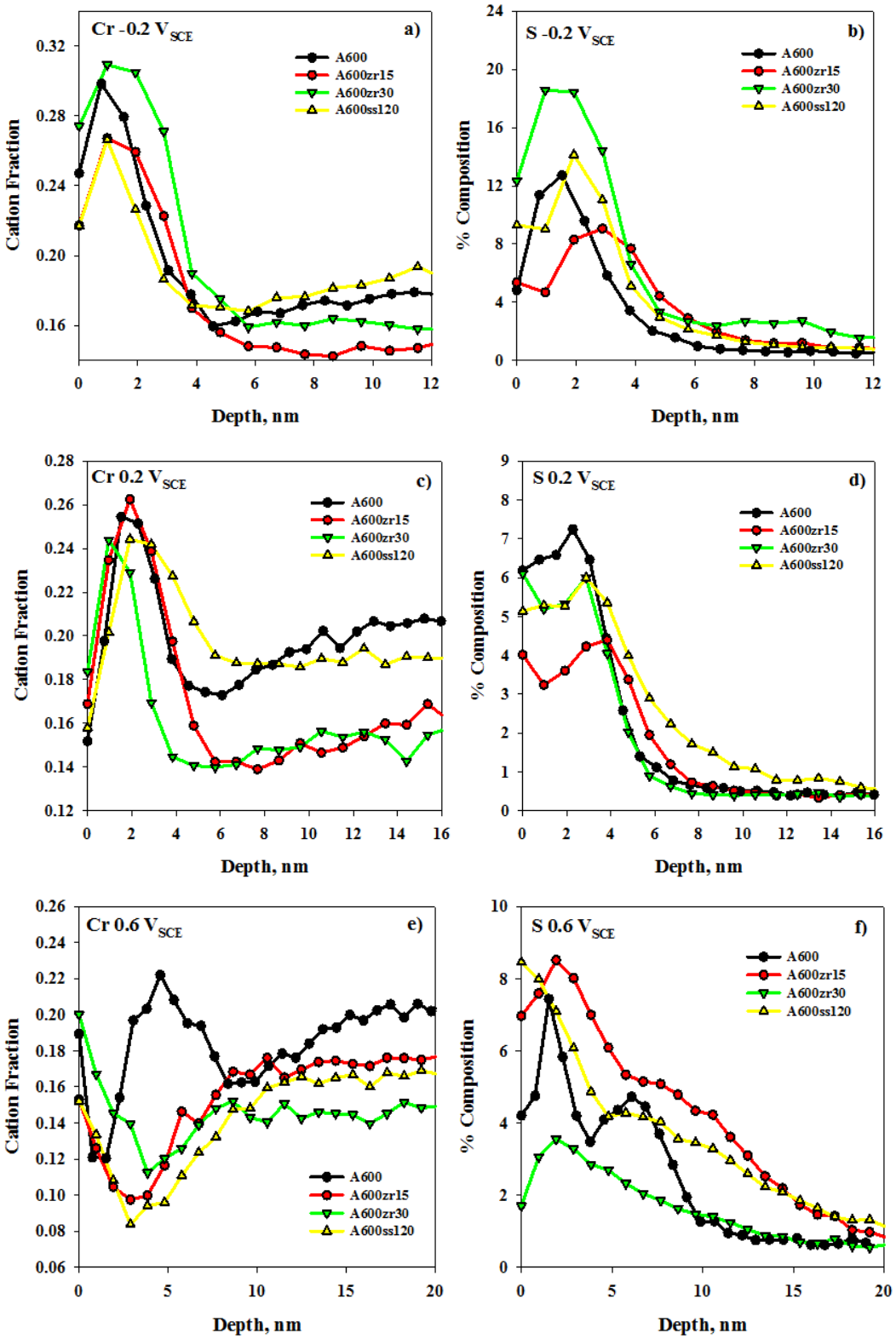

Figure 6.21 Plots comparing the Cr cation fractions to the % composition of S as a function of depth at various potentials for the four electrodes: (a) and (b) -0.2 V_{SCE}; (c) and (d) 0.2 V_{SCE}; (e) and (f) 0.6 V_{SCE}

In Chapter 5, it was shown that a correlation existed between the S and Cr contents in the film. Figure 6.21 compares the Cr and S AES depth profiles at three applied potentials, -0.2 V_{SCE}, 0.2 V_{SCE} and 0.6 V_{SCE}. At potentials negative to the anodic peak (-0.2 V_{SCE}) in region 2, the S is predominantly localized in the Cr barrier layer, Figure 6.21 (a). In the anodic peak potential range (0.2 V_{SCE}), most of the S still remains within the Cr barrier layer, but a significant amount is now located in the outer layer of the oxide. The increase in current density between 0 V_{SCE} and 0.2 V_{SCE}, Figure 6.2, along with the decrease in film thickness, Figure 6.8, indicates that the oxide undergoes breakdown, yielding a more porous film in this narrow potential region. It seems likely this film breakdown leads to the increased S mobility from the oxide/alloy interface to the solution/oxide interface. Figure 6.21 (e) and (f) show the Cr and S profiles in the transpassive region (3), at a potential where the Cr barrier layer is broken down on the SMAT electrodes. In the absence of the barrier layer, the mobility of S in the film is enhanced and the S content becomes more evenly distributed throughout the film, with the profiles being generally the same for all the electrodes.

6.4 Discussion

In previous work [36, 46-55] SMAT has been shown to produce a nanocrystalline layer on a number of materials. However, the SEM imaging in this study did not show any alterations to the grain size at the surface. The treatment parameters used on these samples may not have been severe enough to induce grain refinement through nanocrystallization.

The results from this study demonstrate that the composition of the oxide films of the SMAT samples differ from that on the untreated A600. The structure of the oxide films formed on A600 and the SMAT samples may be determined by ion mobility, with faster diffusing elements like Fe and Ni being transported to the outer layer, and slower diffusing elements, such as Cr, being retained in the barrier layer [56]**.** The diffusion rate through these nanostructured layers has been found to be greatly enhanced compared to that through oxides on lattice grains [21, 46, 49, 57-59]. The severe plastic deformation at high strain rates, which occurs during SMAT, can lead to the formation of a high density of dislocations which can act as precursors for new grain boundaries, leading to the sub-division of coarse grains. It has been found that the grain boundary diffusivity of a nanocrystalline material exceeds that of its coarse-grained counterpart by orders of magnitude [46, 57, 60], and publications have demonstrated the enhanced diffusion of Cr along the nanocrsytalline boundaries formed by SMAT [21, 61]. This enhanced diffusion along interfaces compared to through a lattice can be attributed to the high density of crystalline defects [46]. Results from this study showed an increase in both Cr and Fe in the barrier and outer layers on the SMAT samples. Due to the thermodynamic stability of Fe^{III} oxides in this particular environment, an increase in Fe was only observed in region 3. The data analysis in previous chapters indicated that retention of Cr in the barrier layer, especially at higher potentials, was dependant on the presence of Fe oxides in the outer layer. The SMAT samples were found to have a greater concentration of Cr in the barrier layer with respect to A600. Another change in the oxide film composition resulting from SMAT was a drop in the concentration of Ni hydroxides found in the outer layer. A reduction in $Ni(OH)_2$, combined with an increase in the Fe oxide content could

effectively decrease the porosity of the oxide film, helping to retain more Cr in the barrier layer.

Changes in the electrochemical behaviour of the SMAT samples were accompanied by alterations to the oxide film composition. Despite the formation of an oxide film containing an apparently more robust barrier layer in regions 2 and 3, and a less porous outer layer in region 3, the overall film resistance measured on the SMAT samples was consistently lower than that on A600. The resistance of the barrier layer actually decreased through the passive region (2) as its Cr_2O_3 content appeared to increase. While SMAT is a technique that is typically used to enhance the properties of a material, the result of this treatment appears to be detrimental to the passivity. The effect of SMAT on the corrosion behaviour can be highly dependent on the nature of the sample.

6.5 Conclusions

Both untreated and treated electrodes develop a Cr^{III} enriched barrier layer over the potential range, -0.6 V_{SCE} to -0.1 V_{SCE}, as indicated by an increase in the resistance of the barrier layer oxide accompanied by an increase in Cr_2O_3 content of the thin film, 2 to 4 nm. As observed previously (Chapters 3 and 5) on the untreated alloy, the outer region of the passive film is slightly depleted in Ni and enriched in Fe, irrespective of whether the alloy is treated or not. This can be attributed to the lack of segregation of Ni at these potentials, -0.6 V_{SCE} to -0.1 V_{SCE}. By contrast, Fe, which is more readily oxidized than Ni, is readily segregated to the outer layer, although only in small amounts. At potentials in and greater than the anodic peak (-0.1 V_{SCE} to 0.2 V_{SCE}), the films on both the

untreated and treated electrodes experience a breakdown of the barrier layer. This appears to occur more readily on the treated electrodes than on the untreated electrode. This leads to a significant segregation of both Ni and Fe to the outer regions of the film, with Ni present primarily as $Ni(OH)_2$ and Fe as an unidentified Fe^{III} oxide. Despite this segregation process being more marked on the treated electrodes, indicating a more extensive breakdown of the barrier layer, these electrodes retain a higher Cr_2O_3 content into the transpassive region. This suggests passivity may be retained at some locations but lost at others on the treated electrodes. This claim is supported by the behaviour of S on the electrode surfaces. Present in the reduced form in the passive region, it is more readily transported to the outer regions of the films on the treated electrodes once the barrier layer is degraded. This would be consistent with the claim the barrier layer is locally but not uniformly affected by SMAT.

References

[1] Newsletter on Three Mile Island Unit 1, Nuclear News, 25 (1982) 47
[2] R.C. Scarberry, S.C. Pearman, J.R. Crum, Corros., 32 (1976) 401-406
[3] R. Bandy, R. Roberge, R.C. Newman, Corros., Sci., 23 (1983) 995-1006
[4] R. Bandy, R. Roberge, R.C. Newman, Corros., 39 (1983) 391-398
[5] R. Bandy, D. Van Rooyen, Corros., 40 (1984) 281-289
[6] H. Coriou, L. Grall, C. Mahieu, M. Pelas, Corros., 22 (1966) 280-290
[7] H.R. Copson, G. Economy, Corros., 24 (1968) 55-65
[8] H.R. Copson, S.W. Dean, Corros., 21 (1965) 1-8
[9] D.-J. Kim, H.-P. Kim, S.-S. Hwang, J.-S. Kim, J. Park, Met. Mater. Int., 16 (2010) 259-266
[10] J.R. Cels, Corros., 34 (1978) 198-209
[11] M.-C. Tsai, W.-T. Tsai, J.-T. Lee, Corros. Sci., 34 (1993) 741-757
[12] W-T. Tsai, Z-H. Lee, J-T. Lee, M-C. Tsai, P-H. Lo, Mater. Sci. Eng., A118 (1989) 121-129
[13] D. Van Rooyen, Corros., 31 (1975) 327-337
[14] W. Yang, Z. Lu, D. Huang, D. Kong, G. Zhao, J. Congleton, Corros. Sci., 43 (2001) 963-977
[15] H. Gleiter, Prog. Mater. Sci., 33 (1988) 223-315
[16] C. Suryanarayana, Int. Mater. Rev., 40 (1995) 41-64
[17] K. Lu, Mater. Sci. Eng., R16 (1996) 161-221
[18] D.G. Morris, Mechanical Behaviour of Nanostructured Materials, Trans. Tech. Publications Ltd., Switzerland, (1998) 70
[19] S.X. McFadden, R.S. Mishra, R.Z. Valiev, A.P. Zhilyaev, A.K. Mukherjee, Nature, 298 (1999) 684
[20] J. Lu, M.L. Sui, K. Lu, Science, 287 (2000) 1463
[21] K. Lu, J. Lu, Mater. Sci. Eng., A375-377 (2004) 38-45
[22] N.R. Tao, M.L. Sui, J. Lu, K. Lu, Nanostruct. Mater., 11 (1999) 433-440
[23] G. Liu, J. Lu, K. Lu, Mater. Sci. Eng., A286 (2000) 91-95
[24] G. Liu, S.C. Wang, X.F. Lou, J. Lu, K. Lu, Scripta Mater., 44 (2001) 1791-1795
[25] X. Wu, N. Tao, Y. Hong, B. Xu, J. Lu, K. Lu, Acta. Mater., 50 (2002) 2075-2084
[26] N.R. Tao, Z.B. Wang, W.P. Tong, M.L. Sui, J. Lu, K. Lu, Acta. Mater., 50 (2002) 4603-4616
[27] I.J. Yang, Corros., 49 (1993) 576-585
[28] W.-T. Tsai, M.-J. Sheu, J.-T. Lee, Corros. Sci., 38 (1996) 33-45
[29] T. Sakai, K. Aoki, T. Shigemitsu, Y. Kishi, Zairyo to Kankyo 40 (1991) 736-741
[30] Z. Fang, R. W. Staehle, Corros., 55 (1999) 355-379
[31] T. Sakai, S. Okabayashi, K. Aoki, Proceedings of the 4th International Symposium on Degradation of Materials in Nuclear Power Systems- Water Reactors, Jekyll island, Georgia, 6-10 August (1989)
[32] E.H. Lee, K.M. Kim, U.C. Kim, Mater. Sci. Eng., A449 (2007) 330-333
[33] P. Marcus, A. Teissier, J. Oudar, Corros. Sci., 24 (1984) 259-268
[34] M.G. Faichuk, S. Ramamurthy, W.M. Lau, Corros. Sci., 53 (2011) 1383-1393
[35] W.-T. Tsai, C.-S. Chang, J.-T. Lee, Corros. Sci., 50 (1994) 98-105
[36] Y.-W. Hao, B. Deng, C. Zhong, Y.-M. Jiang, J. Li, J. Iron and Steel Research, Int., 16 (2009) 68-72

[37] R.M Carranza, M.G. Alvarez, Corros. Sci., 38 (1996) 909-925
[38] E. Barsoukov, J. R. Macdonald. Impedance Spectroscopy: Theory, Experiment, and Applications. J. Wiley and sons, (2005)
[39] K. Juttner, W.J. Lorenz, Corros. Sci., 29 (1989) 279-288
[40] L. Zhang, D.D. Macdonald, Electrochim. Acta., 43 (1998) 2661-2671
[41] T. Dan, T. Shoji, Z. Lu, K. Sakaguchi, J. Wang, E.-H. Han, W. Ke, Corros. Sci., 52 (2010) 1228-1236
[42] S. Mischler, A. Vogel, H.J. Mathieu, D. Landolt, Corros. Sci., 32 (1991) 925-944
[43] A.S. Lim, A. Atrens, Appl. Phys., A54 (1992) 343-349
[44] M. Pourbaix, Atlas of Electrochemical Equilibria in Aqueous Solutions, NACE Int. (1974)
[45] D. Briggs, J. Grant, Surface Analysis by Auger and Photoelectron Spectroscopy, IM Publications, (2003)
[46] W. Li, X. Wang, Q. Meng, Y. Rong, Scripta. Mater., 59 (2008) 344-347
[47] G. Liu, J. Lu, K. Lu, Mater Sci. Eng., A86 (2000) 91-95
[48] Y.F. Al-Obaid, Eng. Frac. Mech., 51 (1995) 19-25
[49] Z.B.Wang, N.R. Tao, W.P. Tong, J. Lu, K. Lu, Acta. Mater., 51 (2003) 4319-4329
[50] N.R. Tao, Z.B. Wang, W.P. Tong, M.L. Sui, J. Lu, K. Lu, Acta. Mater., 50 (2002) 4603-4616
[51] K. Lu, J. Mater. Sci. Technol., 15 (1999) 193-197
[52] T. Roland, D. Retraint, K. Lu, J. Lu, Scripta. Mater., 54 (2006) 1949-1954
[53] T. Roland, D. Retraint, K. Lu, J. Lu, Mater. Sci. Eng., A445-446 (2007) 281-288
[54] Z.B. Wang, K. Lu, G. Wilde, S.V. Divinski, Acta. Mater., 58 (2010) 2376-2386
[55] T. Balusamy, S. Kumar, T.S.N. Sankara Narayanan, Corros. Sci., 52 (2010) 3826-3834
[56] J. Robertson, Corros. Sci., 32 (1991) 443-465
[57] Yu. R. Kolobov, G.P. Grabovetskaya, M.B. Ivanov, A.P. Zhilyaev, R.Z. Valiev, Scripta. Mater., 44 (2001) 873
[58] M.D. Baro, Yu. R. Kolobov, I.A. Ovidko, Rev. Adv. Mater. Sci., 2 (2001) 1
[59] Z. B. Wang, N.R. Tao, W.P. Tong, J. Lu, K. Lu, Acta. Mater., 51 (2003) 4319-4329
[60] R. Wurschum, S. Herth, U. Brossman, Adv. Eng. Mater., 5 (2003) 365-372
[61] S.D. Lu, Z.B. Wang, K. Lu, Mater. Sci. Eng., A527 (2010) 995-1002

Chapter 7. Corrosion and Surface Film Properties of Alloy 800 Subjected to Surface Mechanical Attrition Treatment (SMAT)

7.1 Introduction

While the Fe-Ni-Cr Alloy 800 is one of the candidates to replace Alloy 600 as SG tubing in CANDU reactors, reports have shown that Alloy 800 can be susceptible to SCC under certain operating conditions [1-3]. SCC is defined as material failure through slow, environmentally-induced crack propagation, and can occur as a result of a combined interaction between mechanical stress and the corrosion reaction [4-6]. Since the stress concentration required to propagate a crack does not exceed the critical values required for mechanical failure of the material, this type of corrosion is problematic and can be extremely difficult to detect in its early or intermediate stages. A number of different factors can affect the susceptibility of a material to SCC, such as the environmental exposure, tensile stress, and alloy composition [1, 2, 5-7].

A new approach to combat SCC is to optimize the surface microstructure of existing SG tubing. Research has been conducted on nanostructured materials, showing that they display different behaviour to their coarse grained counter parts, such as an increase in hardness and strength, improved tribological properties and increased plasticity at low temperatures [8-13]. One method of achieving these modifications is through the use of SMAT. This technique was developed by Lu, *et al*., and leads to the formation of a thin, nanostructured surface layer [10, 14]. This technique uses smooth, spherical balls that are accelerated towards a sample at various angles and velocities in a

vibrating reflection chamber. The repeated multidirectional impact can induce plastic deformation with a high strain rate on the surface, ultimately leading to grain refinement.

The aim of this study is to examine the effects of SMAT, first described in chapter 6, on Alloy 800, focusing on the changes in the surface and electrochemical properties of the oxide film. Electrochemical techniques such as anodic polarization and EIS were used to examine the effect of SMAT on the passivation of the alloy in a 0.1 M $Na_2S_2O_3$ solution. Surface analysis techniques, such as AES and XPS were used to determine the changes in chemical composition of the oxide film resulting from SMAT.

7.2 Experimental

7.2.1 Sample Preparation

9.5 mm diameter Alloy 800 tubing sections were procured from Rolled Alloys Canada in the mill-annealed condition. The composition is presented in Table 7.1.

Table 7.1 Chemical composition of Alloy 800 SG tubing (wt%).

Element	Ni	Cr	Fe	Mn	Al	Ti	Si	C
Composition %	30.86	20.37	Bal.	0.72	0.40	0.40	0.54	0.07

Several 6 inch sections of Alloy 800 tubing were shipped to Hong Kong Polytechnic University in Hong Kong to undergo SMAT. Process parameters were varied, such as shot composition and treatment time. Samples were subjected to treatment using stainless steel (SS) shots having a mass of either 20 g or 40 g for a time period ranging between 90 and 120 minutes. The electrodes were designated according to the shot

material used and treatment time. For example, a sample treated using a 20 g stainless steel shot for 90 minutes is named A800ss90(20).

Small rectangular prismatic electrodes were carefully cut from this tubing using a Buehler diamond-tipped saw. The average exposed sample area on the outer surface of these electrodes was 20 mm^2. The electrodes were polished with a 0.05 μm alumina grit polishing pad, washed with DI water, and sonicated in acetone.

7.2.2 Electrochemical Measurements

A detailed description of the experimental and analytical procedures can be found in chapters 3 and 4.

7.2.3 Surface Analysis

7.2.3.1 Auger Electron Spectroscopy (AES)

A detailed description of the experimental and analytical procedures can be found in chapters 3 and 4.

7.2.3.2 X-ray Photoelectron Spectroscopy (XPS)

A detailed description of the experimental and analytical procedures can be found in chapters 3 and 4.

7.3 Results and Discussion

7.3.1 Anodic Polarization

Figure 7.1 shows the potentiodynamic polarization curves recorded for the four electrodes in a 0.1 M $Na_2S_2O_3$ solution. As in chapter 3, the anodic polarization curves are broken down into three regions based on the electrochemical behaviour.

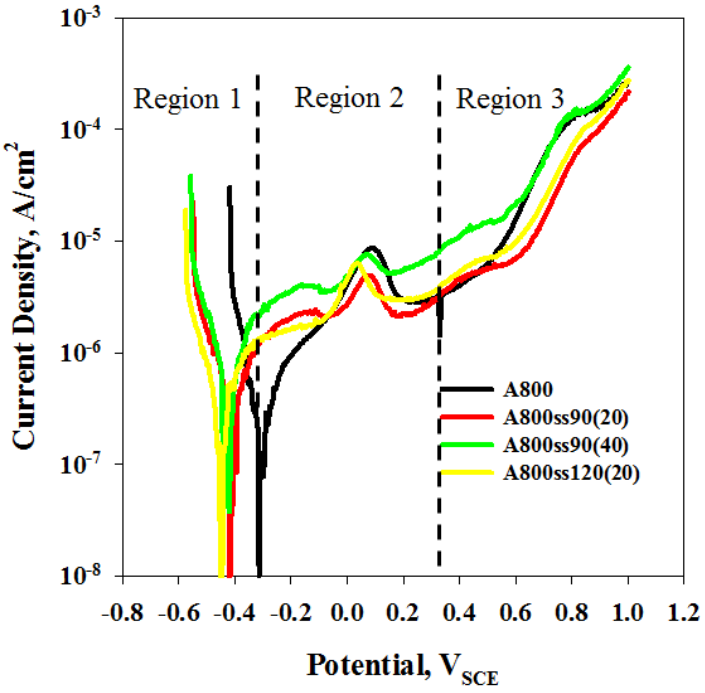

Figure 7.1 Anodic polarization curves for A800, A800ss90(20), A800ss90(40) and A800ss120(20). The curves are divided into three regions described in the text.

In region 1, the electrodes are in a pre-passive state, prior to passive film formation. Compared to A800, the SMAT samples show a shift in E_{corr} by nearly 0.1 V in the negative direction. Similar results have been reported elsewhere [15], and these observations were also made on the A600 SMAT electrodes in chapter 6, although the

shift was minor. The larger effect on A800 indicates a shift to more active behaviour on this alloy, the difference between the two alloys being the fact A800 is an Fe-based alloy while A600 is a more noble Ni-based alloy. Passive film formation occurs in region 2, where the film is expected to be most protective. In the initial stages of this region, the current density measured on the SMAT electrodes is higher than that measured on A800. Immediately following the anodic peak, the measured current densities become similar, with the exception of A800ss90(40), on which the current density is substantially higher. A slight shift in the anodic peak position in the negative direction is observed on the A800ss120(20) electrode. The transpassive region (3) initiates at ~ 0.3 V_{SCE}, where the current density begins to increase at a much higher rate. At potentials greater than 0.6 V_{SCE}, the measured current densities on A800ss90(20) and A800ss120(20) are lower than on the other electrodes.

7.3.2 Electrochemical Impedance Spectroscopy (EIS)

EIS measurements were performed immediately following electrochemical oxide film growth for 3 hours at potentials in the range of -0.4 V_{SCE} to 0.75 V_{SCE}, Figure 7.2. These plots all appear as depressed semi-circular curves, indicating significant frequency dispersion on the electrode surface [16-18]. A high frequency and low frequency response is visible for all of the measured electrodes.

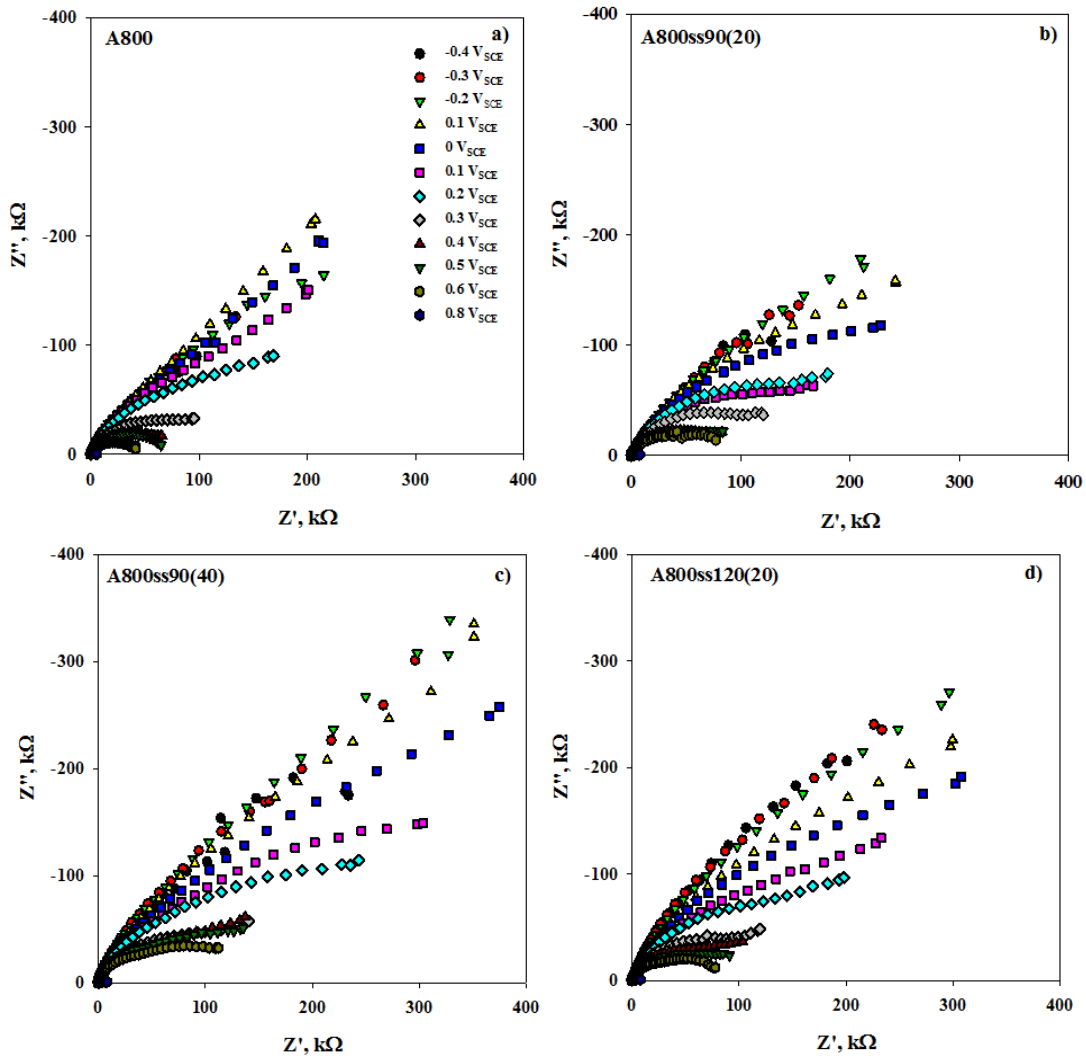

Figure 7.2 EIS Nyquist plots recorded on the electrodes following potentiostatic treatment for three hours at various potentials: (a) A800, (b) A800ss90(20), (c) A800ss90(40), and (d) A800ss120(20).

The Bode plots, Figure 7.3, highlight changes in the phase angle, θ, as a function of frequency. A decrease in θ is observed at low frequencies as the applied potential is increased.

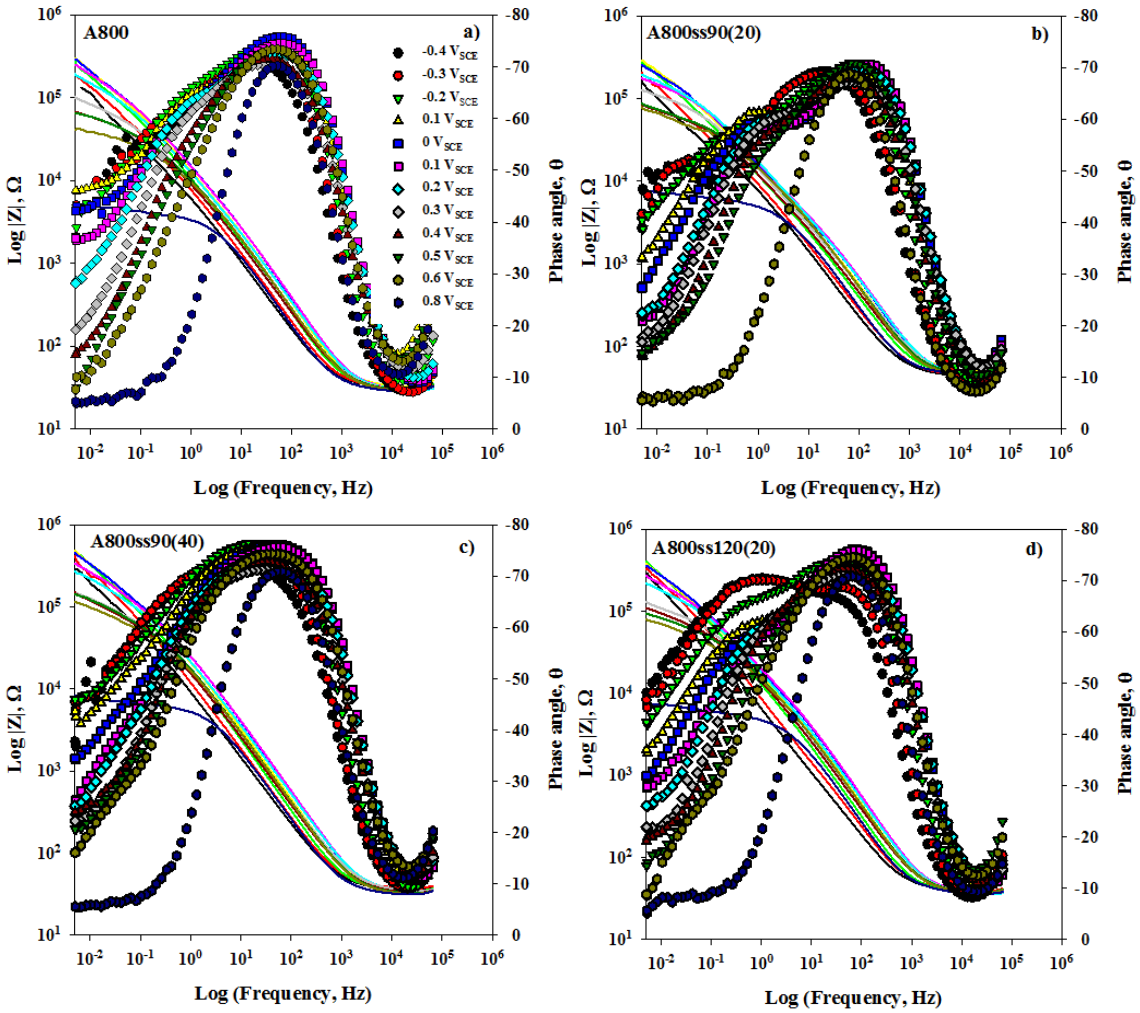

Figure 7.3 Bode plots recorded on the electrodes following potentiostatic treatment for three hours at various potentials: (a) A800, (b) A800ss90(20), (c) A800ss90(40), and (d) A800ss120(20).

The equivalent circuit used to fit the acquired impedance data is presented in Figure 7.4. The same model was used to fit the Alloy 800 data collected in chapter 4. This equivalent circuit contains three time constants in series, with a single resistive element representing the solution resistance, R_s. A CPE is used to account for the non-ideal behaviour observed on the electrode surface.

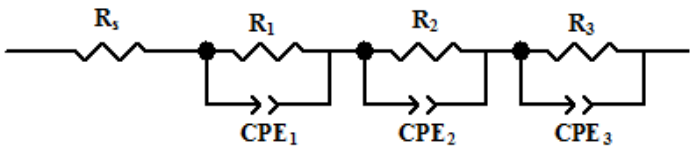

Figure 7.4 Equivalent circuit used to model EIS spectra recorded on A800, A800ss90(20), A800ss90(40) and A800ss120(20).

The time constant, R_3/CPE_3, represents the charge processes occurring at either the solution/oxide or the oxide/alloy interface. The remaining two time constants, R_1/CPE_1 and R_2/CPE_2, represent the outer and barrier layers of the oxide film, respectively. Figure 7.5 shows the fitting of data collected to this equivalent circuit for all four electrodes after film growth at an applied potential of -0.2 V_{SCE}.

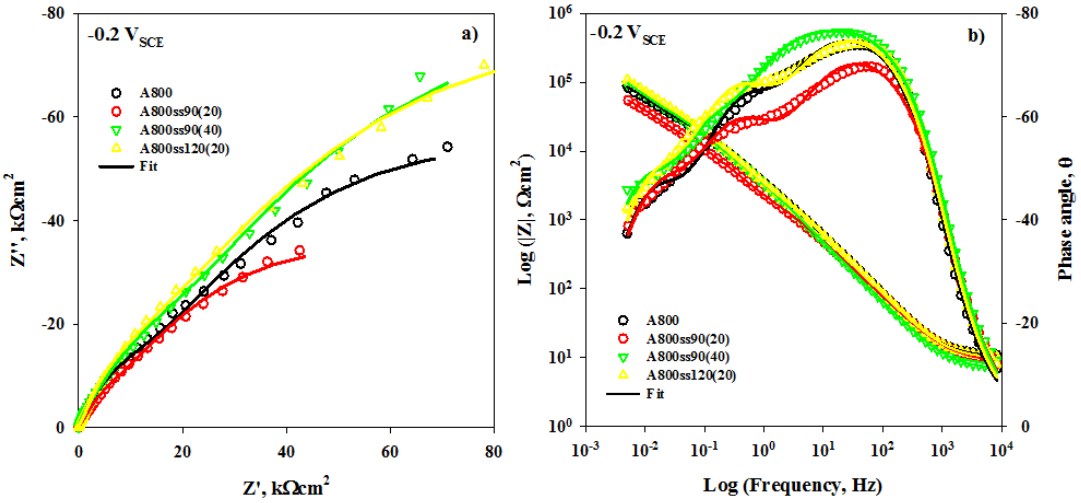

Figure 7.5 Examples of fitted EIS spectra (-0.2 V_{SCE}) for A800, A800ss90(20), A800ss90(40) and A800ss120(20): (a) Nyquist and (b) Bode plots.

Excellent fits were obtained for all of the spectra and the numerical values of the circuit elements are summarized in Table 7.2.

Table 7.2 Summary of the parameters obtained from the fitted EIS spectra for A800, A800ss90(20), A800ss90(40) and A800ss120(20).

Alloy	E (V_{SCE})	R_2 ($k\Omega cm^2$)	CPE_2 (μFcm^{-2})	n	R_1 ($k\Omega cm^2$)	CPE_1 (μFcm^{-2})	n	R_3 ($k\Omega cm^2$)	CPE_3 (μFcm^{-2})	n
A800										
	-0.4	77.13	237.2	0.8187	2.971	294.2	0.8848	0.7227	254.8	0.8436
	-0.3	117.1	265.4	0.8453	12.79	179.0	0.8554	1.030	1721	0.8565
	-0.2	130.7	190.9	0.8557	16.27	103.5	0.8680	0.7200	126.8	0.9031
	-0.1	214.3	164.5	0.8366	19.60	81.66	0.8601	0.7230	78.88	0.9316
	0	179.3	180.4	0.8462	23.03	67.52	0.8719	1.200	59.96	0.9277
	0.1	126.0	207.1	0.8386	25.93	65.40	0.8607	1.070	65.38	0.9138
	0.2	69.70	263.0	0.8281	23.42	74.33	0.8435	0.7398	98.62	0.8892
	0.3	24.98	488.9	0.8046	15.68	96.23	0.8273	0.6583	179.2	0.8497
	0.4	14.18	59.10	0.7699	10.85	108.7	0.8393	1.022	127.3	0.8696
	0.6	7.635	537.6	0.7768	5.655	108.6	0.8775	1.360	68.10	0.8897
A800ss90(20)										
	-0.4	82.89	375.2	0.7505	2.281	248.4	0.8738	0.2141	362.9	0.9146
	-0.3	72.96	369.3	0.8243	4.835	638.0	0.8264	2.0455	171.7	0.8111
	-0.2	91.30	262.9	0.8249	9.486	196.1	0.8263	0.6682	127.6	0.8579
	-0.1	77.37	202.3	0.8014	10.92	137.7	0.8076	0.3030	65.92	0.9264
	0	57.26	221.8	0.8070	12.48	111.4	0.8136	0.3932	48.05	0.9290
	0.1	28.48	451.0	0.8047	17.17	80.39	0.8150	0.4558	49.06	0.9174
	0.2	34.06	337.3	0.7970	16.16	82.65	0.8123	0.3834	67.42	0.9022
	0.3	17.10	654.6	0.7787	14.34	95.16	0.7937	0.2882	129.9	0.8630
	0.4	10.23	917.1	0.7841	9.074	107.7	0.8124	0.3642	127.9	0.8626
	0.6	9.435	847.4	0.8220	6.539	92.26	0.8636	0.9012	63.63	0.8858
A800ss90(40)										
	-0.4	106.9	331.1	0.8842	13.51	196.8	0.8132	0.2422	846.5	0.8123
	-0.3	174.5	335.9	0.9009	25.04	157.0	0.8507	1.3816	297.1	0.8273
	-0.2	199.4	215.3	0.8825	20.65	151.7	0.8847	2.9766	145.0	0.8661
	-0.1	215.6	247.6	0.8793	29.42	121.4	0.8753	4.8992	88.05	0.8607
	0	137.4	181.8	0.8606	19.96	88.16	0.8862	3.2766	72.88	0.8775
	0.1	89.81	196.6	0.8424	17.14	77.05	0.8844	2.4132	77.41	0.8781
	0.2	72.57	238.6	0.8186	16.91	78.35	0.8638	1.4754	126.7	0.8578
	0.3	42.89	704.9	0.8079	13.75	130.5	0.8335	3.1886	135.8	0.8154
	0.4	42.36	703.0	0.8267	10.16	185.2	0.8519	4.7642	102.9	0.8323
	0.6	26.93	426.0	0.7989	7.549	91.92	0.8826	1.1984	116.1	0.8773
A800ss120(20)										
	-0.4	143.7	240.2	0.9376	21.33	192.1	0.7727	0.02548	324.5	1.033
	-0.3	125.1	341.1	0.8315	23.09	183.0	0.8070	0.04603	142.7	1.072
	-0.2	194.4	202.1	0.8603	19.50	119.0	0.8587	0.6917	121.0	0.9093
	-0.1	177.6	157.2	0.8539	20.04	91.22	0.8620	1.162	59.15	0.9135
	0	138.6	152.2	0.8529	21.78	70.30	0.8696	1.361	40.70	0.9296
	0.1	114.1	146.8	0.8362	24.44	61.97	0.8657	1.621	40.33	0.9228
	0.2	82.94	217.7	0.8261	26.88	60.60	0.8470	0.9919	62.40	0.9084
	0.3	60.12	311.3	0.7923	19.60	70.74	0.8284	0.6501	120.2	0.8776
	0.4	30.56	610.5	0.7787	13.69	71.25	0.8475	0.6585	115.7	0.8945
	0.6	17.88	394.6	0.8308	6.938	67.50	0.8857	1.062	59.77	0.9005

Changes to the (a) barrier and (b) outer layer oxide resistances are plotted in Figure 7.6. The barrier layer resistance, Figure 7.6 (a), is nearly an order of magnitude greater than that of the outer layer, Figure 7.6 (b).

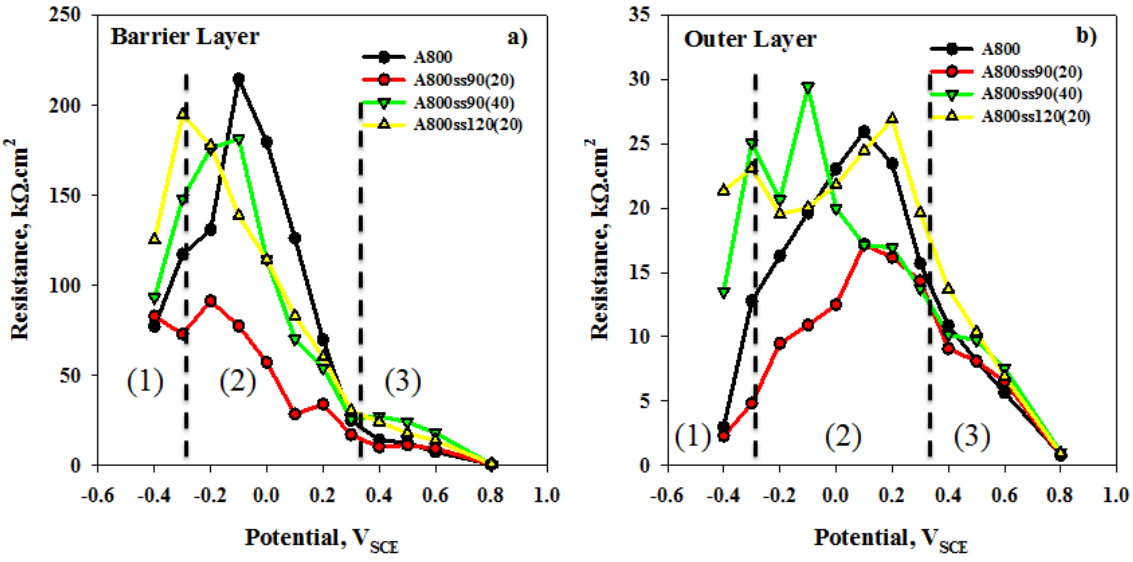

Figure 7.6 Changes in the oxide film resistance as a function of applied potential for A800, A800ss90(20), A800ss90(40) and A800ss120(20) in the (a) barrier and (b) outer layer.

In region 1, and partially into region 2, the barrier layer resistance of the SMAT electrodes exceeds that of A800. This is unsurprising, given the lower E_{corr} values for the SMAT electrodes, Figure 7.1. The only exception is A800ss90(20), which, despite the shift in E_{corr}, does not develop an improved barrier layer resistance in region 2. As expected, the highest barrier layer resistances are observed in the passive region 2, prior to the potential range of the anodic peak. The maximum barrier layer resistance for all SMAT electrodes appears at potentials lower than that observed on A800, indicating the growth of the passive layer occurs at lower potentials. In the potential range of the

anodic peak, the barrier layer resistance on the SMAT electrodes decreases more rapidly than on A800, suggesting that, while barrier layer growth may occur more readily on the SMAT electrodes, the treatment of the alloy is detrimental to the formation of a stable, protective film, allowing for more rapid restructuring and breakdown of the passive oxide. In the transpassive region (3), the barrier layer resistance remains low for all four electrodes, although the resistance measured on A800ss90(40) and A800ss120(20) is higher than on A800.

Changes in the outer layer resistance, Figure 7.6 (b), show trends similar to those observed in the barrier layer. The resistance values obtained for SMAT electrodes A800ss90(40) and A800ss120(20) are higher in region 1 and the initial stages of region 2 compared to A800 and A800ss90(20). Following the anodic peak at 0.1 V_{SCE}, the resistance for all electrodes decreases as a function of potential.

7.3.3 Surface Analysis - AES

The oxide film thickness as a function of film growth potential is plotted in Figure 7.7. The procedure to determine these values from AES depth profiles was discussed in chapter 3. Significant variations in oxide film thickness are observed, but with no obvious systematic differences between individual electrodes. As expected, the oxide grown on all electrodes becomes thicker when the potential is increased into the transpassive region (3). The erratic nature of the data suggests, perhaps, that the location of the oxide/alloy interface in the depth profiles is inexact. For thin films on a SMAT roughened surface, this might be expected. Unlike the A600 SMAT data analyzed in chapter 6, there does not appear to be an obvious thinning of the passive oxide film

within the anodic peak potential region (0 V_{SCE} to 0.2 V_{SCE}) for all of the electrodes measured.

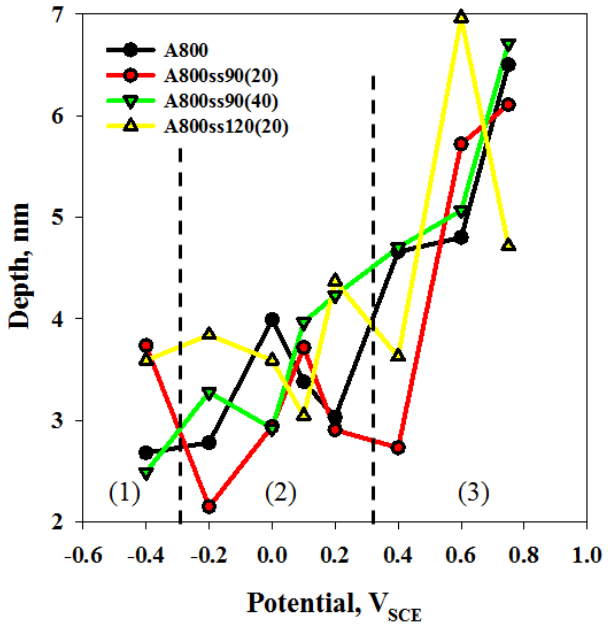

Figure 7.7 Oxide film thickness as a function of film growth potential for A800 and the SMAT electrodes.

The cation fractions for Ni, Fe and Cr are plotted as a function of depth for a range of film growth potentials in Figures 7.8 through 7.10. The procedure to obtain these values from the AES depth profiles was described in detail in chapter 3. Figure 7.8 shows the Ni cation fractions as a function of depth for all four electrodes. On each electrode, the surface of the oxide film is only slightly depleted with respect to the bulk alloy composition, and, as observed previously in chapter 5, Ni becomes enriched within the alloy surface. Depletion of Ni in the outer regions of the film is minor in regions 1 and 2, but becomes more significant in the transpassive region (3), although its enrichment in the alloy surface remains. No significant differences between the electrodes are noted.

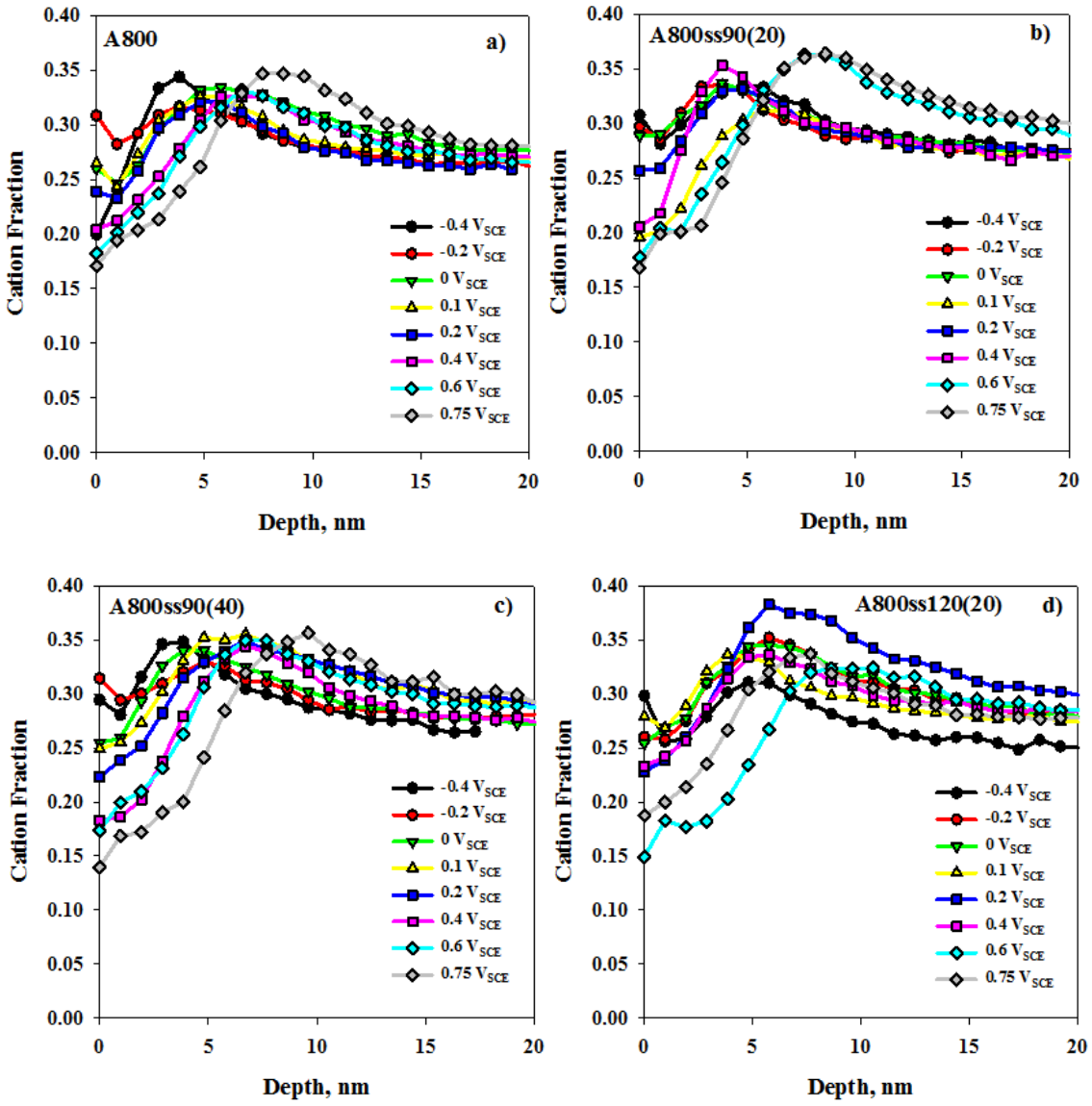

Figure 7.8 Ni cation fractions as a function of depth for a range of film growth potentials.

Figure 7.9 shows the changes in Fe cation fractions as a function of depth for various film growth potentials. For all electrodes, Fe becomes enriched at the outer surface of the oxide film, which can be attributed to the accumulation of Fe^{III} oxides.

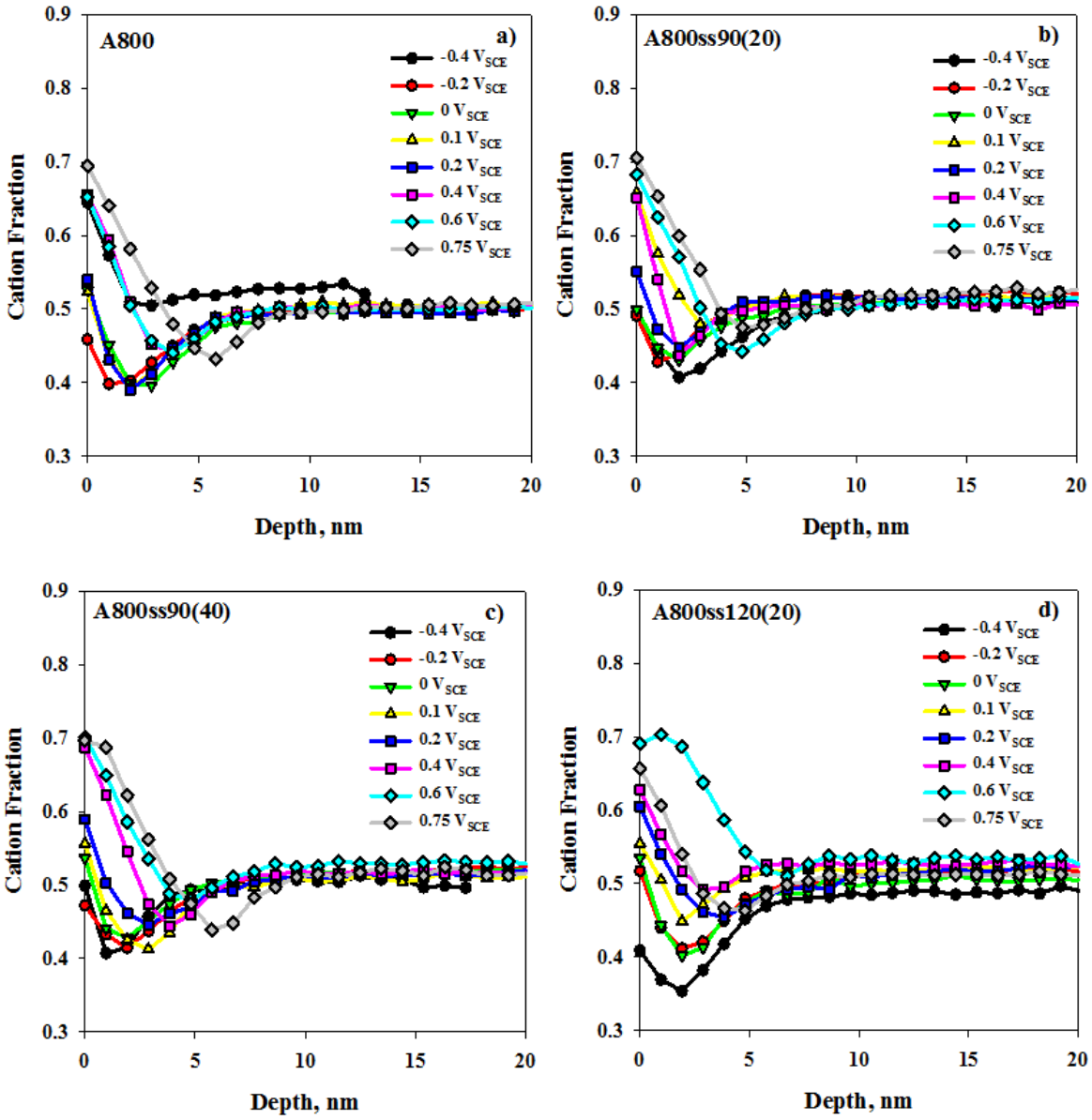

Figure 7.9 Fe cation fractions as a function of depth for a range of film growth potentials.

As previously observed for A800 in chapter 5, the segregation of Fe to the outer regions of the film is accompanied by its depletion close to the oxide/alloy interface; i.e., within the barrier layer.

The distribution of Cr within the oxide film is shown in Figure 7.10. For all electrodes, Cr is localized close to the oxide/alloy interface even in the transpassive region 3.

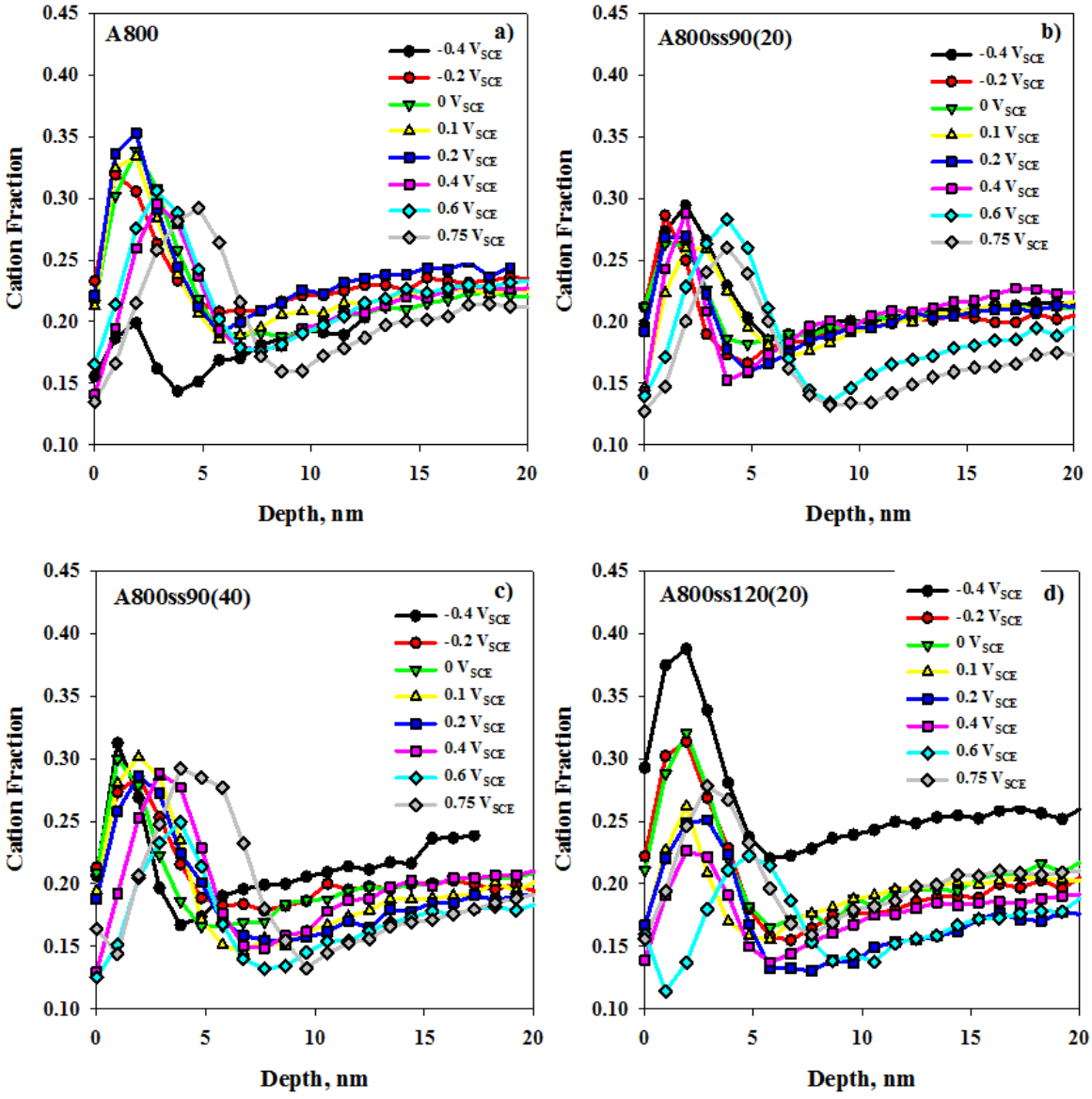

Figure 7.10 Cr cation fractions as a function of depth for (a) A800, (b) A800ss90(20), (c) A800ss90(40) and (d) A800ss120(20) for a range of film growth potentials.

For all the electrodes a depletion of Cr is observed in the surface of the alloy at the oxide/alloy interface. In general, all the electrodes exhibit similar behaviour to that observed for Alloy 800 and discussed in chapter 5. In general, Ni is retained in the alloy surface while Cr becomes depleted in the alloy due to its segregation to form the barrier layer oxide. Fe is segregated to the oxide/solution interface, especially after the anodic film breakdown and as the potential is increased into the passive region. A key observation is that the extent of Cr accumulation in the barrier layer is proportional to the extent of Fe depletion in this layer. For example, A800ss120(20), Figure 7.10 (d), shows the Cr content at -0.4 V_{SCE} to be significantly elevated, while the Fe cation fraction, Figure 7.9 (d), shows the Fe to be similarly strongly depleted. This correlation confirms that the quantity of Cr in the barrier layer is dependent on the degree of segregation of Fe to the outer layer.

Changes in the Ni and Fe cation fractions as a function of film growth potential at the solution/oxide interface are shown in Figure 7.11 (a) and (b). As the potential increases through the passive region (2), the Ni content in the outer layer decreases, although no clear distinction can be made between A800 and the SMAT electrodes. The Fe content increases with potential through region 2, with enrichment on the SMAT electrode surfaces slightly more enhanced than on A800. At transpassive potentials in region 3, the surface of the films on the SMAT electrodes contain slightly less Ni and more Fe than the A800 electrode. This would be expected as a consequence of the more rapid barrier layer breakdown indicated in the barrier layer resistance measurements, Figure 7.6 (a).

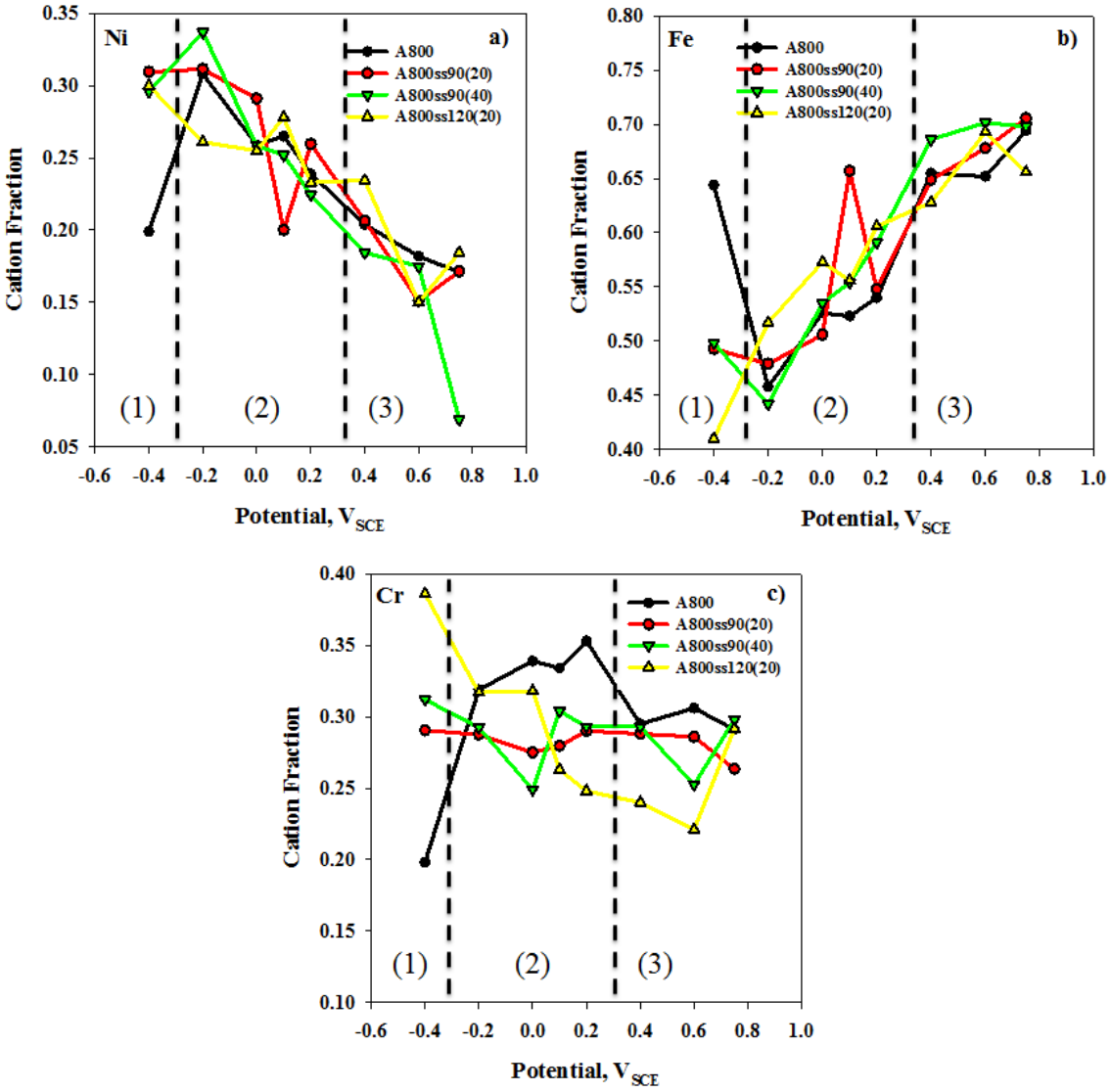

Figure 7.11 Cation fractions of (a) Ni, (b) Fe, and (c) Cr in the outer ((a) and (b)), and barrier (c) layers as a function of applied potential.

Changes in the Cr content of the barrier layer, obtained from the Cr peak maxima in the AES depth profiles, are plotted in Figure 7.11 (c) for each electrode. The elevated Cr content on the SMAT electrodes observed in region 1 is consistent with the earlier formation of the barrier layer observed on these alloys compared to A800. In the passive

region (2), the Cr content of the barrier layer on the SMAT electrodes is significantly lower than that on A800, and this difference increases in the anodic peak potential region.

Consideration of these results and the barrier layer resistances, Figure 7.6, shows that the relative order of resistances in regions 1 and 2 are proportional to the Cr content of the barrier layer. These results indicate that while the barrier layer on A800 may form less readily than the SMAT electrodes in the pre-passive region 1, it eventually forms a layer with a higher Cr content and correspondingly higher resistance in the passive region (2). In addition, this layer, once formed, is not as readily anodically destroyed on A800 in the anodic peak region as is the layer on the SMAT electrodes. Comparing these results to the barrier layer resistance, Figure 7.6 (a), it appears that the reduction in Cr content within the barrier layer adversely affects the protective properties of the passive oxide film. In the transpassive region, all of the electrodes experience a reduction in Cr, and combined with the continued reduction in barrier layer resistance, Figure 7.6 (a), this is consistent with the transpassive breakdown of the film. The SMAT samples in this region, however, display a slight increase in resistance compared to A800, as well as lower current densities, Figure 7.1, which could be due to the higher Fe content in the outer layer.

The inverse relationship between Fe and Cr contents in the barrier layer, which appears to be the two key effects indicating passive layer formation, is highlighted in Figure 7.12. In regions 2 and 3, the SMAT electrodes clearly contain less Cr and, consequently, more Fe than the A800.

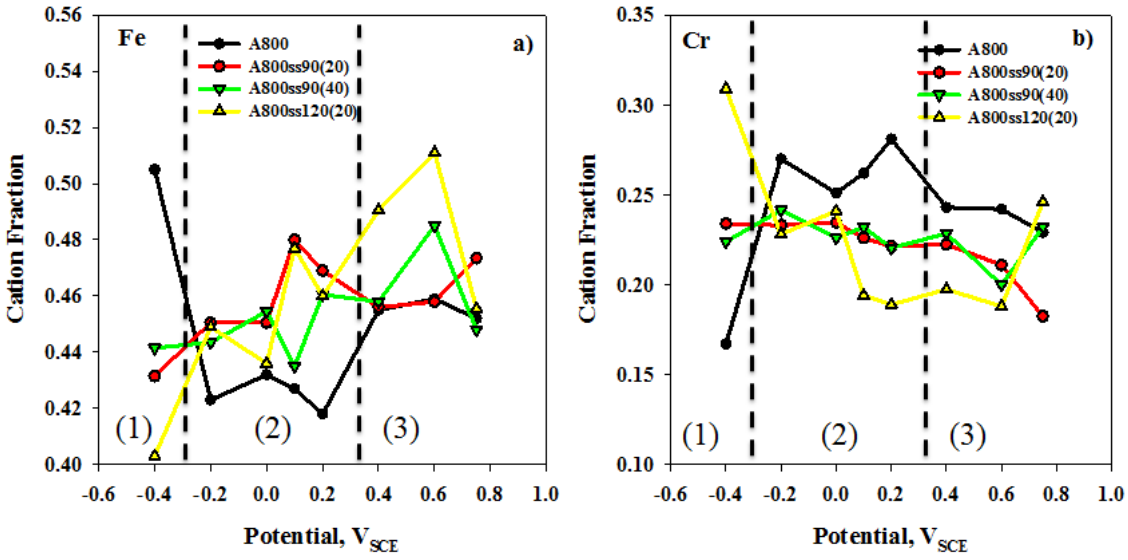

Figure 7.12 Cation fractions of (a) Fe and (b) Cr at the oxide/alloy interface as a function of applied potential.

As discussed in chapter 6, injection of cation vacancies into the barrier layer results in a loss of resistance, and hence, reduced corrosion protection. This degradation process appears to be enhanced by SMAT. This would lead to more defect transport pathways resulting in a greater mobility of Fe to, and its accumulation in, the outer layer, Figure 7.12 (a).

7.3.4 Surface Analysis - XPS

Fitting of the high resolution XPS spectra is shown in Figure 7.13 for (a) Cr $2p_{3/2}$, (b) Ni $2p_{3/2}$, (c) O 1s, and (d) Fe $2p_{3/2}$ on A800ss90(40). With the exception of Cr, all spectra were charge corrected by fixing the main signal of the C 1s peak at a BE of 285.0 eV. Details regarding the fitting of the spectra, as well as the omission of a charge correction for the Cr spectra, are given in Chapter 4.

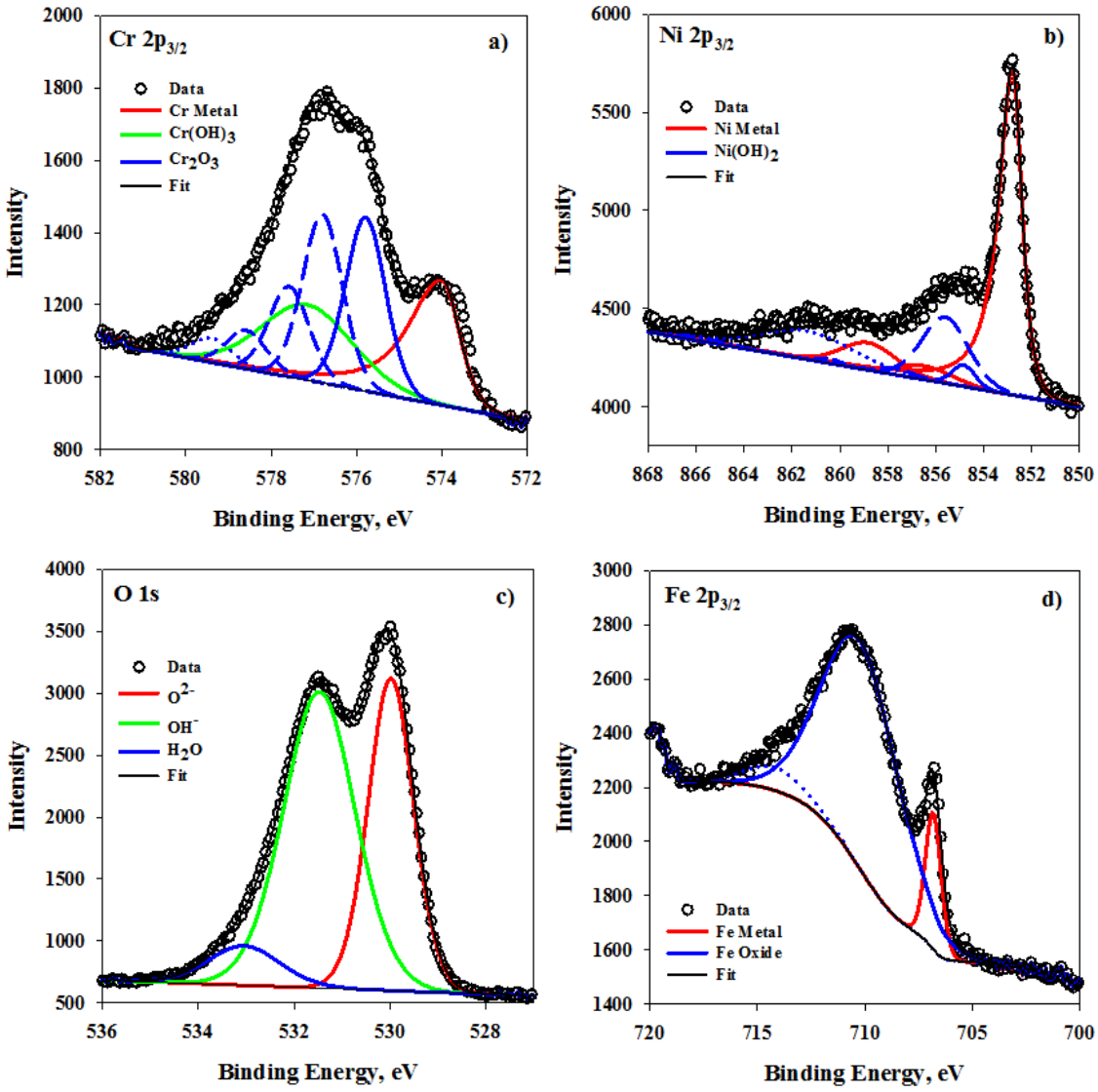

Figure 7.13 A800ss90(40) high resolution XPS spectra for the (a) $Cr2p_{3/2}$, (b) Ni $2p_{3/2}$, (c) O 1s and (d) $Fe2p_{3/2}$ peaks recorded on the electrodes potentiostatically treated at 0.1 V_{SCE}.

Table 7.3 lists the BE's extracted from the spectra. The BE recorded for $Cr(OH)_3$ at nearly every measured potential for all electrodes is higher than anticipated [19, 20] due to the proximity of the $Cr(OH)_3$ component relative to the alloy surface. $Cr(OH)_3$, which exhibits insulating behaviour in these films, is not in electrical contact with the

alloy surface. Typically located at the solution/oxide interface, this component is separated from the alloy by the barrier layer.

Table 7.3 Measured BE's for the various chemical states of O, Cr and Ni in oxide films formed potentiostatically on A800, A800ss90(20), A800ss90(40) and A800ss120(20).

Alloy	E (V_{SCE})	O^{2-} (eV)	OH^- (eV)	Cr (0) (eV)	Cr_2O_3 (eV)	$Cr(OH)_3$ (eV)	Ni (0) (eV)	$Ni(OH)_2$ (eV)
A800	-0.4	529.8	531.5	573.9	576.2	577.8	852.5	855.1
	-0.2	529.8	531.5	573.9	575.8	577.4	852.4	855.1
	0	529.8	531.4	574.0	576.1	577.7	852.4	855.0
	0.1	529.9	531.4	573.9	575.9	577.6	852.5	855.1
	0.2	529.9	531.4	573.9	576.0	577.6	852.5	854.9
	0.4	529.7	531.3	573.9	576.1	577.7	852.3	854.8
	0.6	529.9	531.3	574.0	576.0	577.7	852.4	854.9
	0.75	530.0	531.4	573.9	576.0	577.7	852.7	855.2
A800ss90(20)	-0.4	529.9	531.5	573.9	575.8	577.4	852.5	855.3
	-0.2	530.0	531.4	574.0	575.9	577.5	852.6	855.1
	0	529.9	531.4	574.0	575.9	577.6	852.5	855.2
	0.1	530.0	531.4	574.0	576.1	577.7	852.5	855.1
	0.2	530.0	531.4	574.0	576.0	577.7	852.5	855.0
	0.4	529.9	531.3	574.0	576.0	577.6	852.5	854.9
	0.6	529.9	531.5	574.0	576.1	577.7	852.4	855.0
	0.75	529.9	531.3	574.0	576.0	577.7	852.5	854.9
A800ss90(40)	-0.4	529.9	531.5	574.0	575.8	577.4	852.5	855.4
	-0.2	529.9	531.5	574.0	575.9	577.5	852.6	855.2
	0	530.0	531.6	574.0	575.8	577.4	852.6	855.4
	0.1	530.0	531.6	574.0	575.9	577.5	852.6	855.2
	0.2	530.0	531.4	574.0	575.9	577.5	852.5	855.2
	0.4	529.8	531.4	574.0	576.1	577.7	852.4	854.9
	0.6	529.9	531.3	574.0	576.1	577.7	852.5	855.0
	0.75	-----	-----	574.0	576.1	577.7	852.5	855.0
A800ss120(20)	-0.4	529.9	531.6	574.0	575.7	577.3	852.6	855.3
	-0.2	530.0	531.5	574.0	576.0	577.6	852.6	855.2
	0	530.0	531.5	574.0	575.9	577.6	852.5	855.1
	0.1	529.9	531.5	574.0	576.0	577.7	852.4	855.0
	0.2	529.9	531.4	574.0	576.1	577.7	852.4	855.0
	0.4	529.9	531.4	574.0	576.1	577.7	852.4	855.0
	0.6	529.9	531.4	574.0	576.0	577.7	852.5	855.1
	0.75	-----	-----	574.0	576.0	577.7	852.5	855.0

Cr_2O_3, the primary component of the barrier layer, is in direct conductive contact with the alloy and no significant shift in BE is observed [19, 20]. A shift in BE of the $Ni(OH)_2$ component at -0.4 V_{SCE} is observed for the SMAT electrodes [21].

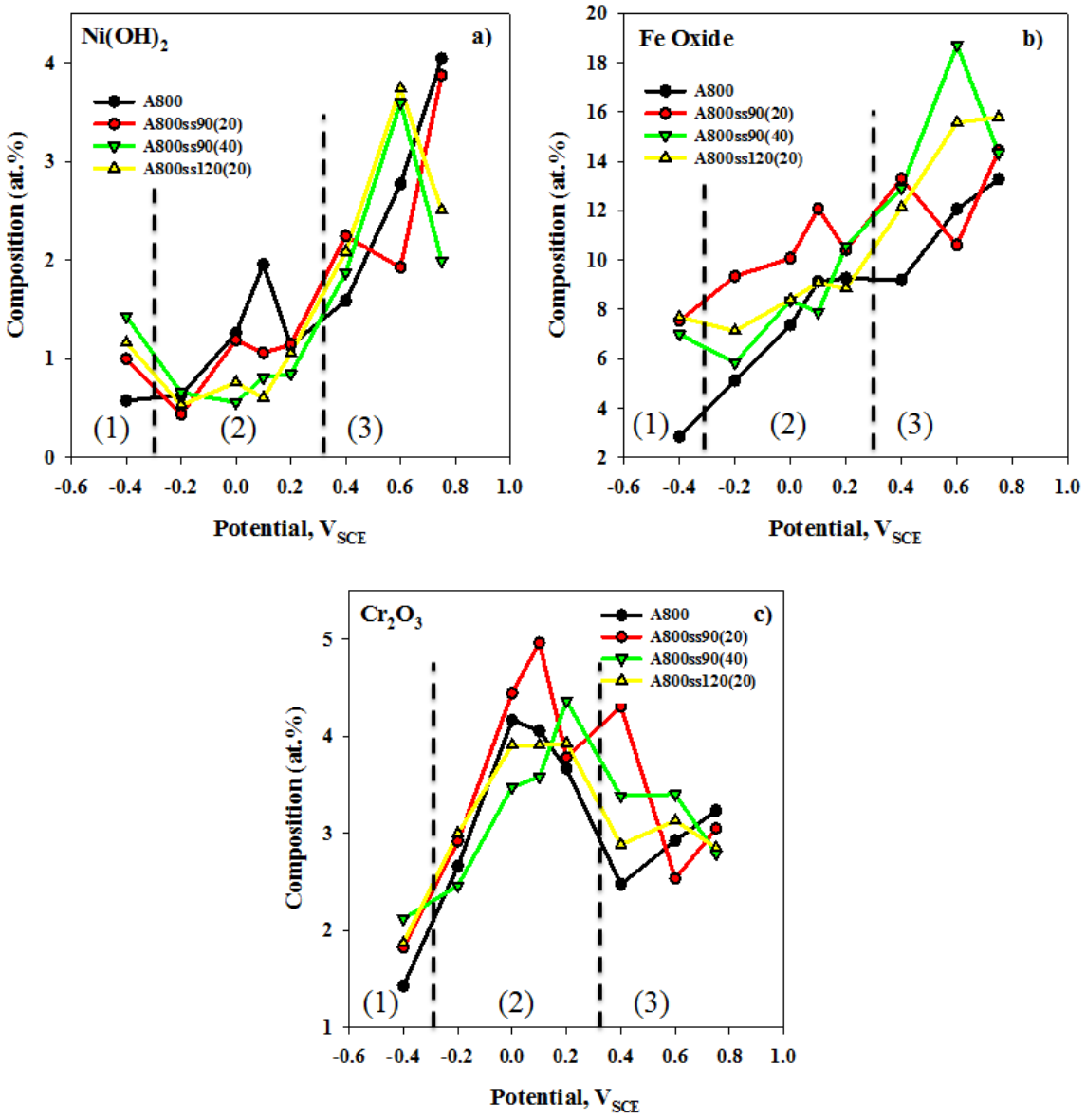

Figure 7.14 Variations in (a) $Ni(OH)_2$, (b) Fe oxide and (c) Cr_2O_3species in the oxide films, determined from high resolution XPS spectra as a function of potential, normalized against the total elemental content from the XPS survey scan.

Figure 7.14 shows a comparison between the Ni, Fe and Cr components of the oxide film obtained by fitting the high resolution XPS spectra. Changes in the $Ni(OH)_2$ component, Figure 7.14 (a), are only minor in the pre-passive and passive regions consistent with the retention of Ni in the alloy surface rather than its segregation to the film/solution interface. The lower $Ni(OH)_2$ content on the SMAT electrodes in the anodic peak region may reflect the increased ease of barrier layer breakdown on these electrodes.

The changes in Cr_2O_3 content, Figure 7.14 (c), accompanied by the increase and decrease in barrier layer resistance, Figure 7.6 (a), are consistent with the development and destruction of the barrier layer as the potential is increased through regions 1 and 2. Interestingly, the maximum Cr_2O_3 content is observed at ~ $0.1V_{SCE}$. This is the potential at which the maximum in the outer layer resistance occurs, Figure 7.6 (b), not that of the barrier layer. This indicates that the Cr_2O_3 content of the film continues to increase over a narrow range of potentials even though the barrier layer is being simultaneously destroyed. Although it cannot be demonstrated on the basis of these experiments, this suggests film breakdown may not be occurring uniformly; i.e., as the potential increases, the overall Cr_2O_3 content increases while the barrier layer becomes simultaneously defective. This would be consistent with breakdown occurring initially locally at (say) grain boundary locations while the barrier layer continues to grow on adjacent grain surfaces.

Since a breakdown of the barrier layer would lead to enhanced ion transport to the outer regions of the film, it would be expected to be accompanied by an increase in the Fe content of the film, especially in the outer layer at the oxide/solution interface. The

barrier layer resistance measurements show that except for a brief period in region 1, and the low potential range of region 2, the value for A800 is higher than those measured on the SMAT electrodes. This, coupled with the observation that the Fe oxide content of the film on the SMAT electrodes, Figure 7.14 (b), especially at the oxide/solution interface (Figure 7.12 (a)) is always higher than that on A800 then indicates the poorer quality of the passive films on the SMAT surfaces.

7.3.5 Sulphur

Changes in the S content as a function of potential are plotted in Figure 7.15 for the four electrodes, and the incorporation of this element into the oxide film has been discussed in the previous chapters. The AES depth profiles show that the majority of S is located within the barrier layer, close to the oxide/alloy interface, on all four electrodes. These profiles share many similarities with the AES Cr depth profiles plotted in Figure 7.10.

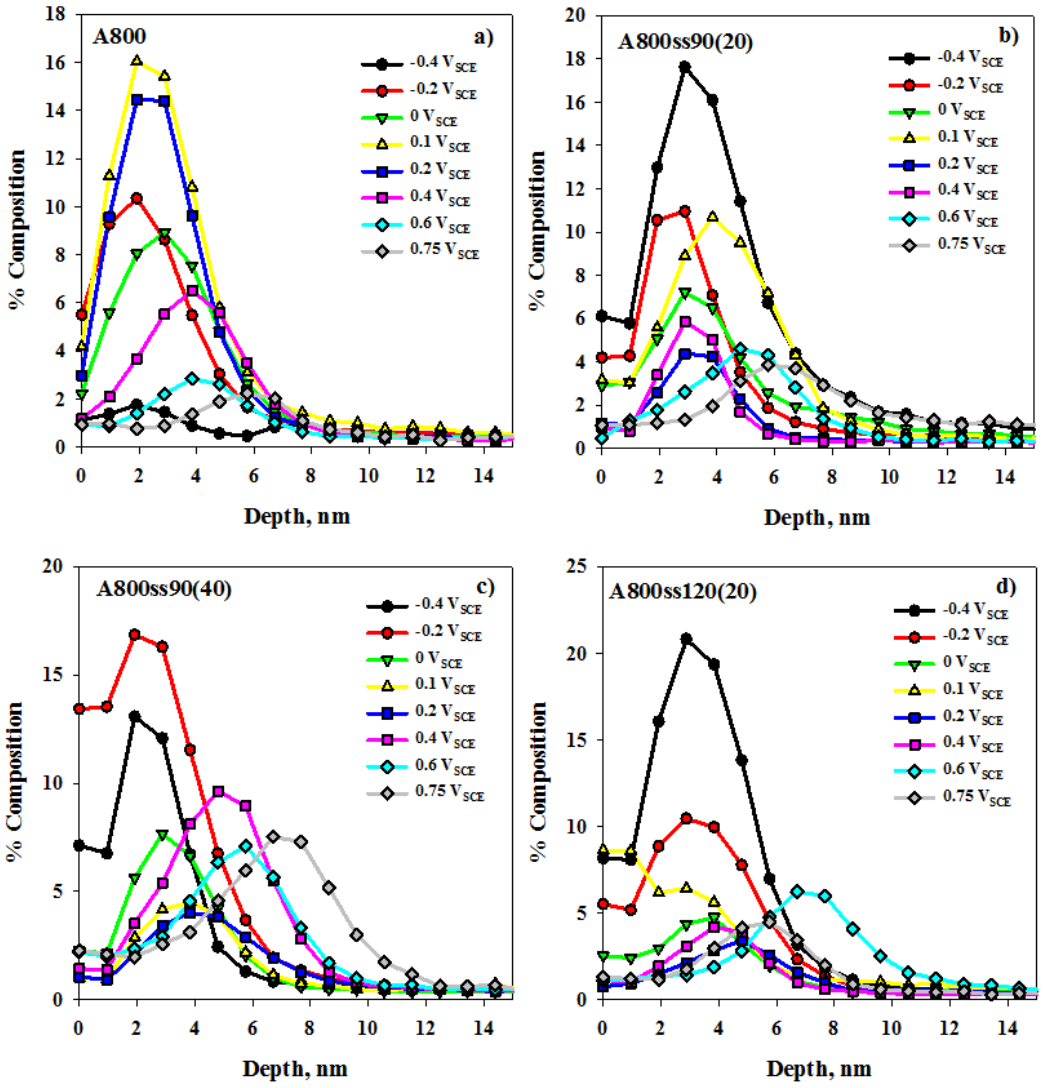

Figure 7.15 AES depth profiles showing the changes in S as a function of depth for (a) A800, (b) A800ss90(20), (c) A800ss90(40), and (d) A800ss120(20).

To better monitor the changes in S content in the film, the values at the solution/oxide interface (outer layer) and at the peak maximum (within the barrier layer) are plotted for each electrode as a function of potential in Figure 7.16.

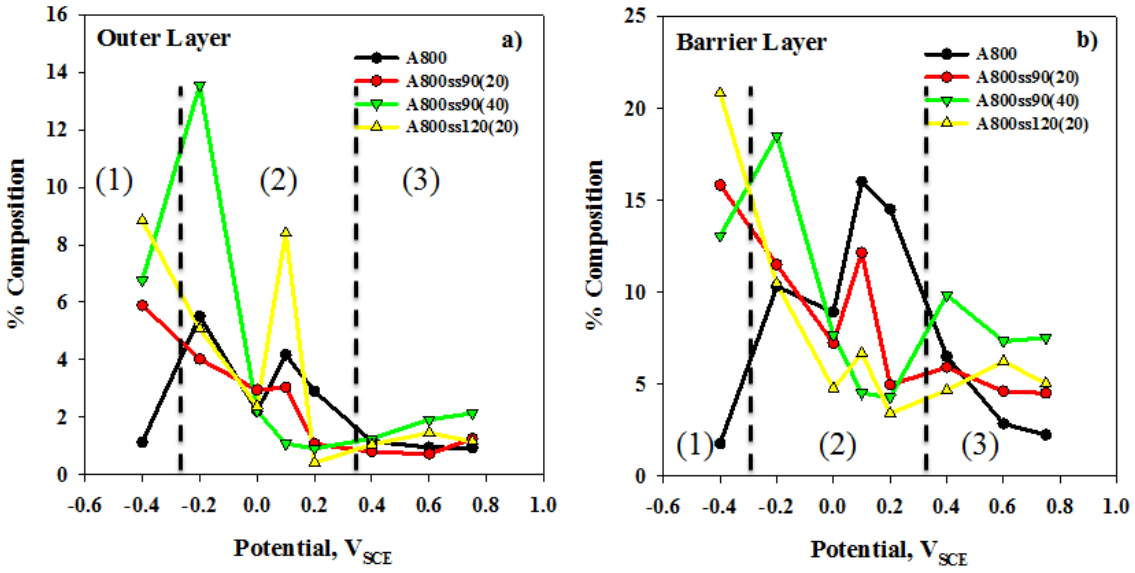

Figure 7.16 Changes in the S concentration in the (a) outer and (b) barrier layer of the oxide films formed onA800, A800ss90(20), A800ss90(40), and A800ss120(20).

Despite some erratic behaviour on two of the SMAT electrodes two general features are noteworthy. The S content of the surface of the three SMAT electrodes is higher than that of the untreated A800 electrode in the pre-passive (1) and transpassive (3) regions. This trend is similar to that for the accumulation of Fe in the outer regions of the film (discussed above). This mobility of S and Fe to the outer layers of the film in these two regions confirms that ion mobility in the passive and transpassive regions is enhanced by SMAT. By contrast, the S content of the barrier layer, especially at potentials immediately after the anodic breakdown in region 2, is considerably higher on the untreated alloy. If the mobility of S is accepted as an indicator of the resistance of the barrier layer then this high content, coupled to the high barrier layer resistance, appears to confirm the better quality of the barrier layer on A800 compared to the SMAT electrodes.

7.4 Conclusions

Comparison of the behaviour observed on the two untreated alloys (Chapters 3 and 4) showed that the barrier layer and outer layer film resistances were higher on A800 than on A600. This was attributed to the segregation of Fe to the outer regions of the film on A800. On A600, the segregation of the more noble Ni in this manner was considerably more muted. This difference is maintained on the SMAT alloys.

In general terms, SMAT on both alloys lead to a degradation of the barrier layer properties. SMAT caused a shift in E_{corr} to more negative potentials, indicating a more active behaviour. This shift was considerably larger (~ 0.1 V) on A800 than on A600 (~ 0.01 V). This can be attributed to the more active behaviour of the Fe-rich A800 than the Ni-based A600. This appears to be demonstrated by the observed segregation of Fe to the outer regions of the film, a process which occurs more readily on the SMAT A800 electrodes than on the untreated A800. This leads to the more rapid formation of the Cr^{III} oxide barrier layer and an improved barrier resistance for the SMAT A800 electrodes in the pre-passive and early potential section of the passive region. This more facile formation of the barrier layer is attributed to increased Fe mobility through the surface oxide produced on the SMAT damaged surface. While the surface of the A600 alloy is similarly damaged by SMAT, a less resistant barrier layer is produced since Ni is not as readily segregated to the outer layers of the film and hence the Cr-enriched barrier layer not as readily formed.

This improvement in barrier layer properties on the SMAT A800 electrodes compared to the untreated A800 is not maintained once the anodic degradation process

begins in the passive region. This degradation occurs more rapidly on the SMAT electrodes. A similar difference in behaviour in this region is observed on SMAT A600 electrodes compared to the untreated A600, but is not as marked as on the A800 specimens.

On the untreated electrodes this loss of barrier layer resistance, attributable to the injection of defect pathways into the barrier layer, leads to the development of an improved outer layer resistance on A800 but not on A600 (Chapters 3 and 4). This was attributed to the Fe content of Alloy 800, Fe being released to the outer regions of the film to form a partially protective Fe^{III} oxide. For the low Fe-containing A600 this does not occur to a sufficient degree to form a protective outer layer. A similar difference is observed for the SMAT A800 and A600, but the ability of this outer layer to protect the barrier layer is much lower. This more significant degradation of the barrier layer leading to enhanced ion transport on the SMAT electrodes compared to the untreated alloys is confirmed by the behaviour of the S. S is present in the inner barrier layer in the reduced form in the pre-passive and passive regions. However, once barrier layer breakdown occurs the S becomes mobile and is either lost from the film or deposited in the outer layers in a more oxidized form. This transition occurs more readily on the SMAT electrodes, confirming the more severe degradation of the passive film as the transition from passive to transpassive behaviour occurs.

SMAT of A800 was shown (above) to be detrimental to the overall structure and corrosion resistant properties of the oxide film formed on the alloy surface. As discussed in this chapter and chapter 6, the SMAT process appears to enhance the injection of cation vacancies into the barrier layer, leading to an accelerated loss of resistance, and

ultimately, a reduction in corrosion resistance. The increase in defect transport pathways created by SMAT would result in greater ion mobility through the oxide film. This was observed, especially in regions 1 and 3, through a substantial increase in Fe and S in the outer layer.

Although the passive film on Alloy 800 formed less readily than on the SMAT electrodes, it ultimately proved to be more resilient. Lower barrier layer resistance measurements on the SMAT electrodes, combined with reduced Cr concentrations in the barrier layer showed that the surface treatment hindered the performance of the passive oxide.

References

[1] D. Van Rooyen, Corros., 31 (1975) 327-337

[2] W. Yang, Z. Lu, D. Huang, D. Kong, G. Zhao, J. Congleton, Corros. Sci., 43 (2001) 963-977

[3] J.R. Cels, Corros., 34 (1978) 198-209

[4] M.G. Fontana, Corrosion Engineering, McGraw-Hill Inc. (1986)

[5] R.H. Jones, Stress Corrosion cracking: Materials performance and evaluation (1992)

[6] L.L. Shreir, R.A. Jarman, G.T. Burstein, Corrosion: Metal/Environmental reactions, Butterworth-Heinemann (1994)

[7] K. Sieradzki, R.C. Newman, J. Phys. Chem. Solids, 48 (1987) 1101-1113

[8] H. Gleiter, Prog. Mater. Sci., 33 (1988) 223-315

[9] C. Suryanarayana, Int. Mater. Rev., 40 (1995) 41-64

[10] K. Lu, Mater. Sci. Eng. R16 (1996) 161-221

[11] D.G. Morris, Mechanical behaviour of nanostructured materials, Trans. Tech. Publications Ltd., Switzerland, (1998) 70

[12] S.X. McFadden, R.S. Mishra, R.Z. Valiev, A.P. Zhilyaev, A.K. Mukherjee, Nature, 298 (1999) 684

[13] J. Lu, M.L. Sui, K. Lu, Science, 287 (2000) 1463

[14] K. Lu, J. Lu, Mater. Sci. Eng., A375-377 (2004) 38-45

[15] Y.-W. Hao, B. Deng, C. Zhong, Y.-M. Jiang, J. Li, J. Iron and Steel Research, Int., 16 (2009) 68-72

[16] R.M. carranza, M.G. Alverez, Corros. Sci., 38 (1996) 909-925

[17] E. Barsoukov, J. R. Macdonald, Impedance Spectroscopy: Theory, Experiment, and Applications, J. Wiley and Sons, (2005)

[18] K. Juttner, W.j. Lorenz, Corros. Sci., 29 279 (1989) 279-288

[19] M.C. Biesinger, B.P. payne, A.P. Grosvenor, L.W.M. Lau, A. Gerson, R. St.C. Smart Appl. Surf. Sci., 257 (2011) 2717-2730

[20] M.C. Biesinger, C. Brown, J.R. Mycroft, R.D. Davidson, N.S. McIntyre, Surf. Interface. Anal., 36 (2004) 1550-1563

[21] M. C. Biesinger, B. P. Payne, L.M.M. Lau, A. Gerson, R.St.C. Smart. Surf. Interface Anal., 41 (2009) 324-332

Chapter 8. Summary and Future Work

In this thesis the properties and composition of the passive oxide film formed on Alloy 600 and Alloy 800 have been studied in a 0.1M $Na_2S_2O_3$ solution at 25°C. The passive film formed on both alloys was comprised of a bilayer oxide with a Cr_2O_3 rich barrier layer located beneath a more porous, and hence less protective, outer layer comprising a mixture of $Ni(OH)_2$, $Cr(OH)_3$ and Fe oxides. At low potentials, the film formed on Alloy 800 was more protective due to the thicker Cr_2O_3 barrier layer formed when Fe segregates to the outer layer and Ni is retained in the surface of the substrate. The high Ni content of Alloy 600 resulted in the formation of a thinner, less resistive barrier layer since the more noble Ni segregates less readily to the outer regions of the film.

The polarization curves recorded on both alloys exhibited an anodic peak indicative of oxide film breakdown. This occurs at lower than expected potentials. On Alloy 600, this disruption lead to the destruction of the barrier layer, and the formation of a thicker, non-protective $Ni(OH)_2$ outer layer. On Alloy 800, the barrier layer was only partially destroyed with a significant portion still being observed at transpassive potentials. Protection of the barrier layer on this alloy can be attributed to the formation of a thicker outer layer of protective Fe^{III} oxide. While this layer extended the alloys corrosion resistance to higher potentials, complete destruction of the barrier layer and loss of corrosion protection still occurred in the transpassive region.

Overall, the SMAT procedure lowered the integrity of the oxide film formed on both Alloy 600 and Alloy 800. The degradation of the barrier layer can be attributed to

the presence of a high density of defect transport pathways, possibly along grain boundaries in the oxide formed on the SMAT damaged surface. These pathways can increase ion mobility through the film, leading to changes in film composition and lowered film resistances.

On Alloy 800, the increased rate of segregation of Fe to the outer regions of the SMAT damaged surface lead to the development of a Cr_2O_3 barrier layer and higher barrier layer resistances at lower potentials. However, once defect injection into the barrier layer commenced at higher potentials the higher density of ion transport pathways through the film lead to a more rapid loss of corrosion resistance on the SMAT specimens compared to the untreated alloy. A similar, though slightly less marked, degradation was observed on SMAT Alloy 600 specimens.

The future direction of this project has changed substantially given the results of this study. Originally, stress corrosion cracking tests were to be performed on the treated samples as further confirmation of the protection afforded by the SMAT process. Instead, the direction of the project will involve the analysis of the passive films formed on Alloy 600 and Alloy 800 at higher temperatures in a $Na_2S_2O_3$ solution.

Curriculum Vitae

Name:	**Melissa Gail Faichuk**
Post-secondary Education and Degrees:	University of Alberta Edmonton, Alberta, Canada (B.Sc.) 2003 – 2007 The University of Western Ontario London, Ontario, Canada (Ph.D.) 2008 – 2013
Related Work Experience:	Research Assistant Henkel KGaA Dusseldorf, Germany May 2007 – Aug 2007 Laboratory Technician University of Alberta Sept 2007 – Jun 2008 Teaching Assistant The University of Western Ontario 2008 – 2013 Research Scientist Atomic Energy of Canada Limited Sep 2013 - Present

Publications:

(1) M. Faichuk, A. Mah, G. Loppnow, Photochemistry of 5-Fluorouracil Dideoxyribonucleoside Monophosphate. Photochem. Photobiol. (2007)

(2) M.G. Faichuk, S. Ramamurthy, W.M. Lau, Electrochemical Behaviour of Alloy 600 Tubing in Thiosulphate Solution. Corros. Sci., (2010)